The University Of Sheffield.

Department Of Mechanical Engineering

Development of Novel Ultrasonic Monitoring Techniques for Improving the Reliability of Wind Turbine Gearboxes

Gary Nicholas

January 2021

A thesis submitted in partial fulfilment of the requirements for the degree of Doctor of Philosophy

ABSTRACT

Wind turbine technology, despite considered more mature compared with their renewable counterparts, still exhibits poor reliability. Wind turbine gearbox breakdowns account for the longest downtime and the costliest repair. Effective monitoring of gearbox bearings has the potential to provide early warning of bearing failure and avoid the cost of unplanned downtimes through better scheduled maintenance. In this work, a novel, non-invasive ultrasonic technique has been proposed for monitoring bearing load and lubrication during turbine operation.

The ultrasonic load measurement method depends on inferring raceway deflection from change in time-of-flight of the ultrasonic pulses. This involves accounting for other sources of contribution of time-of-flight change. To fully quantify the effect of stress on the ultrasonic signals, measurements of the second and third-order elastic constants of bearing steel have been carried out for the first time. This was subsequently used to decouple the contribution of time-of-flight change as a result of variation in stress. Since raceway and roller profiles exist for majority of the cylindrical and tapered roller bearings, typical line contact relationships are not fully representative of the contact conditions. Elliptical contact exists at low loading which gradually transitions into line as the load increases. As such, for conversion of raceway deflection into roller load, a point to line load-deflection relationship which incorporated the bearing roller and raceway profiles has been utilised. The roller and raceway profiles of the bearing were incorporated into the new relationship with relative ease and constants have been introduced to simplify the equations. Apart from that, a new method for qualitative measurement of bearing lubrication condition has been developed. The method exploits the variation in signal amplitude of a reflected wave between an adequately lubricated and insufficiently lubricated raceway surface to provide a distinction between the two conditions. The detection of lubricant within the roller inlet region would correspond to a sufficiently lubricated roller. Consequently, the lubrication condition of each individual roller can be inferred.

The ultrasonic techniques were subsequently tested on a laboratory based full-scale cylindrical roller bearing test rig. The inner raceway was instrumented with bespoke ultrasonic sensors and the lubrication condition of the bearing was successfully inferred through the ultrasonic measurements. Raceway deflection measurements were also successfully measured which provided insight into the alignment condition of the bearing assembly. The measurement techniques were further implemented onto an operational wind turbine gearbox high-speed shaft bearing.

Trends similar to those observed during laboratory testing were observed, demonstrating the robustness of the measurement method and hardware acquisition system implemented for application as a monitoring system in a wind turbine. This included the reduction in minimum reflection coefficient and increase in deflection measurements with increasing bearing load, the variation in deflection and reflection coefficient measurements for each individual roller within the bearing complement which potentially were attributed to differences in roller profiles, and the recurring patterns within the reflection coefficient measurements between roller passes, corresponding to the lubrication condition of the bearing.

ACKNOWLEDGEMENTS

Above all, a big thank you to my two supervisors Rob Dwyer-Joyce and Matt Marshall for both your guidance, support and help throughout the years. Thank you both for providing me this opportunity to do a PhD and continue learning and developing under both your guidance. I am also very grateful with all the opportunities and experiences provided to me which I have learnt a lot from them.

Working within the Tribology group has been a fun and unique experience. It has been wonderful to be a part of such a large research group. Many thanks to my colleagues and friends who have provided support not only technically but also relief during the stressful periods of the PhD. Particularly thanks to Tom Howard, Robin Mills, Xiangwei Li, Michele Schirru, Giorgos Tyreas, Olivia Manfredi, Alan Martin, and Emir Avcioglu for their help and support when I was just starting out my research. Thanks to Ben Clarke, Royce Copley and Will Gray who has worked alongside me for a portion of the project. Many thanks for all the support and help, it must have been frustrating at times.

Thank you, Luc Houpert for your guidance, ideas, and suggestions on load-deflection models. It was an honour to be able to work with a veteran in the field.

Many thanks to the chaps from University of Stratclyde, specifically David Ferguson and Edward Hart for your insight, knowledge, and help.

Thank you to Dave Butcher, who have tirelessly helped and accommodated all my technical requests throughout the years. I appreciate all the time and effort you spent on providing technical advice, despite being extremely busy.

Thanks to the folks at Ricardo, especially Sam Stewart, Michael Wheeldon and Jon Wheals for their advice and support with the technical aspect of the test rig.

Finally, thanks to my parents for all the support throughout the years.

CONTENTS

Abstract ..... **i**

Acknowledgements ..... **iii**

1 Introduction **1**

1.1 Climate change, global warming, and air pollution 1

1.2 Reliability of WT components, failure rates of bearings 5

1.3 Failure modes of WT gearbox bearings 7

1.4 In-situ ultrasonic monitoring of WT gearbox bearings 8

1.5 Research aim & objectives 9

1.6 Thesis layout 9

2 Failure modes of WT bearings and monitoring methods **11**

2.1 Wind turbine fundamentals 11

2.2 Wind turbine gearboxes 16

2.3 Types of wind turbine gearbox bearings 17

2.4 Failure modes of wind turbine gearbox bearings 19

2.4.1 Plastic deformation 21

2.4.2 Cracks and fractures 24

2.4.3 Rolling contact fatigue 24

2.4.4 Lubrication 28

2.4.5 Electrical erosion 31

2.4.6 Corrosion 32

2.5 Condition monitoring methods of bearings 33

2.5.1 Supervisory control & data acquisition (SCADA) 33

2.5.2 Temperature 34

2.5.3 Lubricant analysis 34

2.5.4 Vibration monitoring 38

2.5.5 Acoustic emissions 40

2.5.6 The potential for ultrasound 41

2.6 Methods for stress measurement 42

2.6.1 Strain measurement 42

2.6.2 Digital image correlation 44

2.7 Research gaps 45

2.8 Conclusions 46

3 Ultrasonic measurements on wind turbine gearbox bearings **48**

3.1 Fundamental principles of ultrasound 48

3.1.1 Ultrasonic propagation within medium 48

3.1.2 Speed of sound 50

3.1.3 Acoustic impedance 51

3.1.4 Signal attenuation 51
3.2 Generation of ultrasound 52
3.2.1 The piezoelectric effect 52
3.2.2 Ultrasonic transducers 52
3.2.3 Use of bare piezoelectric elements 54
3.2.4 Sensor instrumentation routine 55
3.3 Ultrasonic reflection from an interface 56
3.3.1 Reflection from a steel-air interface 56
3.3.2 Reflection from a steel-steel interface 57
3.3.3 Reflection from a steel-oil interface 58
3.3.4 Reflection from a mixed interface 59
3.4 Measurement of lubricant film thickness 60
3.4.1 Time-transit method 60
3.4.2 Resonance method 61
3.4.3 The spring model 61
3.4.4 Phase change method 62
3.5 Bearing roller load measurements 62
3.5.1 Contributions to variation in ToF 63
3.6 Application of ultrasonic reflectometry technique on bearings 65
3.6.1 Ultrasonic reflections from a bearing raceway 65
3.6.2 The ultrasonic acquisition system 66
3.6.3 Measurement of lubricant film thickness and peak roller load 68
3.6.4 Data processing for reflection coefficient and ToF 69
3.7 Conclusions 77
4 Contributions to change in sound velocity 79
4.1 Stresses in wind turbine gearbox bearings 79
4.2 Contributing factors to variation in speed of sound 80
4.2.1 Deflection 81
4.2.2 Acousto-elasticity 82
4.2.3 Total change in ToF 89
4.3 Measurement of acoustoelastic constants for EN31 90
4.3.1 Experimental Setup 90
4.3.2 Methodology 92
4.3.3 Results 97
4.4 Discussion 106
4.4.1 Ideal ToF computation algorithm 106
4.4.2 Error Analysis for cross-correlation method 106
4.5 Conclusions 109

5 Ultrasonic roller load measurement method 110
5.1 Measurement of bearing raceway deflection 110
5.2 Conversion of raceway deflection into bearing roller load 111
5.2.1 Line contact model 112
5.2.2 Point contact 115
5.2.3 Point to line contact 117
5.2.4 Comparison between contact models 118
5.2.5 ToF-Load relationship 119
5.3 Application of ToF-Load relationship 120
5.3.1 Measurement of roller and raceway profiles 120
5.3.2 Deducing reduced radius and constants from profile measurements 127
5.4 Conclusions 128
6 Measurements from a full-Scale CRB test rig 130
6.1 Introduction 130
6.2 Experimental setup 130
6.2.1 Test rig 130
6.2.2 Bearing instrumentation and pulsing system 132
6.2.3 Test matrix 134
6.3 Trends from a roller pass 134
6.3.1 General trends 134
6.3.2 Application of spring model on VG320 measurements 140
6.3.3 Filtering of false deflection and reflection coefficient measurements 142
6.3.4 Variation of deflection and reflection coefficient with load 145
6.3.5 Variation of deflection and reflection coefficient with rotational speed 147
6.3.6 Variation of deflection and reflection coefficient across contact length 148
6.3.7 Variation of reflection coefficient patterns with oil viscosity 149
6.3.8 Fringe interference investigation 151
6.3.9 Comparison of ultrasonically inferred rotational speed with demand speed 154
6.3.10 Measurements of deflection and reflection coefficient across all sensors 155
6.3.11 Comparison of reflection coefficient with theoretical EHL film values 157
6.3.12 Comparison of US measured deflection with theoretical values 158
6.4 Discussion 159

6.5 Conclusions 160
7 Field measurements from an operational wind turbine 162
7.1 Background 162
7.1.1 Wind turbine specification 163
7.1.2 Gearbox bearing specification 163
7.2 Methodology 164
7.2.1 Bearing instrumentation 164
7.2.2 Hardware acquisition 166
7.2.3 Acquisition software 168
7.3 Data availability for CMS1 & 2 170
7.4 CMS1 measurements 171
7.4.1 Generator current and voltage 172
7.4.2 Temperature 174
7.4.3 Wind and LSS speed 174
7.4.4 Gearbox input torque 175
7.4.5 Hydraulic brake pressure 177
7.4.6 Trends between CMS1 measurements 181
7.5 CMS2 measurements 182
7.5.1 Ultrasonic measurements – single dataset analysis 182
7.5.2 Trends across CMS2 measurements 211
7.6 Trends between ultrasonic measurements and turbine operating parameters 223
7.6.1 LSS speed 223
7.6.2 HSS temperature 224
7.6.3 Gearbox input torque 225
7.6.4 Wind speed 226
7.6.5 Generator power 227
7.6.6 Minimum reflection coefficient with theoretical EHL film values 228
7.6.7 Bearing lubrication condition with HSS temperature & speed 228
7.7 Discussion 231
7.7.1 Inferences 231
7.7.2 Assumptions and limitations 231
7.8 Conclusions 234
8 Discussion 236
8.1 General discussion 236
8.2 Further Work 236
8.2.1 Validation of the ultrasonic load measurement 236

8.2.2 Alternative methods for deflection-load conversion 237
8.2.3 Measurement of transient load events 237
8.2.4 Measurement of EHL lubricant film thickness and free surface lubricant on raceway 238
8.2.5 Recommendations for improvements for an US WT-CMS239
9 Conclusions 241
9.1 Original contribution of research 241
9.2 Key findings 242
9.2.1 Understanding the effect of stress on ultrasound 242
9.2.2 Influence of roller and raceway profiles on roller load 243
9.2.3 Lab-based, full-scale CRB testing 243
9.2.4 Field measurements of an HSS TRB from an operational wind turbine 246
References 248
Appendix 260

1 INTRODUCTION

The chapter begins with climate change, highlighting its devastating consequences and subsequently the importance in reduction of carbon emissions from electricity generation. The trend in wind energy is discussed, showing its continual growth and adoption, followed by the reliability of wind turbine, which highlight bearing failures as one of the main issues in key components. Subsequently, an ultrasonic-based bearing condition monitoring system is proposed for in-situ monitoring of wind turbine bearings. Finally, the aim and objectives of this research are outlined alongside the thesis' original contribution and structure.

1.1 Climate change, global warming, and air pollution

Climate change has been a trending issue in the recent years. By definition, from the UK Met Office, climate change is a large-scale, long-term variation in earth's weather patterns and average temperatures [1]. Data from the Met office, as illustrated in Figure 1.1, show an increase in global average temperature anomaly with an evident steep increment observed over the past couple decades. These measurements are consistent with those produced by its US counterparts, NASA [2] and NOAA [3] and international organizations such as the Intergovernmental Panel on Climate Change (IPCC) [4].

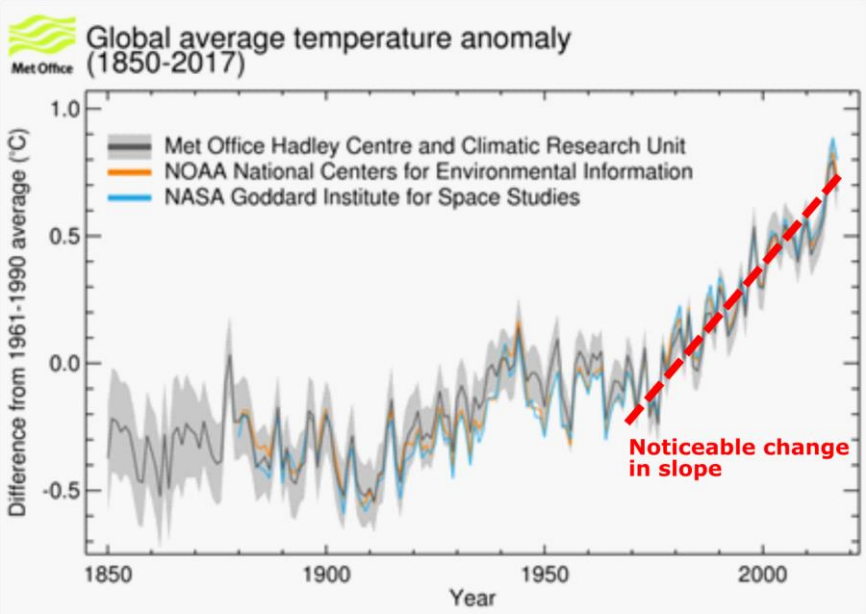

Figure 1.1 – Trend in global average temperature anomaly [5]

Earth's climate system varies with time depending on its own internal dynamics and through external factors influencing climate termed 'forcings' [6]. Internal dynamics

include ocean-atmosphere interactions that result in El Niño and La Niña which are warm and cool phases of repeating climate pattern occurring across the tropical Pacific [7]. On the other hand, forcings include natural processes affecting global temperatures such as volcanic eruptions and solar radiation and human-induced change in Earth's atmospheric content [6].

It is widely accepted that human activities [8], more specifically increasing of atmospheric concentration in greenhouse gases and aerosols, and drastic changes to land topography such as deforestation, development and construction of buildings resulted in the recent climate change. Sceptics exist, most notably the current US Republican president which discredited climate change as man-made [9].

A quarter of the atmospheric greenhouse gases are from burning of fossil fuels for energy generation and transportation with business, residential and agriculture taking up most of the remaining portion [10]. Figure 1.2 shows the different contributions of radial forcing in watts per square metre by both human and natural processes. Positive radial forcing resulting from human activity is evidently larger than the portion contributed from solar irradiation, discrediting claims that climate change is a result of natural occurrences. Aerosols and greenhouse emissions influence the climate through altering the amount of infrared radiation from the Sun, generating a warming or cooling effect depending on the atmospheric abundance and properties of these gases or particles, and consequently disrupting Earth's energy balance.

As such, human activities since the start of the industrial era have been contributing to the warming of the climate, through emissions of long-lived greenhouse gases from burning of fossil fuels. Most notable are the effects of lockdown on the environment due to the recent COVID-19 pandemic. A large drop in air pollution was observed as human activities and travel were limited. In China, restrictions imposed resulted in an immediate increase in air quality, with carbon dioxide emissions reduced by a quarter [11] and nitrogen oxide emissions halved [12]. This improvement in air quality was also seen in the UK and across Europe, due to a 37% and 27% reduction in electricity generation through burning coal and fossil fuel [13]. It is estimated that this side-effect due to lockdown saved as many as 3,425 lives in the UK, 11,000 in Europe [13] and more than 77,000 in China [14]. Several lessons can be learnt from this:

(a) Humans are the cause of air pollution and subsequently global warming

(b) Improvement in air quality reduces premature deaths from asthma and preterm births

(c) Reduction of reliance on coal and fossil fuel for electricity generation considerably reduces carbon emissions

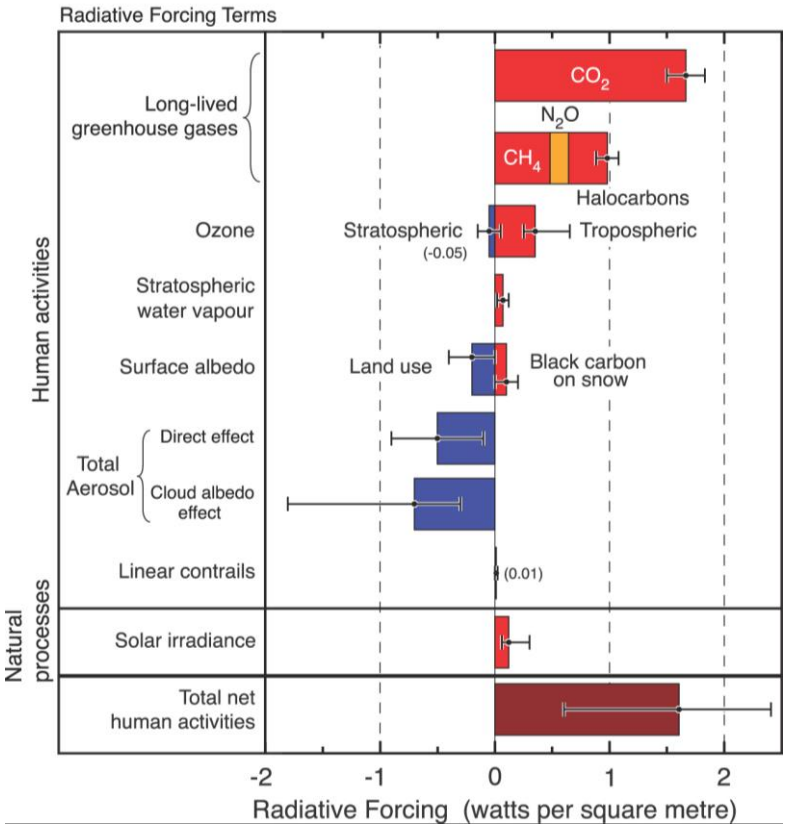

Figure 1.2 – Radiative forcing of climate between 1750 and 2005 [8]

Since 2016, there has been a gradual decline in utilisation of coal and oil for electricity generation in the UK [15], which was subsequently replaced with renewable sources. As such, a steady increase in UK's renewable energy capacity was observed. Towards the end of 2019, UK's renewable energy capacity amounted to 47.4 *GW*, with the highest share of 19.8% originating from offshore and onshore wind energy generation [15]. Figure 1.3 shows the trend in cumulative installed capacity of both onshore and offshore wind farms as well as the amount of energy generated from wind. Wind energy in the UK has seen a gradual increase in cumulative installed capacity and in 2019, the highest increase in electricity generation was observed following the opening of multiple wind farms (Hornsea One, East Anglia One, and Beatrice extension). Over the past decade, energy generation for offshore wind turbines has seen a ten-fold increase and more than four-fold for onshore wind energy.

This trend is consistent with that observed in Europe. In 2016, wind energy with a total installed capacity of 153.7 *GW*, overtook coal as the second largest form of energy generation capacity within Europe and was expected to overtake natural gas installations of just under 200 *GW* by 2019 [16]. Reasons for such increase in wind energy power generation reliance are due to the maturity of the technology and the high-power output of wind turbines compared with other renewable sources such as solar, biomass and marine. The ability of a renewable energy technology to penetrate the market is also crucial, as relatively mature technologies, such as biomass combustion fail to achieve their potential UK market penetration as opposed to onshore wind, partly due to institutional policies [17]. Photovoltaics although second to wind in terms of market penetration, are less favourable due to their prohibitive cost and low efficiency (33.7%) [18].

Consequently, it is expected that UK and EU's wind industry will continue to grow and be relied upon heavily in renewable energy generation to achieve the carbon targets set respectively whilst also satisfying society's increasing energy demands.

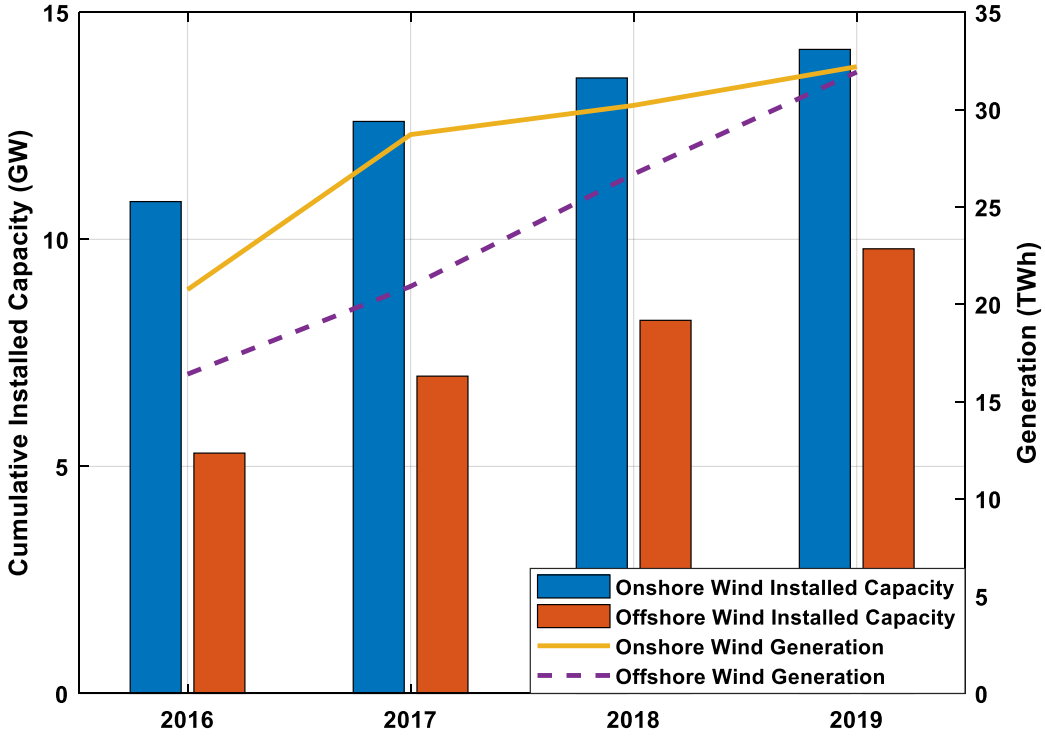

Figure 1.3 – Onshore and offshore cumulative installed capacity and wind generation for 2016 – 2019 (reproduced from [15])

1.2 Reliability of WT components, failure rates of bearings

Since its growth over the last decade, the wind market is gradually moving into maturity. This is evident as failure rates of wind turbines (WTs) per year gradually reduced across the period 1994 to 2005, as shown in Figure 1.4 with statistics from two countries, Denmark and Germany. Both countries show a downward trend in failure rates of WT per year, with Germany exhibiting a more prominent change. This is a result of larger, more complex German turbines employed which raised their average failure rates in the first few years of operation.

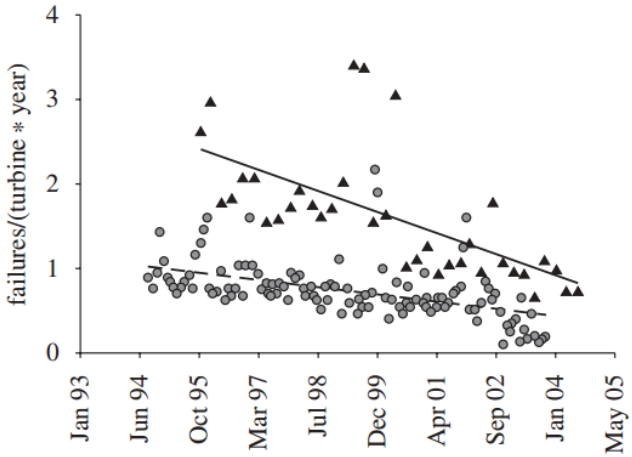

Figure 1.4 – Failure rates per WT per year in Denmark (grey) and Germany (triangle) [19]

An approximate assessment of various wind energy technologies in the UK rated onshore wind technology as 'commercially supported' in terms of maturity along with the highest indicative market penetration index of all other renewable technologies, surpassing the likes of solar and even more mature technologies such as biomass and cogeneration [18]. Despite that, wind turbines still suffer from reliability issues.

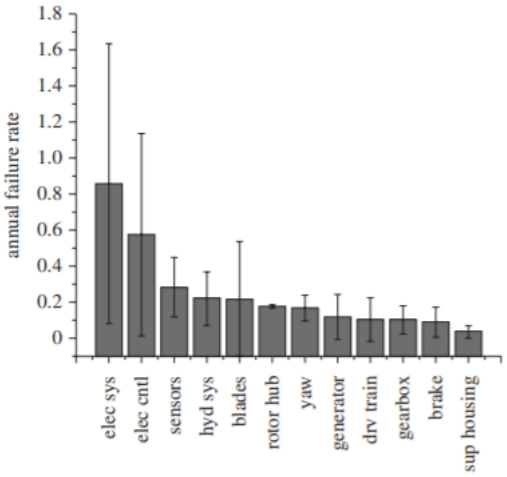

Figure 1.5 – Failure rate of WT subassemblies [20]

Figure 1.5 shows the annual failure rate for various WT subassemblies. From the data collected, amongst the WT subassemblies, electrical and control systems were found to have the highest annual failure rate, each with more than 0.5 failures per year. Despite electrical and control systems having a higher failure count, the repair cost for these are relatively low compared to tribological component failures in gearbox, yaw, and the blade pitch system [19]. Electrical and control components are small, relatively cheap, and easily installed or repaired compared to gearbox, yaw and pitch components that are heavy, large and require heavy machinery to move. The downtime for such repair will often be longer than that of an electrical or control failure, which also translates to additional loss of revenue from the non-operational turbine. Often, the bearings within these system fail prematurely and depending on the location of these bearings, under different failure mechanisms. This is surprising as the conditions within which these bearings operate would have supposedly been taken into consideration during the design and selection process.

Among these failures, it was found that gearbox malfunction typically will result in the longest downtime [21]. This prompted research into direct-drive wind turbines, eliminating the requirement of a gearbox and consequently the problems associated with it. The direct-drive technology is however still not mature enough and as a result, failure rates for direct-drive turbines are still high [22]. Consequently, the benefits from direct-drive WTs over geared WTs are not conclusive. With the rapid expansion of the direct-drive market, concerns were also raised on the amount of rare earth metals mined to produce the generators.

1.3 Failure modes of WT gearbox bearings

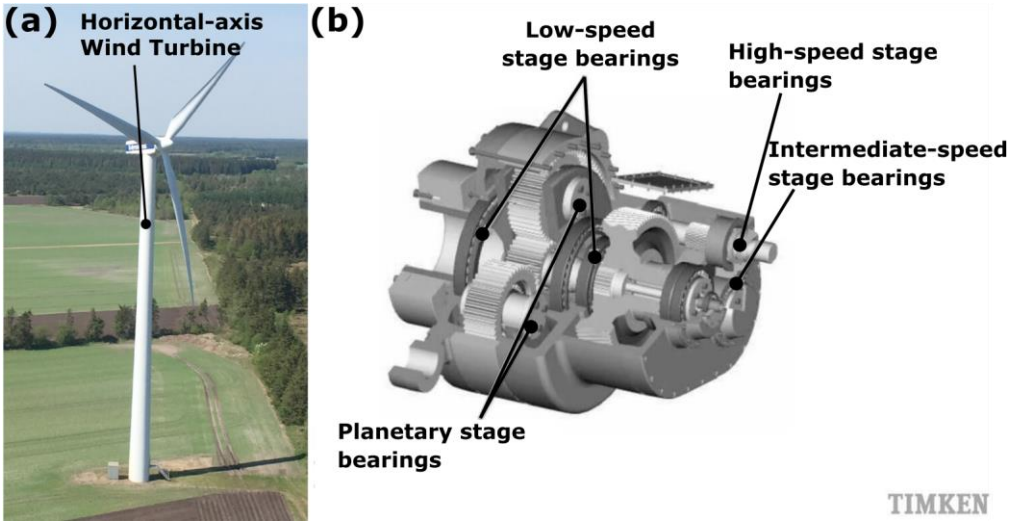

Figure 1.6 – (a) A Vestas V42 horizontal-axis wind turbine [23], (b) Structure of a typical wind turbine planetary gearbox [24]

Typical wind turbines are horizontal-axis and 3-bladed. This is illustrated in Figure 1.6(a). Figure 1.6(b) shows the layout of a typical WT planetary gearbox. Gearbox bearings vary in size and type and operate in different ranges of rotational speed depending on its position within the gearbox. Low-speed stages employ larger bearings due to the higher load bearing requirement compared to bearings located within the intermediate and high-speed stages. Cylindrical and tapered roller bearings are common types used, with some manufacturers opting for the less conventional four-point contact bearing and tube roller bearings [25]. Premature failure, defined as failure occurring prior to the bearing achieving its design life of $20 - 25$ years, occur due to multiple failure modes. Some common failure modes include plastic deformation due to overloading, fatigue failure, white etching cracks (WECs) which is linked to bearing loading history, failures resulting from lubricant and incorrect assembly of bearing.

Due to the transient nature of wind, overloading and load reversals are not uncommon in wind turbine bearings [26]. The latter is also caused by turbine operations such as emergency braking of turbine, pitching of turbine blades as it achieves rated speed [27], and engagement and disengagement of the grid supply as wind farm operators attempt to manage electricity demand [28]. This result in accelerated wear, reduction in L_{10} life of the bearing and potentially plastic deformation of the raceway and rollers. It is expected that overloading and load reversal instances resulted from turbine operations would be high. However, little is known of the magnitude and variability of these loadings.

This effect is further worsened if misalignment is present within the bearing, amplifying the wear and deformation of the contact. Moreover, overloading has been theorised to be one of the causes of White Etching Cracks (WECs) in bearings [29]. These cracks form predominantly in the subsurface and with cyclic loading, propagate rapidly to the surface resulting in material removal and raceway surface failure through White Surface Flaking.

Lubrication serves to prevent metal-metal contact and reduce wear between the rolling surfaces whilst also acting to cool and carry debris and contamination away from the bearings [30]. As such, insufficient or inadequate lubrication will have dire consequences to bearing operation. As the asperities between the two rolling surfaces contact each other, adhesive wear occurs and with continued operation, eventually two surfaces adhere, rendering the bearing inoperable. As the film fails to separate the two surfaces, failure modes such as pitting and micro-pitting are also enhanced.

Apart from that, incorrect bearing assembly and mounting can result in a multitude of issues. Bearings loosely fitted onto a mounting shaft or housing will result in adhesive wear and overheating [31, 32]. If not fixed, the gap between the components will increase, resulting in increased noise and wear [33]. Improper mounting will result in misalignment and subsequently non-symmetrical load distribution within the bearing [28]. This accelerates wear and fatigue of the bearing and result in overheating of bearing. Premature failure is also highly likely as the bearing operates outside of its design point.

1.4 In-situ ultrasonic monitoring of WT gearbox bearings

Evidently, bearing load and lubrication are crucial in ensuring that bearings operate well. As mentioned previously, the variation of bearing load during operation is less understood. Moreover, no suitable in-situ method exists for identifying whether the lubricant supplied to a bearing is effective (lubricating the roller-race interface). Lab-based electrical capacitance and optical interferometry techniques exist for lubricant film measurements. Capacitive sensors require electrical isolation of the contact elements and require the positioning and alignment of small surface-mounted sensors [34] whilst optical methods require a transparent screen to function [35]. In this work, an ultrasonically based monitoring method was proposed as a solution for in-situ monitoring of bearing load and lubrication. A time-of-flight based ultrasonic bearing load measurement method which accounted for roller and raceway curvatures has also been developed. The method has been tailored specifically for monitoring the bearing load during turbine operation. A method for

monitoring the lubrication condition of each of the rolling elements within the bearing has also been developed.

1.5 Research aim & objectives

The aim of this thesis is to develop ultrasonic-based measurement techniques for in-situ monitoring of bearing condition, specifically load and lubrication, in wind turbine gearboxes. Key objectives of the research include:

- Understand the effect of stress on ultrasonic waves and measure the second and third-order elastic constants of EN31 bearing steel
- Develop a time-of-flight bearing load measurement technique which includes consideration of roller and raceway profiles
- Develop a method for monitoring lubrication within the roller-raceway contact of rolling bearings
- Validate the ultrasonic load and lubrication measurement technique through laboratory testing
- Implement the ultrasonic load and lubrication monitoring techniques onto field measurements from an operational wind turbine

1.6 Thesis layout

This thesis is arranged in the following manner. Chapter 2 begins by introducing the basic fundamentals of a wind turbine and common wind turbine gearbox bearings and subsequently exploring the failure mechanisms of wind turbine gearbox bearings, followed by a review of the current existing monitoring systems present which also involved existing methods of measuring load and lubrication. Chapter 3 introduces the fundamentals of the ultrasonic technique, the method of generation of ultrasound, typical sensor instrumentation process, measurement of film and load using ultrasound and the data processing routine involved.

Chapter 4 consists of two parts. The first part describes in detail the contributions of change in speed of sound for an ultrasonic wave whilst the second part include investigations in the acoustoelastic effect, which is the change in sound speed as it travels through a medium under stress. Subsequently, Chapter 5 introduces the utilisation of a new load-deflection relationship which accounted for transition of contact from point to line and consideration of roller and raceway curvatures.

In Chapter 6, the ultrasonic measurements obtained from laboratory testing was analysed and discussed. Trends of the ultrasonic measurements were presented

which were associated with specific aspects of bearing operation. Chapter 7 also explores the trends of ultrasonic measurements, however on measurements obtained from a field operating wind turbine high-speed shaft gearbox bearing. Some trends observed from the measurements were similar with that seen from laboratory testing. The trends in ultrasonic measurements were also correlated with wind turbine operating parameters such as wind speed and generator power. The field measurements validated the robustness of the ultrasonic technique for utilisation as a monitoring technique in an operational environment.

Chapter 8 consists of general discussion of the potential value of the ultrasonic load and lubrication measurement system on WT durability, limitations and further work necessary to address these limitations. Finally, the conclusions of the research are detailed in Chapter 8.

2 FAILURE MODES OF WT BEARINGS AND MONITORING METHODS

The chapter begins with the fundamentals of wind turbine and common types of bearings used in wind turbine gearboxes. The causes of bearing failures and its failure mechanisms are subsequently introduced. A range of existing methods of failure detection are then discussed. Methods of measuring load and lubrication are also reviewed. Finally, the ultrasonic techniques currently proposed are presented.

2.1 Wind turbine fundamentals

A wind turbine is a machine which harnesses the kinetic energy in wind and converts it into electricity. It relies on wind, which blows through the aerodynamically designed rotor blades, to generate a net positive torque on the rotating shaft which is then converted into electrical energy [36]. Due to its nature, wind, like its counterpart solar, cannot be stored or physically moved, and thus the output of wind energy will inherit its variability and availability. This results in a difficulty in maintaining a relatively stable energy output to the grid. Today, electricity grid power lines compensate to a certain extent, wind's inability to be transported. Energy storage could help with the variable production of wind energy and facilitate planning to satisfy the fluctuation of energy demand. Short duration energy storage of less than 10 hours can be achieved through lithium-ion batteries [37]. Beyond that range, the cost renders it unfeasible. Potential solutions in the future include hydrogen energy storage cells or flow batteries.

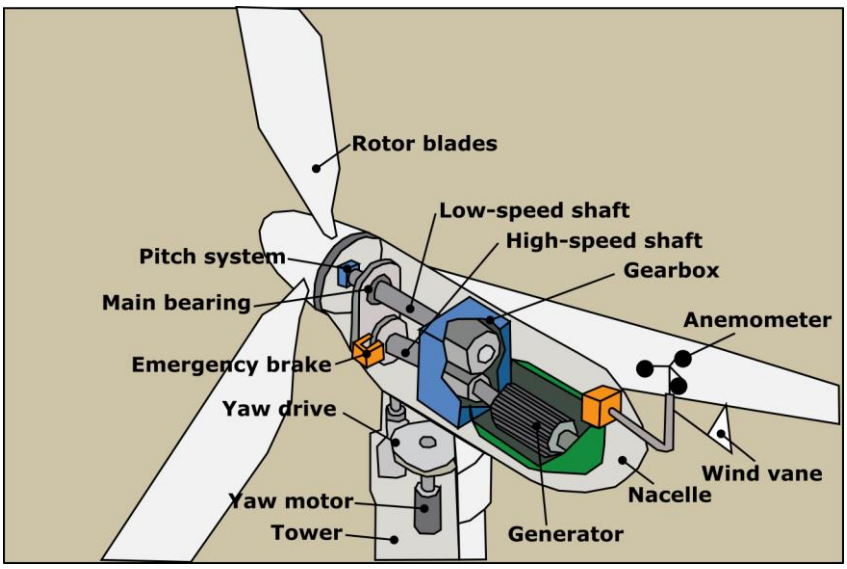

Figure 2.1 – Schematic of a horizontal-axis wind turbine (adapted from [36])

Several designs of wind turbines exist, most common are of horizontal and vertical-axes orientations. Horizontal-axis wind turbine (HAWT) consists of either up-wind or down-wind designs with the former more common due to their high efficiency. Figure 2.1 shows the schematic of the components within a HAWT. They consist of a tower, nacelle which houses the drivetrain system, yaw, and electrical systems as well as rotor blades. Most HAWTs have upwind rotors with a 3-bladed arrangement. The yaw system is necessary to keep the rotor shaft aligned with the wind direction whilst the drivetrain steps up the slow rotation of the rotor blades to the required generator input speed of around $1500\ RPM$. Most rotor blades are made out of lightweight glass fibre reinforced plastic.

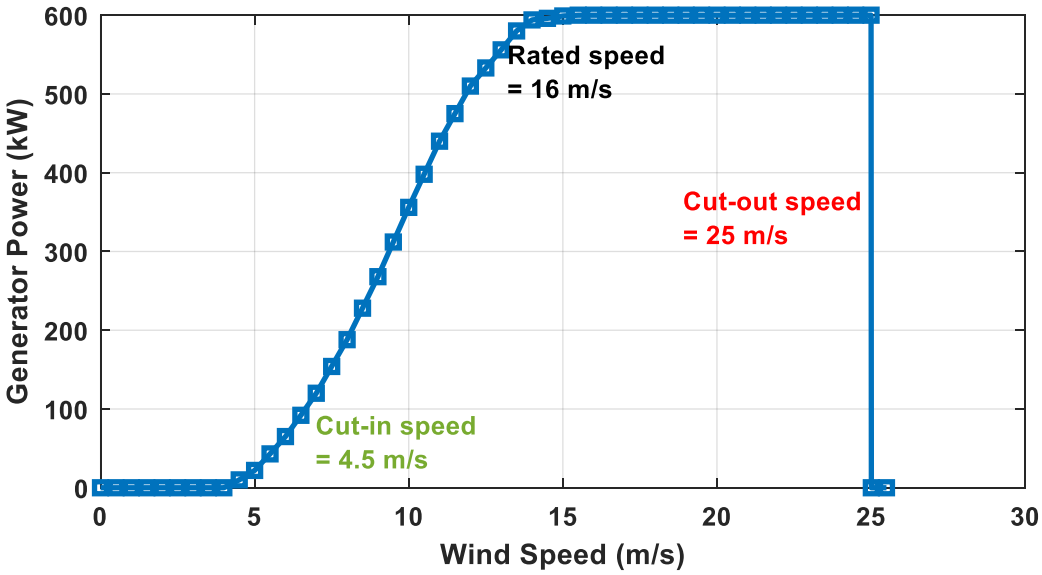

Figure 2.2 – Theoretical power curve of a Vestas V42 wind turbine [38]

HAWTs are lift propelled machines which generate lift through wind flowing across aerodynamic blades. Figure 2.2 illustrates the theoretical power curve of a Vestas V42 wind turbine. When the wind speed reaches cut-in wind speed, the lift generated is sufficient enough that the turbine blades start rotating. At this point, the turbine starts generating power which gradually increases with increasing wind speed until it reaches rated wind speed. The turbine control mechanisms then kick-in to maintain a constant rotor rotational speed for fixed power generation (rated power). This occurs between the rated wind speed up until the cut-out wind speed where the hydraulic brakes are applied, and the turbine is brought to rest to avoid damage from high winds. The constant rotor speed is required as typically generators used in HAWTs are only designed to be efficient at a fixed rotational speed with very small tolerances. It is prudent to note that the power curve assumes that the turbine shaft is rotating at its designed speed.

As stated previously, when the wind speed reaches rated value, various wind turbine control mechanisms are employed to maintain constant rotor rotational speed. Two main control mechanisms exist for HAWTs, namely pitch and stall regulated. For pitch regulated WTs, when the generator power output is excessive, the rotor blades are rotated out of the wind to reduce or limit the power generation. This is usually achieved with hydraulics. For passive stall regulated WTs, the rotor blades are designed in a way that would prevent excessive lifting force to act on the rotor blades. When the wind speed is excessively high, a turbulence is induced on the pressure side of the rotor blades which prevents the lifting force of the rotor blade to act on the rotor.

Apart from that, a turbine is also classified as constant-speed or variable-speed which impact electricity generation differently. Figure 2.3 shows the relationship between turbine power and shaft rotational speed for wind speeds of 7, 9, 11 and 13 m/s for both fixed-speed and variable-speed wind turbines. Separate dome-shaped curves exist for each wind speeds and consequently a maximum point exist for each wind speed, designated as P, Q, R and S within the plot. For the fixed-speed control scheme, the shaft speed was limited at 28 m/s and as the wind speed increases, the turbine power tracks vertically through points U, Q, V and T. Clearly these are not the maxima of each wind curve, which causes poor efficiency due to its inability to track maximum power. A variable-speed wind turbine on the other hand is designed to run at maximum power production points of P, Q, R and S, however this requires more complicated electronics and higher cost.

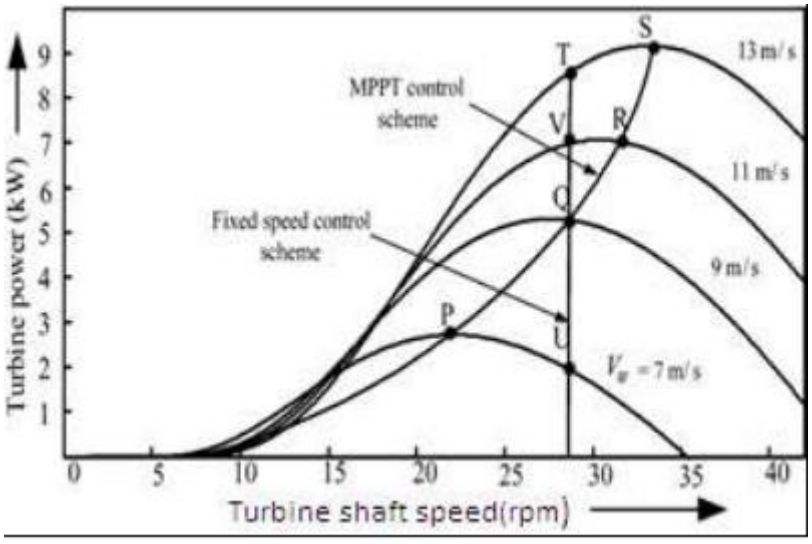

Figure 2.3 – Relationship between turbine power and shaft rotational speed [39]

Fixed-speed WTs employ induction generator such as squirrel cage or wound rotor (SCIG, WRIG), connected directly to the grid through a coupling transformer. A

capacitor bank is used to reduce reactive power compensation. They are favoured due to their low cost and simplicity.

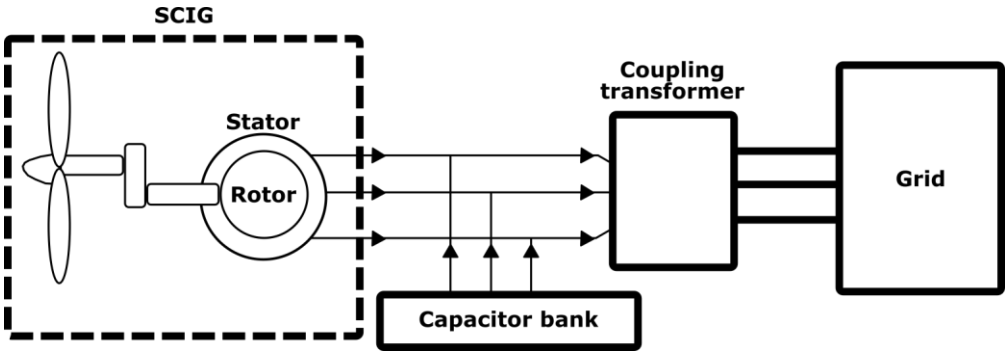

Figure 2.4 – Line diagram of a constant-speed wind turbine [40]

However, there are several other drawbacks of the system apart from the lower power conversion efficiency mentioned previously. A constant-speed wind turbine provides additional mechanical stress to the system. Due to the shaft rotating at constant speed, variations in wind speed are converted into torque pulsations which result in mechanical stress [41]. This is alleviated through design of higher safety factors for the drivetrain and gearbox components. Moreover, the power generated from a fixed-speed wind turbine varies with wind fluctuations. Any variation in wind speed is transmitted through the drivetrain into the grid. Pitch regulated constant-speed wind turbines compensates for minor wind fluctuations, however, is unable to alleviate sudden gusts. Due to the output power constantly varying with wind speed, the voltage fluctuations require constantly varying input of reactive power from the grid [41], resulting in line losses.

For variable-speed wind turbines, the rotor speed of the induction generators is adjusted through a converter system. The converter system adjusts the rotor speed through varying the rotor current which subsequently vary the torque-speed characteristic. They are further categorised into three different types according to the type of converter system utilised. These are wound rotor induction generator (WRIG) with variable speed resistance, doubly fed induction generator (DFIG) with rotor converter and variable speed wind turbines with full power converter [41]. Figure 2.5 illustrates the line diagrams for the various configurations of variable-speed wind turbines. In WRIGs, the power converter is used to vary the resistance of the rotor and subsequently the rotor current and torque-speed characteristics. The rotor is however not connected to the grid. In DFIGs, the wind turbine is connected to the grid through a three-winding transformer. Two of the windings connect the stator to the grid whilst the remaining winding connect the rotor to the grid via an AC-DC-AC converter. This configuration allows for rotor speed and

reactive power input control, leading to power quality improvement of the system. A variable-speed wind turbine with full power converter can be utilised alongside a SCIG, DFIG or a synchronous generator. Due to the full power converter, better power quality is transferred to the grid. When a synchronous generator is used at low speed with multiple poles, a gearbox is not required, and the system becomes a direct-drive wind turbine.

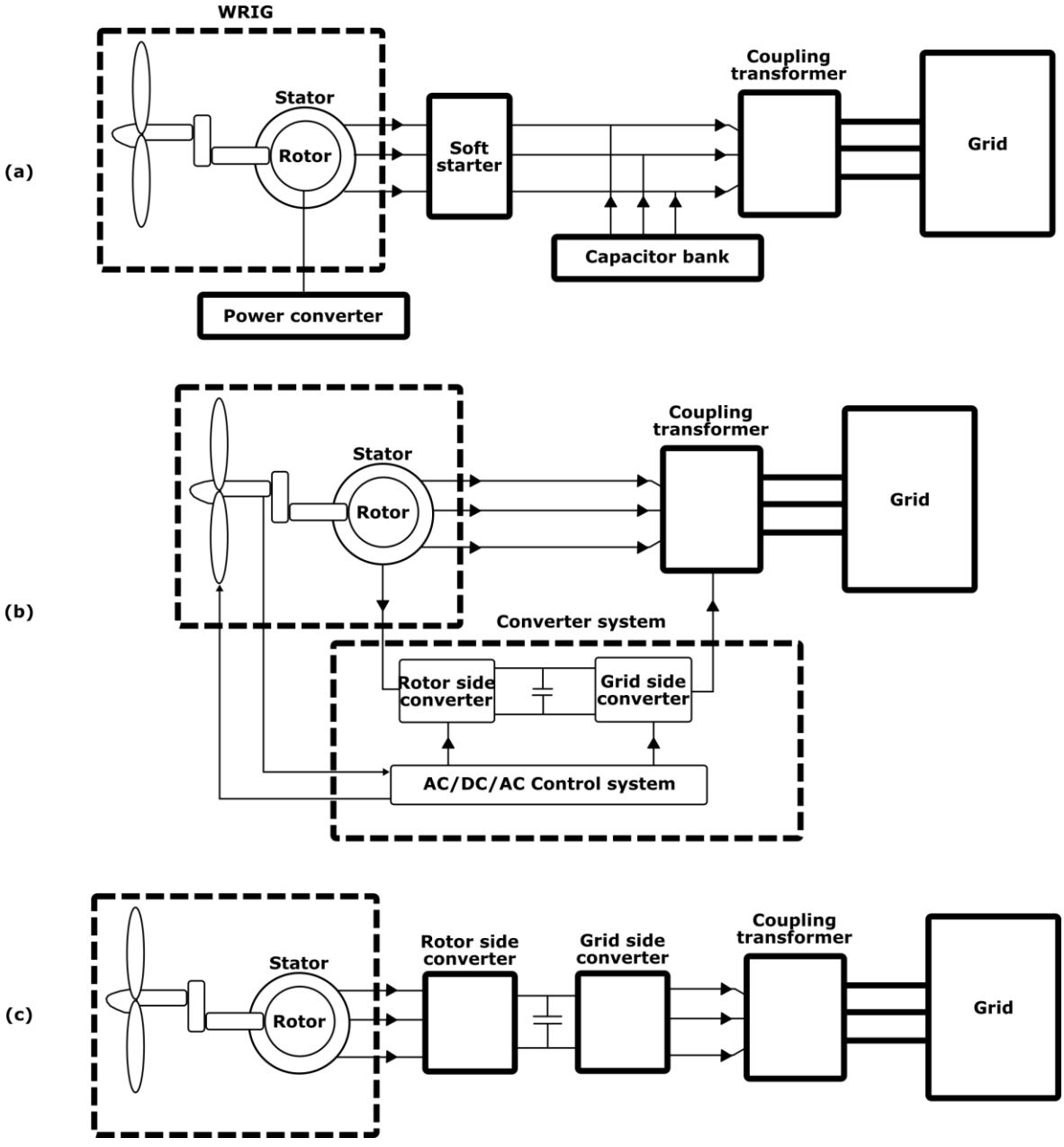

Figure 2.5 – Line diagrams for (a) wound round induction generator (WRIG), (b) doubly fed induction generator (DFIG) and (c) full power converter variable-speed wind turbine

$$P_{ideal} = {}^{1}/_{2}\, C_p \rho A V^3 \qquad (2.1)$$

Ideal turbine power, P_{ideal} is related to wind speed, V through Equation (2.1) where C_p is the power coefficient, ρ is the density of air and A is the rotor swept area. The power coefficient determines the portion of kinetic wind energy that is able to be converted into electrical energy, with an ideal value of 0.59. Current wind turbines can typically achieve a power coefficient of 0.35-0.45 [42]. However, this does not consider the mechanical losses from gearbox, bearings and generators which will further decrease the portion of wind energy converted into electricity. From the equation, a two-fold increase in wind speed will result in an eight-fold increase in power. It is desirable thus to design wind turbines that operates at high rated wind speeds. However, operating at higher wind speeds will also increase the stresses the tribological components within the turbine experience, accelerating failure and resulting in more frequent maintenance and repair.

2.2 Wind turbine gearboxes

Typical wind turbine gearboxes employ planetary gearing systems rather than parallel axis gearing systems. The epicyclic gearbox allows for high gear ratios whilst maintaining a small nacelle footprint. Figure 2.6 illustrates the typical architecture of a single stage epicyclic WT gearbox. The main low-speed rotor shaft is connected to a planet carrier which holds multiple planet gears. These planetary gears mesh with the stationary annulus, resulting in planetary rotation. The rotational motion drives the sun gear and subsequently transmits rotation to a series of parallel stages which step up the rotational speed to match the requirement of the generator (typically between 1500-1650 *RPM*). Two stages are typically employed, intermediate and high-speed stages before connecting to the generator.

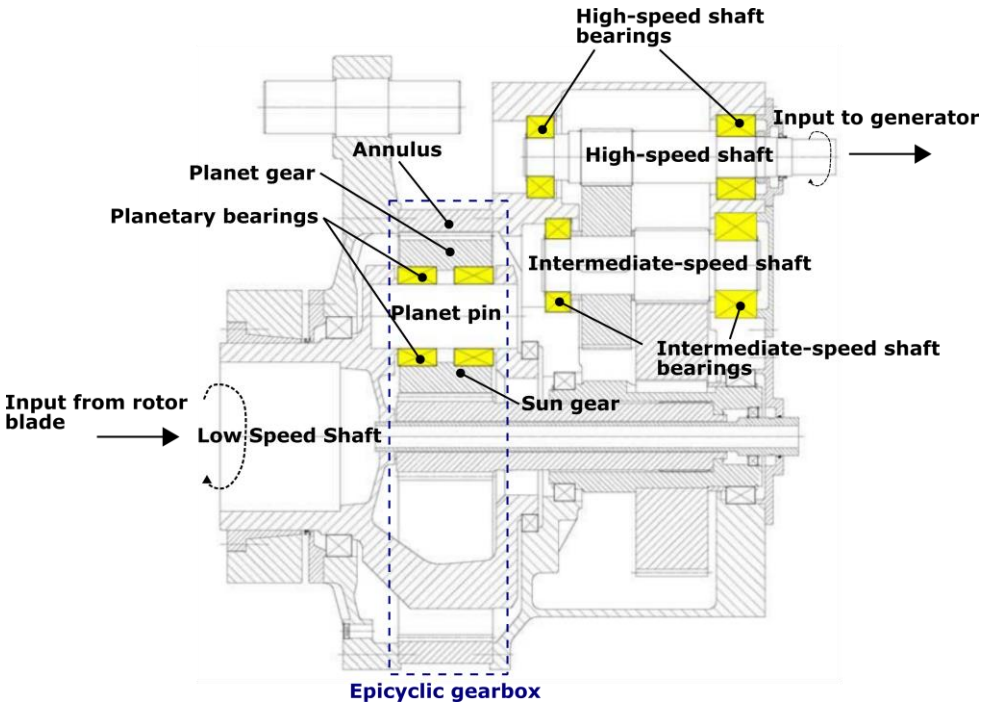

Figure 2.6 – Cross section of a typical single stage epicyclic wind turbine gearbox (adapted from [43])

2.3 Types of wind turbine gearbox bearings

Bearings within the wind turbine gearbox are utilised to support shafts in various stages and subsequently will vary in their size and type. Figure 2.7 shows the position of wind turbine gearbox bearings and their failure occurrence rate and mode. The planetary bearings located on the low-speed shaft are typically the largest bearing within the gearbox [44]. Bearings located at intermediate and high-speed stage bearings are typically less loaded and thus smaller. They, however, are still required to withstand both axial and radial loads. From the figure, gearbox bearings in different position fail under a different mode. The occurrence rate of failure was observed to be dependent on shaft rotational speed with the low-speed planetary bearing having the lowest failure rate and the high and intermediate speed stages having the highest failure rate. The types of bearing typically employed in a wind turbine gearbox are cylindrical and tapered roller bearings. These are illustrated in Figure 2.8.

A cylindrical roller bearing (CRB) is utilised when high radial bearing capacity is required. The inner and outer raceways and also the rolling elements are made of EN31 high carbon alloy steel, typically heat treated to $\sim 700\ HV$. The rollers are typically harder, which is thought to reduce bearing damage. The typical configuration of a CRB is single row, however multiple row configuration exist which

increase the radial load-carrying capacity of the bearing. Each row consists of evenly spaced rollers distributed around the circumference of the bearing. The rollers are held in place through a cage, typically made of brass or bronze. During operation, either the inner or outer raceway is held stationary, typically mounted onto a static housing component whilst the other is attached onto a rotating shaft.

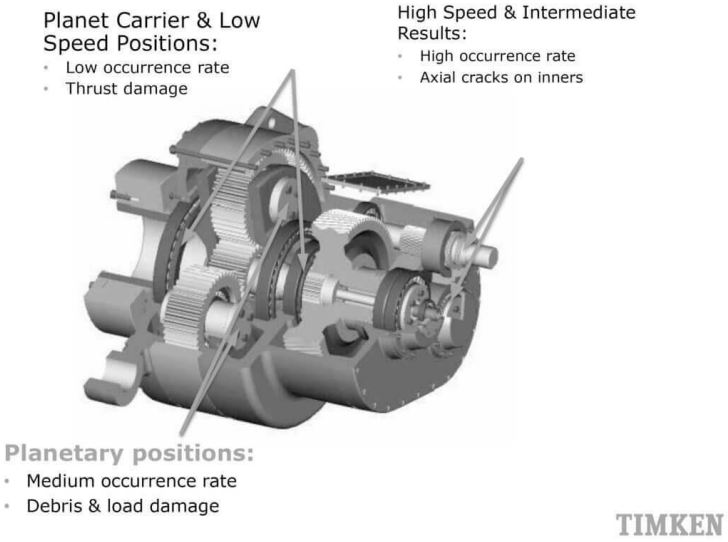

Figure 2.7 – Schematic of a typical wind turbine gearbox with critical bearing positions highlighted [24]

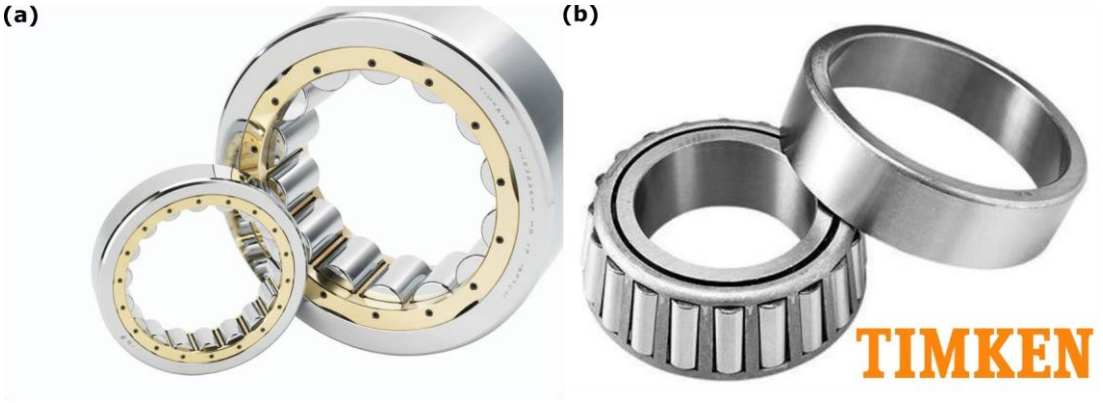

Figure 2.8 – A (a) radial cylindrical and (b) tapered roller bearing [45]

Unlike a CRB which can only withstand a small amount of thrust loading, a tapered roller bearing (TRB) is designed to support both radial and thrust loading. These were invented by *TIMKEN* in 1898. The inner raceway is termed the cone whilst the outer raceway is called the cup. Due to the difference between the cone and cup angle, a force component exist which drives the tapered rollers against the guide flange [43]. TRBs are typically designed with no clearance or play. The cone and cup angle can be increased or decreased depending on the magnitude of the thrust load

desired to be supported. TRBs are typically mounted in pairs with the bearings facing away from each other or towards each other, ie. back-to-back or face to face arrangements. Multiple-row configuration also exist for heavy radial load applications such as rolling mills [46]. The cage for TRBs are typically one-piece and thus cannot be taken apart. These two bearings are preferred over deep groove ball bearings (DGBB) for gearbox applications due to their high static and dynamic loading capacity. Instead, DGBBs are used in generators under medium radial and axial loading and high rotational speed.

Due to the small contact area at the roller-race interface, contact stresses are high and the presence of edge loading would drastically reduce the bearing life. To alleviate this, rollers are typically crowned as illustrated in Figure 2.9. This also minimizes the effect of misalignment. Multiple roller profile exists such as blended edges, multi radius profiles and logarithmic profiles [47, 48]. The exact micro-geometry however is not available in the public domain as these are closely guarded secrets among bearing manufacturers.

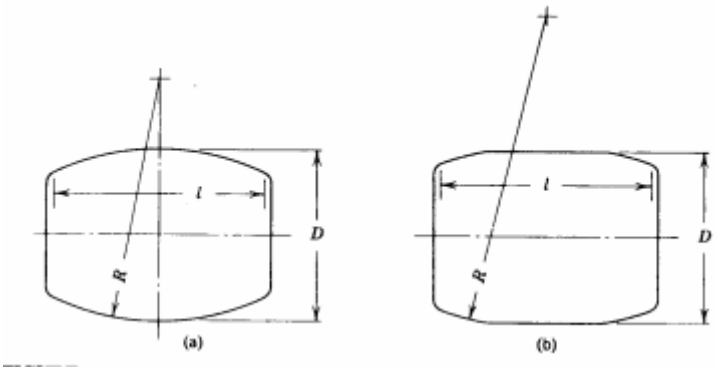

Figure 2.9 – Profile of (a) a fully crowned spherical roller and (b) partially crowned cylindrical roller [46]

2.4 Failure modes of wind turbine gearbox bearings

As mentioned previously, bearings positioned at different locations within the gearbox would have different and possibly even multiple failure modes due to the subjected operating conditions and type and size of bearing. This section aims to classify these failure modes in terms of its characteristics in hopes of better understanding the failure mechanisms to develop methods of mitigation.

The definition of a failed bearing is one which ceases to operate as intended, rather than it being completely obliterated [46]. The life of all products including bearings are finite, despite ISO 281:2007 calculations demonstrating that a bearing operating at stress below the fatigue limit and well lubricated would have infinite life. This is

because the fatigue limit concept is based upon testing on a small-sized bearings which has a smaller probability of having inclusions within them. This would not hold for large bearings as they would have imperfections and inclusions within their microstructure which serves as crack initiation sites and eventually resulting in failure. Through normal and ideal operating conditions, bearings fail through rolling contact fatigue (RCF). The typical L_{10} design life of a wind turbine gearbox based on RCF as the failure mode is between 20 – 25 years. Gearbox bearings which fail before then will be classified as premature failure. WT gearboxes however can easily consist of more than 10 bearings [49] and if each of these bearings have a 10% chance to fail in less than 20-25 years, the probability of one or more gearbox bearings failing within the design life is 83.33% including the main bearings, gearbox, and generator bearings. Research conducted by Musial et al. [21] on the reliability of wind turbine gearboxes found that most gearbox problems are generic in nature and not a result of poor adherence to design practices. Majority of WT gearbox failures were also found to be a result of bearing degradation. Figure 2.10 was produced in attempt to summarise the vast array of documentation present on bearing failure modes and causes. Majority of the failure modes are associated with either load or lubrication of the bearing. The five main causes of bearing failure were initially identified and considered unavoidable. These are listed below from high occurrence rate to low. The thesis would try to address the varying and unpredictable loads through directly measuring these loads using ultrasonic sensors.

- Exposure to excessive and varying bearing loads, including load reversals resulted from transient wind conditions or wind turbine operation
- Insufficient or excess lubricant within the bearing and the use of contaminated lubricant and unsuitable lubricant selection
- Incorrect mounting, assembly or preload application of bearing, incompatible bearing selected
- Chemical corrosion of bearing surfaces primarily resulting from friction or humidity.
- Presence of electrical current due to leakage or from lightning strikes

Subsequently, each failure mode is discussed in detail within their respective sections.

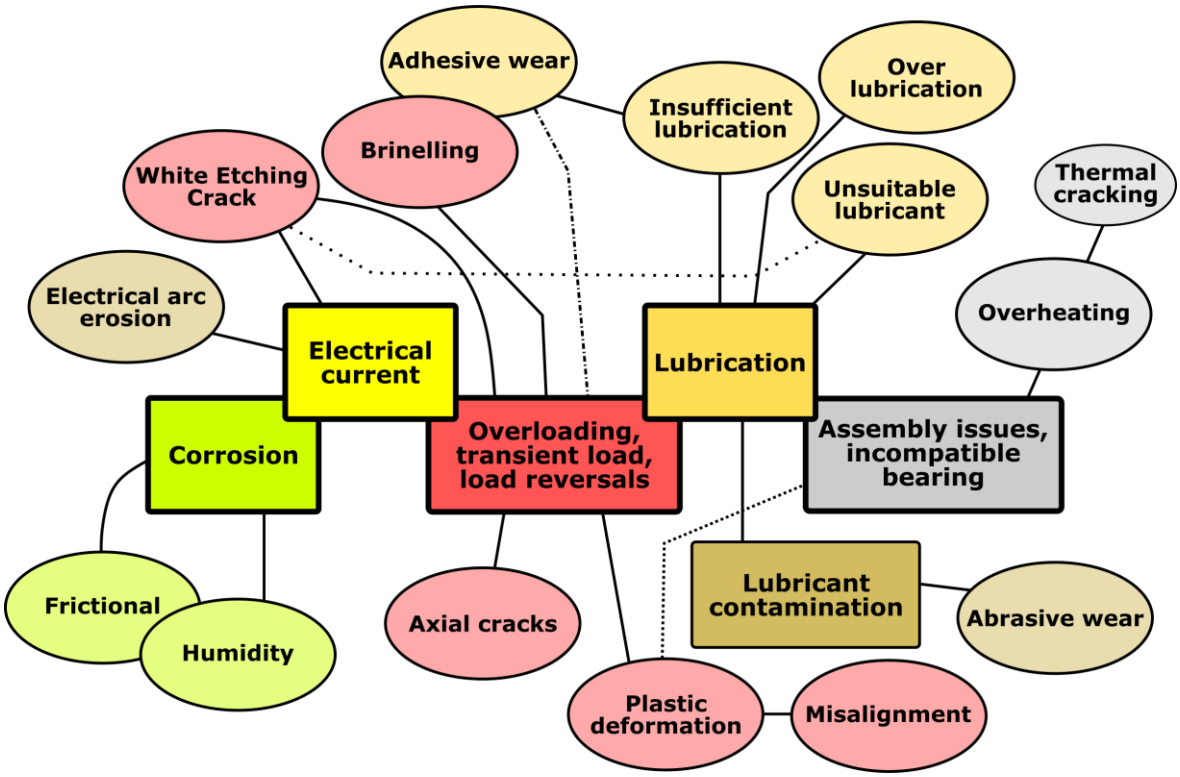

Figure 2.10 – Failure mechanisms of a wind turbine gearbox bearing

2.4.1 Plastic deformation

Plastic deformation occurs when a material is loaded beyond its elastic limit thus deforming permanently. The process is thermally activated in the microscopic scale and resulted from the motion of dislocations within the stressed material [50]. As such, it is resulted from loading beyond the static and dynamic loading limit of the bearing. Plastic deformation can occur in either macro or micro scale and the subsequent failure mode would vary. A macroscale plastic deformation occurs across a large region, ie. a deformed raceway or tiny indentations on the raceway. A microscale plastic deformation occurs within the microstructure of the bearing and would not be visible.

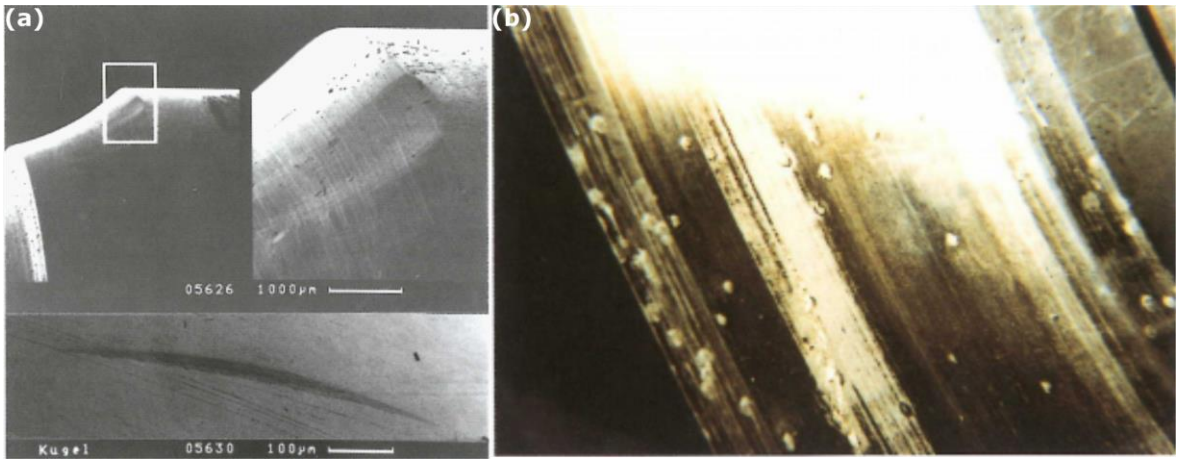

Figure 2.11 – Consequences of plastic deformation: (a) deformed raceway surface due to overloading, (b) indentations on raceway surface resulted from foreign bodies [51]

Figure 2.11 shows the damage on two bearing specimens, resulted from plastic deformation. A consequence of plastic deformation in this case is bearing misalignment. Due to a permanent change in geometry of the rollers and raceways, rollers may not move within their original design path, giving rise to uneven loading, overheating and vibration issues [52].

Poor selection of mounting material or installation practices also contributes to misalignment and plastic deformation. Bearings mounted on rubber bushings frequently encounter misalignment problems. This is a result of the rubber bushings deflecting under high torques and stresses [53], subsequently misaligning the assembly. The deterioration of rubber bushings also results in relative motion between the housing or shaft and the raceway surface. Consequences of misalignment and loose fittings can be seen in Figure 2.12. The tilted track on the TRB resulted in uneven loading and subsequently spalling on the edge of the raceway. On the other hand, relative motion between the mounting and outer raceway resulted in overheating and fretting corrosion [33] and subsequently the discolouration and scored tracks around the circumference of the raceway. If operation is continued, under excessive friction, the high frictional heat can potentially lead to thermal fracture, albeit unlikely in a rolling contact. Thermal cracks propagate axially, perpendicular to the direction of rotation [54].

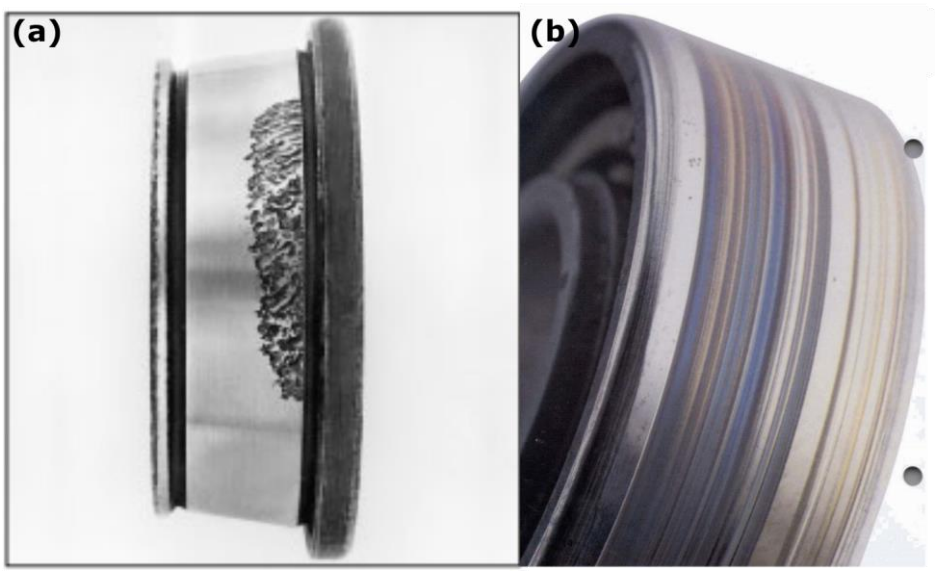

Figure 2.12 – (a) Spalling on a misaligned TRB track [55] (b) Scored marks and discolouration resulting from loose mounting [33]

Brinelling

Brinelling damage can be categorised into true or false brinelling. True brinelling is a failure mode also caused by overloading, resulting in plastic deformation of raceway surfaces. It can be characterised by uniformly spaced raceway indentations and is also a cause of increased vibration and noise [33]. The indentations are also called Brinell marks. Figure 2.13(a) shows these indentations on a ball bearing inner raceway.

False brinelling on the other hand, occur as a result of fretting wear. The main cause is not due to excessive loading, but a lack in rotational motion and vibrations or surface oscillation. Due to the small oscillatory vibrations, the lubricant is pushed out of the roller-raceway contact and this accelerates wear. The wear debris formed subsequently oxidizes and accelerate the process even more [33]. For CRB or TRBs, the wear marks appear elliptical pointing in an axial direction, perpendicular to the rolling direction. False brinelling is a well-known failure mechanism for wind turbine pitch bearings [56]. Handling and transportation of pre-assembled machines can also result in false brinelling as the bearing is loaded under static conditions and the vibrations induced from transportation is potentially sufficient to cause false brinelling [57].

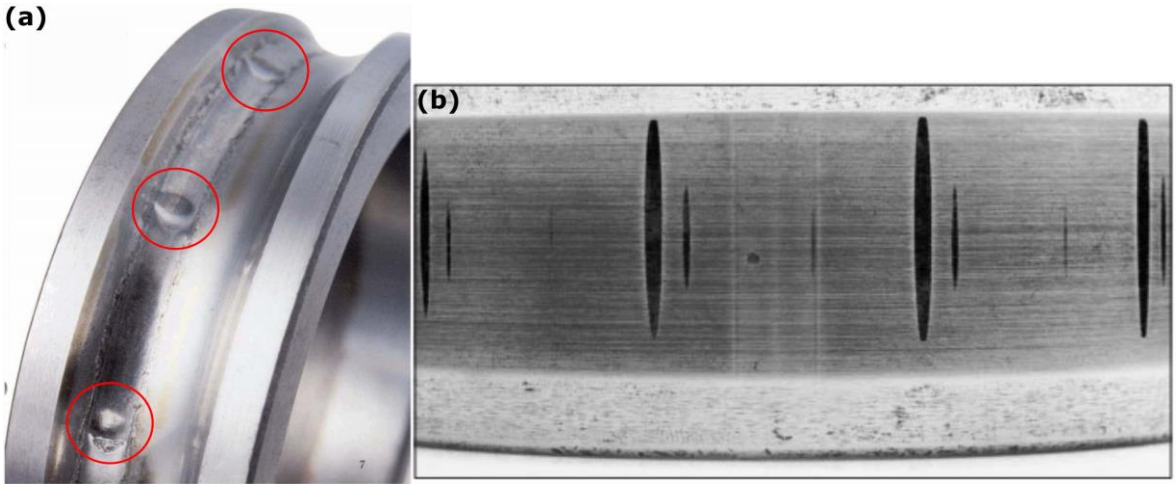

Figure 2.13 – (a) True brinelling on a ball bearing raceway [33] (b) false brinelling on a CRB inner raceway [55]

2.4.2 Cracks and fractures

Cracks and fractures of a bearing component is driven by multiple factors such as temperature, loading and intensity of load application [58]. Fractures of a component are resulted from propagation of cracks. They are categorised into 2 different types, namely forced and thermal fracture [44, 59].

Forced fracture

Forced fracture is a rare occurrence in bearings and is a result of overloading or edge loading which causes stress concentration exceeding the tensile strength of the material [59]. Impact due to poor handling during bearing mounting or dismounting also causes this. Excessive interference when mounting results in the high tensile stresses, causing the fracture. Tensile stresses do result from friction but is not sufficient to cause fracture. An axial crack, perpendicular to the direction of rotation is apparent on the failed specimen. Figure 2.16(a) shows an inner raceway of a CRB failed through axial cracking. The axial crack can be seen to nearly propagate fully through the width of the bearing. Fractures differ from rolling contact fatigue as the latter requires many number of cycles for crack to initiate and propagate.

2.4.3 Rolling contact fatigue

Rolling contact fatigue occurs when the fatigue life of a material is exceeded, and failure is achieved through rolling contact fatigue. This is the main life limiting failure mode for bearings and it is how L_{10} bearing life are predicted based on the S-N curve shown in Figure 2.14 where τ is the shearing stress, τ_u the fatigue limit, L the bearing

life and n the stress life exponent. If fatigue limit is not exceeded, theoretically, the bearing can have infinite life. However, this is clearly not the case. The experimental results supporting the fatigue limit is based on testing of small-sized bearings. Statistically, smaller-sized bearings would have less probability of imperfections and inclusions within their matrix and thus would exhibit infinite life. For large WT bearings, this is not the case as inclusions and imperfections exist within the matrix, rendering the fatigue limit concept invalid. The surface can also fail through flaking or pitting. This mechanism of failure is unavoidable even under the best operational condition where surfaces are free of contamination, smooth, well lubricated and under no sliding.

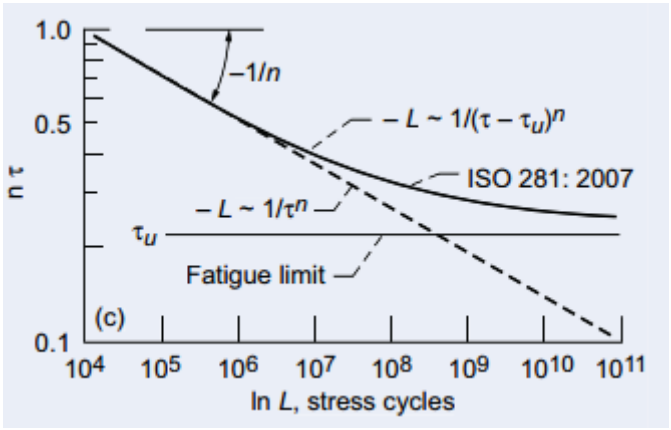

Figure 2.14 – Stress-life (S-N) curve showing life approaches infinity as applied stress approaches fatigue limit [60]

Fatigue failure initiates in the sub-surface, especially within the maximum shear stress zone of the bearing, arising through cyclic application of load onto the region of bearing raceway within the loaded zone as the rolling element traverses across the region. This can be visualised from Figure 2.15. Initiation sites within the bearing subsurface are usually voids or non-metallic inclusions, positioned typically at steep angles relative to the rolling surface [19]. With increasing cyclic loading, the crack grows and gradually propagates to the surface, resulting in material removal and spalling. Bearing surfaces with existing cracks or imperfections can also serve as initiation sites for crack propagation. The cracked surface alters the geometry of the raceway-roller contact whilst also introduces third-body particles resulting in other failure modes such as abrasive wear and plastic deformation, further accelerating bearing failure [61]. Spalling is used to describe when failure from cracks which initiate from the subsurface whilst pitting is reserved for surface-initiated material removal. Figure 2.16(b) shows a spalled outer raceway of a TRB alongside small dents

along the raceway resulted from another failure mechanism termed micro-pitting which will be explained in the subsequent section.

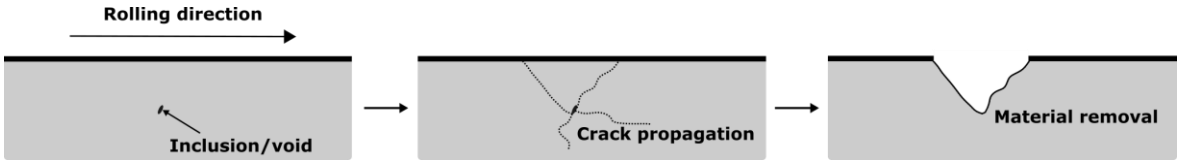

Figure 2.15 – Progression of subsurface initiated rolling contact fatigue failure

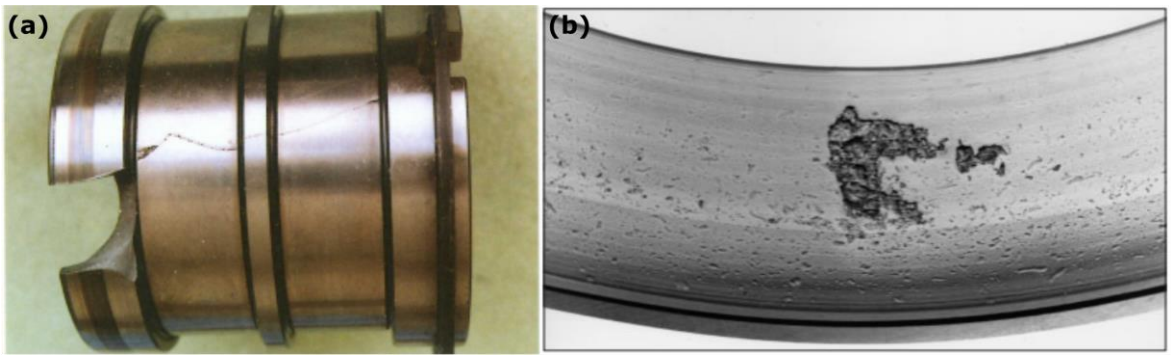

Figure 2.16 – (a) Forced fracture of a CRB inner raceway [51] and (b) spalling of a TRB outer raceway [55]

White Etching Crack

White etching crack (WEC) is a mechanism of rolling contact fatigue failure which trigger white structure flaking (WSF) on the raceways of wind turbine gearbox bearings. The premature failure can happen as early as 6 to 24 months into the service of the bearing [62, 63]. The occurrence of WEC is not a new phenomenon, with the earliest documentation dated back to 1966 on EN31 bearing steel and high-speed tool steel [64]. It is also not exclusive to the wind industry, with bearings in automotive vehicles [65], naval industry pod drives [66], hydrogen fuel cell systems [67] and paper machinery [68] all experiencing this problem.

WEC is associated with various terminologies such as brittle flaking, WSF, butterfly cracks, irregular white etching area (irWEA), peculiar white structure, white etching constituent, and hydrogen embrittlement [28]. It corresponds to a multi-branching network of cracks of typically less than $1\,\mu m$ in width [68, 69], which typically initiates in the bearing subsurface. The boundaries or region around the crack consist of microstructural alterations called white etching area (WEA). The term WEA owes its name from its white coloured appearance when examined under light optical microscopy after polishing and nital-etching of the sectioned region. WEA consists of nano-ferrite grains between $5 – 300$ *nm* in diameter or length, which are aligned in equiaxed or lamellar form alongside a fine distribution of carbide particles

[68]. Nano-hardness testing of WEA found that it is between 10 – 50% higher than the bulk matrix [68, 70, 71].

The presence of voids, non-metallic inclusions and inhomogeneities within the steel matrix serve as initiation sites for cracks which develop independently or cooperatively [28, 69]. These act as localized stress raisers which facilitates localized microstructural changes and crack initiation during rolling contact fatigue [69]. The size as well as orientation, morphology and location of the inclusions all influence the initiation and propagation of WECs [28, 72]. WEA "wings" or butterflies subsequently form at approximately 45° to the rolling surface, due to crack rubbing and high local shearing within the maximum shear stress region of the bearing.

Figure 2.17 shows the development of butterfly wing with bearing rotation for both unidirectional and alternating rolling motion. For the alternating rolling motion, butterfly "wings" in the form of "x" was observed.

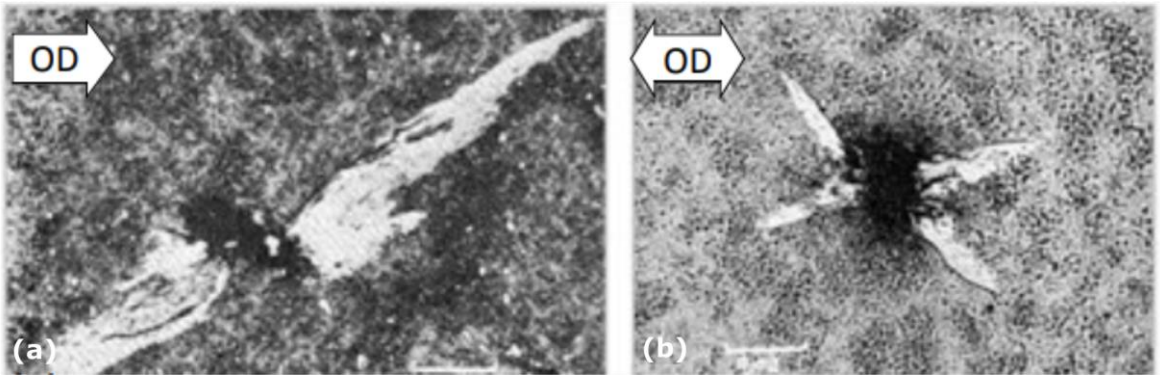

Figure 2.17 – Development of a butterfly wing as a result of (a) one directional rolling motion and (b) alternating rolling motion [73]

Figure 2.18(a) shows an image obtained using a scanning electron microscope of a network of WECs whilst Figure 2.18(b) shows a prematurely failed inner raceway with axial cracking resulted from WECs.

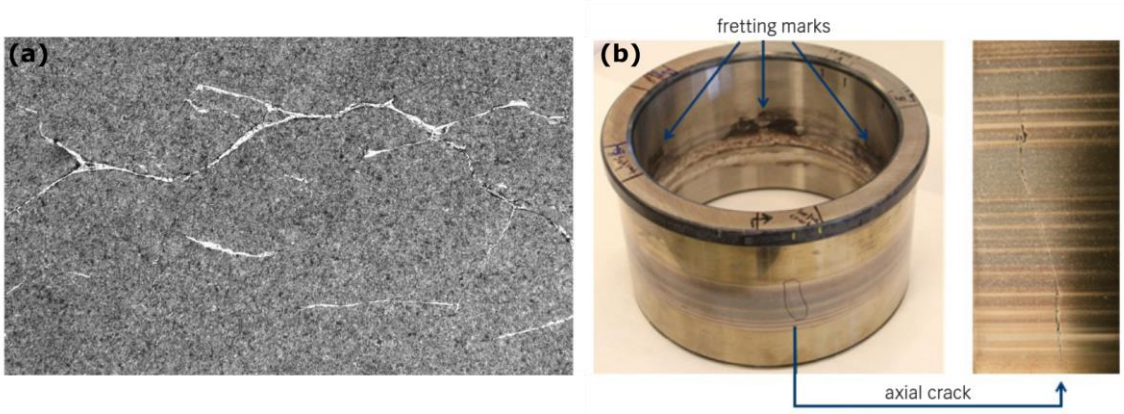

Figure 2.18 – (a) Network of WECs viewed under SEM [74] and (b) axial cracking of a bearing inner raceway due to WECs [75]

The exact cause of WECs has been a fiercely debated issue and multiple hypotheses were proposed [74-83]. Majority of these tribo-chemical drivers promote hydrogen uptake which subsequently result in embrittlement cracking of bearing. These include water contamination within the lubricant [79, 80], electric currents and potentials [81, 82], specific additives in lubricants such as anti-corrosion sulfonates [83] and high sliding kinematics [77]. Other theories for WECs include subsurface yielding at manganese sulphide inclusions [84]. More recent finding [74] found a dependence between WEC formation and the stress history of the component. A short-lived, high stress followed by steady, moderate stress resulted in early crack initiation and subsequently WECs through rubbing of crack face. This loading condition is not uncommon in WT bearings due to the transient nature of wind and thus the importance in monitoring the loading profile of the bearing during operation.

2.4.4 Lubrication

All surfaces, regardless how smooth they appear, will consist of asperities [85]. Lubrication serves as a means to prevent the asperities of two bodies from contacting and thus minimising friction and wear. The lubrication regime which a bearing operates in is determined by the lubricant viscosity, η the bearing rotational speed, ω and the nominal bearing pressure, p. Figure 2.19 shows the various lubrication regime and their frictional coefficient. The ratio between the minimum film thickness, h_{min} and the root mean square (rms) roughness of the two surfaces,

R_q termed the "lambda ratio" (Λ), for each lubrication regime is also included. Equation (2.2) shows the lambda ratio in mathematical form.

$$\Lambda = \frac{h_{min}}{R_q}, R_q = \sqrt{{R_{q1}}^2 + {R_{q2}}^2} \quad (2.2)$$

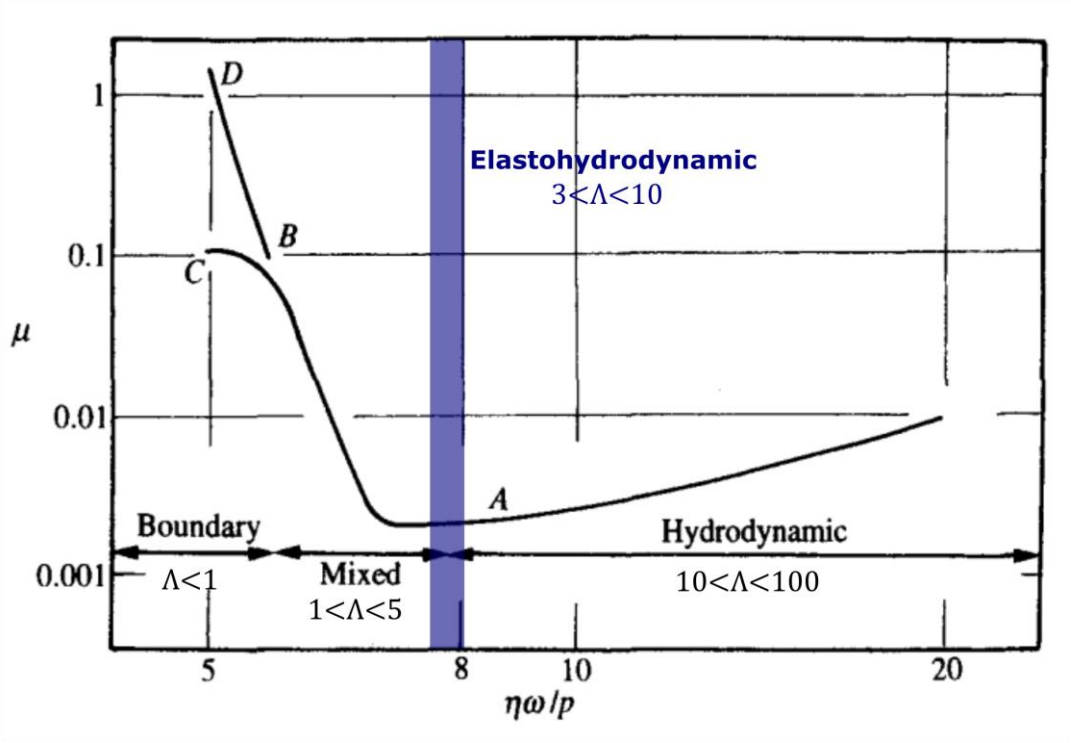

Figure 2.19 – Stribeck curve with highlighted elastohydrodynamic lubrication region where rolling element bearing operates within [85, 86]

In boundary lubrication, Λ values are less than unity. The load is supported mainly by the contact points of the asperities subsequently resulting in high friction. The pair of material under contact dictates the frictional coefficient, resulting in two very different curves (BC & BD). A silver-steel pair would follow the BC route whilst a steel-steel pair would result in the high friction BD curve. Mixed lubrication is characterised by the presence of both asperity contacts and regions with full fluid separation. The minimum frictional coefficient point where viscous shear forces are low and film separation is sufficient exists within the mixed regime. Consistent operation at this point is however not feasible as the point is unstable and small changes to operating conditions will potentially shift the operating point into boundary conditions [85]. Hydrodynamic lubrication is characterised by lubricant film thickness fully separating the contacting surfaces. Examples of this include journal and thrust bearings. Elastohydrodynamic lubrication is a form of hydrodynamic lubrication occurring in counter formal surfaces where elastic

surface deformation and lubricant viscosity increase with pressure play a key role [85, 86]. Rolling element bearings, gears and seals operate within this regime.

Failure in lubrication including insufficient lubrication, over lubrication, contaminated lubricant and poor selection of lubricant all have adverse consequences and result in premature bearing failure [87].

Insufficient lubrication

An insufficiently lubricated bearing ($\Lambda < 1$) will experience increased wear, vibration, and overheating. If the lubricant film thickness is too thin to separate the asperities, the bearing will operate in boundary or mixed lubrication. Other symptoms of failure include discoloured tracks of blue or brown colour [33]. Typical failure mechanism associated with this include smearing, seizure, scuffing, micro-pitting, and adhesive and abrasive wear [85, 87].

Adhesive wear occurs due to the high stresses experienced by the peaks of the asperities, resulting in localized bonding at the peaks [88]. The asperities subsequently break, resulting in material transfer between the two contacting surfaces. Typically, the surface which is harder will have material deposited whilst the softer surface will have material removed. Smearing or scuffing wear, illustrated in Figure 2.20(a) and (b) respectively, are types of adhesive wear where material is removed from one surface and deposited in the other. Under high loading, two surfaces with limited lubrication will seize up due to the high friction, restricting bearing rotation [89].

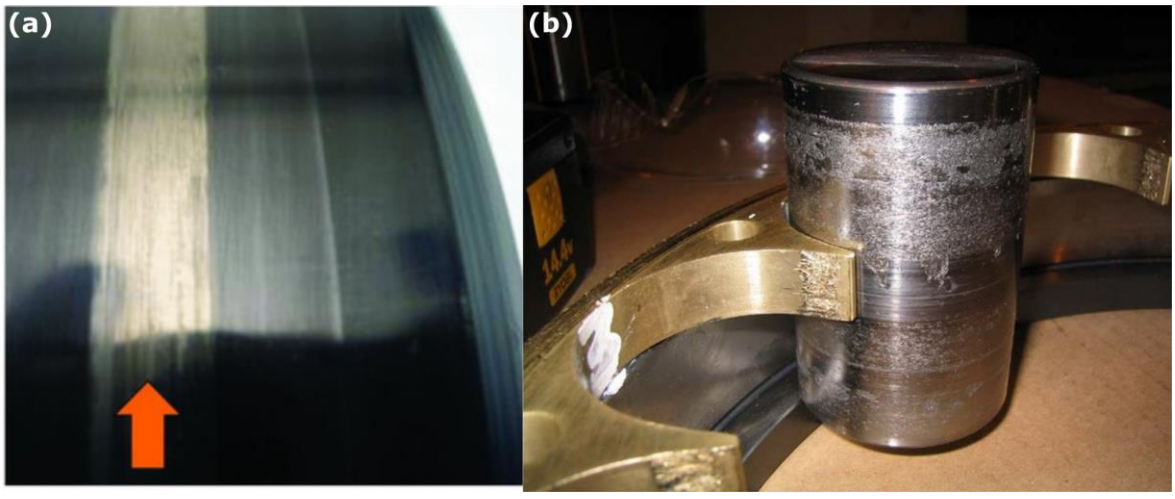

Figure 2.20 – (a) Smearing on a bearing inner raceway [90] and (b) a roller [91]

Abrasive wear can be categorized into either two or three body abrasive wear. Two-body abrasion occurs when two surfaces slide across one another, resulting in scratch marks, grooves, and polishing on the softer surface [86]. Asperities may also

break off resulting in embedded wear particles. This causes three-body abrasive wear where the harder abrasive particles ploughs into the contacting surfaces, causing surface damage on the raceway and roller. Three-body abrasive wear can also occur as a result of contaminated lubricant.

Over lubrication

The supply of lubricant exceeding the recommended amount or flowrate increases the frictional coefficient and subsequently the energy required for bearing operation. The increase in friction result in a temperature rise in the bearing which reduces the viscosity and life of the lubricant. It is reported that a $10\ ^{\circ}C$ rise in temperature above $65\ ^{\circ}C$ can reduce the life of a lubricant by 50% [92]. An unsuitable lubricant selected with a higher viscosity than required also results in the same effect.

2.4.5 Electrical erosion

Electrical erosion is caused by flow of electric currents through the roller-raceway contact interface, resulting in the material removal from the bearing roller and raceway. It is separated into two types, namely electrical pitting, and fluting [44]. These two damage can be distinguished by their wear pattern; irregular patterns are generated for electrical pitting whilst fluting produces regular pattern [55]. The source of the electricity can be from lightning strikes, leaked current from the grid or unintentionally charged components [93].

Electrical pitting

Electrical pitting is resulted from excessive voltage differences between the bearing housing and shaft. Without adequate grounding, this causes current to flow through the lubricant film separating the roller and raceway contact. The current result in sparks and arcs causing localised melting and welding of the raceway and roller surfaces [93]. Electrical discharge machining is formed from the same principle [94]. As the surfaces slide, the welded regions are sheared off resulting in surface roughening and material removal [95]. Figure 2.21(a) shows the craters or pits resulted from electrical pitting on a CRB raceway. Electrical pitting also influences the material properties around the localised melting zone, resulting in high stress concentration. These subsequently act as initiation sites for crack initiation and micro-pitting [95].

Electrical fluting

Electrical fluting is a consequence of electrical pitting and is resulted from constant passage of lower magnitude alternating or direct current across the roller-raceway

contact interface [94]. The current is typically leaked from the generator or grid [95]. Consequently, generator bearings are more prone to suffer from fluting. Rolling elements traversing across the craters generated from electrical pitting cause mechanical resonance vibration [95]. This subsequently cause brownish, equally spaced, axial shallow ridges along the circumference of the entire raceway as shown in Figure 2.21(b).

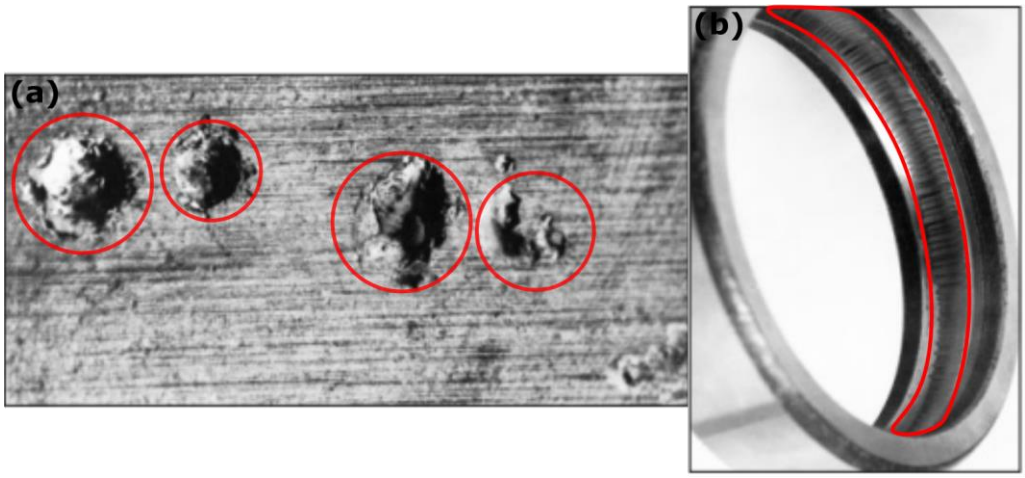

Figure 2.21 – Damage resulted from (a) electrical pitting and (b) electrical fluting [55]

2.4.6 Corrosion

Corrosion of bearings are a result of chemical reactions occurring on the bearing surfaces. This include rusting or moisture corrosion and tribo-corrosion [31].

Moisture corrosion

Rusting of metals is an inevitable process, however the process can be significantly accelerated through exposed to moisture or acids [96], as well as poor handling, packaging, and storing practices [97]. Common handling mistakes include touching bearing surfaces with bare hands. The bearing surfaces eventually decay as the material is converted into oxides, producing yellow or brown-reddish stains of various sizes and shapes. Small amount of rusts can be removed with fine grade abrasive paper, however severely rusted parts would require re-grinding and machining. If unremedied, the rust condition will worsen and eventually result in material removal through macro pitting [96].

Corrosive wear

Frictional corrosion or tribo-corrosion is the degradation of material as a result of combined wear and corrosion [31]. The relative rubbing or sliding in the presence of vibration, of two surfaces under friction and load result in the oxidation and wear of the surfaces in contact. Fretting wear can also be classified under corrosion.

2.5 Condition monitoring methods of bearings

Having reviewed the failure mechanisms of wind turbine gearbox bearings, majority of the failure modes are observed to be triggered by load or/and lubrication. Subsequently, these should be critical parameters in a condition monitoring system. The following section explores the monitoring techniques commonly employed by wind turbine operators for failure detection of bearings.

2.5.1 Supervisory control & data acquisition (SCADA)

Despite high losses [98] resulting from gearbox failures and multiple literatures [19, 21] suggesting bearing failure to be the root cause, bearing monitoring has not been widely adopted in wind turbines. The main reasons for this would be the cost of implementing sensor systems, difficulties in sensor instrumentation due to limited gearbox space.

The first monitoring system that is widely adopted is the Supervisory Control & Data Acquisition (SCADA) system. They provide information on basic turbine operational, performance and maintenance condition such as wind speed, shaft rotational speeds and torques, yaw brake pressures and even oil pressure measurements, and are commonly adopted in most modern-day wind turbines. Bearing condition are often not the focusing parameters within SCADA measurements. Consequently, they only provide an indication of general turbine health. Typically, data from each wind turbine within a wind farm is fed to a control room to ease monitoring. With some processing, the SCADA data can be used for failure prognostics and diagnostics [99]. Parameters such as the ratio of torque and speed and rotational speeds of the high-speed shaft against that of the low-speed shaft were utilised. Baseline values and trends during normal operation were initially determined which allow premature fault detection.

Due to the high amount of measurement channels and thus potential large size of data, the quality of SCADA data is typically sacrificed through reducing the number of parameters measured or the sampling time [100]. This consequently results in difficulty in failure prognostics and diagnostic using SCADA measurements. SCADA systems might also vary between turbines, hampering efforts for standardised data processing [101]. Automated processing of SCADA measurements also requires complex algorithms such as artificial neural networks and fuzzy systems to churn through large amount of data and provide an indication of turbine and bearing health [101]. Often enough, independent, more advanced condition monitoring systems are installed in addition to SCADA systems.

2.5.2 Temperature

Throughout history, the temperature of machinery components has been widely used to assess the machine operation state. A steaming, overheating car engine would indicate impending breakdown compared to one that is running at normal temperatures. Bearing issues and failures are also accompanied by an increase in temperature above steady-state operating temperature. This is associated with lubrication failure, resulting in more asperity contacts and additional heat generation, as the bearing transitions into boundary or mixed lubrication [86]. Temperature rise of as high as 5% can also be resulted from a misaligned shaft arrangement [102].

Thermocouples or resistance temperature detectors (RTDs) are often employed to monitor bearing temperatures, with a range of different types depending on accuracy, desired measurable temperature range and application. They operate based on thermoelectricity or the "Seedbeck effect" where a temperature difference between two dissimilar electric conductors will result in a voltage variation [103]. RTDs are favoured compared to thermocouples due to their higher accuracy and better stability. They however are more fragile and expensive [104]. A PT100 RTD sensor have a measurable range of $-200\ ^{\circ}C$ to $650\ ^{\circ}C$ and an accuracy between $0.1 - 1\ ^{\circ}C$ [104], well suitable for measurement of bearing temperatures.

To obtain the most accurate measurements, the sensor is required to be placed as close as possible to the rolling surfaces to pick up flash temperatures occurring at the rolling element-raceway contact interfaces. This is extremely challenging as it often requires modifications to the bearing raceways and housing, thus jeopardizing structural integrity. Consequently, sensors are often installed as close as possible to the region of interest typically on the bearing housing, lubrication inlet or outlet ports or on outer raceway. Measurements consequently exhibit a lag to the temperature at roller-raceway interface and would potentially delay failure detection. Temperature measurements are also influenced by ambient conditions and often multiple sensors are required across the wind turbine.

2.5.3 Lubricant analysis

Lubricants, apart from reducing friction, also carry away debris or contamination that might disrupt normal bearing operation [85]. The composition of used lubricant thus contains information on bearing health. With time however, the lubricant may gradually degrade and lose their main function of separating two bodies from contacting and thus the purpose of oil monitoring [105].

Three main purposes exist for lubricant analysis [106]:

- Assessment of lubricant condition to determine whether the lubricant is in healthy condition or require changing
- Assessment of lubricant contamination to ensure oil quality and provide insight to the amount of contaminant within lubricants
- Assessment of component wear to ensure normal wear levels of components

The typical testing methods employed for lubricant analysis include [107, 108]:

- Particle count analysis
- Moisture/acid content analysis
- Oxidation analysis
- Viscosity analysis
- Spectometric Oil Analysis Program (SOAP)
- Ferrography

Particle count analysis

The main drive for particle count analysis is potential for detection of wear particles within the lubricant, and subsequently crack detection. The most common particle sensing method is through particle counters which function through the principle of scattering of light. A light source penetrates the lubricant and the detector measures the amount of scatter which corresponds to the number of impurities or particles within the lubricant. Debris counter operating using a magnetic coil also exist. It operates by measuring the magnetic field disturbance resulted from debris particles. This was successfully demonstrated to be able evaluate remaining useful life of the bearing and predict spalling of the gearbox bearings through measurement of rate of debris generation and size of debris [109].

Another method of detecting presence of debris is through monitoring the electrostatic charge within the lubricant as charge generation is associated with component degradation [110, 111, 112]. The method could potentially detect onset of failure earlier compared to conventional particle counting [111], however signal processing and feature extraction (differentiating charges generating from damage and charges originating from other sources) are challenging and the accuracy of the sensor is dictated by the sensor size and resolution.

Moisture/acid content analysis

Water can exist within a lubricant in three different states (dissolved, free, emulsified) with each state having a different effect [107]. The presence of free water will result in the oxidation and rusting of bearing surfaces. Emulsified water can affect the effectiveness of the additives present in the lubricant. Hydrolysis or breakdown of water into its ionic component (H^+ and OH^-) is also problematic as the hydrogen ion causes embrittlement and WEC in bearings. The ionic components also act to reduce the lubricants' effectiveness [107].

Acid content within lubricant provides indication to the amount of water, oxidation, types of additives and chemical breakdown of products. The presence of acid such as nitric and sulfuric indicates the occurrence of combustion [107]. Quantification of acid content within lubricants is carried out using the total acid number (TAN). High acid levels potentially indicate excessive oxidation or depletion of lubricant additive which may result in corrosion [106].

Oxidation analysis

Measurement of oxidation levels within a lubricant is typically carried out through monitoring reaction by-products such as carbonates, carboxylic acids, ketones and aldehydes [113]. Increased oxidation levels are undesired as this increases the acidity of lubricant resulting in an excessive increase in lubricant viscosity and corrosion. The excessive increase in viscosity is due to the formation of large polymer by-products which cause sludging in the lubricant [107].

Viscosity analysis

Measurements of viscosity provide insight to the lubricant condition after operation and ensure viscosity is maintained after operation. Viscosity is influenced by multiple parameters including water contamination, TAN, lubricant degradation, and temperature.

SOAP

In spectometric oil analysis program (SOAP), the lubricant is subjected to a series of laboratory tests to determine the presence and extent of ferritic particles within the lubricant. This can be either done directly on the oil sample or the wear particles filtered from the oil. Various spectroscopy method exists, such as energy dispersive X-ray fluorescence (EDXRF), infrared (IR) and Fourier-transform infrared (FTIR). In EDXRF, the oil sample is excited with X-rays which upon returning to the ground state, emits fluorescence radiation. The difference in radiation wavelength emitted by different molecules within the oil allows for identification of the molecules

present in the lubricant. FTIR spectroscopy exploits the fact that all molecules absorb infrared radiation at different wavelengths. Infrared radiation is passed through the lubricant and the amount of radiation absorbed can be used to deduce and identify the elements present within the oil sample.

Ferrography

Ferrography is used to study wear of machine components through analysing the contaminants present in the lubricating oil. It can identify the stage of component wear and thus the onset of component failure. The debris present within the lubricant is initially separated and deposited onto a glass slide. The debris is then examined under a microscope to distinguish the particle size, shape, magnetism, concentration, and composition of the wear particles. The cost of conducting ferrography analysis is relatively high due to the specialised instruments required, however its benefits significantly outweigh the costs.

Sampling methods

Lubricant monitoring can be separated into two categories: real-time continuous monitoring and offline oil sampling [114]. Continuous monitoring of oil involves automated sampling and analysis of oil, thus the ability to observe trends in measurement and timely detection of failure. For offline oil sampling, routine samples of oil were taken manually and sent off to be analysed. Subsequently, feedback and recommendations will be relayed to the owner/turbine operator based on the oil analysis. Due to the prohibitive cost of online lubricant monitoring systems, manual oil sampling is often preferred [105].

2.5.4 Vibration monitoring

Vibration monitoring has been the most widely used method in wind turbine rotating machineries. [105] They are regarded as the most efficient premature fault detection method for rotating machinery [115]. Vibration sensors vary in their functionality based on their frequencies. Low-frequency sensors act as position transducers, mid-ranged frequency sensors as velocity transducers and high-ranged frequency transducers as accelerometers. These sensors are widely utilized within wind turbine gearbox and bearings [116].

Generation of vibration levels from a bearing do not necessarily indicate presence of a fault. Sources of vibration apart from defects, include variable compliance, surface roughness and waviness [117].

Variable compliance vibrations arise through cyclic passage of rolling elements across the bearing loaded zone, causing a change in the internal load distribution. Vibration levels increase with running clearance and the number of rolling elements within the loaded zone. High levels of surface roughness and waviness within a bearing, although rare due to the increased precision and control of bearing's manufacturing process, will also result in vibrations. High surface roughness ($\Lambda < 1$) will result in asperity interactions between two sliding surfaces, causing vibration as the asperities contact. On the other hand, vibrations produced from surface waviness are a result of rolling element sliding along the surface contours. Vibrations generated as a result of surface roughness occur at frequencies greater than sixty times the bearing rotational speed, whilst frequencies below sixty times is attributed to surface waviness [117].

The presence of defects on bearing raceways, rolling elements and cage will generate high energy pulses during bearing operation. The frequency at which these vibrations are generated is dependent on the defect location. Defects located at the inner and outer raceway will have vibrations generated at ball pass frequency of the inner and outer raceways, respectively. Rolling element defects will be generated at twice the ball spin frequency and also at the fundamental train frequency. Defects located at the cage is generally undetectable unless it originated from the bearing manufacturing process. Random bursts are generated as the rolling element traverses across the defects, resulting in a wide possible range of frequencies.

Methods of calculations for inner and outer raceway ball pass frequency, $(f_i \ \& \ f_o)$ and ball spin frequency, (f_b) are shown below where Z is the number of rolling elements, ω_{brg} is the bearing rotational speed (RPM), d and D are the mean roller and pitch diameter respectively and φ is the cone or cup angle (0° for CRB) [117].

$$f_i = \frac{Z \cdot \omega_{brg}}{120}\left(1 + \frac{D}{p_d} cos\phi\right) \quad (2.3)$$

$$f_o = \frac{Z \cdot \omega_{brg}}{120}\left(1 - \frac{D}{p_d} cos\phi\right) \quad (2.4)$$

$$f_b = \frac{p_d \cdot \omega_{brg}}{120 \cdot D}\left[1 - \left(\frac{D}{p_d} cos\phi\right)^2\right] \quad (2.5)$$

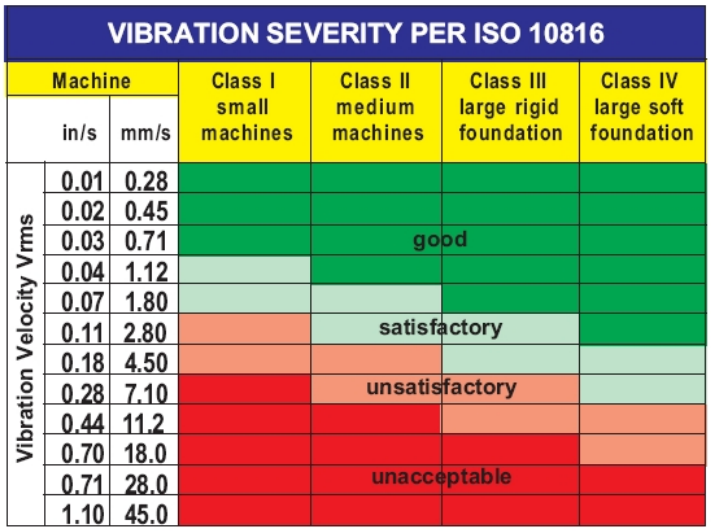

Figure 2.22 – Vibration severity per ISO 10816 [118]

Similar to temperature monitoring, a gradual increase in vibration above baseline steady state operation conditions is usually associated with degradation of components within the drivetrain. The most common time-based data processing involves taking the rms of the signal and establishing a baseline "undamaged" condition which if exceeded indicate the presence of bearing defect [119]. Other popular parameters include the kurtosis which is a measure of peakness of a signal, the ratio of the peak signal value to its rms value, termed the crest factor and the energy index defined as the ratio of rms of a segmented signal against the overall rms value [120]. For processing in the frequency domain, fast-fourier transform (FFT) is typically employed where information of the type, location and root cause of any defects may be inferred from the prominent frequencies and harmonics [121].

For gearbox monitoring, vibration measurements are typically taken using an accelerometer which is usually mounted on the gearbox casing due to limited access

within the gearbox. This typically will result in added difficulty in processing and interpreting data due to presence of additional noise compared to if mounted closer to the potential failure zones. Poor signal to noise ratio at low frequency ranges result in difficulty of fault detection within such range [105]. Standard exists for defining the position and use of vibration sensors, as well as acceptable levels of machine vibration [118] illustrated in Figure 2.22.

2.5.5 Acoustic emissions

Acoustic emissions (AE) is a sensing method that is gradually gaining popularity. Although both signals are essentially elastic waves propagating through a component, the main difference between vibration and acoustic emissions signals is the frequency range which they are associated with. Vibrational signals are typically of low frequencies, below 20 kHz whilst AE are generally associated with sound waves between 100 $kHz - 1\ MHz$ and thus their range of sensitivities [122].

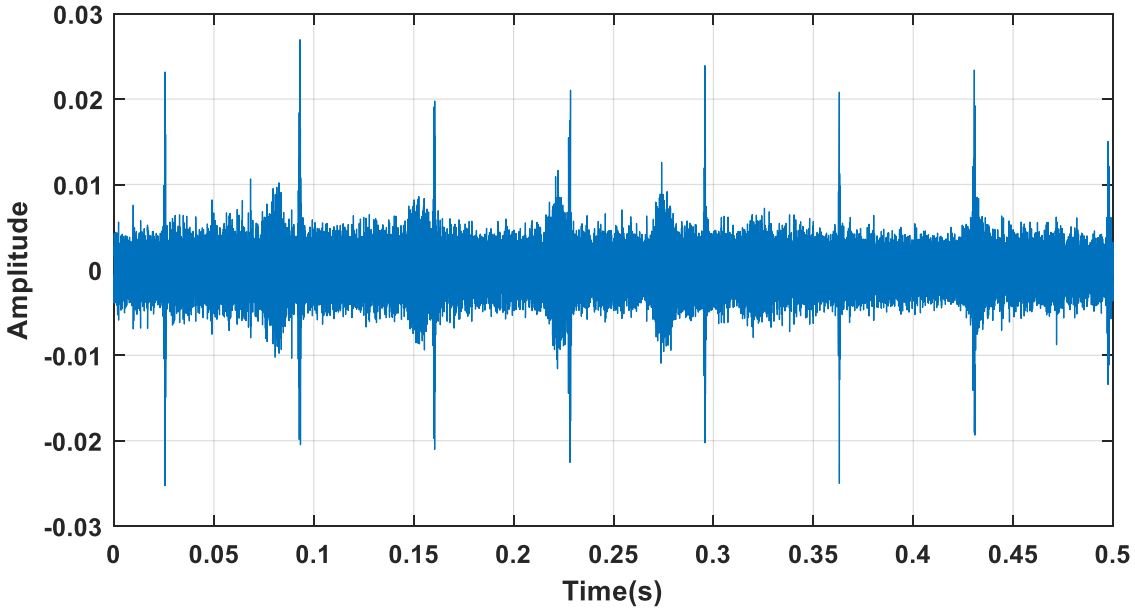

Figure 2.23 – Raw AE measurements obtained from a CRB at 100 *RPM* (courtesy of I Efremov)

Acoustic emissions are transient elastic waves generated during permanent deformation events within the material. These events include crack formation and propagation, matrix cracking, breaking of fibres and fretting corrosion [123, 124]. It is based on the Kaiser effect. Consequently, through AE monitoring it is possible to pick up signals released from sub-surface cracks and potentially predict the onset of premature bearing failure [119]. Piezoelectric transducers or fibre optic displacement sensors are commonly employed for AE measurement [122].

The processing techniques employed for AE are similar to those used for vibration analysis. However, it was documented that AE has a higher sensitivity in early detecting of faults compared to vibration measurements [125, 126, 127]. With novel processing and analytical techniques, it is possible to provide further information on bearing defects such as relating AE burst duration with the size of defects [127]. Through strategic positioning of multiple AE sensors, localisation of defect on a bearing raceway is possible, through triangulation and delta T method [128, 129]. Figure 2.23 shows an AE signal in time domain, obtained from a sensor positioned on a CRB inner raceway. The periodic bursts of amplitude higher than 0.015 are generated from rolling elements traversing across an artificially created notch on the inner raceway.

AE measurements require relatively high sampling rates to ensure measurements are captured with sufficient resolution. Acquisition rates of 2 *MHz* are common. Huge volumes of data can be easily generated, causing storage issues and the high acquisition rates resulted in the requirement of advanced and costly data acquisition hardware. Due to the high sensitivity of AE sensors, they also come with a high price tag [130]. Measurements are often very sensitive to noise which result in the need for extensive signal processing, through complex, computationally intensive algorithms to yield meaningful data. Apart from that, AE and vibration techniques are not widely adopted for condition monitoring of turbines.

2.5.6 The potential for ultrasound

Ultrasound is defined as mechanical vibrations which occur at a frequency beyond the audible range of human (above $20\,kHz$). It is investigated as a method of providing information on bearing performance, particularly load and lubrication and subsequently the ability to detect the onset of bearing failure. The rationale behind this can be explained through Figure 2.24 which illustrates the typical development of component failure. For a condition monitoring method to be deemed effective and efficient, the time at which faults contributing to premature failure are detected (preventive time) is required to be as long as possible to minimise component damage and repair cost. Based on this criterion, vibration and AE measurements are far superior compared with temperature monitoring. Through monitoring bearing operating conditions (load, lubrication, and rotational speed), ultrasonic sensors have a particular advantage over all the existing monitoring methods as faults can potentially be detected earlier and also provide more information from the measurements. The measurements also provide information regarding to how wind

turbines are loaded and lubricated in actual operation, data crucial for the design of better, more robust bearings.

Active ultrasonic testing techniques are widely utilised for structural evaluation of wind turbine tower and blades however its application in bearing fault prognostics and diagnostics have yet to be extensively explored [131, 132]. Sound waves are propagated into the structural composite components and its reflections captured can be processed to obtain laminate thickness of the various layers of composite and subsequently the ability to detect delamination [108].

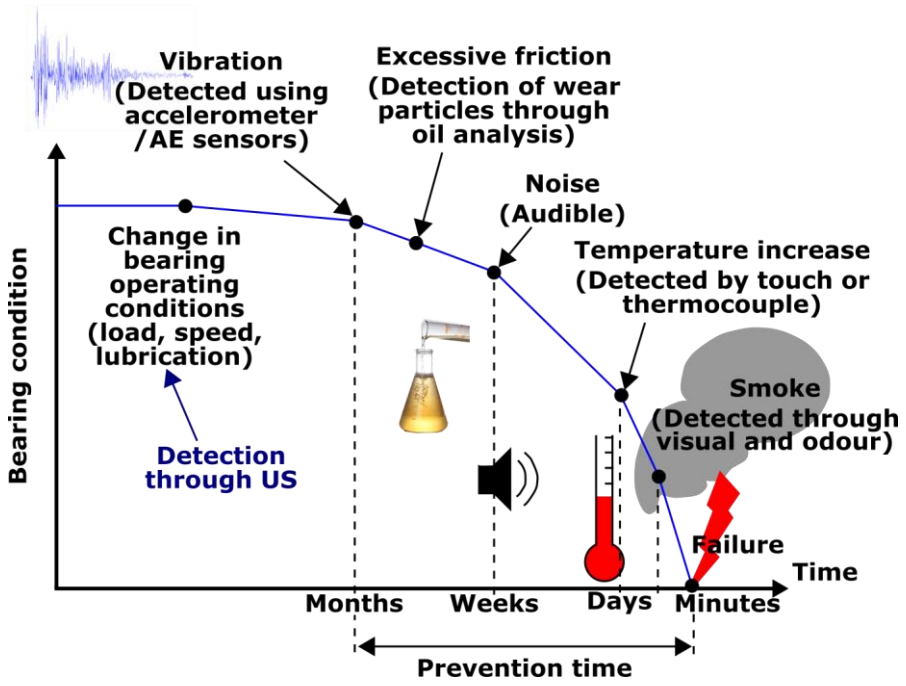

Figure 2.24 – Typical development of mechanical failure (adapted from [108])

Previously, ultrasonic reflectometry techniques have been successfully tested and implemented, on rolling element bearings laboratory test rigs for both lubricant film thickness [133, 134] and contact load measurement [135] with decent accuracy. In the subsequent chapters, these methods will be further refined for application in wind turbine gearbox monitoring.

2.6 Methods for stress measurement

The following sections will briefly discuss methods available for stress measurements.

2.6.1 Strain measurement

Measurement of stress are typically carried out indirectly through the use of strain gauges which measure strain and subsequently convert the strain measurements to

load or stress. Strain gauges were invented in 1938 by American engineers. Figure 2.25 shows the general build of a strain gauge and a WT high-speed shaft fitted with strain gauges. A strain gauge typically consists of an active grid length, alignment marks and solder tabs printed onto an insulating flexible backing [136]. The grid orientation will dictate which direction the strain measurement is most sensitive, vertical in the case for the strain gauge shown in Figure 2.25(a).

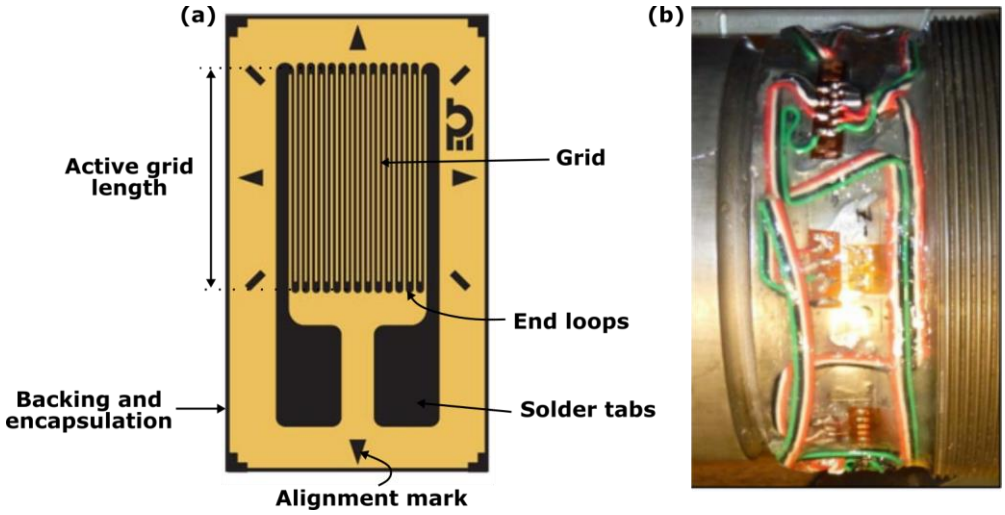

Figure 2.25 – (a) Structure of a strain gauge [137] (b) High-speed shaft instrumented with strain gauges [138]

The gauge is typically attached to the test specimen using adhesive such as cyanoacrylate. The bonding process is crucial as a poor bond layer will influence the accuracy of the strain gauge. As the object undergoes deformation, the foil is deformed resulting in an electrical resistance change. This change is due to the grid deforming and becoming narrower and longer during tension or thicker and shorter during compression [139]. The electrical resistance increases during tension and decreases during compression. This change is subsequently measured through a Wheatstone bridge and is related to the strain through a quantity known as gauge factor. Equation 2.6 shows the gauge factor in mathematical form. ΔR is the change in resistance caused by strain, R_0 is the resistance of the undeformed strain gauge and ε is the strain. Typical metallic foil gauges have a gauge factor of around 2 [140].

$$GF = \frac{\Delta R/R_0}{\varepsilon} \quad (2.6)$$

Strain measurements are widely used in measurements where bulk materials are stressed. Their main disadvantage is the difficulty to be applied in tribological contact conditions, especially bearings and potential inaccuracy due to operational temperature fluctuation. Recently, efforts have been made to incorporate them in

measurement of bearing loads. These include raceway [141] and rolling elements [142] embedded with strain gauges for load measurement. To facilitate such instrumentation, machining is required to be performed on the component. The instrumented rollers would need to be of considerable size to allow for such instrumentation and thus limited to large bearings.

2.6.2 Digital image correlation

Digital image correlation (DIC) is an optical technique used to measure strain and displacement. It works by contrasting digital photographs of a test specimen under various stages of stress or deformation. Through tracking blocks of pixels, measurement of surface displacement, and subsequently full 2 and 3 dimensional deformation vector fields and strain maps are possible [143].

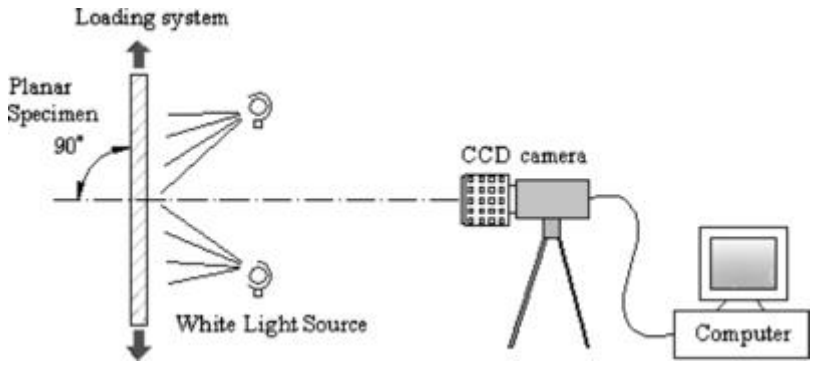

Figure 2.26 – Schematic of DIC test setup [144]

The implementation of DIC comprises of three steps, namely specimen preparations, image recording of the planar specimen surface prior to, during and after the application of load, and data processing of the acquired images to extract displacement and strain information [144]. Figure 2.26 depicts a typical DIC experimental setup. The specimen is required to have a random gray intensity distribution. This is typically acquired through airbrush, aerosol paint sprayers and transferable stickers as it is required to deform alongside the specimen surface and act as a carrier of deformation information. The optical axis of the camera is required to be normal to the test surface, as the camera captures images of the planar specimen surface in different loading states.

Stereoscopic imaging is typically employed where each individual point is focused on a specific pixel within the image plane of the sensors. The image surface is divided into a series of squares with recognizable pattern within each squares. As the orientation of the sensors with respect to each other and the imaging parameter for each sensor are known, the 3-D positions of each specimen point can be computed.

A cross-correlation technique is then used to trace how each point has shifted as a result of deformation during the test.

The cross-correlation algorithm computes the maximum of the correlation array between the captured pixel intensity array subsets of images of the test specimen under various stress states, which provides the translational shift between them [143]. Strain measurements are then derived from the displacement vectors [145].

The resolution is scalable as it is dependent on the field of view or photo capture region. DIC can be applied in material testing for Young's Modulus, Poisson's Ratio or elasto-plastic behaviour, fracture mechanics, deformation or strain measurements, surface contour measurements, 3D displacement and strains [145, 146].

As the method is highly reliant on data processing, the error sources include speckle pattern, imaging distortion, image capture and digitization noise and also errors attributed to the cross-correlation algorithm such as sub-pixel algorithm and interpolation employed, correlation function used, and subset size [144]. Due to the nature of the DIC measurement, it is not suitable to be applied in situ to observe stresses in tribological contacts and is very much limited to laboratory environments.

2.7 Research gaps

Having completed the literature review, the following research gaps were identified:

- The 20-25 year 'design life' of a WT gearbox is misleading as its overall life is dependent upon the life of all its components, each of which is stochastic and not deterministic.
- For fatigue life calculations, the existence of a fatigue load limit which a bearing would possess infinite life if operating below this threshold requires further proof of its applicability in large-sized bearings as used in WT gearboxes, as WT gearbox bearings still fail through RCF.
- No literature or public domain data exists which systematically reports and categorizes the number of gearbox bearing failures and its failure modes.
- Fatigue L_{10} life calculations fail to account for bearing life when bearings fail prematurely through WECs.
- The definitive root cause of WECs is still up for debate, with most theories associated with the loading on the bearing (loading history [74], overloading [84], roller slip within the loaded zone [77]).

- No literature exists presenting turbine operational data on the variation in gearbox bearing load and lubrication.
- Focused monitoring of WT gearboxes in existing WTs are scarce and general gearbox health monitoring are preferred through temperature and vibration sensors on the casing.
- No bearing condition monitoring methods exist which measure in-situ bearing operational load and lubrication.

This study attempts to address the latter three research gaps through developing an ultrasonic-based in-situ method for measuring the load and lubrication of an operational wind turbine gearbox bearing in the field. Measurements of load can inform on the loading history of the bearing and instances of overloading which are thought to be the causes of WECs [74, 84].

2.8 Conclusions

- Fundamentals of wind turbine operation and types of bearings utilised in wind turbine gearboxes were explored.
- Subsequently, emphasis was placed on understanding the failure modes of wind turbine gearbox bearings.
- Bearing degradation through rolling contact fatigue is inevitable however multiple factors accelerate the rate at which bearing degradation occurs, resulting in premature failures.
- Majority of the factors identified which drive premature bearing fatigue are associated with the bearing's operating condition (load & lubrication).
- Multiple methods exist for condition monitoring of wind turbine gearbox bearings. These include vibration, acoustic emissions, temperature, and lubricant analysis.
- SCADA systems are widely utilised in WTs for general status monitoring of the turbine and not focused specifically on monitoring wind turbine gearbox bearings.
- AE, vibration, and temperature are well developed lab-based methods for monitoring of rolling bearings. However, they provide limited information on the operating condition of the bearing (load & lubrication) as the parameters measured are a consequence of the bearing's operating condition.

- In-situ ultrasonic monitoring of bearing load and lubrication has the potential to detect bearing faults quicker as well as understanding better how the bearings are loaded and lubricated in actual operation. The focus was placed on understanding the load and lubrication measurements and relating the trends within measurements to bearing operation.

3 ULTRASONIC MEASUREMENTS ON WIND TURBINE GEARBOX BEARINGS

This chapter begins by outlining the physics behind ultrasonic waves propagating in solids, followed by methods of generating ultrasound. Specific emphasis is placed on utilisation of bare piezo ceramic elements for measurements, with procedure of bearing instrumentation detailed. Ultrasonic reflections from interfaces commonly encountered within a bearing is then explored. Subsequently, various methods of lubricant film thickness measurement are explored which is superseded by a brief description of the ultrasonic load measurement technique. Finally, application of these ultrasonic techniques onto bearing are discussed. This includes description of the sensor instrumentation procedure and ultrasonic pulsing hardware (FMS), the generic data processing routine carried out and features obtainable from the measurements, of which all are utilised for work conducted in §6 and 7. Methods detailed from §3.2.3 to 3.5 were inherited from previous work conducted at University of Sheffield. The author contributed to the signal processing methods detailed in §3.6.

3.1 Fundamental principles of ultrasound

Sound waves are mechanical disturbances occurring within a medium of solid, liquid or gas with energy transfer occurring between particles. Due to the requirement of energy transfer within a medium for sound propagation, sound waves cannot be sustained within a vacuum. Ultrasound refers to sound waves occurring beyond the audible range of humans, above 20 *kHz*.

3.1.1 Ultrasonic propagation within medium

All matter is comprised of particles, connected together through elastic or ''electrostatic'' bonds. The elastic bonds connecting each particle, which consist of a certain mass, can be visualised as springs as illustrated in Figure 3.1. Similar to a weight attached to a spring, if pulled down, the mass will oscillate about its equilibrium position. If an external force is applied, a group of particles within the medium would be excited. The mechanical disturbance would attempt to displace the particles from their original position, however the elastic bonds between the particles and the inertia of the particles act to oppose this [147]. Consequently, this result in the particles oscillating about their equilibrium position. The elastic forces holding the particles in place then act to transmit the oscillatory motion to the adjacent stationary particles or particles in the next plane and the cycle repeats. A

sound wave is thus the propagation of mechanical energy through a medium due to transferral of oscillatory and vibratory motions to adjacent particles via the elastic bonds. In an elastic wave, the particles within the medium will revert to its initial position after the transfer of energy. The width of particle oscillation would be defined as the wave amplitude whilst its frequency, f would quantify the number of oscillations per second. The distance between two peaks or trough of a wave, shown in Figure 3.1 describes the wavelength, λ_{wave}. The wave speed is subsequently defined as the product of its frequency and wavelength.

$$c = f\lambda_{wave} \tag{3.1}$$

If all the particles were interconnected rigidly, then transmission of energy from one end to the other would be instantaneous, all the particles would be in the same phase. However, this is not the case in elastic materials and a certain period of time is required for the motion to be transmitted. Thus, the stiffness between the bonds dictates the speed at which the sound wave propagates through the medium. The stiffer the bonds, the more efficient the transfer of energy and thus a faster bulk speed of sound.

Multiple propagation modes exist for sound waves in solids, differentiated by their direction of particle vibrations. These include longitudinal, transverse, Rayleigh, and plate waves. Longitudinal and shear waves, shown in Figure 3.1 are conventionally used in ultrasonic testing of materials. In a longitudinal wave, the particle oscillates parallel to the direction of wave propagation whilst in a shear wave, the particle oscillates perpendicular to where the wave propagates. Due to the oscillatory motion of particles, zones of compression and rarefaction are produced, corresponding to the peaks and troughs of a wave. An example of longitudinal waves would be sound waves produced during clapping or speaking and for shear waves, ripples in water.

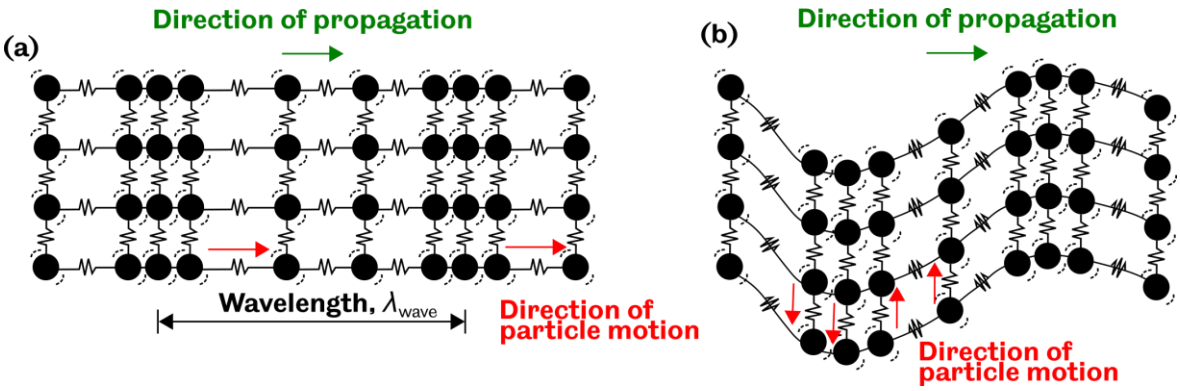

Figure 3.1 – Schematic showing the electrostatic bonds between particles and the direction of propagation and particle motion of (a) longitudinal and (b) shear wave

3.1.2 Speed of sound

As explained previously, the stiffness of the particle bonds and consequently, the mechanical properties of the material influence the sound speed within a medium. The presence of foreign particles within a material, ie. air inclusions in ceramics also affects sound speed and thus, the century old method of tapping on porcelain to evaluate its structural integrity. Sound speed is however independent of frequency and consequently free of dispersion. This is valid only for sound waves travelling through homogenous materials. Acoustic dispersion is the phenomenon where a sound wave disintegrates into its component frequencies as it travels through a material [147]. These separated waves of different component frequencies would have different sound speed. The cracking of ice sheets describes the phenomenon, where higher frequency components of the sound are transmitted quicker through the ice and thus reaches the listener first followed by the deeper frequencies after a time lag.

Sound velocity for longitudinal, C_L and transverse waves, C_T travelling in solids can be defined by the equations below where E is the modulus of elasticity, υ is the Poisson's ratio, ρ is the density of material and G is the shear modulus.

$$C_L = \sqrt{\frac{E}{\rho}\frac{1-\upsilon}{(1+\upsilon)(1-2\upsilon)}} \qquad (3.2)$$

$$C_T = \sqrt{\frac{E}{\rho}\frac{1}{2(1+\upsilon)}} = \sqrt{\frac{G}{\rho}} \qquad (3.3)$$

Typically, the Poisson's ratio and modulus of elasticity of steels are ~0.28 and ~210 GPa. The ratio of transverse and longitudinal velocity can be defined in

Equation (3.4), typically around 0.55 for steel. Thus, velocity of transverse wave in steel is roughly half of that of a longitudinal wave.

$$\frac{C_T}{C_L} = \sqrt{\frac{1-\upsilon}{2(1+\upsilon)}} \quad (3.4)$$

Typically, speed of sound within a material is determined through measuring the time-of-flight of the ultrasonic wave within a material of known thickness. For bearing steel, the longitudinal wave speed is around 5900 *m/s* whilst the shear wave speed is around 3400 *m/s*.

Apart from material properties, the sound speed within a material is also influenced by temperature and stress (acoustoelastic effect). Sound speed decreases with temperature, on average around 1 *m/s* per degree up to 1200 $^{\circ}C$ [148]. Effect of stress on sound speed is more complicated as it depends on the direction of applied stress and type of wave propagating through the stress field. A longitudinal wave propagating parallel through a compressive stress would increase the sound speed whereas a tensile stress would decrease the sound speed. This is further investigated in Chapter 4.

3.1.3 Acoustic impedance

Acoustic impedance, z is a physical property of a material which describes the resistance of sound waves travelling through the material. It is defined as the product of material density, ρ and speed of sound, c. The unit for acoustic impedance is $Rayls$ or Ns/m^3. Acoustic impedance of steel for longitudinal waves is $\sim 46\ MRayls$.

$$z = \rho c \quad (3.5)$$

3.1.4 Signal attenuation

If a sound wave is excited at one end of a very long steel plate, ideally the sound wave would have the same pressure or amplitude as it travels along the plate. In reality, there are losses and sound pressure would decrease as it travels within a material. Two basic causes of signal attenuation are explored here, scattering and absorption.

Scattering occurs when a sound wave travels through a material which is not strictly homogenous. Within the material, there exist boundaries or regions with abruptly different acoustic impedance. This is potentially resulted from foreign inclusions or genuine flaw within the material or an inherent property of the material. Cast iron for example, is inherently in-homogenous due to its combination of ferrite and

graphite grain structure. When sound wave strikes these grain boundaries at an oblique angle, a portion of the sound wave is reflection whilst some is transmitted through. This is repeated for the subsequent grain boundaries the wave encounters and the initial sound wave is constantly split into partial waves which are gradually converted into heat and lost through absorption [147].

For longitudinal waves of $10\ MHz$, a $0.06\ mm$ inclusion or grain size (1/10th of the wavelength) would be required to cause significant scattering in the wave [147]. Inclusions of such magnitude are extremely unlikely as bearing steel (EN31) is kept to the utmost cleanliness and consequently scattering will not be an issue. Prior austenite grain boundaries within the bearing matrix however potentially affect the signal as their size are of the same order of magnitude. Provided that the proportion is small within the steel matrix, the effect would be minimal.

Absorption arises when sound energy is converted into heat and consequently 'absorbed' by the material. It can be roughly visualised as the braking of the oscillating particles and thus is dependent on sound frequency. Rapid particle oscillation incurs a higher loss than lower frequency oscillations. The losses however are at a slower rate compared to scattering [147]. As such, there exists an optimum frequency where absorption is minimized, and the wavelength is not within 1/10th of the grain size of the material it is propagating through.

3.2 Generation of ultrasound

3.2.1 The piezoelectric effect

Piezoelectricity is the build-up of electric charge within certain solid materials when acted upon by mechanical stress. It was discovered in 1880 by French physicist Pierre Curie and Jacques [149]. The opposite is also true where mechanical deformations can be produced when electric charges are supplied to a piezoelectric material. This was subsequently exploited to produce acoustic sensors. Examples of material which show piezoelectric properties include barium titanite, lead zirconate titanite, lithium sulfate and quartz.

3.2.2 Ultrasonic transducers

In order to draw distinction between the sensors used in this work against those commercially sold, it is necessary to understand the build of conventional ultrasonic monolithic transducers. These transducers come in a range of sizes, shapes, and frequencies; however, all consist of a common internal structure. Figure 3.2 shows the internal structure of such a sensor. The active element is either a circular,

square, or rectangular shaped piezo ceramic which converts the electrical excitation pulses supplied from the electrical circuitry, into ultrasonic vibrations. A wear plate separates the active element from the testing material's surface to protect the piezo ceramic from damage. Damping of the piezo ceramic is provided through a backing material to reduce signal reverberations and echo from the back face. Coaxial radio frequency (RF) connectors are typically employed for commercial transducers.

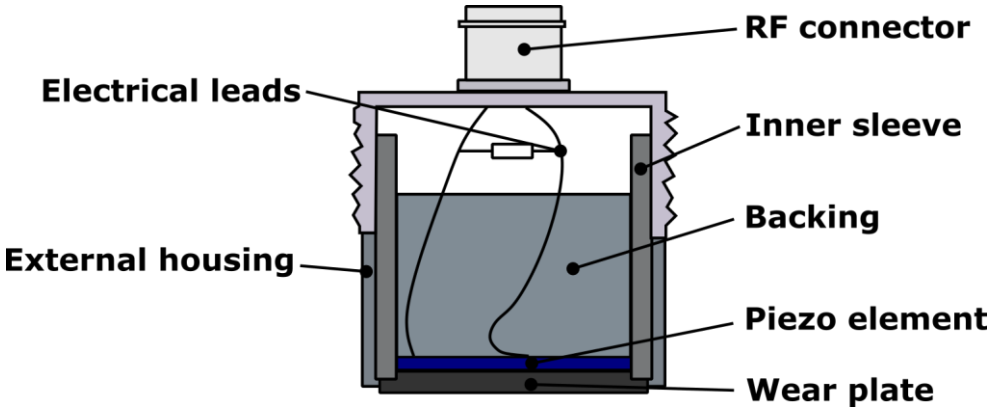

Figure 3.2 – Structure of a conventional monolithic transducer (reproduced from [150])

Conventional transducers however have several limitations which restricts their application in an industrial environment, such as within a wind turbine gearbox bearing. The transducers are typically of a relatively large size (20-40 *mm* in diameter, 10-20 *mm* in length) which necessitates significant modifications to the component for instrumentation. Wind turbine operators are usually reluctant to allow excessive material removal of components as this would potentially jeopardise the component's structural integrity. To ensure good signal, couplings are typically used between the transducer and the instrumented component. Signal quality would depend on how stable and invariant the coupling interface is and often enough maintaining such a stable interface is a challenge. Transducers would be required to be immobilised through mechanical means such as clamping. Permanently bonding these onto the workpiece is often not financially viable as these transducers range from £200 - £1,000 per unit. Above all, the operating temperature of commercial transducers is limited to $\sim 50\,^{\circ}C$ [151], which undoubtedly relegated its application to only lab-based validation work if deemed necessary.

3.2.3 Use of bare piezoelectric elements

Consequently, use of bare piezo-ceramic elements were deemed necessary. The piezo elements avoided all the limitations posed from the conventional transducer. They come in all sizes and shapes and can be trimmed down into specific dimensions to suit application. The thickness of the piezo ceramic is frequency dependent. They are significantly cheaper than conventional transducers. A 7 *mm* diameter, 10 MHz piezo ceramic would cost only £1 when purchased in bulk. This enables mass instrumentation of a component and permanent bonding of sensors which allows for excellent signal transmission whilst eliminating the need for a coupling. Operating temperatures for the piezo elements vary depending on their grades.

Piezo-ceramic elements are available in disc, ring or plates. They typically are composed of lead (Pb), zirconate (Zn) and titanium (Ti) and different formulations exist, regulated by an existing standard [152]. PZT-5A are used in this study as their material properties remain fairly stable across the recommended operating temperature range of 0 – 250 *°C* [153, 154]. Although the piezo elements might have the same shape and size, they might still vary in their electrode configuration. This is shown in Figure 3.3 with two main difference being wrap around or non-wrap around configuration. For non-wrap around or solid configuration, the top and bottom faces of the piezo element are coated with a thin electrode layer. For the wrap around configuration, the lower electrode covers most of the exposed area of the piezo element except a centre portion where the upper electrode is coated onto. The active sensing region between the two configurations thus differs as only a portion of the piezoceramic is covered by both upper and lower electrode for the wrap-around configuration as opposed to the solid element. The solid piezo however face complexities in wiring the lower portion of the electrode as this would be in contact with the test specimen.

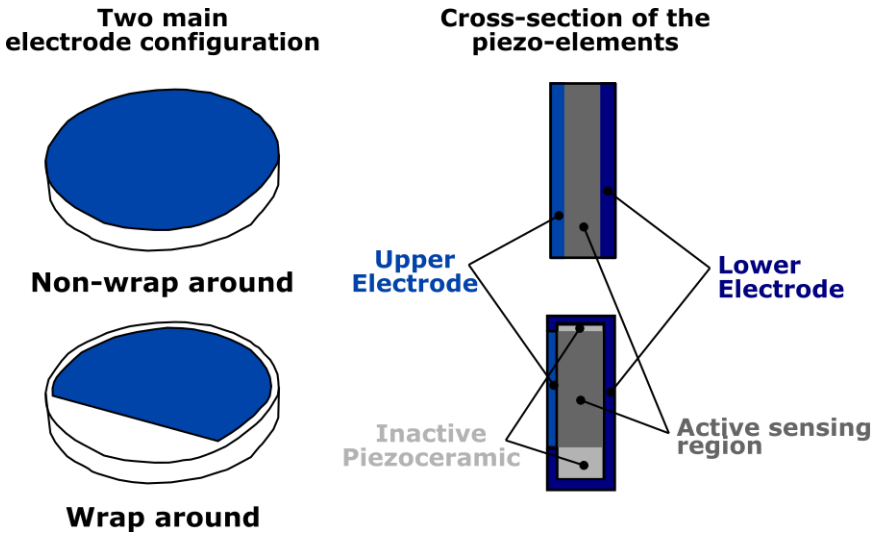

Figure 3.3 – Main electrode configuration for piezo-elements and their cross section [155]

3.2.4 Sensor instrumentation routine

The following section will detail the basic sensor instrumentation procedure applied for studies conducted in §4, 6 and 7. In these studies, wrap around sensors were utilized. The default sensors used were longitudinal sensors of 10 *MHz*. Instrumentation process requires dexterity as the piezo elements are extremely fragile as they are very thin. The process is illustrated in Figure 3.4. The thickness of the piezo is half of their wavelength. Piezo-electric elements of 7 *mm* in diameter were trimmed down into rectangular strips of 5 *mm* x 1 *mm*. This was to reduce the size of the sensing region of the piezo element, increasing the resolution of the sensor and also allowed for instrumentation in regions of limited space. Piezo elements were typically permanently bonded onto the test surface to ensure excellent signal transmission between sensor and test piece. This was achieved through the use of high-performance strain gauge epoxy. The thickness of the epoxy bond layer was controlled to ensure a well damped signal. Surface where the sensor was positioned was required to be smooth to reduce signal scattering. Subsequently, coaxial cables were used to minimise noise from the measurement with the live terminal soldered onto the upper electrode whilst the ground onto the lower electrode. A layer of epoxy was then applied across the sensor for protective and damping purposes.

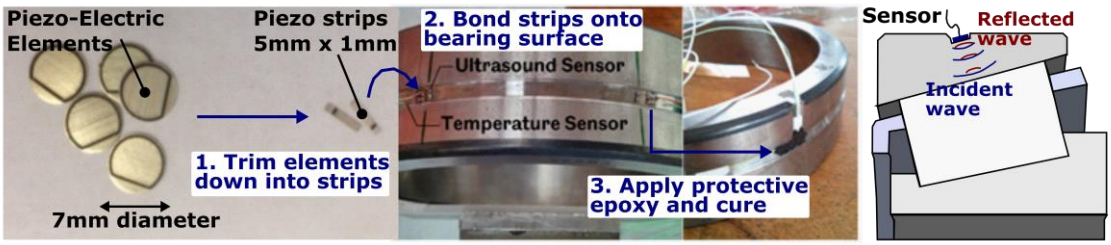

Figure 3.4 – Typical instrumentation process where piezo elements are trimmed into custom sizes and bonded onto a test specimen

3.3 Ultrasonic reflection from an interface

When an ultrasonic signal strikes an interface between two acoustically differing materials, a portion of the energy is reflected back, whilst the remaining portion is transmitted through. The proportion of ultrasonic energy reflected is defined as the reflection coefficient, *R*. The reflection coefficient is dependent on how acoustically matching the two materials are. It is defined in Equation (3.6) where z_1 and z_2 are the acoustic impedances of the materials at either side of the interface. Since ultrasound is applied for bearing monitoring, interfaces involving steel, lubricant and air are typical. These cases are explored in the following sections.

$$R = \frac{z_2 - z_1}{z_2 + z_1} \tag{3.6}$$

3.3.1 Reflection from a steel-air interface

Figure 3.5 shows the ultrasonic reflection from a steel-air interface. The reflection coefficient from a steel-air interface can be easily calculated through Equation (3.6). As steel and air are very acoustically dissimilar, almost all the ultrasonic energy is reflected back.

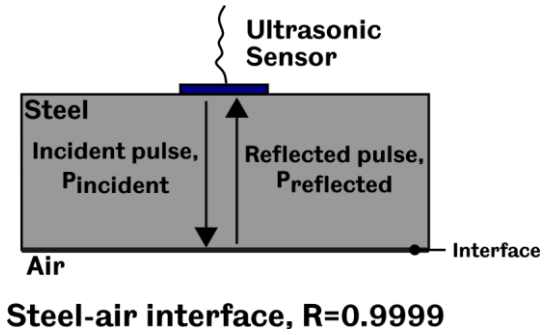

Figure 3.5 – Ultrasonic reflection from a steel-air interface

Practical measurements of reflection coefficient would require readings of incident, P_{in} and reflected pulse, P_{refl} with the former often trickier to measure

experimentally. In this work, an engineering approach was taken instead. Since the reflection coefficient for a steel-air interface differs by 0.01% from unity, the reflected pulse from a steel-air interface, $P_{\text{refl (steel–air)}}$ would be used as the incident pulse to compute the reflection coefficient.

$$R_{meas} = \frac{P_{\text{refl}}}{P_{\text{in}}} \approx \frac{P_{\text{meas}}}{P_{\text{refl (steel–air)}}} \quad (3.7)$$

3.3.2 Reflection from a steel-steel interface

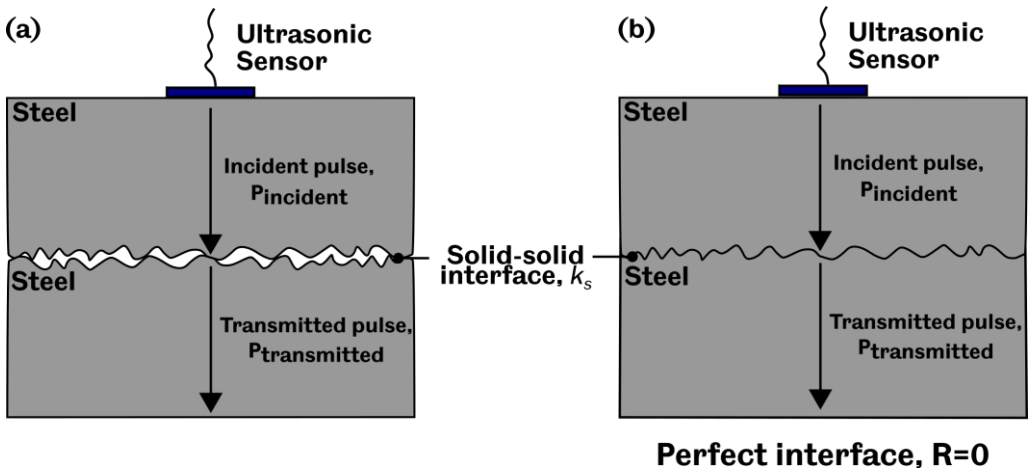

Figure 3.6 – Ultrasonic reflections from (a) a typical steel-steel interface and (b) a fully-bonded, ideal steel-steel interface

Figure 3.6 shows ultrasonic reflections from a typical steel-steel and ideal steel-steel interface. For two materials of very similar composition, such as different grades of steel, in an ideal scenario, ultrasonic transmission would be close to unity as shown in Figure 3.6(b). However, real life materials have surface roughness and contact between two materials would occur between the asperities of the two material. Consequently, there exist regions of solid-solid and solid-air contact within the interface. The amount of ultrasonic energy reflected would therefore depend on the proportion of the two regions. Air pockets act similarly as inclusions to reduce ultrasonic transmission. A material is considered 'smooth' if the roughness of the contacting face is an order of magnitude smaller than the wavelength of the ultrasound [147].

When two surfaces are pressed together, the surfaces would elastically deform and conform to each other. This would clearly affect the reflection coefficient as more ultrasonic energy would be transmitted through. This effect is accounted through the introduction of an imaginary term in the reflection coefficient as shown in Equation (3.8). The imaginary term accounted for the interfacial stiffness, K which

is the ratio of nominal pressure applied, δp against the approach of the two surfaces, δu defined in Equation (3.9) [133] where ω is the angular frequency of the ultrasonic wave, calculated using $2\pi f$.

$$R = \frac{z_2 - z_1 + i\omega\left({}^{z_1 z_2}/_{K}\right)}{z_1 + z_2 + i\omega\left({}^{z_1 z_2}/_{K}\right)} \quad (3.8)$$

$$K = -\frac{\delta p}{\delta u} \quad (3.9)$$

As the interface conforms more with increasing pressure and approaches a perfect interface, the stiffness would tend to infinity and Equation (3.8) would revert back to Equation (3.6). Ultrasonic measurements of reflection coefficient would relate to its magnitude, $|R|$. By taking the modulus of the reflection coefficient, Equation (3.8) can be rewritten as,

$$|R| = \sqrt{\frac{(z_2 - z_1)^2 + \left({}^{\omega z_1 z_2}/_{K}\right)^2}{(z_1 + z_2)^2 + \left({}^{\omega z_1 z_2}/_{K}\right)^2}} \quad (3.10)$$

If the material at either side of the interface is the same, the equation can be further simplified into Equation (3.11).

$$|R| = \frac{1}{\sqrt{1 + \left({}^{2K}/_{\omega z}\right)^2}} \quad (3.11)$$

3.3.3 Reflection from a steel-oil interface

Figure 3.7 shows ultrasonic reflections from a two layered steel-oil system and a three-layered, steel-oil-steel interface. The reflection coefficient for a two layered steel-oil interface of 0.95 can be calculated rather straightforwardly. Despite having a relatively small difference in reflection coefficient of 0.05 between an unlubricated surface (steel-air interface), this can still be used to distinguish between a lubricated and unlubricated surface as shown later in §6 and 7.

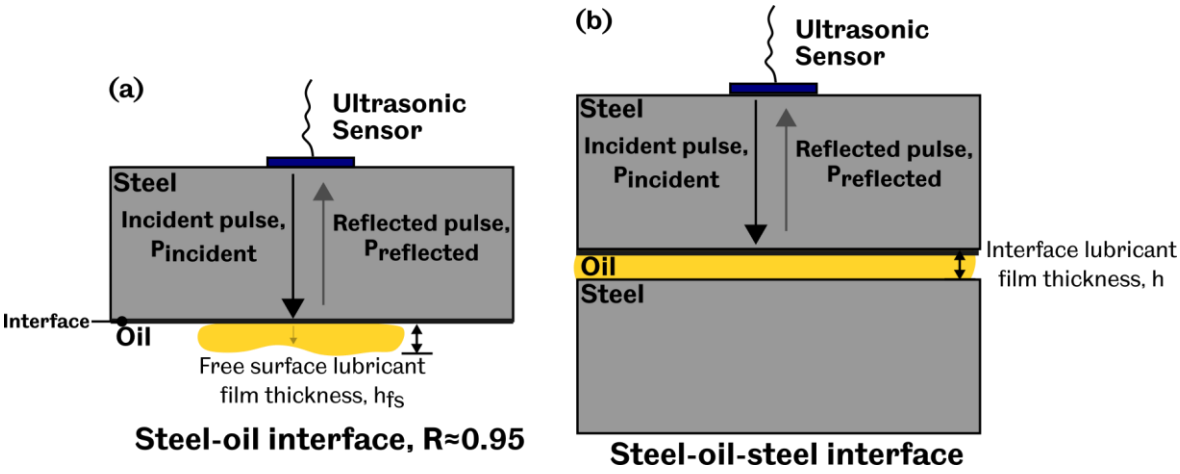

Figure 3.7 - Reflection from(a) a steel-oil interface and (b) a steel-oil-steel interface

Reflection coefficient for a lubricant film between two steel components is more complicated and would again need to account for the interfacial stiffness. In this case, this would be the stiffness of the lubricant film layer, K_l dictated by the bulk modulus of the oil film, B and the thickness of the oil, h [133].

$$K_l = \frac{B}{h} = \frac{\rho c^2}{h} \qquad (3.12)$$

Since the lubricant film stiffness is related to its film thickness, a relationship between the film thickness and reflection coefficient can be established. This is termed 'the spring model' for measuring lubricant film thickness and is discussed in §3.4.3.

3.3.4 Reflection from a mixed interface

For a mixed interface, there exist both solid-solid and solid-liquid contact. The stiffness of such an interface would be a combination of the solid and liquid stiffness. This is often the case for rolling element bearings operating in WTs as the rotational speed is insufficient to entrain and sustain a lubricant film whilst the high loading squeezes the two surfaces closer together, promoting metal to metal contact between the asperities of the two surfaces.

$$K_{mixed} = K_s + K_l \qquad (3.13)$$

The composite stiffness can also be rewritten as:

$$K_{mixed} = -\frac{\delta p}{\delta u} + \frac{\rho c^2}{h} \quad (3.14)$$

It is apparent that a portion of the composite stiffness is related to the lubricant film thickness, h. If the liquid stiffness portion can be identified in the ultrasonic readings, then measurements of lubricant film thickness is possible.

A number of previous studies conducted [156-158] has successfully demonstrated the applicability of the spring model in mixed lubrication condition for measurement of lubricant film thickness, h through measurement of the liquid stiffness component, K_l.

3.4 Measurement of lubricant film thickness

This section details various methods of measuring lubricant film thickness available using ultrasound. The ultrasonic measurement methods primarily differ against one another through their measurable range of lubricant film thickness. Non-ultrasonic methods of measuring lubricant film thickness do exist such as optical interferometry [35], electrical resistance [159] and capacitance [34, 160] techniques, and eddy current [161] sensors. However, this section will only focus on the ultrasonic techniques for measuring lubricant film thickness and the reader is referred to the references for further information.

3.4.1 Time-transit method

For a steel-oil-steel interface illustrated in Figure 3.7(b), reflection coefficient would be dependent on the thickness of the lubricant film. For lubricant film thicker than 40 μm, the reflections occurring at either side of the interface can be distinguishable [133] and film thickness can be inferred through time-transit method. Equation (3.15) can be used to calculate the film thickness, h where c_{oil} is the speed of sound in oil whilst T_1 and T_2 are the time of flight for the reflection at the closer and further side of the interface.

$$h = \frac{1}{2} c_{oil}(T_2 - T_1) \quad (3.15)$$

However, lubricant film in bearings are often extremely thin that these reflections superimpose each other, and subsequently the method outlined is not suitable for measuring film thickness in bearings.

3.4.2 Resonance method

An alternative of evaluating lubricant film thickness from overlapping, undistinguishable reflections is to measure the through-thickness resonances of the lubricant film and deduce the film thickness that corresponds to that specific resonant frequency. For a specific lubricant film thickness, there exist a resonant frequency associated to it. This is first demonstrated by Pialucha et al. [162] and Equation (3.16) relates the lubricant film thickness, h and its sound speed, c to the resonant frequency, f_m and its mode, m.

$$h = \frac{cm}{2f_m} \tag{3.16}$$

From the equation, the thinner the lubricant film, the higher the resonant frequency associated to it. Consequently, the thinnest measurable lubricant film is dictated by the sensor's maximum frequency. As detailed previously, attenuation of signal is dependent upon sensor frequency and the higher the frequency, the greater the attenuation. As a result, for ultrasonic measurements in bearing steel, the maximum frequency is limited to between 40 - 60 *MHz* [133]. The method thus, is capable of measuring film thicknesses greater than 12 μm.

3.4.3 The spring model

For thin lubricant layers of less than 20 μm, the embedded lubricant film is small compared to the wavelength of the ultrasonic wave. The film layer thus acts as a unique reflector and can be viewed as a distributed spring with stiffness, *K* which will influence the value of reflection coefficient, *R* based on Equation (3.10). Substituting Equation (3.12) into Equation (3.10) yields:

$$h = \frac{\rho c^2}{\omega z_1 z_2} \sqrt{\frac{|R|^2 (z_1+z_2)^2 - (z_1-z_2)^2}{1-|R|^2}} \tag{3.17}$$

Again, for a film interface consisting of the same material for both sides of the interface ($z_1 = z_2 = z$), the equation can be simplified down to:

$$h = \frac{\rho c^2}{\omega z} \sqrt{\frac{|R|^2}{1-|R|^2}} \tag{3.18}$$

Measurement of lubricant film thickness using the spring model has been successfully carried out previously on rolling element bearings within the EHL

regime [163-166]. These are all conducted under laboratory conditions, using longitudinal sensors, with beam focused through a water bath to reduce the sensing width.

3.4.4 Phase change method

When an ultrasonic signal strikes an interface and is reflected, the phase change of the reflection coefficient, Φ_R. Parameters dictating the phase change are shown in Equation (3.19) [167]. From the equation, the phase between an incident and reflected pulse can vary between $0 - \pi/2$. The stiffness plays a major role in the phase. As the stiffness approaches infinity, the phase would approach $\pi/2$ and as the stiffness approaches 0, then there would be no phase change. For the case of a vanishingly thin film where $z_1 > z_2$, the phase difference would be π [167].

$$\Phi_R = \arctan\left[\frac{Re(R)}{Im(R)}\right] = arctan\left[\frac{2\omega {z_1}{z_2}^2/K}{(z_1 - z_2) + \omega^2(z_1 z_2/K)^2}\right] \qquad (3.19)$$

In the presence of a lubricant film across the interface, the liquid stiffness, K_l can be related to the phase, Φ_R by combining Equation (3.12) and Equation (3.19). Subsequently, a relationship between lubricant film thickness, h and phase, Φ_R can be obtained. The method, similar to the spring model can be applied only for thin films (<20 μm).

$$h = \frac{\rho c^2(\tan\Phi_R)({z_1}^2 - {z_2}^2)}{\omega z_1 z_2 \pm \sqrt{(\omega z_1 {z_2}^2)^2 - (\omega z_1 {z_2}^2)^2(\tan\Phi_R)^2({z_1}^2 - {z_2}^2)}} \qquad (3.20)$$

Apart from these methods, qualitative detection of lubricant film is also possible. This was achieved through observation of amplitude and time-of-flight (ToF) change with the variation of bearing lubrication [168]. Amplitude variation in ultrasonic signals also corresponds to wear particles, surface damage and degree of deterioration in bearings [169].

3.5 Bearing roller load measurements

The following section details the method of measuring bearing load through ultrasonic reflections from a bearing raceway. The method detailed in [135], measures the raceway deflections caused by the traversing rollers and from raceway deflection, using appropriate contact models to infer roller and subsequently bearing loads. Figure 3.8 shows an ultrasonic sensor instrumented on the outer raceway, transmitting ultrasonic pulses through the raceway. The time-of-

flight of these pulses would differ when there is no roller directly incident under the sensor (Figure 3.8(a)) against when there is indeed one, shown in Figure 3.8(b). When no roller is incident under the ultrasonic sensor, all of the ultrasonic energy are reflected back from a nominally un-deformed, unstressed portion of the bearing raceway. On the other hand, when a roller transverses across the sensor sensing region, it deflects the raceway and thus reduces the ultrasonic transmission path which resulted in a change in ToF of the pulses. The ToF change can then be used to infer deflection of raceway and subsequently, roller and bearing load.

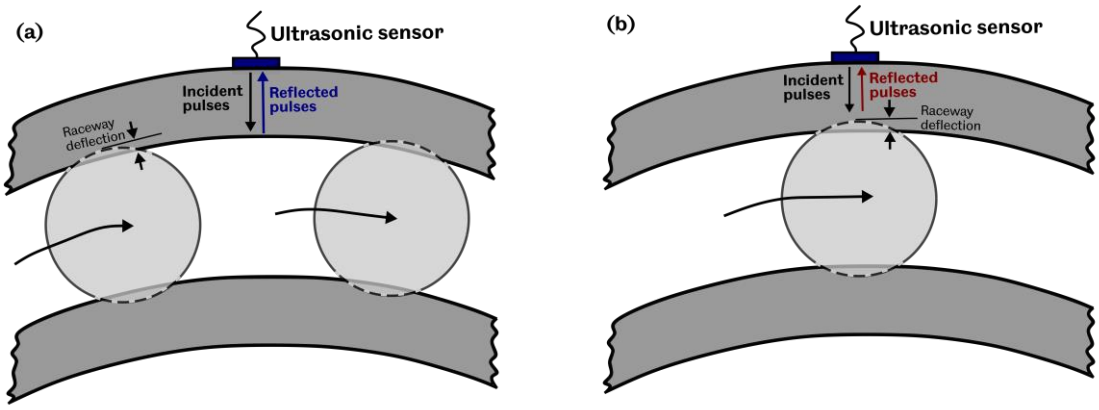

Figure 3.8 - Ultrasonic transmission through an outer raceway for a) when roller is remote from the sensor (raceway portion unloaded) and b) when roller is directly beneath sensor (raceway portion loaded)

3.5.1 Contributions to variation in ToF

Apart from raceway deflection, the variation in ToF of an ultrasonic pulse is, unfortunately influenced by several other factors which contributions are significant enough not to be neglected [135]. These are listed below:

(a) Variation of ultrasonic speed due to stress (Acoustoelasticity)

(b) Phase change due to presence of interface

(c) Deflection of raceway

The first contribution is resulted from a change in speed of sound as sound waves travel through a material under stress. This is termed the acoustoelasticity effect [170]. The variation in sound speed manifests itself as a change in ToF in the measurements. The variation depends on the type of ultrasonic wave (longitudinal or shear) and also the direction of applied stress (tension or compression, uniaxial or biaxial or triaxial) within the material. For a longitudinal wave, the ToF change due to acoustoelastic effect, Δt_{Lzz} can be expressed as shown below, where δ is the

raceway deflection, L_{zz} is the acoustoelastic constant and $(c_{zz})_0$ is the unstressed speed of sound.

$$\Delta t_{Lzz} = -\frac{2L_{zz}\delta}{(c_{zz})_0} \quad (3.21)$$

The acoustoelastic constant was previously found experimentally to be -2.24 [135]. This is discussed and investigated in depth in §4. Stresses present within the bearing raceway such as tangential stress due to friction and residual stresses will be accounted through using the acoustoelastic constant.

The second contribution is resulted from an apparent change in ToF due to phase change of ultrasonic pulses as it is reflected from an interface. The phase change is explained in §3.4.4 and the ToF change resulted from the phase variation, Δt_Φ can be written as:

$$\Delta t_\Phi = \frac{\Phi_R}{2\pi f} \quad (3.22)$$

A data processing means using Hilbert Transform was used to nullify this. The method as well as its robustness are detailed and explored in §4.4.2.

The final contribution to the change in ToF, Δt_δ is resulted from deflection of raceway. Raceway deflection reduces the transmission distance of the ultrasonic wave which therein affects the transit time of the ultrasonic waves. This can be expressed mathematically as shown below, where

$$\Delta t_\delta = \frac{2\delta}{(c_{zz})_0} \quad (3.23)$$

By summing up Equation (3.21), Equation (3.22) and Equation (3.23), the total change in ToF, Δt for a loaded rolling bearing contact can be mathematically described as shown in Equation (3.24) [135], with the second term negated through data processing means.

$$\Delta t = \frac{2(1-L_{zz})\delta}{(c_{zz})_0} + \frac{\emptyset_R}{2\pi f} \quad (3.24)$$

Rearranging the term to obtain deflection, δ in terms of ToF change yields:

$$\delta = \frac{\Delta t(c_{zz})_0}{2(1-L_{zz})} \quad (3.25)$$

For deducing roller load from deflection, contact models are used. This is further discussed in §5 where various contact models are compared against each other. Processing of the ultrasonic measurements to obtain bearing deflection and load was carried out through Matlab. Considerable amount of time was spent on writing, improving, and optimising the processing routine. A general script for the processing routine can be found in the appendix.

3.6 Application of ultrasonic reflectometry technique on bearings

The section discusses the application of ultrasonic measurements onto bearing raceways and the data processing routine implemented to obtain reflection coefficient and roller load measurements.

3.6.1 Ultrasonic reflections from a bearing raceway

For measurements in rolling element bearings, ultrasonic sensors are typically bonded onto either the inner or outer raceway. The static raceway is preferable as it simplifies instrumentation through eliminating the need for a slip ring and also much straightforward data processing as only the rollers are traversing across the stationary sensor. Figure 3.9 shows the ultrasonic reverberations obtained from a sensor instrumented on a static raceway. The ultrasonic sensor although static, measures various interfaces as the roller traverses across the sensor, mainly raceway-air and raceway-roller interfaces. The blue waveform shows the reflections captured when a sensor is not in line with a roller or the raceway is unloaded, whilst the red signal depicts reverberated when the raceway portion is loaded. The first waveform is the initial excitation pulse sent to excite the piezo-element and is of no interest. Subsequent pulses are reverberations from the raceway interface with each reverberation having an amplitude reduction due to attenuation. An interesting observation can be made between the second and third reverberation where a waveform of higher amplitude exists, and this is due to a reflection from the opposite roller edge. It is typically sufficient to capture one reverberation for subsequent data process and for maximum signal-to-noise ratio, the first reflection was selected, and a capture window was assigned over it.

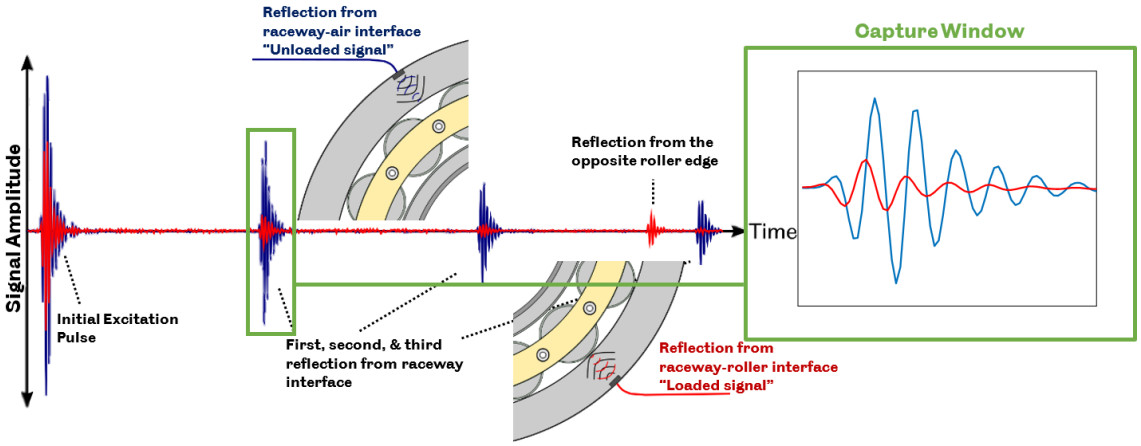

Figure 3.9 – Raw ultrasonic reflections from multiple interfaces within a roller bearing

3.6.2 The ultrasonic acquisition system

The Film Measurement System (FMS)

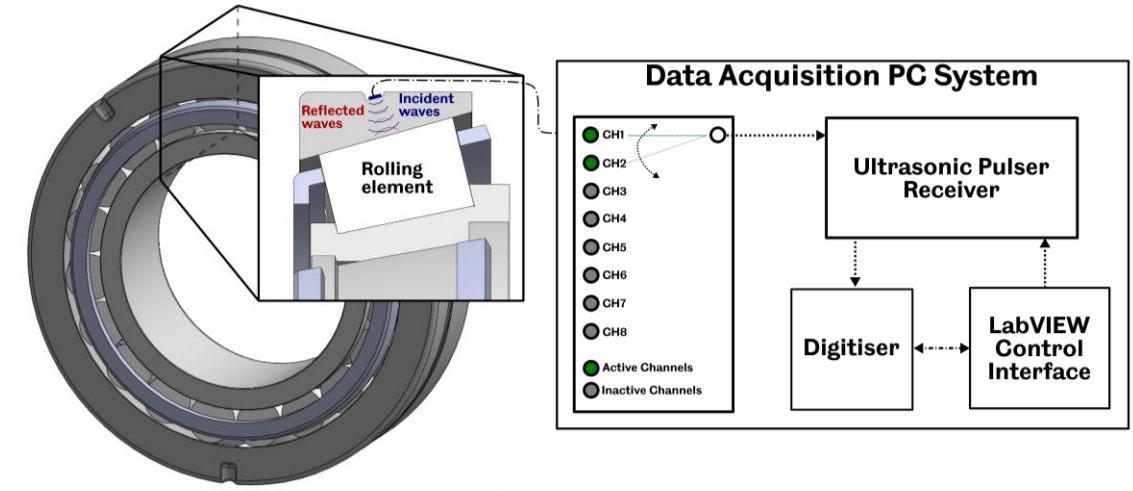

Figure 3.10 – Schematic of the ultrasonic data acquisition hardware

Work conducted in the subsequent chapters utilized a PC based data acquisition system for ultrasonic measurements. The system was manufactured by *Tribosonics Ltd* and it comprised of two custom PCI cards for ultrasonic pulsing and acquisition.

The Ultrasonic Pulse Receiver (UPR) generates a square waveform of a certain assigned voltage to excite the piezo-electric elements. The UPR is capable of excitation up to 300*V* and the pulse width of the square waveform can be customised to suit the resonant frequency of the piezoelectric element. The maximum rate which the UPR can excite the sensor is 80 *kHz*, although a recent LabVIEW script optimisation was able to increase this up to 100 *kHz*. This is termed

the pulse repetition rate (PRR), the number of pulses recorded per second. The PRR determines the number of data points captured within a bearing rotation and subsequently resolution of the roller-raceway contact. The faster the bearing rotational speed, the higher the PRR required to allow for sufficient data points within the contact. A maximum of 8 channels can be excited, with each channel pulsed sequentially in rapid succession. The PRR thus are shared between the number of active channels (ie. a PRR of 20 *kHz* with 2 active channels would result in each channel having 10 *kHz* of pulse rate).

The subsequent reverberation signals obtained from the sensor was then received by the UPR and transferred to the Digitiser for digitisation and storage. Time and voltage resolution of the system's digitiser is unconfigurable. The time resolution is limited to 100 *MHz* or 10 *ns* whilst the voltage resolution is limited to 12 bits.

The FMS acquisition PC was controlled through a custom written LabVIEW interface which allows for customised test settings to suit each test. Configurable settings include the excitation voltage applied to the sensor, the pulse width of the square excitation signal, range and delay for windowing purposes and the gain for each channel. The gain however is a multiplier applied to the signal after measurement and thus would not result in any signal-to-noise ratio improvements.

Typically, as measurements are taken at high PRRs, large amount of data are generated rapidly, much faster than the write speed of the PC. Waveforms measured were initially stored within the hardware buffer and subsequently transferred to the PC drive at a slower write speed. Measurements of the ultrasonic pulses or data stream would consist of an assembly of the windowed waveform, typically the first reflection plotted against their respective capture time. This is shown in Figure 3.11. The data stream would form a dense, compact outline with the peak amplitudes of the reflected pulses, dictating the bounds. A magnified view of a portion of the data stream reveals 4 reflected interface pulses with identical pulse envelopes or shape. The plot consisting of the dense data stream is termed Amplitude scan (A-scan).

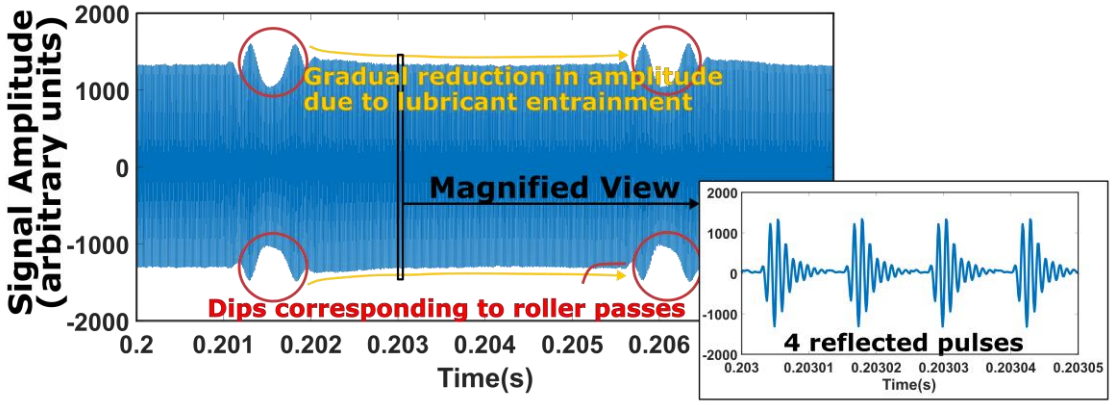

Figure 3.11 – Ultrasonic data stream consisting of a series of first interface reflected pulses with a magnified section illustrating four reflected pulses

3.6.3 Measurement of lubricant film thickness and peak roller load

For application of spring model to obtain lubricant film thickness, reflection coefficient measurements are required. The reflection coefficient, $|R|$ is obtained through dividing the spectral amplitude of the measured pulses with that of the reference pulse. This was touched upon briefly in §3.3.1. The reflection coefficient equation was rewritten in terms of the measured parameters of the ultrasonic pulse and shown in Equation (3.26), where $A(f)_{meas}$ and $A(f)_{ref}$ are the spectral amplitudes of the measured and reference pulses. Time domain amplitudes, such as peak-to-peak measurements are not used to determine reflection coefficient because the measurements entail the average sensor response across the entire bandwidth of the transducer, containing information on a wide range of frequencies. Since reflection coefficient is frequency dependant, processing for reflection coefficient at a given frequency is much more appropriate.

$$|R| = \frac{A(f)_{meas}}{A(f)_{ref}} \qquad (3.26)$$

For the current instrumentation configuration in rolling element bearings, where an ultrasonic sensor is bonded onto a stationary raceway, the sensor will only observe a roller pass occasionally and very briefly across its sensing region. Apart from a roller pass, the remaining measurements are attributed to a steel-air or a steel-oil interface. This means that, provided that the capture duration is long enough to include at least two roller passes and the correct referencing region is selected (steel-air interface), a reference pulse will always be present within the measurement dataset. This 'live' reference accounts for any changes to the sensor response which may arise through temperature variations during operation and thus eliminates the requirement of a reference calibration testing.

Acquisition of a reference waveform

As only a small portion of the dataset is attributed to roller measurements, the most efficient method of extracting a reference is to obtain the modal waveform. This will be resulted from either a steel-air or steel-oil interface, depending on the duration the raceway remains insufficiently lubricated after a roller pass. To obtain the correct waveform, distinction between the two is required. A method for identifying the correct waveform will be explained in §7 alongside its corresponding datasets.

Method of obtaining the modal waveform is detailed in Figure 3.12. There exist a similar number of datapoints for each captured pulse. The modal waveform would be built from the mode of each of datapoint value, $A(x)$ across all the captured pulses. The modal waveform would consequently correspond to measurements from the longest occurring interface (ie. steel-air or steel-oil) within the capture duration.

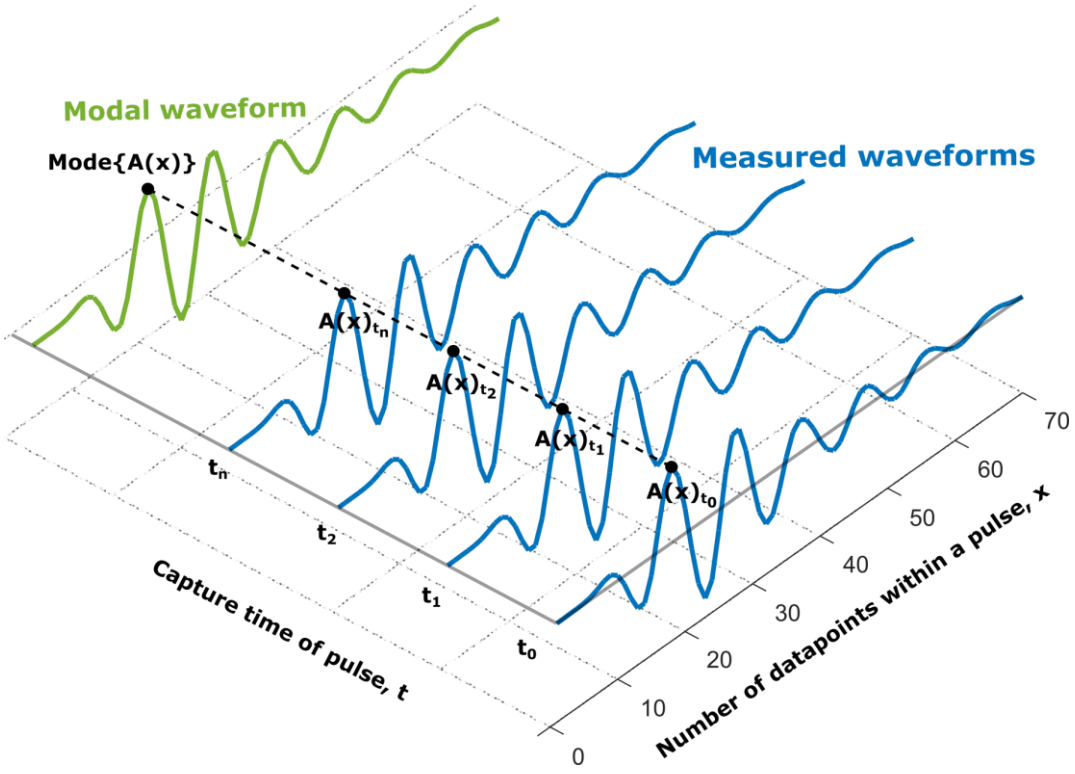

Figure 3.12 - Method of obtaining a modal reference waveform from the data stream (adapted from [171])

3.6.4 Data processing for reflection coefficient and ToF

After acquiring the modal reference, two routes of data processing can be followed to respectively obtain reflection coefficient and raceway deflection. This is detailed in Figure 3.13. Amplitude based processing was utilised to understand the amount of

ultrasonic energy transmitted into the rollers and lubricant to investigate lubrication condition whilst ToF based processing was utilised to extract the ultrasound travel length and consequently raceway deflection and load.

To obtain reflection coefficient, a FFT was initially performed on the measured pulses. Before performing the FFT, the time domain waveforms were zero-padded to increase the resolution of the frequency spectra. In reality, this however only had an interpolation effect on the frequency spectra and does not add additional new information into the existing data. Measurements of reflection coefficient were then obtained from using Equation (3.26), resulting in reflection coefficient measurements for every frequency within the sensor's bandwidth. Measurements of reflection coefficient can then be further processed to obtain ball pass frequency, indication of surface lubrication and if appropriate, applied in the spring model for quantitative measurements of lubricant film.

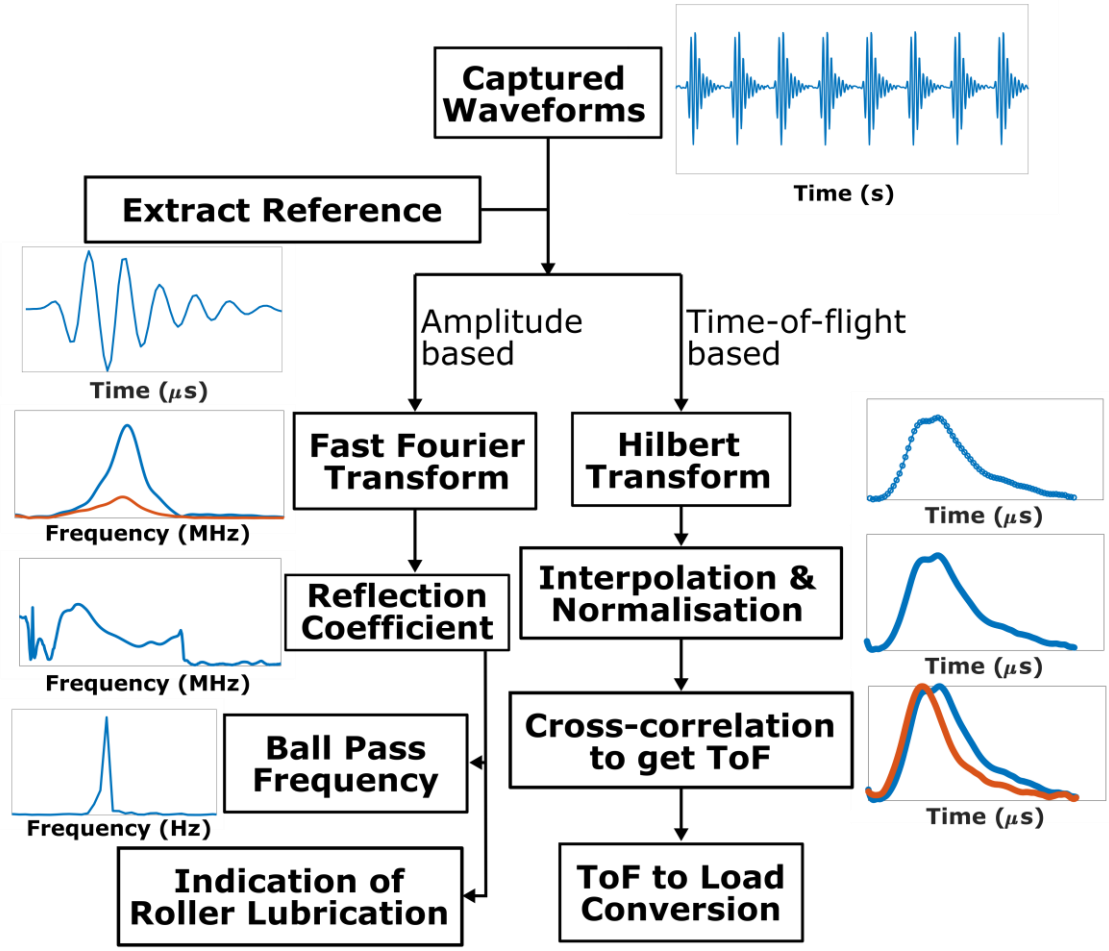

Figure 3.13 – Summary of data processing routine to obtain reflection coefficient and ToF from ultrasonic data stream

ToF based processing would be more complicated. To obtain the waveform envelopes, a Hilbert Transform was initially carried out on both the reference (unloaded) and loaded ultrasonic pulses. Since the time shift is measured to the closest sampling point, the method's accuracy is restricted to the time sampling frequency of the FMS (100 *MHz*). Consequently, increasing the resolution of the reference and loaded waveform was necessary to improve the accuracy of the measurement. This was achieved through interpolation of the measured pulses. A sampling frequency of 100 *MHz* would correspond to a digitisation rate of 10 *ns*. After a 100-point interpolation, this would reduce to 0.01 *ns*. The envelopes were subsequently normalized against their respective maximum amplitudes before cross-correlating to obtain the time shift. After the time shift is obtained, Equation (3.25) can be used to convert the *ToF* to deflection measurements and thereafter roller load through appropriate contact models. The contact models utilized for conversion of deflection to roller load are discussed in §5.

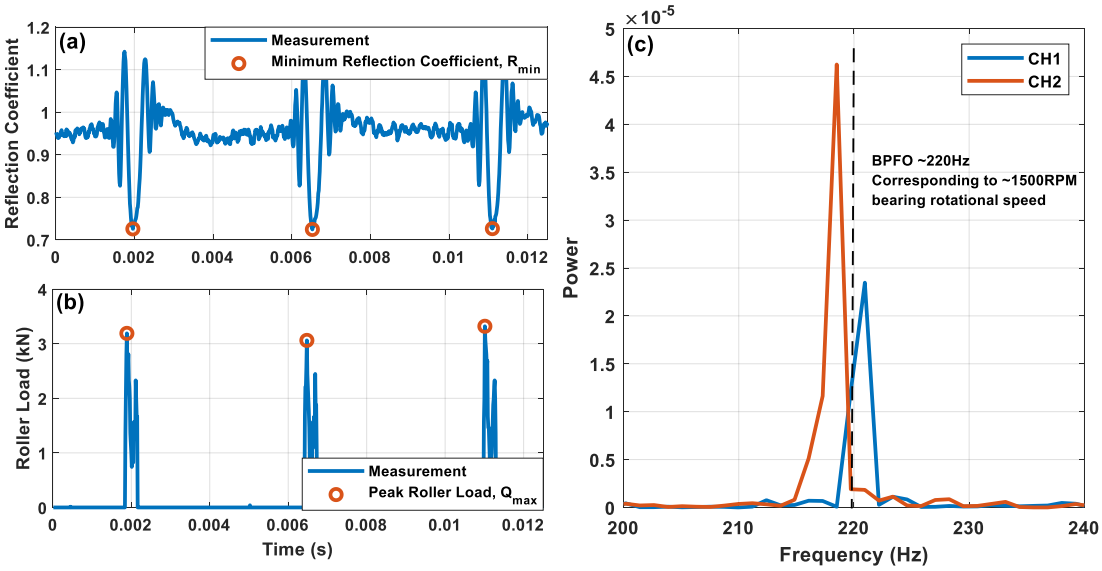

Figure 3.14 – (a) Reflection coefficient and (b) roller load measurements for 3 rollers pass and (c) the power spectral density of the reflection coefficient

Figure 3.14 illustrates the reflection coefficient and roller load measurements for 3 consecutive roller passes. Peaks within the roller load measurement and dips within the reflection coefficient measurement are resulted from roller passes. The measurements show that reflection coefficient, R increases from 0.95 between roller passes, up to a peak of ~1.10 before falling down to a minimum ~0.70 before rising up again. Reflection coefficient should not increase above unity as this indicate that additional ultrasonic energy is measured by the sensor. The reverberations manifesting at the contact entry and exit regions are termed "interference fringes",

resulting from both the sensor beam spread and finite size of the sensor relative to the raceway-roller contact region. The ratio between the two would dictate the width of both the reflection coefficient dips and also the roller load peaks. Across the measurement region corresponding to roller passes, the minimum reflection coefficient, R_{min} and peak roller load, Q_{max} are extracted for each roller pass to be further analysed. Interference fringes are explored and discussed in depth in §6.

Inferring Bearing Rotational Speed

Due to roller passes manifesting themselves as dips within the reflection coefficient measurements, if the bearing geometry is known, measurement of ball pass frequency and subsequently bearing rotational speed, ω_{brg} is possible. This is shown in Equation (3.27) where *Z* is the number of rollers, f_i or f_o are the inner or outer race ball pass frequency, *d* and *D* are the mean roller and pitch diameter respectively and φ is the cone or cup angle. For cylindrical roller bearings, φ would be 0°. If the ultrasonic sensor was placed on a static inner raceway, then the sign for the denominator term would be positive. If the opposite is true, then the sign would be negative. As bearing cage speed is also possible to be derived from this, with the presence of an encoder as an additional bearing speed measurement, it is possible to derive slip.

$$\omega_{brg} = \frac{120 \cdot f_{i/o}}{Z\left(1 \pm \frac{d}{D} cos\varphi\right)} \quad (3.27)$$

Indication of Roller Lubrication

As mentioned previously, reduction in reflection coefficient is resulted from the presence of lubrication on a bearing raceway. This effect can be observed within the reflection coefficient measurements in the gap between roller passes. An insufficiently lubricated raceway surface (steel-air interface) would have a reflection coefficient of 1, whilst a well lubricated bearing surface (steel-oil interface) would have a reflection coefficient of 0.95. It is prudent to mention that the pattern and behaviour of reflection coefficient is dependent on the lubricant film and thus the viscosity of the lubricant film, the rotational speed of the bearing and also the frequency and type of the sensor. Categorisation work conducted was for measurements shown in §6 and 7, using 10 MHz longitudinal sensors instrumented within a bearing lubricated using VG320 oil. Features of the lubricant behaviour for low and high rotational speed are shown respectively in Figure 3.15 and Figure 3.16.

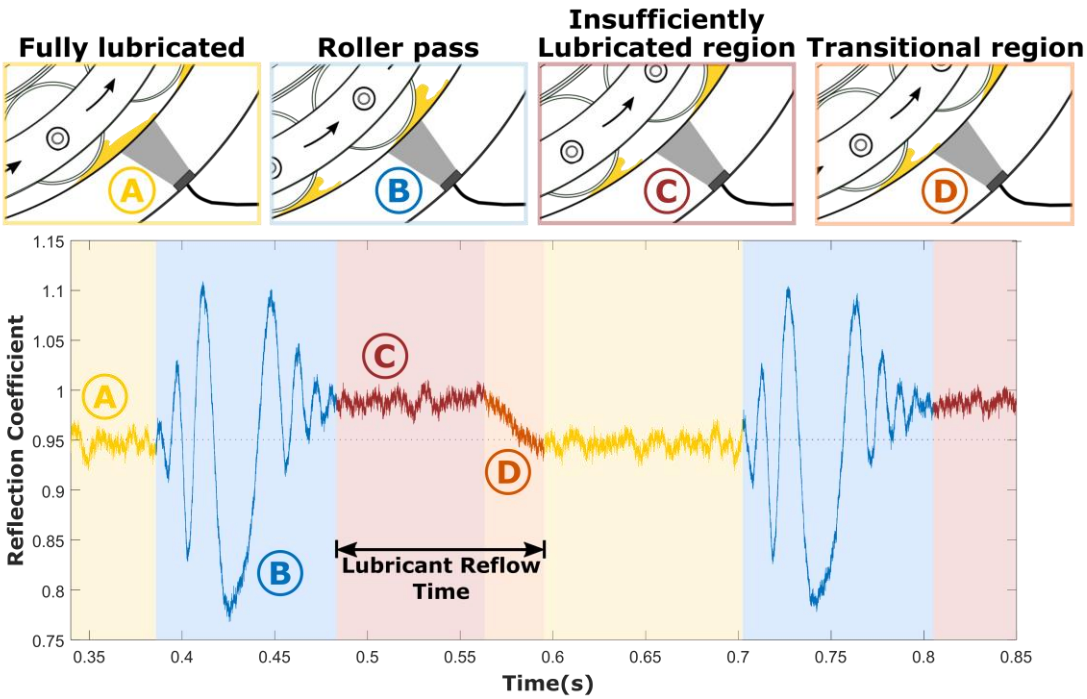

Figure 3.15 – Lubricant behaviour between roller passes (VG320, rotational speed <200 *RPM*)

Under low rotational speeds, the raceway is swept clean of lubricant after a roller pass. This results in a reflection coefficient of 1 as this corresponds to a steel-air interface. For a period of time, the rolling surface remains clear of lubricant. As the lubricant gradually reoccupies the voided region, reflection coefficient subsequently reduces from unity to ~ 0.95. When tested under no lubricant, such a pattern ceases to exist between roller passes, thus confirming that the reflow patterns are resulted from lubricant flow on bearing surface.

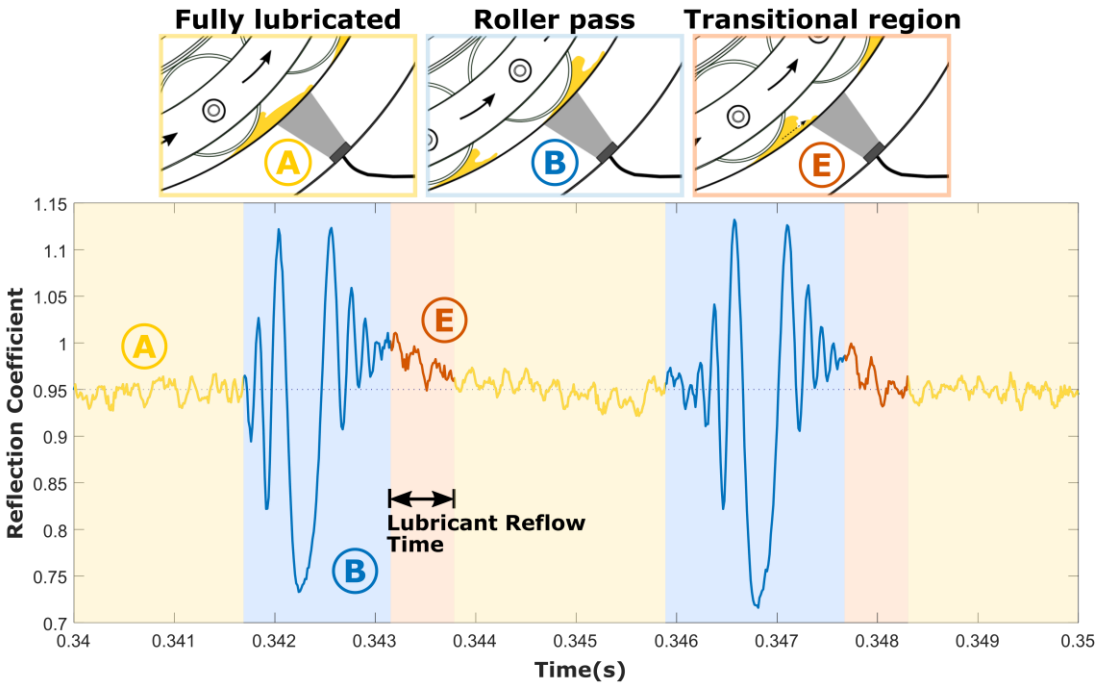

Figure 3.16 – Lubricant behaviour between roller passes (VG320, rotational speed >200 RPM)

Figure 3.16 depicts the lubricant behaviour at high rotational speeds of 1500 *RPM*. The steel-air region where reflection coefficient is unity is significantly shorter than that of a slow rotating bearing. After a roller pass, the reflection coefficient immediately begins to reduce from unity to 0.95. This is theorised to be caused by of the incoming roller pushing and forcing lubricant to flow into the region previously swept clear by the previous outgoing roller and also potentially a higher temperature lubricant, from the higher bearing rotational speed, resulting in a less viscous flow.

The sensitivity of the measurement would be influenced by the transducer's frequency and also the free surface oil film thickness. This theory is based on Equation (3.16). As a sensor's central frequency increases, the free surface oil film thickness would decrease. It is also sensible to assume that the oil film necessary to register a reflection coefficient of 0.95 would also reduce. Consequently, the minimum detectable amount of oil film is dictated by the sensor frequency and a lubricant film too thin would register a reflection coefficient >0.95. Longitudinal sensors with frequency of $10\,MHz$ work well in characterising lubricated and unlubricated instances for typical gearbox lubricant (VG320). The limitation for the method would be its sensitivity range between 0.95 to 1.00.

Limitations of spring model

In Figure 3.13, application of spring model to obtain lubricant film thickness from reflection coefficient was left out of the data processing. The rationale for this is discussed in this section. Figure 3.17 shows the spectral amplitude, reflection coefficient and lubricant film thickness for a dataset obtained from §7. The plot of interest is the lubricant film thickness measurement shown in Figure 3.17(e) & (f), the supplementary figures are for completeness purposes. The lubricant film thickness within the sensor's bandwidth should be frequency independent, however this is not the case as the lubricant film thickness exhibit a decreasing slope. This rendered the film measurements invalid and the spring model inapplicable. As such the slope of the reflection coefficient spectra within the sensor bandwidth can be used to determine the applicability of spring model.

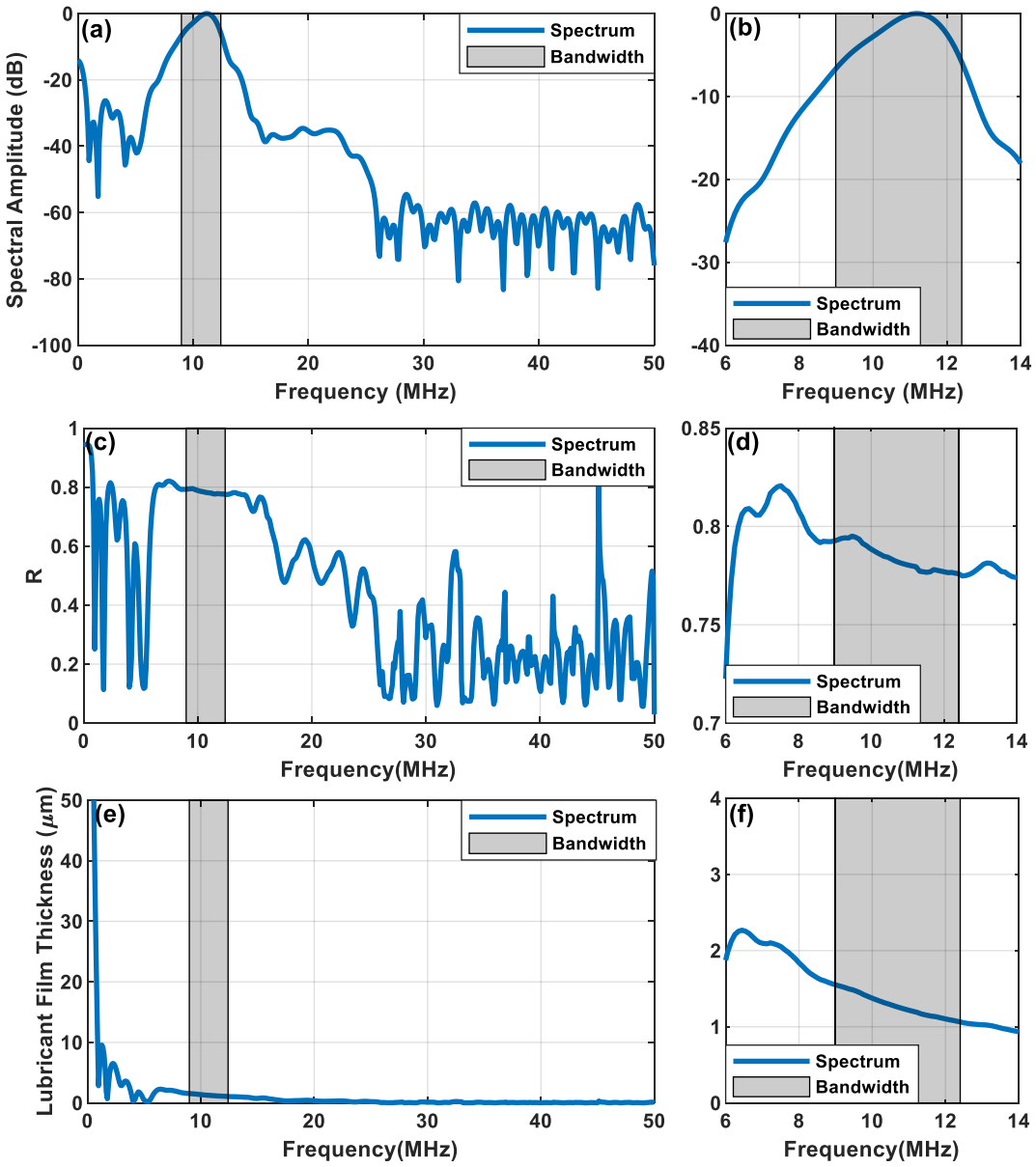

Figure 3.17 – Spectral amplitude measurement for (a) full frequency range (b) focused bandwidth region, Reflection coefficient measurement for the (c) full frequency range and (d) focused bandwidth region and lubricant film thickness measurement for (e) full frequency range and (f) focused bandwidth region

Figure 3.18 summarizes two problems resulting in the inapplicability of the spring model in this work. The first issue is resulted from the inherent nature of the application. Rolling element bearings operate within the mixed or elasto-hydrodynamic regime, consisting of a mixture of regions separated by lubricant as well as metal to metal contact as shown in Figure 3.18(d), unlike hydrodynamic bearings where both surfaces are constantly separated by a lubricant film, illustrated in Figure 3.18(c).

The roughness of the contacting surfaces would affect the proportion of asperity-to-asperity contacts and the regions fully separated by oil. This is typically quantified using the lambda ratio, Λ as explained in §2.4.4. As a result, measurement of lubricant film thickness will not yield any meaningful result.

The subsequent and primary challenge lies in generating an ultrasonic beam focal size which is smaller than the contact width of the roller-raceway interface (Figure 3.18(b)) without significant modifications to the bearing. An ultrasonic beam size greater than the contact region would result in averaged measurements.

Consequently, a combination of having both mixed lubrication and a sensor focal size larger than then contact region, resulted in the inability to convert reflection coefficient measurements, R into lubricant film thickness, h. Reflection coefficient measurements were instead used as a qualitative indication of film thickness and bearing lubrication condition inferred from reflection coefficient patterns between roller passes.

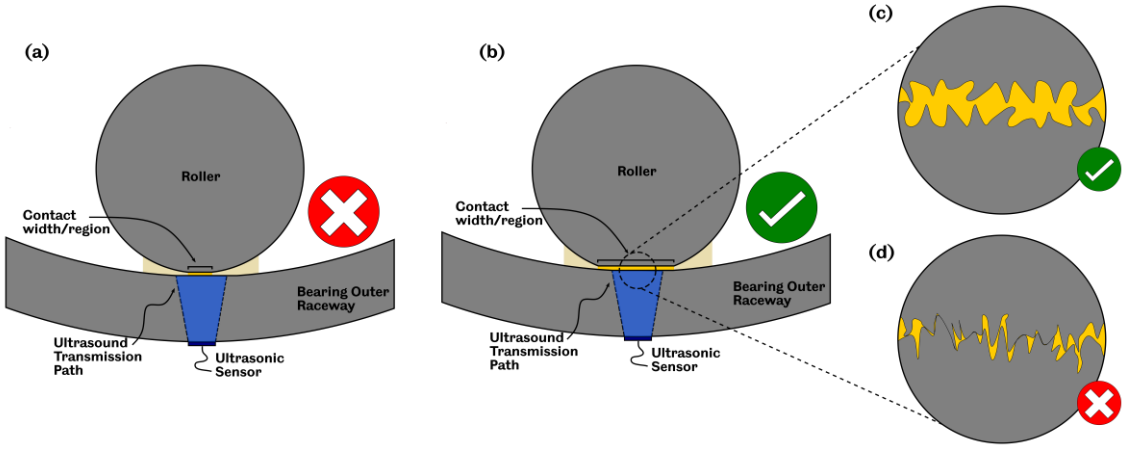

Figure 3.18 – (a) Averaged measurements across the ultrasound sensing region for when (a) contact width is less than ultrasonic beam size (b) contact width is more than ultrasonic beam size, (c) lubricant fully separating the asperities within contact and (d) mixed interface consisting of both solid-solid asperity contacts and solid-liquid contact

3.7 Conclusions

- Ultrasound are elastic waves caused by disturbance within a media and propagates at frequencies beyond the audible range of human hearing (> 20 *kHz*). Propagation of ultrasonic energy occurs through transferral of particle

energy or oscillations through the bonds between particles and not the translation of particles.

- It is possible to generate ultrasonic signals without compromising signal quality through utilisation of low cost, piezoelectric elements.
- Piezo-ceramic elements bonded onto a bearing surface were able to generate stable and repeatable signals, eliminating the issues of intermittent signal quality resulting from couplant usage.
- Ultrasonic waves reflected from an interface contain information on the interface. The proportion of ultrasonic energy reflected back from a bearing raceway (amplitude) is dependent on the lubricant film thickness whilst the time-of-arrival of the ultrasonic pulse is stress dependant.
- The procedure for measurement of reflection coefficient, bearing rotational speed, indication of raceway lubrication and roller load in rolling element bearings were detailed and outlined.

4 CONTRIBUTIONS TO CHANGE IN SOUND VELOCITY

Having introduced the fundamentals of ultrasound, various methods of measuring lubricant film thickness ultrasonically, and briefly on the roller load measurement method in the previous chapter, the current chapter explores in depth the variation of sound speed with stress or the acoustoelastic effect. The chapter is structured to consist partly of background information and partly of novel experimental work on measurements of second and third-order elastic constants of EN31 steel. Initially, the underlying physics governing the acoustoelastic effect are explained. This is succeeded by experimental investigations into the second and third order acoustoelastic constants of EN31 bearing steel. A uniaxial compression test setup is utilised to obtain the acoustoelastic constants of bearing steel. The acoustoelastic constants obtained are used subsequently in §5.2.5 to decouple the portion of change in time-of-flight as a result of acoustoelasticity in the ToF-deflection relationship. Rolling contact stresses are indeed multi-axial and non-proportional, however the ultrasonic method does not measure stress directly, but infers raceway deflection from ToF after eliminating time shift contributions from these stresses (through acoustoelastic constant) and also the apparent time shift resulted from the presence of a lubricant interface. The raceway deflection is then used to calculate roller and bearing load using contact models.

4.1 Stresses in wind turbine gearbox bearings

Wind turbine gearbox bearings experience a range of stresses depending on their location within the wind turbine, the type of bearing and the size or power rating of the wind turbine. Design standards [172] exist which specify guideline values for maximum contact stress for a 20-year gearbox operational life. These values are shown in Table 4.1 in ascending order. The stress limit ranges from 1300 to 1650 *MPa* with the high-speed and low-speed shaft bearings having the lowest and highest stress limit imposed on them respectively.

Position of bearing	Maximum contact stress limit (MPa)
High speed shaft	1300
Low-speed planet	1500
Intermediate planet	1500
Intermediate sun shaft	1650

Low speed intermediate shaft	1650
High speed intermediate shaft	1650
Low speed shaft	1650

Table 4.1 - Hertzian contact stress limit for bearings at various locations within the gearbox (reproduced from [172])

During operation, the bearing stress might exceed the design limits imposed in the standard or vary from respective bearings located at the same position. For bearings within the planetary gear, previous studies [173-176] reported a variation in load carried between the upwind and downwind bearings. The upwind bearings were reported to carry up to 30% more load than their downwind counterparts [175]. In the event where the downwind bearings are withstanding maximum contact stresses, the upwind bearings would be overloaded beyond their design point.

During a modelling study conducted on an NREL 750kW gearbox [176], a stress of around 1500MPa was found during normal operating conditions for planetary bearings. The stress however exceeded 1700MPa during shut down, 14% higher than the maximum design limit. The maximum contact pressures were calculated for the inner race as the WTGBs are most prone on failure in the inner race.

In ISO 281:2007 [177], the fatigue limit used corresponds to a maximum contact stress of 1500MPa which translates to an equivalent von-Mises stress of 900MPa. Measurements of acoustoelastic constant would thus be taken up to 900MPa and not beyond despite previous studies showing potential bearing stresses exceeding design limit during operation. This was due to increased difficulty in ensuring the test samples do not brittle fracture under such high compressive stresses.

4.2 Contributing factors to variation in speed of sound

The acoustoelastic effect manifests itself as a change in time-of-flight (ToF) in measurements as an ultrasonic wave propagates through a material under stress in contrast to the same unstressed material. Mathematically this is defined below, where ToF_0 and ToF_σ are the transit times of ultrasound under unstressed and stressed states.

$$\Delta ToF = \Delta t = ToF_0 - ToF_\sigma \quad (4.1)$$

As briefly detailed in the previous chapter, several other factors also affect the sound speed as it travels through a material under stress. These will be discussed in depth in this section.

4.2.1 Deflection

Deformation of the material under stress will result in the change in the travel length of the ultrasonic wave, and consequently a variation in *ToF*. The *ToF* change purely results from material deflection, Δt_δ can thus be defined as shown in Equation (4.2) where δ is the deflection of the component as illustrated in Figure 4.1 and $(c_{zz})_0$ is the unstressed speed of sound. The first letter of the subscript corresponds to the propagation direction of the ultrasonic wave whilst the second letter corresponds to the direction of particle motion.

$$\Delta t_\delta = \frac{2\delta}{(c_{zz})_0} \quad (4.2)$$

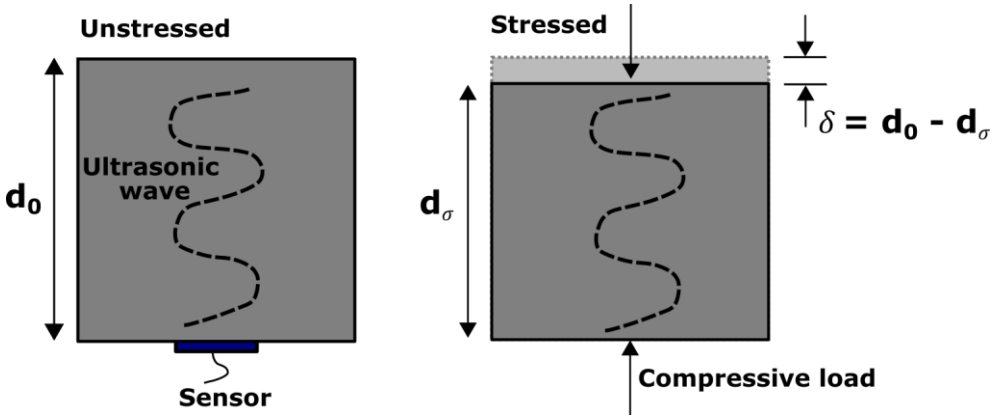

Figure 4.1 – Ultrasonic wave travelling through an unstressed and stressed component

The speed of sound can be related to material elasticity and rigidity through the Newton-Laplace equation. For longitudinal waves this is shown in Equation (4.3) and for shear waves, Equation (4.4) where E is the bulk modulus, ρ is the density, v is the Poisson's ratio and G is the shear modulus.

$$c_L = c_{zz} = \sqrt{\frac{E}{\rho} \cdot \frac{(1-v)}{(1+v)(1-2v)}} \quad (4.3)$$

$$c_T = c_{zx} = c_{zy} = \sqrt{\frac{E}{\rho} \cdot \frac{1}{2(1+v)}} = \sqrt{\frac{G}{\rho}} \quad (4.4)$$

4.2.2 Acousto-elasticity

The stress-strain curve for a linear-elastic material (ie. steel) subjected to uniaxial loading is shown below. For typical engineering applications, it can be approximated as a linear relationship, however for acousto-elasticity it is the non-linear components that are of interest. The following section aims to demonstrate theoretically, the source of the non-linear components.

The strain energy per unit volume can be expressed as shown in Equation (4.5) [178].

$$\psi(\varepsilon) = \frac{1}{2} E \varepsilon^2 \quad (4.5)$$

According to this definition, the stress acting on a material can thus be expressed as shown in Equation (4.6). Consequently, a generalised expression of stress can be produced as shown in Equation (4.7).

$$\sigma = \frac{\partial \psi}{\partial \varepsilon} = E\varepsilon \quad (4.6)$$

$$\sigma_{ij} = \frac{\partial \psi}{\partial \varepsilon_{ij}} = \sum C_{ijkl} \varepsilon_{kl} \quad (4.7)$$

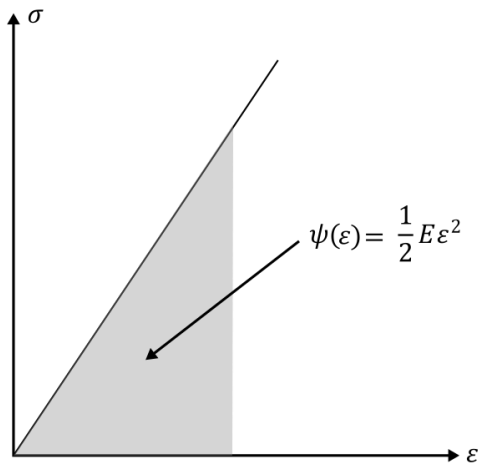

Figure 4.2 – Stress-strain plot for a linear elastic material under uniaxial stress [178]

Taylor series expansion of the generalized Hooke's law yields Equation (4.8) where the terms C are the components of the stiffness tensor of different orders. The nonlinearity which manifests itself as acousto-elasticity is a result of the higher order terms in the Taylor series expansion. As mentioned previously, in most engineering applications these non-linear terms are typically omitted as they have little effect, however when investigating the variation of sound speed with stress, the simplification is not valid.

$$\psi = C^{(0)} + C_{ij}^{(1)}\varepsilon_{ij} + \frac{1}{2}C_{ijkl}^{(2)}\varepsilon_{ij}\varepsilon_{kl} + \frac{1}{6}C_{ijklmn}^{(3)}\varepsilon_{ij}\varepsilon_{kl}\varepsilon_{mn} + \cdots \qquad (4.8)$$

For an isotropic material, there exists two second-order elastic constants and three third-order elastic constants. Second-order elastic constants or Lame constants define the linear elastic stress-strain response of a material through λ and μ. Conversely, third-order elastic constants or Murnaghan constants, given by the convention l, m and n describe the non-linear elastic stress-strain response. The third-order elastic constants can be related to the variation in speed of sound for a given stress. The opposite is true where the Murnaghan constants can be determined ultrasonically through measurement of longitudinal and shear velocities through a material with varying orientation and stress field.

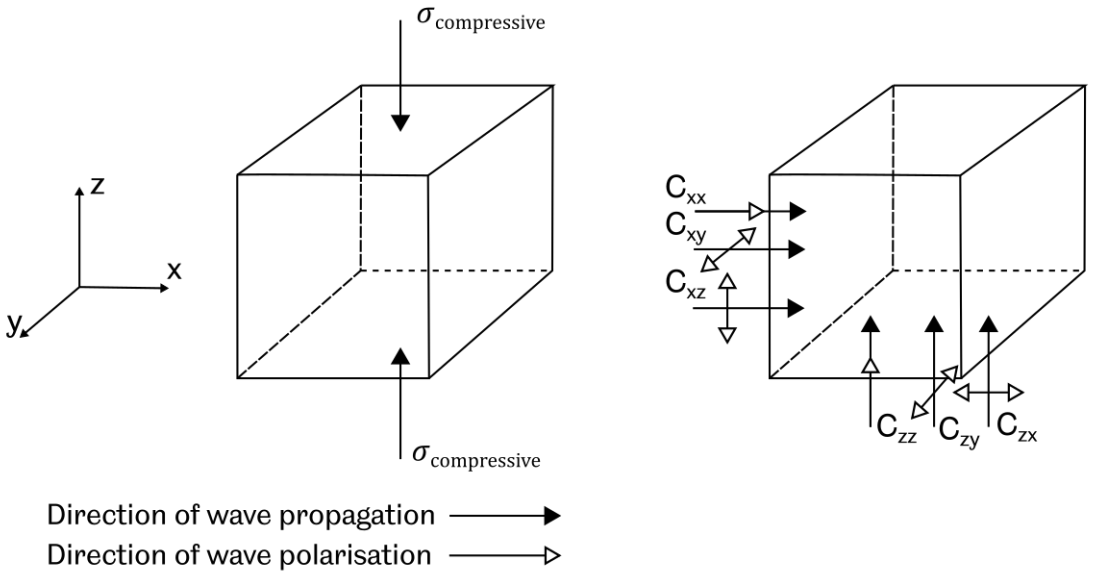

Figure 4.3 – Notation for longitudinal and shear waves with reference to the direction of applied stress

Consider longitudinal and shear waves propagating in two directions, parallel and perpendicular to the uniaxial compressive stress as shown in Figure 4.3. Equation governing the speed of sound propagating parallel to the principal stress and having

particle displacements in x, y and z directions are given in Equation (4.9) where ρ_0 is the unstressed density, c_{zz} is the speed of sound, first subscript is the propagation direction whilst the second is the polarisation direction, λ and μ are second order elastic constants, ν is poisson's ratio, ε is strain and the Murnaghan constants are given as l, m and n.

$$\rho_0 c_{zz}^2 = \lambda + 2\mu + \left[4(\lambda + 2\mu) + 2(\mu + 2m) + \nu\mu\left(1 + \frac{2l}{\lambda}\right)\right]\varepsilon \qquad (4.9)$$

For a longitudinal wave travelling perpendicular to the stress, this is given as:

$$\rho_0 c_{xx}^2 = \rho_0 c_{yy}^2 = \lambda + 2\mu + [2l(1 - 2v) - 4v(m + \lambda + 2\mu)]\varepsilon \qquad (4.10)$$

Equation (4.11) gives the relationship for a shear wave travelling parallel to the stress, with polarisation perpendicular to the stress.

$$\rho_0 c_{zx}^2 = \rho_0 c_{zy}^2 = \mu + \left[4\mu + v\left(\frac{n}{2}\right) + m(1 - 2v)\right]\varepsilon \qquad (4.11)$$

Equation (4.12) provides the relationship for a shear wave travelling perpendicular to the stress with polarisation parallel to the stress.

$$\rho_0 c_{xz}^2 = \rho_0 c_{yz}^2 = \mu + \left[(\lambda + 2\mu + m)(1 - 2v) + \frac{1}{2}nv\right]\varepsilon \qquad (4.12)$$

Equation (4.13) provides the relationship for a shear wave with both propagation direction and polarisation direction perpendicular to the stress.

$$\rho_0 c_{yx}^2 = \rho_0 c_{xy}^2 = \mu + \left[(\lambda + m)(1 - 2v) - 6v\mu - \frac{1}{2}n\right]\varepsilon \qquad (4.13)$$

The bulk modulus, B of a material can be defined in terms of Lame constants:

$$B = \lambda + \frac{2}{3}\mu \qquad (4.14)$$

Various studies have sought to determine the Lame and Murnaghan constants for a range of steels. These values along with the bulk modulus are summarised in Table 4.2. Unfortunately, information on EN31 bearing steel is not available in the literature for comparison.

The acoustoelastic constant for a specific type of steel is expected to not vary significantly, however there are factors that would influence the acoustoelastic constant such as residual stress and material anisotropy. Residual stress as a result of processing or machining of specimen can influence the acoustoelastic constant of the material, similar to how an applied stress influences the material. The quality of EN31 bearing steels are very well controlled and thus anisotropy is not an issue. Residual stress however is potentially a problem, as bearing raceways typically have compressive residual stresses introduced into them during the manufacturing process to limit fatigue crack propagation and improve bearing life. They have also been thought to vary with operation and with depth. The presence of residual stress can be roughly evaluated through comparing the unstressed speed of sound measurements of the raceway with a reference value where the material has no residual stress. A difference greater than 5% between the two measurements indicate the presence of residual stress.

	Rail steel [179]	Rail steel [180]	Hecla 17 steel [181]	S40 Steel [182]	Aluminium A3004 [183]	Aluminium 7075-T651 [184]	Pure copper (99.9%) [185]	Nickel-steel S/NTV [185]
λ (GPa)	112.9	115.8	110.5	113	56.3	54.9	104	109
μ (GPa)	80.8	79.9	82	85	26.6	-26.5	46	81.47
l (GPa)	-88.9	-248	-328	-916	-564.6	-252.2	542	-56
m (GPa)	-591.6	-623	-595	-402	-231.7	-325	-372	-671
n (GPa)	-903.8	-714	-668	-1012	-353.6	-351.2	-401	-785
L_{zz}	-2.07	-2.52	-2.46	-1.85	-3.56	-4.44	-0.68	-2.63
L_{zx}/L_{zy}	-0.34	-0.25	-0.14	0.13	-0.52	-1.09	0.04	-0.48

Table 4.2 – Values of Lame & Murnaghan constants for various steels

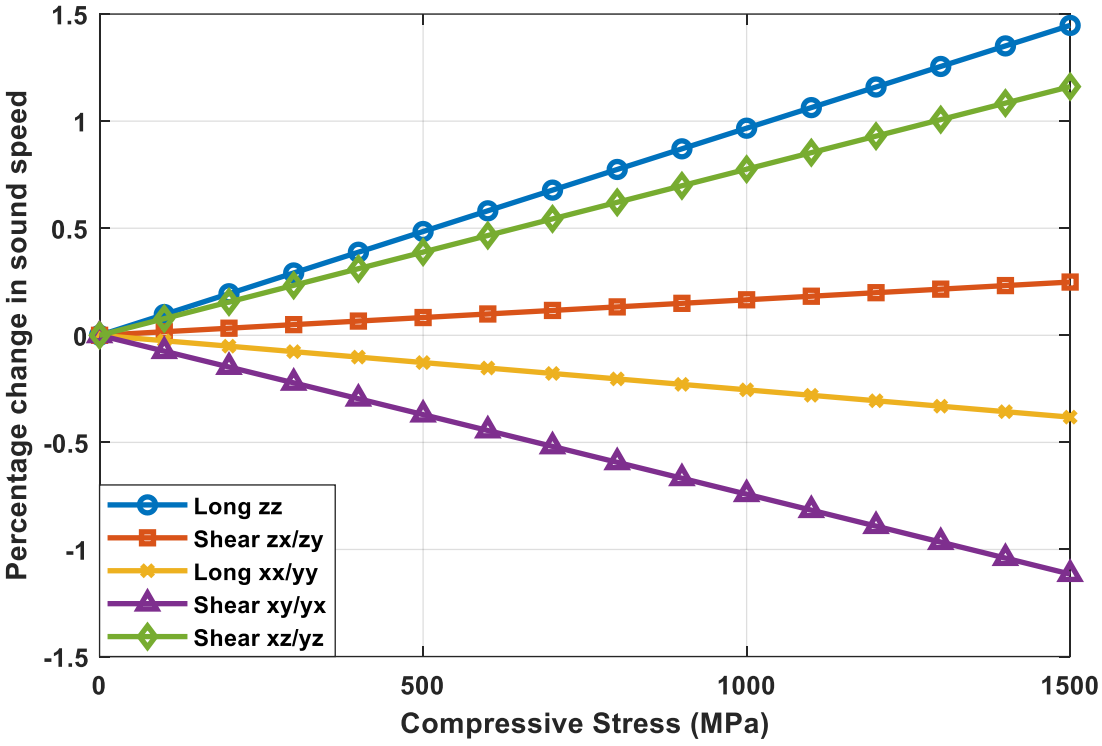

Figure 4.4 – Percentage change in sound speed with increasing compressive stress for rail steel calculated using second and third order elastic constants from [179]

Figure 4.4 shows the variation in speed of sound with increasing compressive stress for rail steel calculated using elastic constants from [179]. From the figure, it is evident that the percentage change in sound speed appear to be linear with increasing stress. As such, the higher order elastic constants are commonly approximated using a linear relationship between sound speed and stress as shown in Equation (4.15) where L_{ac} is the acoustoelastic constant, determined experimentally and unique for each wave propagation and polarisation direction as well as stress orientation.

$$L_{ac} \cdot \sigma = \frac{\Delta c}{c} \qquad (4.15)$$

Based on Equation (4.10), the longitudinal sound speed for a material under an unstressed state is given by:

$$\rho_0 (c_{zz})_0^{\,2} = \lambda + 2\mu \qquad (4.16)$$

Differentiating Equation (4.9) yields:

$$\rho_0(c_{zz})_P d(c_{zz})_P = \left[2(\lambda + 2\mu) + (\mu + 2m) + \nu\mu\left(1 + \frac{2l}{\lambda}\right)\right] d(\varepsilon_z)_P \qquad (4.17)$$

If change in speed of sound is small, the following assumption can be made.

$$\rho_0(c_{zz})_P(c_{zz})_0 \approx \rho_0(c_{zz})_0{}^2 = \lambda + 2\mu \qquad (4.18)$$

Dividing Equation (4.17) with Equation (4.18) yields,

$$\frac{d(c_{zz})_P}{(c_{zz})_0} = \left[2 + \frac{(\mu+2m)+\nu\mu\left(1+\frac{2l}{\lambda}\right)}{\lambda+2\mu}\right] d(\varepsilon_z)_P \qquad (4.19)$$

The acoustoelastic constant is defined as a ratio of change in speed of sound against unstressed sound speed divided by the change in strain. Equation (4.19) can thus be rearranged to express the acoustoelastic constant for a longitudinal wave travelling parallel to the direction of principal stress, L_{zz} in terms of Lame and Murnaghan constants. This is shown in Equation (4.20).

$$L_{zz} = \frac{d(c_{zz})_P/(c_{zz})_0}{d(\varepsilon_z)_P} = 2 + \frac{(\mu+2m)+\nu\mu\left(1+\frac{2l}{\lambda}\right)}{\lambda+2\mu} \qquad (4.20)$$

Table 4.3 shows the acoustoelastic constants for ultrasonic waves travelling parallel and perpendicular to the direction of stress as well as their different polarisation.

Acoustoelastic constant	
L_{zz}	$2+\frac{(\mu+2m)+\nu\mu\left(1+\frac{2l}{\lambda}\right)}{\lambda+2\mu}$
L_{zx}/L_{zy}	$2+\frac{\nu n}{4\mu}+\frac{m}{2(\lambda+2\mu)}$
L_{xx}/L_{yy}	$-2\nu\left(1+\frac{m-\mu l/\lambda}{\lambda+2\mu}\right)$
L_{xy}/L_{yx}	$\frac{\lambda+2\mu+m}{2(\lambda+2\mu)}+\frac{\nu n}{4\mu}$
L_{xz}/L_{yz}	$\frac{(m-2\lambda)}{2(\lambda+\mu)}-\frac{n}{4\mu}$

Table 4.3 – Acoustoelastic constants for different ultrasonic waves travelling perpendicular or parallel to the direction of stress

The change in speed of sound is defined as the difference between the sound speed travelling through a material in an unstressed and stressed state.

$$d(c_{zz})_P = (c_{zz})_0 - (c_{zz})_P \tag{4.21}$$

The change in strain on the other hand can be defined as:

$$d(\varepsilon_z)_P = -\varepsilon_z \tag{4.22}$$

Substituting these two expressions into Equation (4.20) yields:

$$(c_{zz})_P = (c_{zz})_0(1 - L_{zz}\varepsilon_z) \tag{4.23}$$

The ToF change purely resulted from the acoustoelastic effect can be computed from the difference between the ToF of the unstressed and stressed states.

$$(\Delta t_{zz})_L = \frac{2d_0}{(c_{zz})_0} - \frac{2d_0}{(c_{zz})_P} \tag{4.24}$$

Substituting Equation (4.23) into Equation (4.24) and rearranging the equation yields Equation (4.25).

$$(\Delta t_{zz})_L = \frac{2d_0}{(c_{zz})_0}\left(\frac{-L_{zz}\varepsilon_z}{1-L_{zz}\varepsilon_z}\right) \quad (4.25)$$

Since deflection, δ is defined as the product of strain, ε_z and undeformed length, d_0, the equation can be rewritten as shown below. This would quantify the contribution purely from acoustoelastic effect in the ToF change.

$$(\Delta t_{zz})_L = \frac{-2d_0 L_{zz}\delta}{(c_{zz})_0(d_0-L_{zz}\delta)} \quad (4.26)$$

4.2.3 Total change in ToF

The total time of flight change for an ultrasonic wave travelling across a stressed material would thus be a summation of the contributions from deflection, density and acoustoelasticity. This can be written as:

$$\Delta t = \Delta t_\delta + \Delta t_L \quad (4.27)$$

For longitudinal waves travelling parallel to the direction of applied stress, the total variation in transit time is shown in Equation (4.28). Conversely, the equation for shear waves is shown in Equation (4.29) with the difference being the unstressed shear speed of sound, $(c_{zx})_0$ and the acoustoelastic constant for a shear wave travelling parallel to the direction of stress, L_{zx}.

$$\Delta t_{long} = \frac{2\delta}{(c_{zz})_0}\left[1-\left(\frac{L_{zz}d_0}{d_0-L_{zz}\delta}\right)\right] \quad (4.28)$$

$$\Delta t_{shear} = \frac{2\delta}{(c_{zx})_0}\left[1-\left(\frac{L_{zx}d_0}{d_0-L_{zx}\delta}\right)\right] \quad (4.29)$$

4.3 Measurement of acoustoelastic constants for EN31

With the theoretical background explained in the previous sections, the current section will detail the experimental setup implemented to measure the acoustoelastic constants of EN31 bearing steel and investigate the percentage contribution of each of the time-of-flight contributing parameters outlined previously. The current experiment aims to measure these under more controlled conditions and with a higher stress range compared to previous work [135].

4.3.1 Experimental Setup

Two experimental configurations were utilised, one utilised an EN31 test specimen in the shape of a cylindrical puck whilst the other a tall square column. Different range of compressive stress were applied on each tests. All of the testing were carried out on a 1000 *kN* hydraulic machine. A spherical seat attachment was fitted onto the top head of the compression machine to eliminate or minimise any misalignment.

Cylindrical puck test setup

The cylindrical puck was selected due to ease of machining, with a diameter of $29\ mm$ and length of $30\ mm$. To ensure a uniform stress distribution across the test specimen, the test specimen is to be "sandwiched" between two flat surfaces of steel, made from O1 tool steel to prevent adhesion. Figure 4.5 illustrates the experimental setup whilst Figure 4.6 shows the sensors instrumented on the cylindrical puck and bottom base plate.

The top specimen is a square plate with the contacting surfaces ground flat. The bottom base specimen is of cylindrical shape with a groove cut out at the bottom face to facilitate instrumentation of the sensors. 3 pairs of ultrasonic sensors, two $10\ MHz$ longitudinal and four $5\ MHz$ shear sensors were instrumented within the groove with the same procedure as detailed in §3.2.3. Four K-type thermocouples were also installed to monitor the temperature of the three steel specimens and ambient temperature. Prior to testing, the 3 steel specimens were hardened to minimise any plastic deformation on the surface which would affect the acoustoelastic measurements. In hindsight, an additional strain gauge should have been installed to provide strain measurements perpendicular to the applied stress.

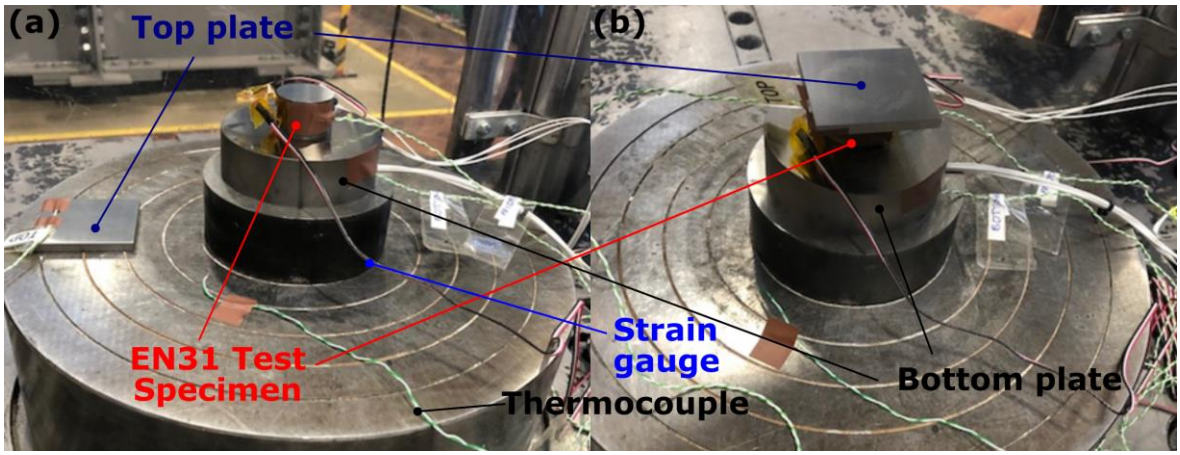

Figure 4.5 – Experimental setup with top plate (a) resting on base of hydraulic rig (b) attached onto the test specimen ready for loading

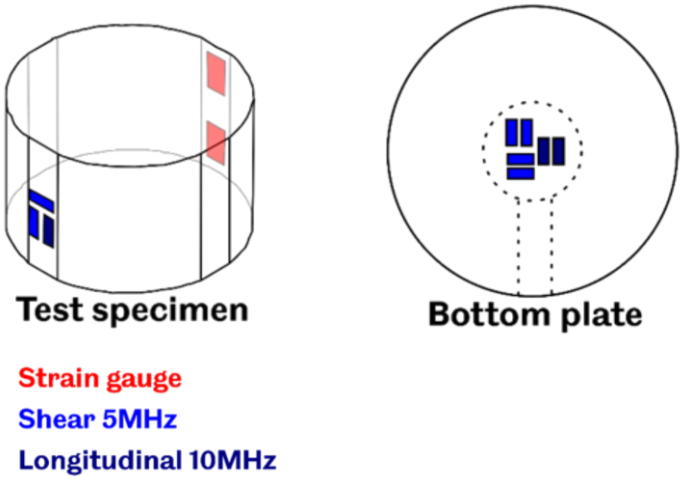

Figure 4.6 – Sensor orientation and position on the test specimen and bottom plate

Square column test setup

Test configuration for the square column is straightforward and was shown in Figure 4.7. The test specimen was placed centrally onto the base of the compression machine with an additional spherical seat attachment placed on top of the specimen in addition to the existing one installed on the machine to cancel out any load misalignment. The test column was instrumented with 3 ultrasonic sensors, 1 longitudinal of $10\ MHz$ oriented parallel to the compressive stress and 2 shear of $5\ MHz$, oriented perpendicular and parallel to the stress.

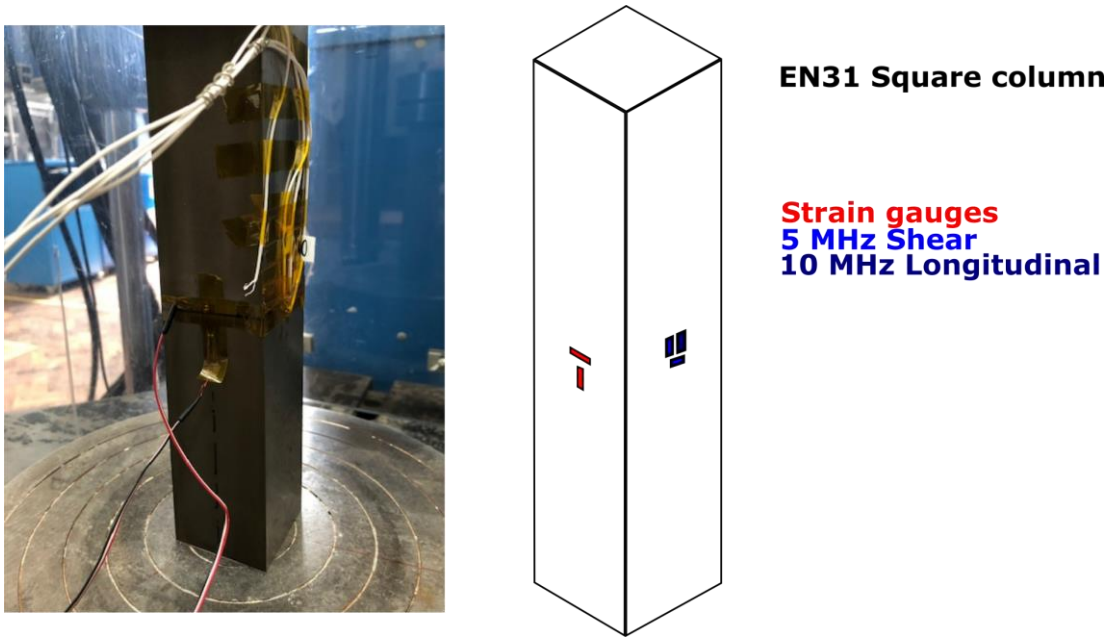

Figure 4.7 – Square column test setup

4.3.2 Methodology

Cylindrical puck test setup

Two tests were conducted on the cylindrical puck test setup, up to the full capacity (1 *MN*) and half the capacity (520 *kN*) of the loading machine. For full capacity testing, compressive load was applied at a rate of 0.8 *kN/s* in loading steps of 40 kN up to 1 *MN*, corresponding to a stress of 1500 *MPa*. The unloading phase also followed the same increments and three cycles of measurements were planned. Unfortunately, due to the high stress, the base plate failed through brittle fracture towards the end of the 2nd loading cycle and testing was halted there.

The half capacity test utilising the same configuration with a shorter test specimen (18 *mm*) and half the loading range (520 *kN*). Loading steps for the shorter test specimen were fully defined in Table 4.4 where at the lower load range (0 – 120 *kN*), a finer step increment of 10 *kN* was employed and this was gradually increased to 20 *kN* and subsequently 40 *kN* as the load approaches 520 *kN*.

The half capacity test was conducted for 3 main reasons. These were:

(i) To obtain 3 full cycles of data as the base plate shattered during the loading phase of the second cycle for the full capacity test

(ii) To better understand the variation of acoustoelastic constant at low stress (< 700 *MPa*)

(iii) To eliminate the potential of data aliasing as a result of large fluctuations in acoustoelastic constants at low stress.

The primary objective was to investigate the fluctuations in time-of-flight measurements under low stress which resulted in acoustoelastic constants deviating from expected values. The unloading phase also followed the specified step increments, and three cycles of measurements were taken.

The ultrasonic sensors were connected to the FMS system which sends a top hat excitation signal to all the sensors. Due to the FMS only having 8 ports, only 5 out of 6 sensors (2 longitudinal, 3 shear) for the bottom plate were used. All 3 sensors (1 longitudinal, 2 shear) were utilized for the test specimen.

Load range (*kN*)	**Steps increment (*kN*)**	**Steps**
0 – 120	10	12
120 – 240	20	6
240 – 520	40	7
		25 Total

Table 4.4 – Loading range and step increments in a cycle

Square column test

For the square column test, a test specimen of 250 *mm* long with a cross sectional area of 50 x 50 *mm* was utilised. Testing was conducted up to half the capacity of the machine (500 *kN*) and a 50 *kN* loading step was employed for both loading and unloading. 6 cycles were conducted on the square column. As only 3 ultrasonic sensors were utilised, all sensors were pulsed, and data were captured using the FMS, previously detailed in §3.6.2.

Measurement of ToF

Figure 4.8 shows the ultrasonic measurement from a side sensor of longitudinal polarisation. Acquisition of transit time for sensors located on the side of the test specimen is straightforward as this would be the time difference between the first and second reflected pulse as illustrated in Figure 4.8. The first pulse is a portion of the initial excitation sent to excite the sensor, captured as the FMS transitioned from pulsing a top-hat signal to receiving. It is possible to measure ToF using the initial excitation and first reflection however this would incur error. Error originates from difficulty in comparing the two pulses as only a portion of the initial excitation is typically captured, and it is also of a different waveform shape. Consequently, the first and second reflection are used.

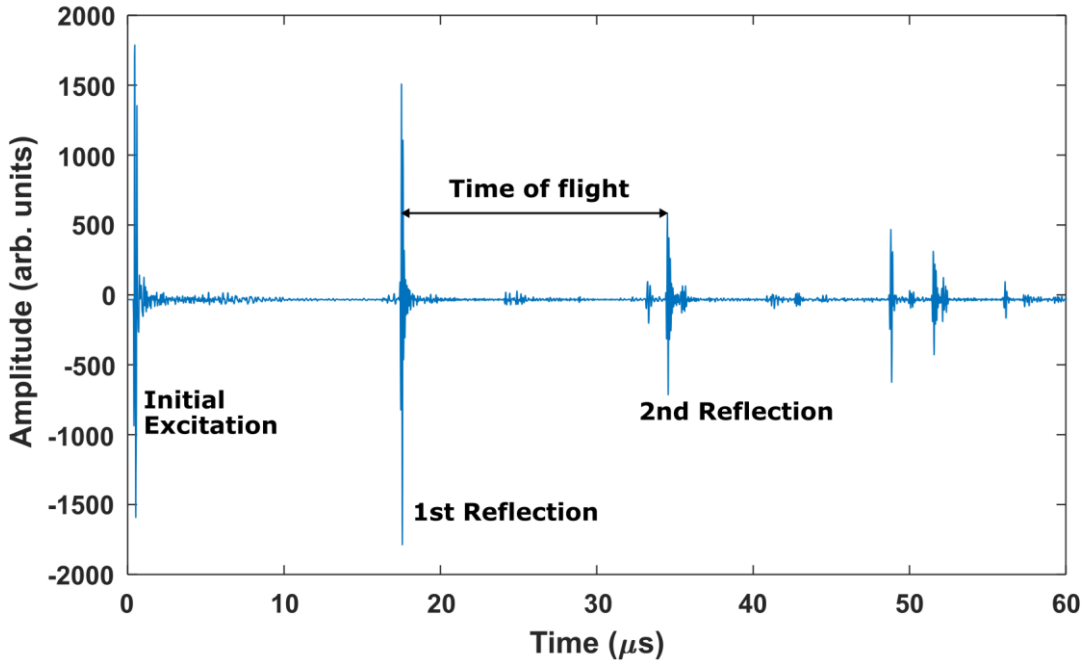

Figure 4.8 – Method of computing ToF from measured pulses

Two methods exist in computing the ToF between pulses:

(i) Zero-crossing

(ii) Cross-correlation

For a basic zero-crossing method, a point where the pulse crosses zero is selected in both the first and second reflections and the time difference between the two pulses is computed. This is shown in Figure 4.9 where the zero-crossing point after the first trough was selected. The consistency in selection of zero-crossing point is crucial to avoid any errors. To increase the accuracy of the method, the two pulses

were initially normalised against their respective maximum values and subsequently interpolated to increase their resolution before obtaining the zero-crossing point of the respective pulses. The interpolation factor is dependent on the sampling frequency of the ultrasonic acquisition system. For a 100 *MHz* sampling frequency, a factor of 10^6 was deemed sufficient.

It is not necessarily required to take the zero-crossing point of the normalised pulses as long as the point selected is consistent across the two pulses (ie. one may wish to take the point which correlates to 50% or 70% of the maximum amplitude of the pulses if this eases automation in data processing). Obtaining *ToF* measurements using peaks or troughs of the pulses is avoided as these regions within the measurements are most susceptible to aliasing.

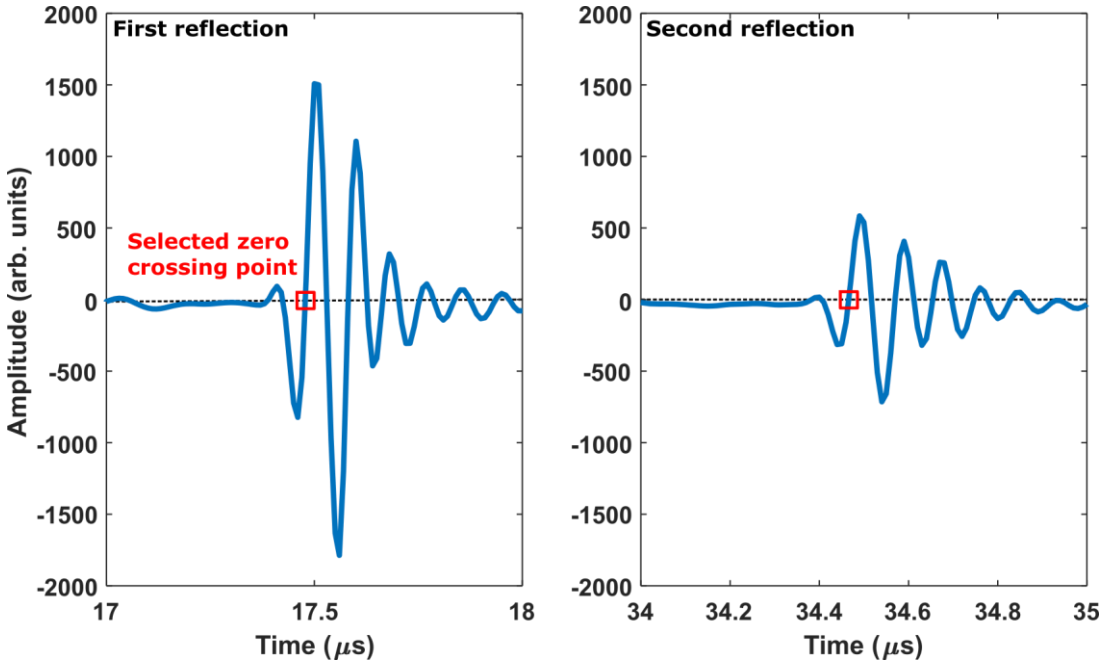

Figure 4.9 – Zero-crossing method for computing ToF

Cross-correlation is the measure of how similar two pulses are as one displaces the other. Mathematically, this is defined as:

$$w(t) = x(t) \otimes y(t) \triangleq \int_{-\infty}^{\infty} x^*(\tau) y(\tau + t) d\tau = \int_{-\infty}^{\infty} x^*(\tau - t) y(\tau) d\tau \quad (4.30)$$

The argument $w(t)$ is termed the delay of waveform $u(t)$ against $v(t)$ where t is the time step. Figure 4.10 illustrates the cross-correlation algorithm applied onto artificial pulses A & B. The peak of the cross-correlation corresponds to the lag at which the two pulses line-up best. In this case, the cross-correlation peak between the first and second reflection would correspond to the *ToF* between the two

pulses, vastly simplifying the code required to obtain ToF. Again, the ultrasonic waveforms will need to be normalised against their respective maximum amplitudes and interpolated before cross-correlating to maximize accuracy. Hilbert transform (HT) can also be performed onto the pulses before cross-correlation as this negates the apparent time shift resulted from the presence of an interface.

Measurements taken from the square column test specimen employed the Hilbert transform cross-correlation method.

For the cylindrical puck testing, the ultrasonic waves from the bottom plate is required to penetrate through the bottom plate and into the EN31 puck and reflected from the top plate interface. As such, a high voltage and gain were required which resulted in data clipping in certain channels. Measurements that were affected cannot use the Hilbert Transform cross-correlation method to compute ToF and zero-crossing was used instead. As such, the measurements that employed zero-crossing were susceptible to errors from not accounting the apparent time-shift due to presence of interface.

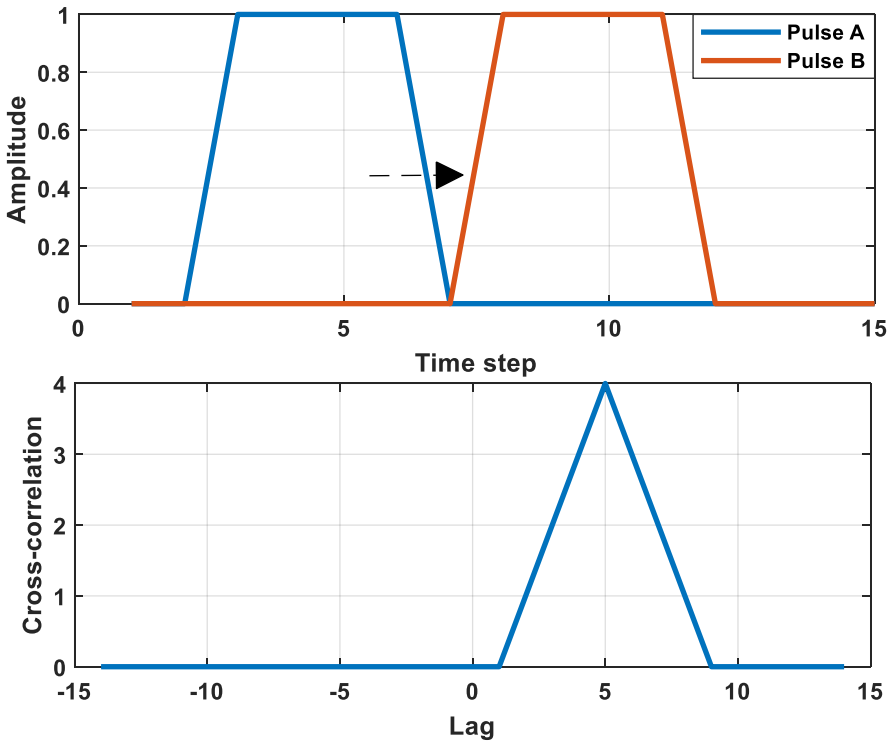

Figure 4.10 – Cross correlation algorithm

4.3.3 Results

Cylindrical puck – Full Loading Capacity

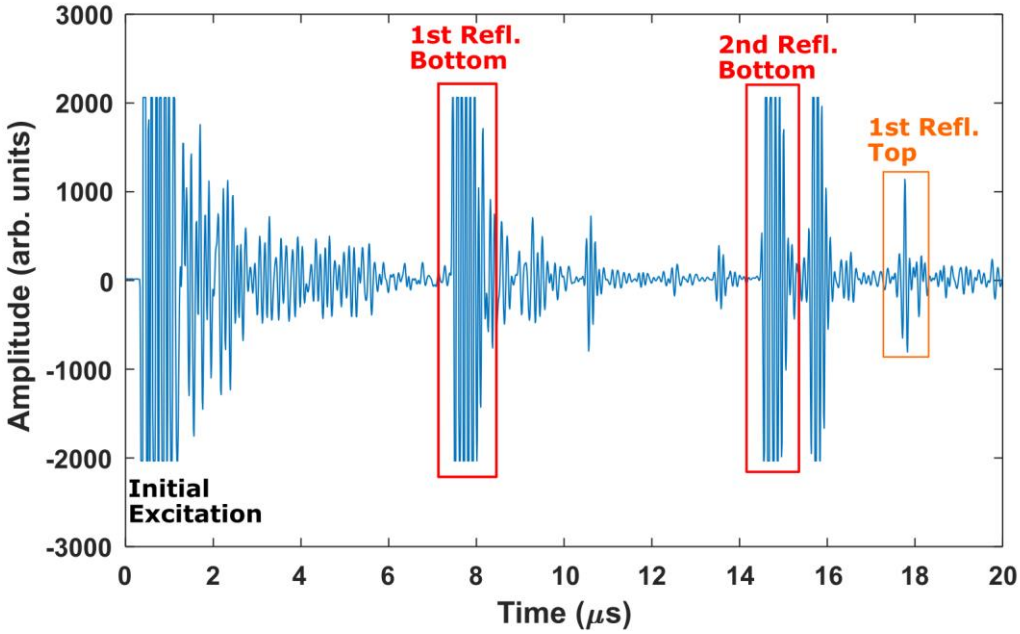

Figure 4.11 – Measured signal from a longitudinal sensor located at the bottom plate

Figure 4.11 shows the ultrasonic measurements obtained from one of the longitudinal sensors located under the bottom plate. The first and second pulses (highlighted in red) after the initial excitation corresponds to reflections from the bottom plate and cylindrical puck interface, whilst the pulse highlighted in orange corresponds to the first reflection from the cylindrical puck and top plate interface. The time of flight was subsequently obtained by subtracting the time taken for the first reflection from the bottom plate to the first reflection from the top plate. This will correspond to the total time taken for the signal to travel to and from within the cylindrical puck. The change in ToF was then computed by finding the difference in ToF between the stressed and unstressed measurements.

Figure 4.12 shows the ToF change for longitudinal and shear waves as it passes through the cylindrical puck. Different channels are illustrated with different colours, ie. longitudinal CH1 (blue), longitudinal CH2 (amber) and so on. ToF change for both longitudinal and shear sensors orientated parallel to the stress field tend to increase as the compressive stress increases and no hysteresis were observed within the measurements. This indicates that minimal plastic flow occurred during testing. The measurements also do not scatter significantly with each other. The ToF change for longitudinal and shear sensors can be seen to increase from 0 to 0.25 μs as the stress increased. Both longitudinal and shear sensors seem to have a linear

increase in ToF change, but shear measurements seem to start with an offset, potentially an indication of the presence of referencing error. Note that the polarisation of the shear sensors did not affect the ToF change measurements as CH3 & 4 were positioned 90 degrees to CH5.

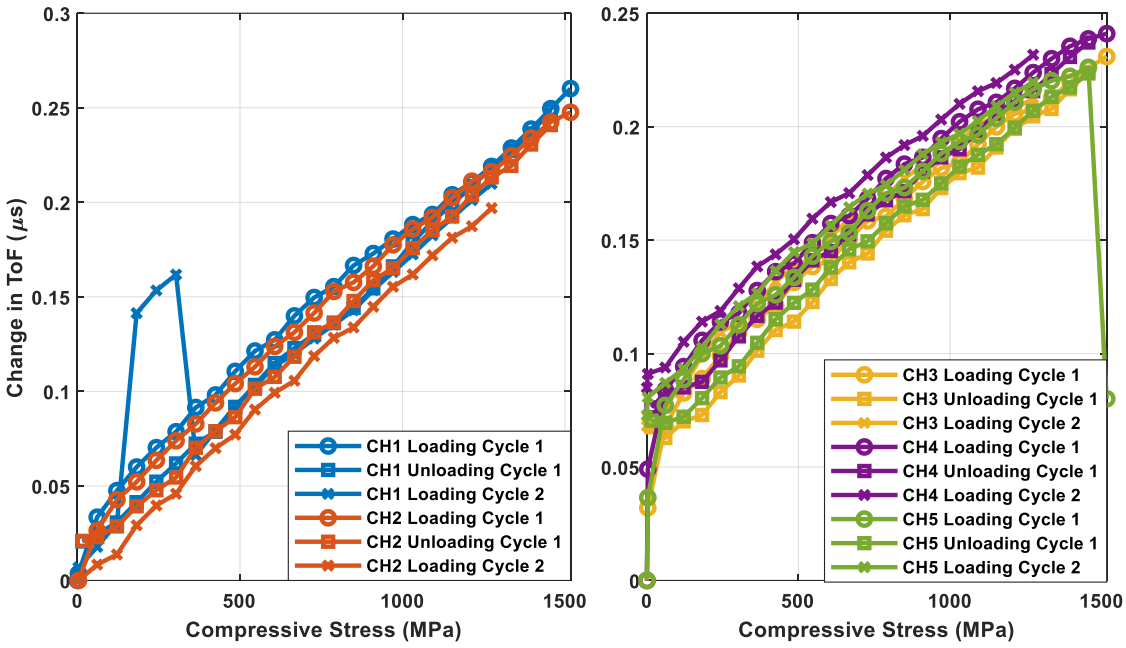

Figure 4.12 – Change in time of flight for longitudinal (CH1 & 2) and shear sensors (CH 3, 4 & 5) positioned parallel to the principal stress

Figure 4.13 shows the ToF change for the longitudinal and shear sensors positioned perpendicular to the stress field. The ToF change registered for CH6 and 7 seem to be very small (<0.1 μs). Measurements from both sensor exhibit erratic behaviour. Albeit that, some patterns can still be identified. ToF change for CH6 seem to increase with stress from 0 to 0.02 μs. Measurements during the loading phase of the first cycle differs considerably with the subsequent unloading and loading phases and is most likely spurious. Measurements in CH7 captured the hysteresis behaviour of the test specimen as the loading and unloading cycles do not follow each other and resemble an oval shape. Measurements for CH8 however exhibited a linear decrease with increasing compressive stress from 0 to -0.15 μs and is extremely consistent over the loading cycles. The spurious measurements captured in CH6 & 7 is potentially a result of the presence of non-uniform stress field across the cylindrical puck due to its geometry.

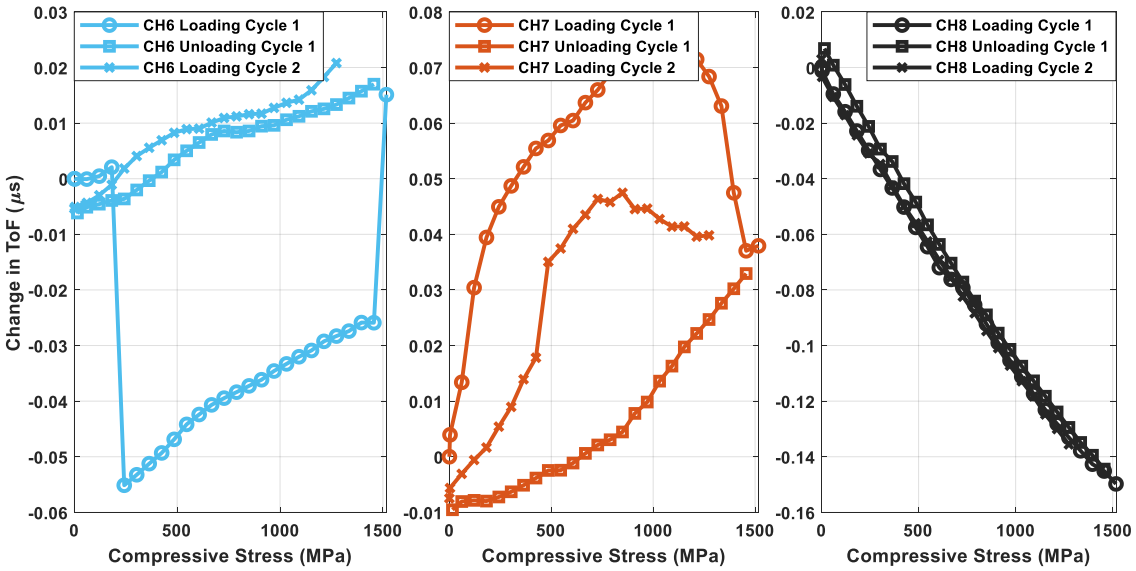

Figure 4.13 – Time of flight change for longitudinal (CH6) and shear sensors (CH7 & 8) positioned perpendicular to the principal stress

Figure 4.14 and Figure 4.15 shows the acoustoelastic constants obtained from calculations performed on the ToF measurements shown previously. Measurements for L_{zz} and L_{zx} seem to have an exponential pattern where the difference between the measurements are significant at low stress and the difference gradually tapered off as the stress is increased. Measurements somewhat plateaued after 600 *MPa* with an average of -2.62 for L_{zz} and -0.94 for L_{zx}. The exponential behaviour might be attributed to signal noise. At low load, the ToF change is small and thus noise in ToF measurement would potentially take up a higher proportion and result in higher errors. As noticed in the ToF change measurements, the acoustoelastic measurements do not seem to vary significantly across the loading and unloading cycles. Acoustoelastic constants for CH6 & 7 however do seem to vary significantly across cycles, with CH8 showing somewhat consistent measurements after 700 *MPa*. This is expected as the acoustoelastic constants are a function of ToF change and measurements from CH6 & 7 seem erratic. Averages for L_{xx}, L_{xy} and L_{xz} were computed at 0.32, 0.19 and -1.37 respectively.

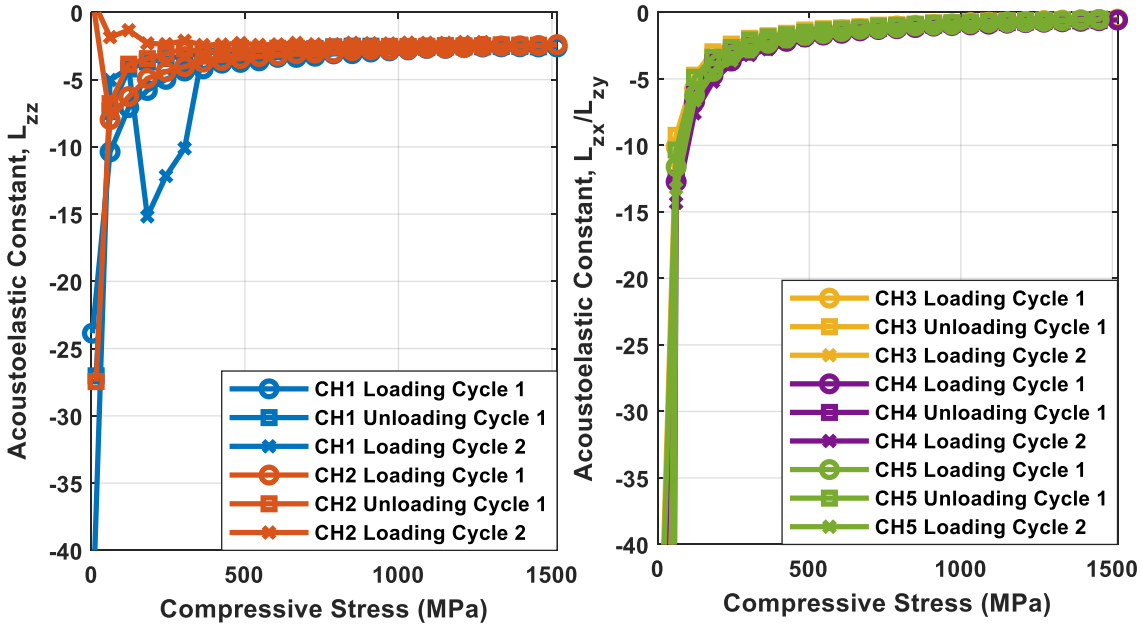

Figure 4.14 – Acoustoelastic constants for longitudinal (CH1 & 2) and shear sensors (CH 3, 4 & 5) positioned parallel to the principal stress

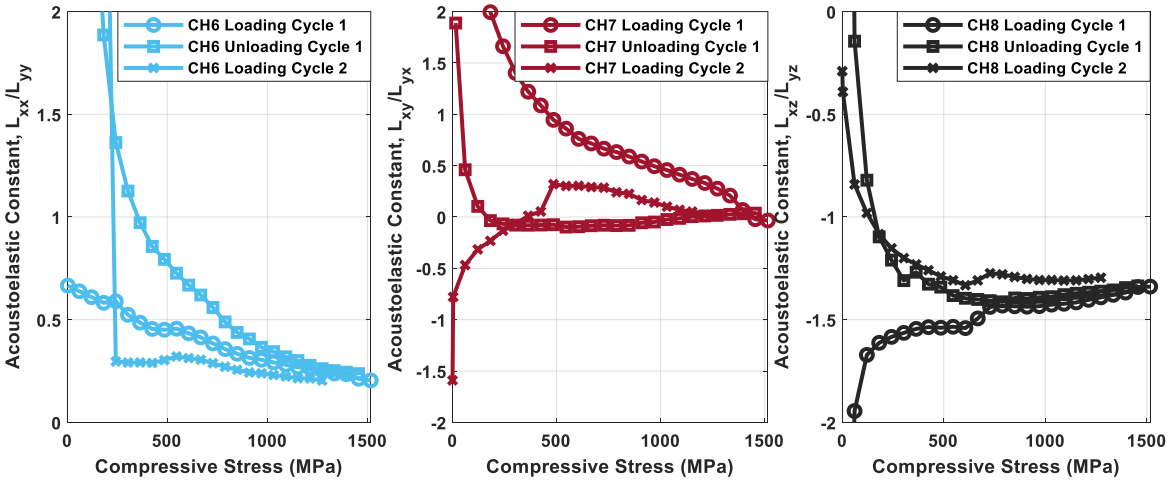

Figure 4.15 – Acoustoelastic constants for longitudinal (CH6) and shear sensors (CH7 & 8) positioned perpendicular to the principal stress

Cylindrical puck – Half Loading Capacity

ToF measurements for the bottom sensors of the half loading capacity cylindrical puck testing will not be shown as the trends mirror that shown for the fully capacity testing. Figure 4.16 shows patterns of acoustoelastic measurements for longitudinal and shear sensors positioned parallel to the stress field. These patterns are consistent with the full capacity testing. The measurements seem to again resemble an exponential decay plot where the values plateau at higher stresses. In this test, the measurements plateaued at stresses exceeding 400 *MPa* with average values of -2.16 for L_{zz} and -0.29 for L_{zx}.

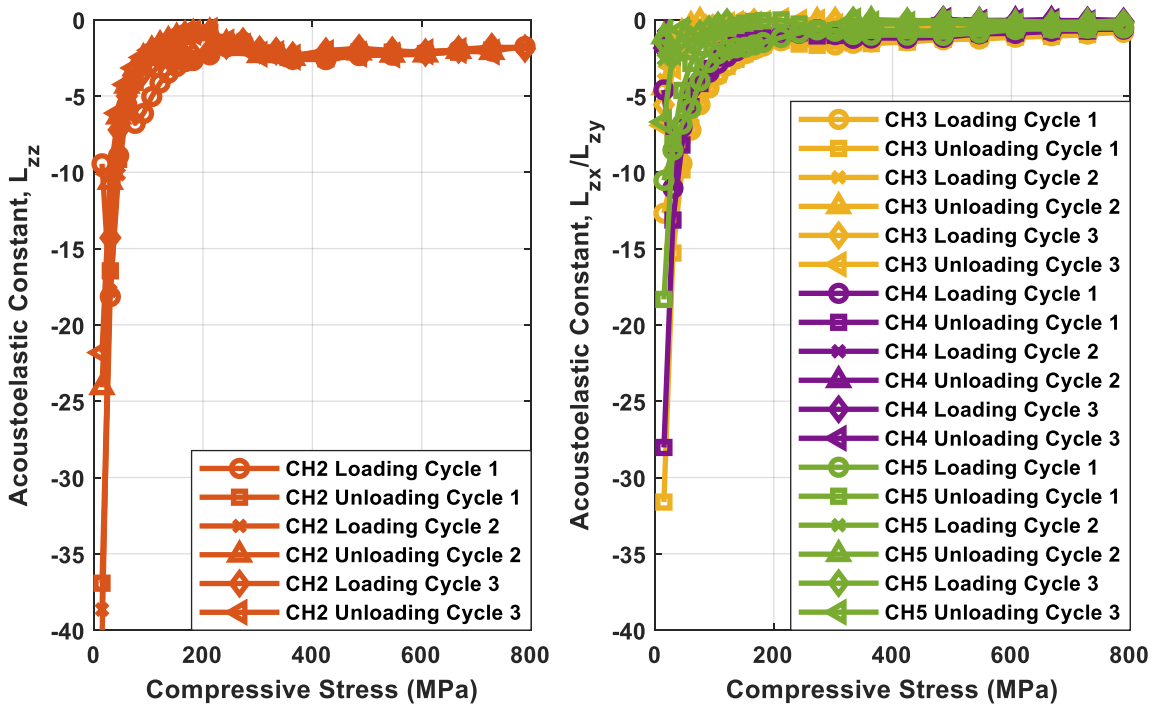

Figure 4.16 – Acoustoelastic constants for longitudinal (CH1 & 2) and shear sensors (CH 3, 4 & 5) positioned parallel to the principal stress

Figure 4.17 illustrates the ToF change for the sensors positioned parallel to the principal stress. Trends in the measurements resemble that obtained during the fully capacity testing with CH6 & 7 exhibiting erratic behaviour whilst CH8 showing a linear decrease in ToF change. Upon conversion to acoustoelastic constants, the measurements do not seem sensible and as such, the measurements will be omitted.

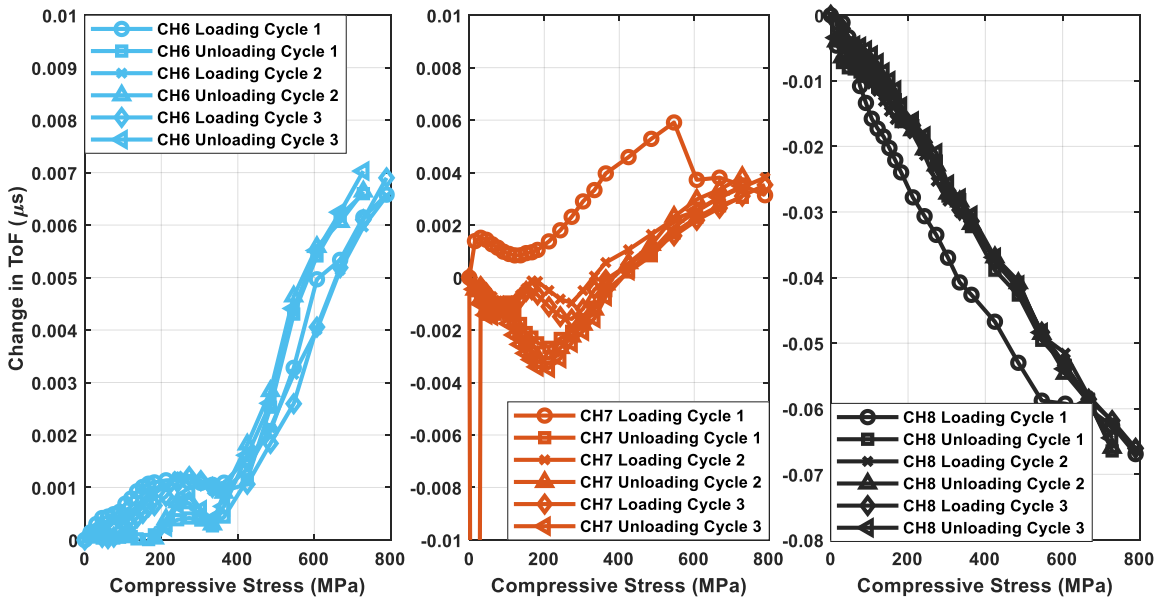

Figure 4.17 – Change in time of flight for longitudinal (CH6) and shear sensors (CH7 & 8) positioned perpendicular to the principal stress

Square column – Half Loading Capacity

Due to suspicion that measurements from sensors positioned perpendicular to the stress field are affected by the non-uniform stress field as a result of the geometry of the test specimen, the square column testing was conducted.

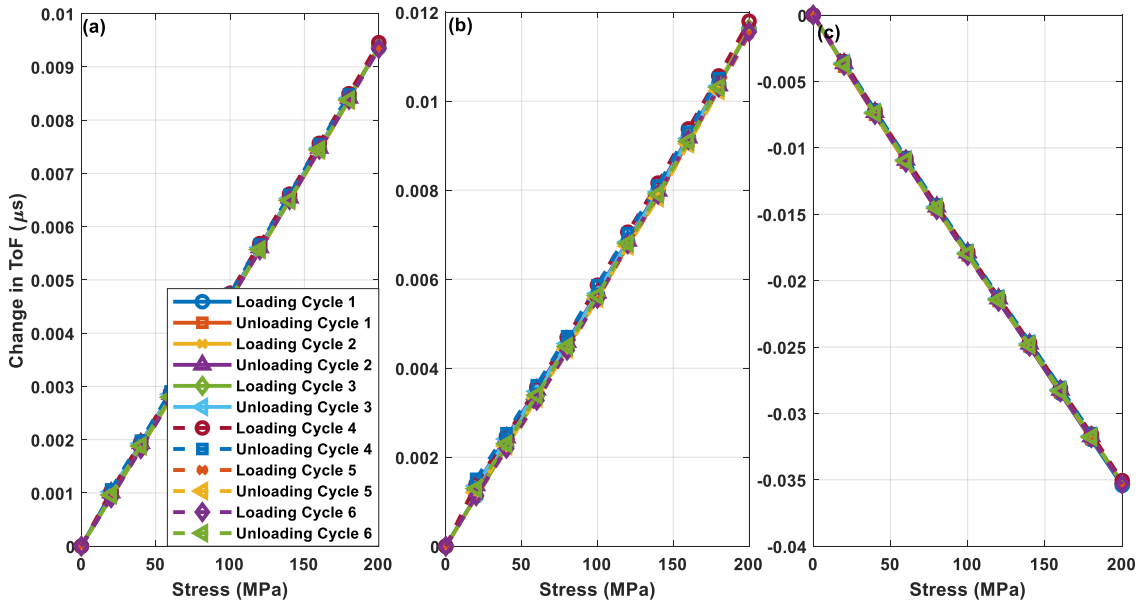

Figure 4.18 – Change in ToF for (a) longitudinal and (b & c) shear sensors positioned perpendicular to the principal stress

Figure 4.18 shows the ToF change obtained for longitudinal and shear side sensors from the square block testing. All 3 measurements exhibit extremely clean linear trends, with the longitudinal and shear measurements shown in Figure 4.18(a) and (b) exhibiting an increase in ToF change whilst Figure 4.18(c) show a decrease in ToF change. All the measurements also show good consistency across the 6 load cycles applied as no significant measurement scatter is observed. This confirmed the hypothesis that the geometry of the cylindrical puck is influencing the measurements obtained from the side sensors.

Figure 4.19 shows the acoustoelastic constants obtained for longitudinal and shear sensors positioned perpendicular to the principal stress. The measurements again showed an exponential decay pattern, however with a lower stress reaching plateau point (~100 *MPa*). Averages for L_{xx}, L_{xy} and L_{xz} were computed at 0.30, 0.10 and -1.48 respectively.

Through using Equation (4.31) and Equation (4.32), the acoustoelastic constant for longitudinal and shear waves propagating parallel to the stress field can be computed. Figure 4.20 shows the calculated values of the acoustoelastic constants for longitudinal and shear waves propagating parallel to the stress field. Averages for L_{zz}, L_{zx}/L_{zy} were computed at -2.35 and -0.21 respectively.

The acoustoelastic constant measurements obtained from all 3 experiments were summarised in Table 4.5.

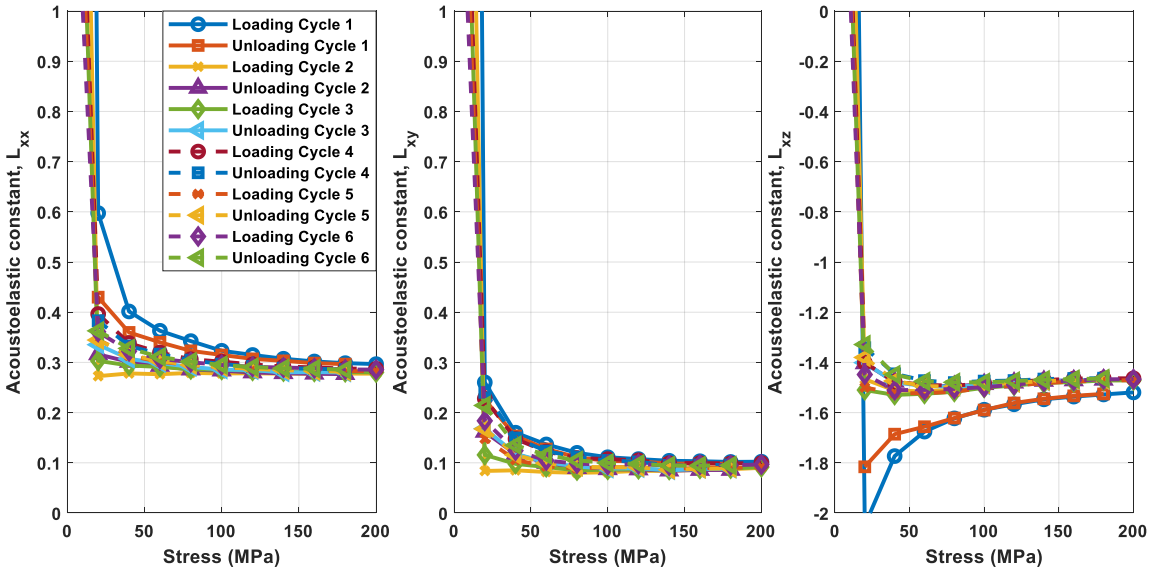

Figure 4.19 – Acoustoelastic constants for longitudinal and shear sensors positioned perpendicular to the principal stress

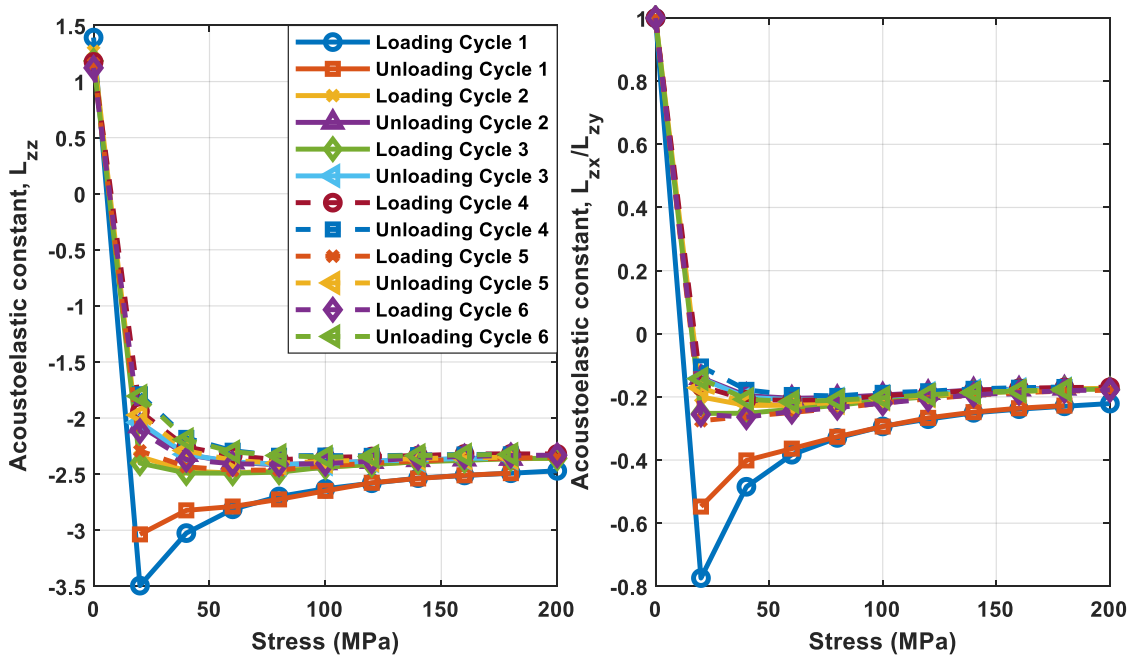

Figure 4.20 - Calculated values of acoustoelastic constants for longitudinal and shear wave positioned parallel to the principal stress

Test	Cylindrical puck – Full Capacity	Cylindrical puck – Half Capacity	Square Column – Half Capacity	Averaged values
L_{zz}	-2.62	-2.16	-2.35	-2.255
L_{zx}/L_{zy}	-0.94	-0.29	-0.21	-0.250
L_{xx}/L_{yy}	0.32	-	0.30	0.310
L_{xy}/L_{yx}	0.19	-	0.10	0.145
L_{xz}/L_{yz}	-1.37	-	-1.48	-1.425

Table 4.5 – Acoustoelastic constant measurements obtained from all 3 experiments

$$L_{zz} = L_{xx} + \frac{2}{1-v}\left(L_{xz} + v \cdot L_{xy}\right) + \frac{(1+v)(1+2v)}{2(1-v)} \qquad (4.31)$$

$$L_{zx}/L_{zy} \; or \; \frac{dV_{12}/V_{12}^{0}}{d\varepsilon} = 1 + v + \frac{dV_{21}/V_{21}^{0}}{d\varepsilon} \qquad (4.32)$$

The acoustoelastic constant, L_{zz} seemed to be consistent across the 3 tests, with the full capacity test registering the highest value. The values seemed sensible when compared with the value -2.24 obtained from previous work [135], with perhaps the

full capacity test data being an outlier. A similar trend can be said for L_{zx}/L_{zy} with the error potentially occurring from incorrect referencing of the shear sensors. Measurements from the subsequent tests yielded a value between -0.21 and -0.29 and the averaged acoustoelastic constants for longitudinal and shear sensors positioned parallel to the stress field (L_{zz} & L_{zx}/L_{zy}) were shown in the final column of the table, without taking into account values from the full capacity puck testing. These values coincide well with the known acoustoelastic constants of rail and Hecla steel documented in Table 4.2.

Measurements for the remaining acoustoelastic constants (L_{xx}/L_{yy}, L_{xy}/L_{yx} & L_{xz}/L_{yz}) seemed consistent between the full capacity cylindrical puck and half capacity square column testing with the latter measurement having a higher confidence due to the quality of the data. Despite this, the measurements were averaged, and values displayed on the final column in the table. Again, these measurements are very similar to that obtained by Egle & Bray [179] for rail steel.

Since all the 5 acoustoelastic constants are known, it is possible to calculate the second and third-order elastic constants through rearranging of the equations displayed in Table 4.3. This yields [179]:

$$l = \frac{\lambda}{1-2v}\left[\frac{1-v}{v}\cdot L_{xx} + \frac{2}{1+v}\left(L_{xz} + v\cdot L_{xy}\right) + 2v\right] \quad (4.33)$$

$$m = 2(\lambda+\mu)\left(\frac{v}{1+v}\cdot L_{xy} + \frac{1}{1+v}\cdot L_{xy} + 2v - 1\right) \quad (4.34)$$

$$n = \frac{4\mu}{1+v}\left(L_{xz} + L_{xy} - 1 - v\right) \quad (4.35)$$

Values for the second-order elastic constants were calculated using the subsequent equations. The calculated values are shown in the table below. The second and third order elastic constants again do not vary significantly with that of rail and Hecla steel.

$$\lambda = \frac{vE}{(1+v)(1-2v)} \quad (4.36)$$

$$\mu = \frac{E}{2(1+v)} \quad (4.37)$$

Steel	v	E (GPa)	λ (GPa)	μ (GPa)	l (GPa)	m (GPa)	n (GPa)
EN31	0.29	208.609	111.654	80.853	-214.041	-574.462	-717.022

Table 4.6 - Second and third-order elastic constants for EN31 steel

4.4 Discussion

4.4.1 Ideal ToF computation algorithm

Although ToF measurements were successfully obtained through the implementation of zero-crossing algorithm, the method is extremely susceptible to error. The method relies on a stable pulse waveform which varies in a linear fashion. Often enough, the method is inconsistent in selecting of the correct zero-crossing point and manual correction is necessary. For large amounts of dataset this is inefficient and time consuming. In addition, a change in pulse shape would result in difficulty in determining the correct zero-crossing point, incurring additional errors. The cross-correlation method albeit having its own flaws, alleviates all these limitations. Manual intervention is only necessary to check the results, and this vastly reduces the time to extract ToF measurements from the waveforms. As such, cross-correlation is the preferred method of computing ToF measurements.

4.4.2 Error Analysis for cross-correlation method

Measurements from the square column half capacity acoustoelastic experiment can be used to quantify the error contained within the processing steps required to obtain ToF. The aspects investigated include:

(i) Optimum number of interpolation points
(ii) Method of yielding time of flight (pulse and HT cross-correlation)

The measurements used for this study was the reference dataset obtained prior to the first load cycle. Due to the sampling limit of the FMS, the time resolution of the data was limited at 100 *MHz* or 0.01 μs. This however can be "improved" through interpolation of the existing digitized pulse. Theoretically, the higher the number of interpolation points, the smaller the time of flight error. However, there is also an increase in computational power required to execute the algorithm. As such, there is an optimum number of interpolation points where the order of magnitude of the error is negligible, without requiring intensive computational power. Figure 4.21 shows the difference in ToF measurements with increasing number of interpolation points. ToF measurements obtained at interpolation points of 5×10^7 were selected as reference value. As we increase the interpolation points, the difference decreases

and plateaus. From Figure 4.21(b), it was decided that the optimum number of interpolation points is 5×10^5, giving a time resolution greater than 3.98×10^{-6} μs, keeping the error in the 10^{-12} magnitude whilst not utilising excessive computational power.

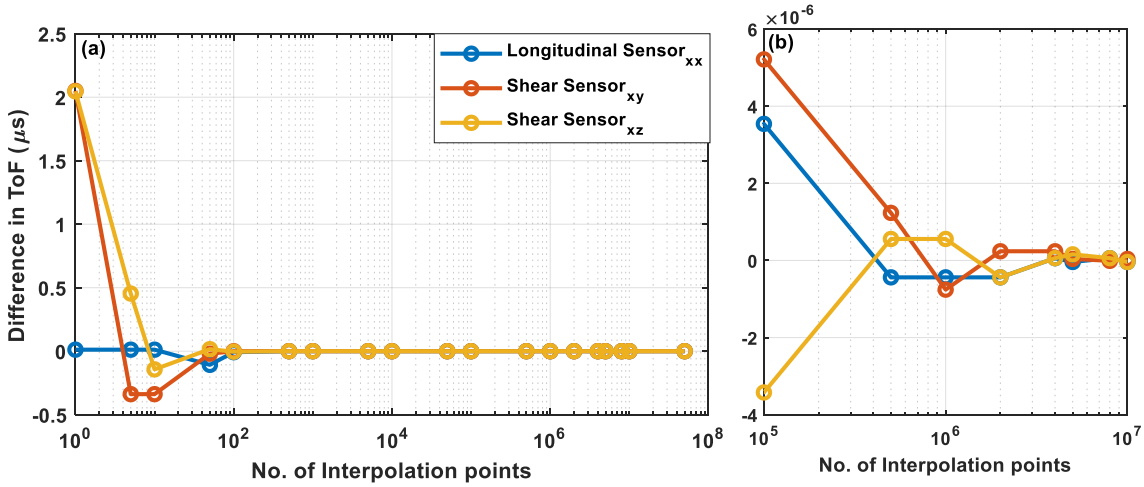

Figure 4.21 – Difference in ToF measurements for longitudinal and shear sensors positioned perpendicular to the principal stress (a) full plot (b) zoomed in region of interest

Hilbert Transform Cross Correlation

It is theorized that through utilising the pulse envelope for cross-correlation, it is possible to negate the apparent change in ToF due to phase change in the presence of an interface or lubricant film. This hypothesis is based upon the phase change although affecting the pulse amplitude, it does not affect the pulse envelope of the waveform. Subsequently, a cross-correlation of the HT of the pulses would negate the apparent ToF corresponding to the phase change.

However, carrying out HT on a pulse and cross correlating the envelopes will invoke additional errors as the HT uses the pulse peak values to "map" the pulse envelope. Validity and accuracy of cross-correlation of the envelopes also depend on how similar the two pulse envelopes are. Figure 4.22 shows the measured first and second reflections alongside their HT envelopes. From inspection, it is apparent that the envelopes towards the final oscillations of the two pulses do not match up, potentially incurring errors.

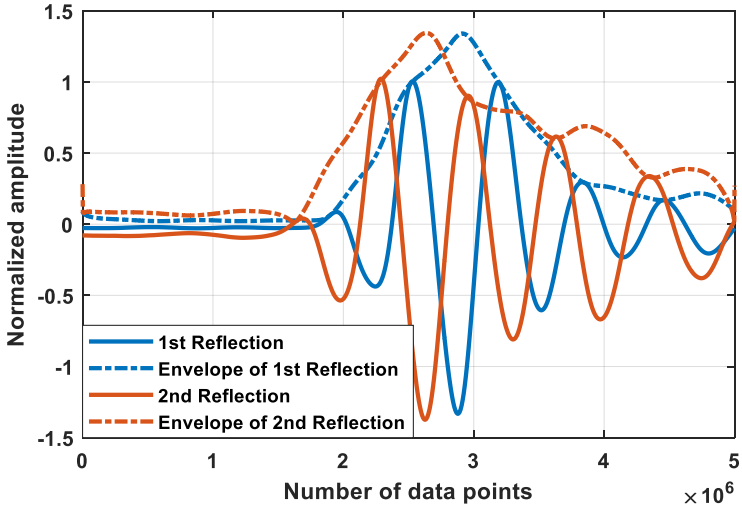

Figure 4.22 – Measured first and second reflections alongside their HT envelopes

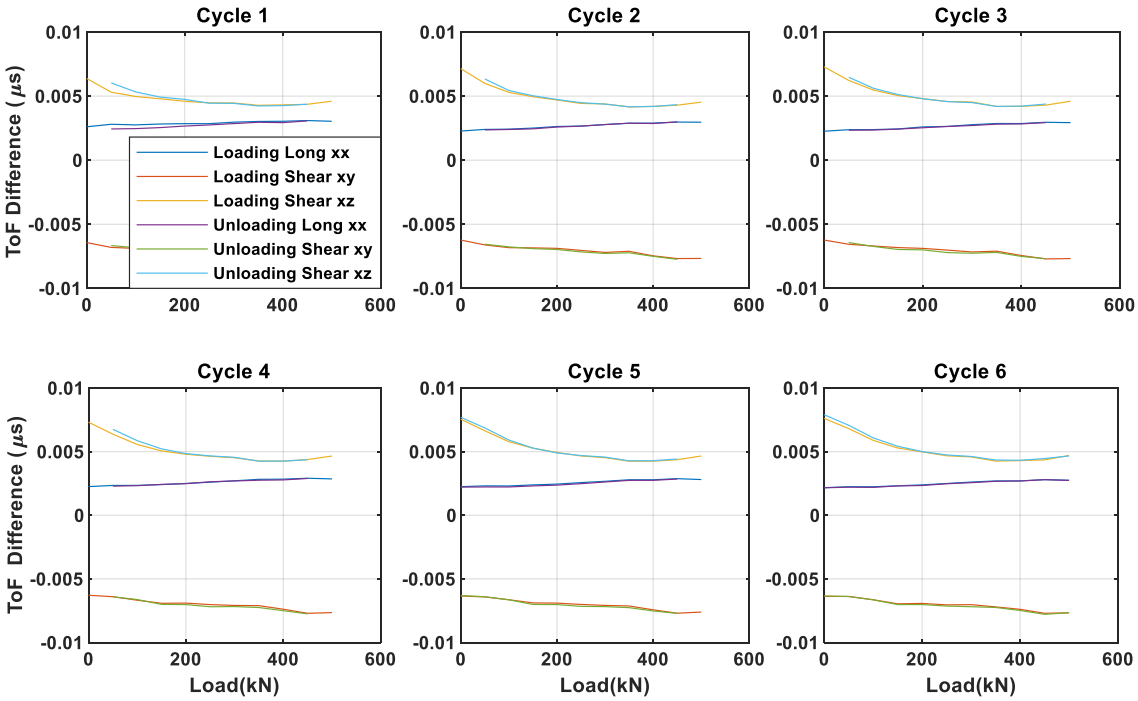

Figure 4.23 – Difference in ToF between measurements obtained from pulse cross-correlation against that from HT cross-correlation

Figure 4.23 shows the difference in time-of-flight between cross correlating pulses in time domain against that obtained from cross-correlation of the envelopes of the pulses. The measurements shown are taken from the square column testing with a load range of 0 to 500 *kN*. Each plot shows the difference for each cycle consisting of a loading and unloading step. The difference in ToF for the same sensor between

loading and unloading steps within a cycle is very similar. This pattern is consistent across all the cycles and the values also do not seem to vary across cycles across each cycle. Subsequently, an error of $\pm 0.01\,\mu s$ was concluded from the investigation. This however only holds valid for a pulse that has a reasonable bell shape and for pulses with more erratic waveform, it would be expected that a higher error exists.

4.5 Conclusions

- Contributions of time of flight change for longitudinal and shear sensors oriented perpendicular and parallel to the direction of applied stress were outlined and explained.
- A method to determine and measure the acoustoelastic constants and subsequently second and third-order elastic constants was designed and outlined and the results from the experiment shown.
- Measurement of acoustoelastic constant for EN31 bearing steel was found to be very close with those measured from rail and Hecla steel.
- A similar observation can be made of the second and third-order elastic constants where they do not differ much from those of rail and Hecla steel.
- The acoustoelastic constant L_{zz} measured was -2.26, with less than 1% difference from that measured in previous work [135].
- Shear acoustoelastic constant, L_{zx} was measured at -0.25, which indicates much less contribution of acoustoelastic effect to ToF change compared with deflection and potentially better usage for measurement of roller load.
- The acoustoelastic constant obtained is subsequently utilised in the ToF-Load relationship in §5.2.5 for measurement of roller load.

5 ULTRASONIC ROLLER LOAD MEASUREMENT METHOD

This chapter applies the knowledge gained from the previous chapter in the context of bearings for measurement of raceway deflection and subsequently conversion of deflection to roller and bearing load. Various deflection-load relationships are explored, and the most suitable relationship is identified and utilised. A ToF-Load relationship is subsequently developed, and measurements of roller and raceway profiles are taken to fully define the relationships which are later used in §6 (CRB NU2244) and §7 (TRB 32222).

5.1 Measurement of bearing raceway deflection

To recap, the previous chapter outlined the various contributions of ToF change for an ultrasonic wave and explored the effect of stress on the variation in ToF. The acoustoelastic constants for EN31 bearing steel were experimentally determined and these will be used in this chapter to separate out the ToF change due to stress.

For measurement of raceway deflection, two possible sensor configurations are possible, as illustrated in Figure 5.1. The sensor could either be placed at the inner or outer bores of the inner or outer raceways, provided that the surface which the sensor is bonded is parallel to the rolling surface. For a cylindrical roller bearing this is rather straightforward, however slight modifications are required when instrumenting a tapered roller bearing. A sensor positioned at the inner raceway would measure deflection of inner raceway, δ_i whilst one located at the outer raceway would measure outer raceway deflection, δ_o. As explained in the previous chapter, the total variation in ToF for a longitudinal sensor can be written and expanded as shown below, where the final term is negated through data processing means.

$$\Delta t = \Delta t_\delta + \Delta t_L + \Delta t_\Phi \tag{5.1}$$

$$\Delta t = \frac{2\delta}{(c_{zz})_0} + \frac{-2L_{zz}\delta}{(c_{zz})_0(1-L_{zz}\varepsilon_z)} \tag{5.2}$$

Since the strain, ε_z is typically small, the denominator term $(1 - L_{zz}\varepsilon_z)$ would tend to unity and as such the equation can be further simplified into [135],

$$\Delta t = \frac{2\delta}{(c_{zz})_0} + \frac{-2L_{zz}\delta}{(c_{zz})_0} = \frac{2\delta(1-L_{zz})}{(c_{zz})_0} \quad (5.3)$$

Rearranging for deflection yields,

$$\delta = \frac{(c_{zz})_0}{2(1-L_{zz})}\Delta t \quad (5.4)$$

For a shear sensor, one would use the unstressed shear sound speed, $(c_{zx})_0$ and shear acoustoelastic constant, L_{zx} to compute raceway deflection.

$$\delta = \frac{(c_{zx})_0}{2(1-L_{zx})}\Delta t \quad (5.5)$$

Since the acoustoelastic constant and unstressed speed of sound are constants, the raceway deflection is a linear function of the total variation in ToF. Note that the deflection measured here is the inner or outer raceway deflection ($\delta = \delta_{i/o}$) depending on the position of the sensors which would need to be summed together to obtain the total deflection, δ_{total}. This is important as some line contact relationships as detailed in Table 5.1 have slightly different relationships for inner and outer raceway deflection.

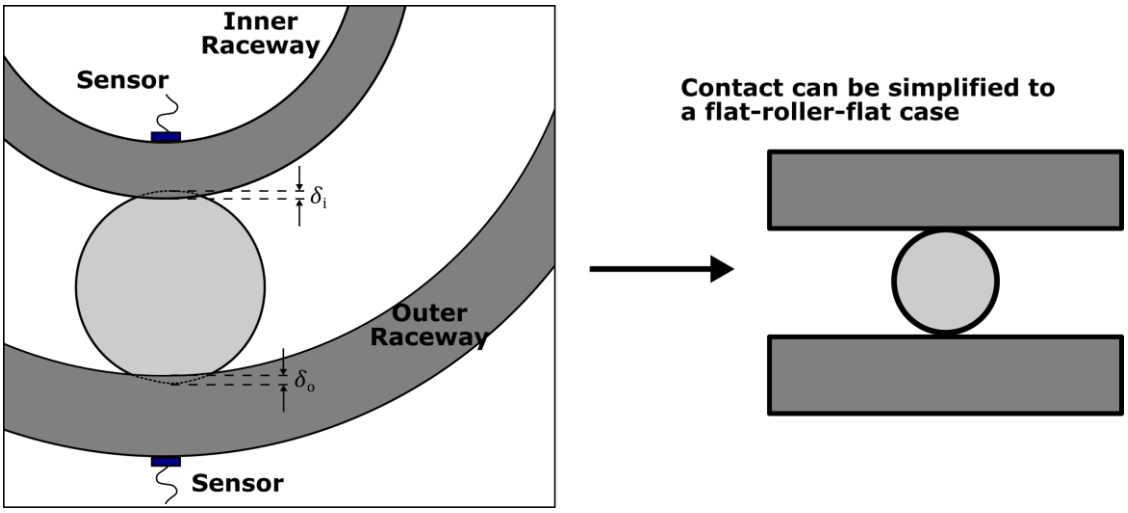

Figure 5.1 – Schematic of a typical cylindrical roller bearing showing the possible sensor positions along the inner/outer bore of the inner/outer raceways

5.2 Conversion of raceway deflection into bearing roller load

For conversion of raceway deflection into bearing load, contact models are required. The contact model is dependent on the type of contact at the roller-raceway interface, either an elliptical/point contact (PC) or a line contact (LC).

Contact in cylindrical and tapered roller bearings are typically assumed to be line contact and can be simplified to a roller on flat configuration. However, rollers typically are crowned to minimise and avoid edge loading and as such contacts are elliptical at low loading and gradually transitions to line contact as the load increases. In the order of increasing complexity, line contact relationships are initially introduced followed by point/elliptical relationships.

5.2.1 Line contact model

Hertz [186] pioneered the research into contacts between elastic solids and developed an analytical load-deflection relationship for elliptical contact. This subsequently resulted in elastic contacts being categorized as either Hertzian or non-Hertzian.

For contacts to be Hertzian, the following is required to be satisfied:

(i) The contact area is much smaller than the radii of the two contacting solids

(ii) Deflections of the two contacting surfaces are much smaller compared to the radii

(iii) Each of the contacting solids can be considered as an elastic half-space

(iv) The contacting surfaces are frictionless

Bearing components (rollers and raceways) are clearly of finite length (stress variation exists at the edge of the rollers), thus violating the elastic half-space criteria. and as a result, such the contacts are non-Hertzian. Multiple load-deflection relationships for line contact exist, typically utilising an analytical or empirical approach. These are listed below in Table 5.1 whilst Figure 5.2 illustrates the positions of inner and outer raceway deflection within a rolling element bearing.

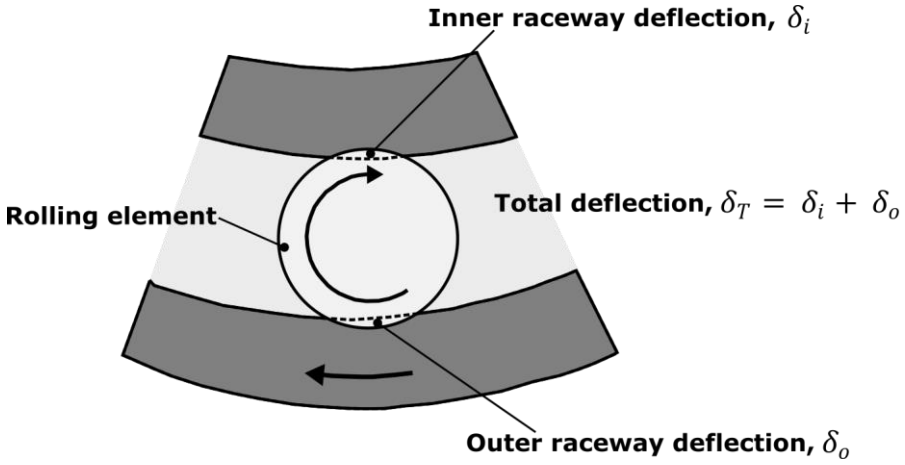

Figure 5.2 – Inner and outer raceway deflection as a result of roller load

Palmgren [46]	$\delta_T = \delta_i + \delta_o = 3.84 \times 10^{-8} \cdot \frac{Q^{0.9}}{(L \times 1000)^{0.8}}$	(5.6)
Kunert [187]	$\delta_T = \delta_i + \delta_o = 4.05 \times 10^{-8} \cdot \frac{Q^{0.925}}{(L \times 1000)^{0.85}}$	(5.7)
Tripp [188]	$\delta_i = \left(\frac{2 \cdot Q}{\pi \cdot L}\right) \cdot \left[\frac{(1-v_1^2)}{E_1}\left(\ln\frac{4 \cdot R_1}{b} - \frac{1}{2}\right) + \frac{(1-v_2^2)}{E_2}\left(\ln\frac{4 \cdot R_2}{b} - \frac{1}{2}\right)\right]$	(5.8)
	$\delta_o = \left(\frac{2 \cdot Q}{\pi \cdot L}\right) \cdot \left[\frac{(1-v_1^2)}{E_1}\left(\ln\frac{4 \cdot R_1}{b} - \frac{1}{2}\right) + \frac{(1-v_2^2)}{E_2}\left(\ln\frac{2 \cdot t}{b} - \frac{v_2}{2(1-v_2)}\right)\right]$	(5.9)
Zantupulos [189]	$\delta_T = \delta_i + \delta_o = \frac{4 \cdot Q}{\pi \cdot E' \cdot L} \ln\left(\frac{\pi \cdot E' \cdot L}{e \cdot Q}\right)$	(5.10)
Houpert [190]	$\delta_i = \left[\frac{Q \cdot (1-v^2)}{0.2723 E' L}\left(\frac{p_d}{\cos\beta}\right)^{0.074}\right]^{1/1.074}$	(5.11)
	$\delta_o = \left[\frac{Q \cdot (1-v^2)}{0.27835 E' L} \cdot \left(\frac{t}{1+D/p_d}\right)^{0.078}\right]^{1/1.078}$	(5.12)

Table 5.1 – Deflection-load relationships for line contact in bearings

Palmgren [46] and Kunert [187] employed empirical relationships for determining the raceway deflection, δ as a result of roller load, Q. The deflection is dependant purely on roller load, Q and roller length, L. Zantupulos [189] developed an analytical relationship which accounted for an additional term, the reduced modulus of elasticity, E' calculated using the equation below where v_1, v_2 and E_1, E_2 are the Poisson's ratio and Modulus of elasticity of roller (index 1) and inner/outer raceway (index 2) contacting each other.

$$\frac{1}{E'} = \frac{1}{2}\left[\frac{1-v_1^2}{E_1} + \frac{1-v_2^2}{E_2}\right] \quad (5.13)$$

Deflection values for inner and outer raceways calculated for the previously mentioned equations will be the same, as the relationships are approximations. However, the inner raceway deflection would be larger by a very small margin than that of the outer raceway.

On the other hand, Tripp [188] and Houpert [190] both opted for two separate equations for calculating inner and outer raceway deflection. Tripp [185] chose a depth of reference equal to the diameter of the roller at which no local deformation occurs which formed Equation (5.8). It is interesting to note from Equation (5.9), the outer raceway deflection, δ_o has a dependence on the outer raceway thickness, t. The contact half-width, b is required to be known and this complicates calculations. Houpert's relationship for line contact [190] are built upon Tripp's [188] where the depth of reference was taken as the sum of thickness of outer raceway and housing section thickness. Approximate curve fittings were produced based on Tripp's relationships and this eliminated the dependence of contact half-width, b and resulted in the relationships shown in Equation (5.11) and Equation (5.12). According to Houpert, Tripp's equation was selected as it was the most accurate for line contact calculations.

A line-contact dimensionless load parameter, W_{LC} was introduced for calculating the maximum Hertzian pressure, P_{max} and semi contact width, b for line contact. Equation for calculating the reduced radius in x-axis, R_x is also shown below where R_{x1} and R_{x2} are the roller and raceway radiuses in the rolling direction.

$$\frac{1}{R_x} = \frac{1}{R_{x1}} \pm \frac{1}{R_{x2}} \quad (5.14)$$

$$W_{LC} = \frac{Q}{E' R_x L} \quad (5.15)$$

$$P_{max} = E' \sqrt{\frac{W_{LC}}{2\pi}} \quad (5.16)$$

$$b = R_x \sqrt{\frac{8}{\pi} W_{LC}} \quad (5.17)$$

5.2.2 Point contact

For elliptical or point contacts, relationships for the contact length and width of the ellipse as well as deflection are shown in Equation (5.20), Equation (5.21) and Equation (5.22) respectively, where a^*, b^* and δ^* are elliptical integrals whilst $\sum \rho$ is the sum of curvature, calculated using Equation (5.18). Calculation of elliptical integrals is complicated and as such approximations are often utilised such as the least squares linear-regression method [46] or the curve-fitting approach [190].

$$\sum \rho = \frac{1}{R_{x1}} + \frac{1}{R_{y1}} \pm \frac{1}{R_{x2}} \pm \frac{1}{R_{y2}} \quad (5.18)$$

$$F(\rho) = \frac{\frac{1}{R_{x1}} - \frac{1}{R_{y1}} + \left(\pm\frac{1}{R_{x2}}\right) - \left(\pm\frac{1}{R_{y2}}\right)}{\sum \rho} \quad (5.19)$$

$$a = a^* \left[\frac{3Q}{2\sum \rho}\left(\frac{1-v_1^2}{E_1} + \frac{1-v_2^2}{E_2}\right)\right]^{1/3} \quad (5.20)$$

$$b = b^* \left[\frac{3Q}{2\sum \rho}\left(\frac{1-v_1^2}{E_1} + \frac{1-v_2^2}{E_2}\right)\right]^{1/3} \quad (5.21)$$

$$\delta = \delta^* \left[\frac{3Q}{2\sum \rho}\left(\frac{1-v_1^2}{E_1} + \frac{1-v_2^2}{E_2}\right)\right]^{2/3} \cdot \frac{\sum \rho}{2} \quad (5.22)$$

Houpert's curve-fitting approach will be explored further as the method is much more accurate and easier to utilize compared to other existing relationships.

Houpert introduced a reduced radius in y-direction, R_y as well as the ratio between reduced radius in y and x-axis, k and a point-contact dimensionless load parameter. These are defined below where R_{y1} and R_{y2} are radius of the profiles of the roller and raceway.

$$\frac{1}{R_y} = \frac{1}{R_{y1}} + \frac{1}{R_{y2}} \tag{5.23}$$

$$k = \frac{R_y}{R_x} \tag{5.24}$$

$$W_{PC} = \frac{Q}{E' R_x^2} \tag{5.25}$$

Equation (5.18) up to Equation (5.22) can thus be rewritten in terms of R_y, k and W_{PC}. This resulted in the following equations where CA, CB, CD and CP are parameters which the curve-fitting were carried out.

$$a = a^* \left(\frac{3k}{1+k}\right)^{1/3} \cdot R_x \cdot W_{PC}^{1/3} = CA \cdot R_x \cdot W_{PC}^{1/3} \tag{5.26}$$

$$b = b^* \left(\frac{3k}{1+k}\right)^{1/3} \cdot R_x \cdot W_{PC}^{1/3} = CB \cdot R_x \cdot W_{PC}^{1/3} \tag{5.27}$$

$$\delta = 0.5 \cdot \delta^* \left[\frac{9(1+k)}{1+k}\right]^{1/3} \cdot R_x \cdot W_{PC}^{2/3} = CD \cdot R_x \cdot W_{PC}^{2/3} \tag{5.28}$$

$$P_{max} = \frac{3Q}{2\pi ab} = \frac{3E'}{2\pi a^* b^*} \left(\frac{1+k}{3k}\right)^{2/3} W_{PC}^{1/3} = CP \cdot E' \cdot W_{PC}^{1/3} \tag{5.29}$$

For maximum accuracy, the curve-fittings were done on various ranges of k values and as such multiple equations exist for different k values. For tapered and cylindrical roller bearings, k values range from 122.44 up to 13576 and the relevant curve-fitted equations were shown below. The curve-fitted equations differ from

numerical results by less than 1%. An advanced curve-fitting exist [191] with higher accuracy, which reduces the error down to less than 0.05%, however since only less than 1% error is present for the current set of curve-fitted equations, this would have a minor effect on the load measurements.

$$a \approx 1.5528 \cdot k^{0.3737} \cdot R_x \cdot W_{PC}^{1/3} \quad (5.30)$$

$$b \approx 1.1063 \cdot k^{-0.1866} \cdot R_x \cdot W_{PC}^{1/3} \quad (5.31)$$

$$\delta \approx 1.7138 \cdot k^{-0.2743} \cdot R_x \cdot W_{PC}^{2/3} \quad (5.32)$$

$$P_{max} \approx 0.2779 \cdot k^{-0.1871} \cdot E \cdot W_{PC}^{\frac{1}{3}} \quad (5.33)$$

Consequently, point and line contact load-deflection relationships can be written as,

$$Q_{PC} = K_{PC} \cdot \delta^{1.5} \quad (5.34)$$

$$K_{PC} = \frac{E' \sqrt{R_x}}{1.7138^{1.5} \cdot k^{-0.2743 \cdot 1.5}} \quad (5.35)$$

$$Q_{LC} = K_{LC(inner/outer)} \cdot \delta^{1.074/1.078} \quad (5.36)$$

$$K_{LC(inner)} = 0.2723 \cdot E' \cdot L \left(\frac{\cos\beta}{d_m}\right)^{0.074}, \quad K_{LC(outer)} = 0.2785 \cdot E' \cdot L \left(\frac{1 + {}^{D\cos\alpha}/_{p_d}}{t}\right)^{0.078} \quad (5.37)$$

5.2.3 Point to line contact

As stated previously, at low loading the contact is elliptical and gradually transitions from elliptical to line contact. A transitional deflection is thus introduced where the contact transitions from elliptical to line contact. The transitional deflection was obtained by taking the derivative of Equation (5.34) and (5.36) with respect to δ and comparing them as they will be equal to each other at the transitional point. The numerator value of 1.074 and denominator power value of 0.426 is used for an inner raceway-roller contact whilst 1.078 and 0.422 are utilised for an outer raceway-roller contact.

$$\delta_{trans} = \left(\frac{1.074\ or\ 1.078}{1.5}\frac{K_{LC}}{K_{PC}}\right)^{\frac{1}{0.426\ or\ 0.422}} \quad (5.38)$$

When the deflection, δ is less than the transitional deflection,

$$Q_{PC-LC} = K_{PC} \cdot \delta^{1.5} \quad (5.39)$$

When the deflection, δ is greater than the transitional deflection, the load-deflection relationship is shown in Equation (5.40) where dQ is an offset value introduced to maintain continuity between Equation (5.39) and Equation (5.40).

$$Q_{PC-LC} = K_{LC(inner/outer)} \cdot \delta^{1.074\ or\ 1.078} - dQ \quad (5.40)$$

$$dQ = \left(\frac{1.074\ or\ 1.078}{1.5} \cdot \frac{K_{LC(inner/outer)}}{K_{PC}}\right)^{\frac{1.1}{0.426\ or\ 0.422}} \left(\frac{0.426\ or\ 0.422}{1.5} K_{LC(inner/outer)}\right) \quad (5.41)$$

5.2.4 Comparison between contact models

To contrast between the various line and point contact models described in the previous section, a simple theoretical study was conducted on the NU2244 CRB. A total deflection, δ_T between $0 - 150\ \mu m$ was defined and the corresponding roller load for the various line and point contact models was calculated. This was shown in Figure 5.3(a) for line contact models whereas the Houpert relationships were shown in Figure 5.3(b). Tripp's line contact equations [188] were omitted since Houpert's LC model was based on them. For line contact models, Zantupulos' relationship was found to be most conservative, followed by Kunert's and Houpert's with Palmgren's relationship the least conservative.

For the Houpert relationships, prior to the deflection exceeding its transitional threshold defined in Equation (5.38), the point-line contact model is equal to the point contact model defined in Equation (5.39). After exceeding the threshold point, the point-line contact model is equal to the line contact model with an offset, dQ defined in Equation (5.41). The offset was introduced to ensure smooth transition between the point and line contact models [190].

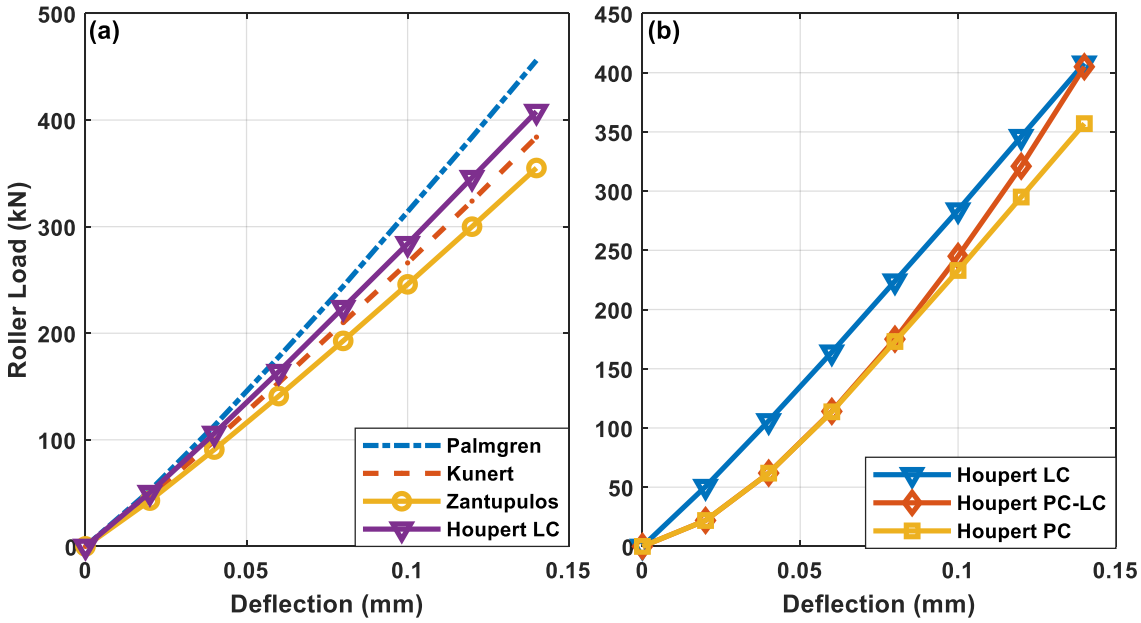

Figure 5.3 – Comparison of (a) various line contact relationships and (b) Houpert's point, line and point-line contact relationships

5.2.5 ToF-Load relationship

Houpert's equation vastly simplifies the load-deflection relationship into Equation (5.39) and Equation (5.40), where K_{PC} and K_{LC} are constants which are a function of the geometry of the bearings and as such, fixed for a specific designation of bearing. As such, a ToF-Load relationship can be written as shown below.

For cases when the deflection, δ is less than the transitional deflection, δ_{trans} Equation (5.42) applies, whereas when the deflection, δ is greater than the transitional deflection, δ_{trans} Equation (5.43) is required to be used.

$$Q_{PC-LC} = K_{PC} \cdot \left(\frac{(c_{zz})_0}{(1-L_{zz})}\Delta t\right)^{1.5} \quad (5.42)$$

$$Q_{PC-LC} = K_{LC(inner/outer)} \cdot \left(\frac{(c_{zz})_0}{(1-L_{zz})}\Delta t\right)^{1.074\ or\ 1.078} - dQ \quad (5.43)$$

The relationships shown are valid for a longitudinal sensor positioned at the centre of the raceway, under the maximum loaded region and thus, measuring the maximum raceway deflection. Relationships for shear sensors can also be obtained easily through replacing the unstressed speed of sound, $(c_{zz})_0$ and longitudinal

acoustoelastic constant, L_{zz} with the shear unstressed sound speed, $\left(c_{zx/zy}\right)_0$ and shear acoustoelastic constant, $L_{zx/zy}$.

5.3 Application of ToF-Load relationship

The line-contact constant, K_{LC} can be fully defined through dimensional specifications provided by bearing manufacturers, however the constant K_{PC} can only be partly defined. As seen from Equation (5.35), the point-contact constant, K_{PC} is a function the ratio, k. To compute k, the reduced radius, R_y is required which in turn requires knowledge of the roller and raceway curvatures in the y-direction (direction perpendicular to the rolling direction). This information is rarely publicly available as they are a closely guarded secret among bearing manufacturers. Subsequently, measurement of the roller and raceway profiles are necessary.

5.3.1 Measurement of roller and raceway profiles

The profiles of two bearings were measured, a NU2244 cylindrical roller bearing (CRB) and a 32222 tapered roller bearing (TRB). The NU2244 CRB was used in full-scale laboratory testing detailed in §6, whilst the 32222 TRB was used in field testing within an operational wind turbine as detailed in §7.

NU2244 CRB

Key specifications of the NU2244 CRB were listed in Table 5.2.

NU2244 CRB	
Bore diameter, d_i	220 *mm*
Outer diameter, d_o	400 *mm*
Pitch diameter, p_d	313 *mm*
Width, b	108 *mm*
Inner raceway thickness, t	19.5 *mm*
Dynamic load rating, C_ω	1600 *kN*
Fatigue load limit, C_u	250 *kN*
Number of rollers, Z	15
Roller diameter, D	54 *mm*
Roller length, L	82 *mm*

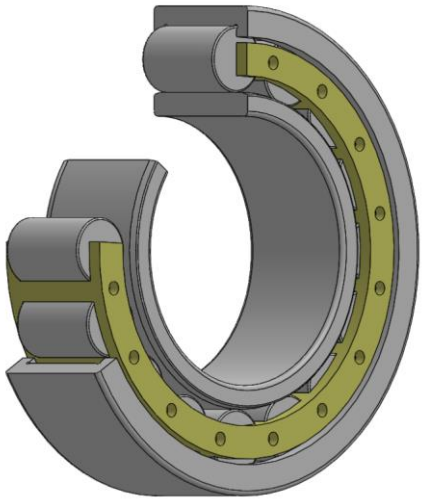

Table 5.2 – Dimensional specification of NU2244 CRB

Measurement of the roller and raceway profiles were conducted using a non-contacting optical profilometer (Alicona) as shown in Figure 5.4(a). The Alicona uses continuous focus variation optical microscopy to measure and map surface contours. The Alicona has a range of 50 *mm* and a 10x focusing lens was used for this measurement, resulting in a measurement uncertainty of 1 μm. A new, unused roller and raceway from a NU2244 cylindrical roller bearing was used for profile measurement. Due to the specimen size and weight constraint of the profilometer, the inner raceway was required to be sectioned into chunks of approximately 50 *mm* wide. 3 measurement locations for the roller were selected, 120 degrees apart from each other, whilst two sectioned pieces of the raceway were measured, also at 3 locations. These are the centre and 1 *mm* left and right from the centre. This was to ensure that the measured region was sufficiently far away from the sectioned edges. The measured test specimens can be seen in Figure 5.4(b)&(c).

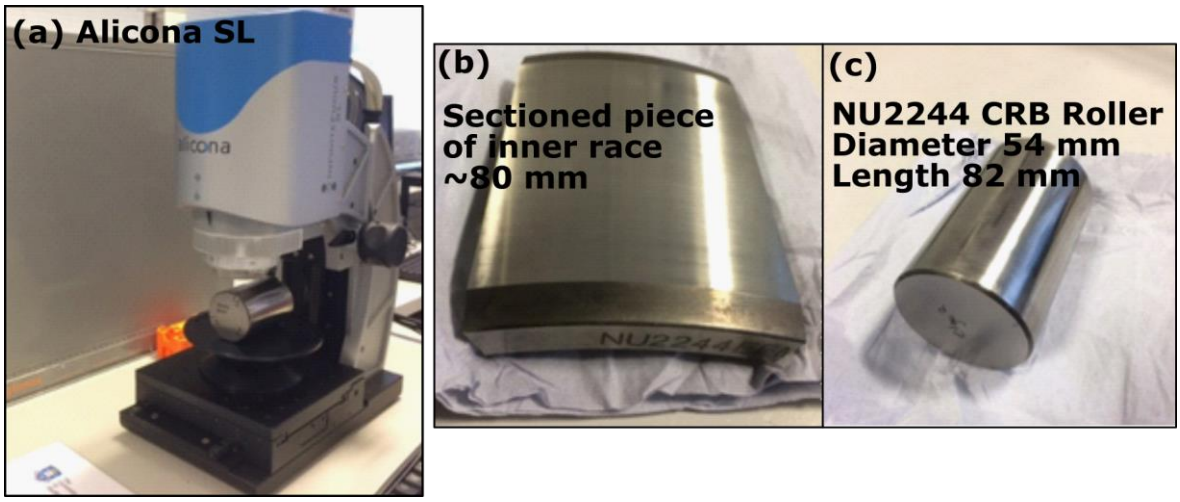

Figure 5.4 – (a) Measurement setup (b) Sectioned piece of inner raceway (c) NU2244 CRB rolling element

Figure 5.5 shows the roller and inner raceway profiles obtained from the optical profilometer. The measurements needed to be taken in two halves as the raceway and roller lengths exceed the range of the Alicona.

Measurements of roller profile seemed to be consistent for their respective halves for the 3 measurements along the circumference, with the roller indeed having a multi-radius or logarithmic profile with a maximum height averaged around 48.5 μm. However, despite showing symmetry, there seemed to be an offset in the measurements between the two halves as the centre portion do not seem to

overlap. The slight difference in left and right edge measurements were most probably due to slight difference in positioning of the roller (angles, orientation).

Measurements for the raceway despite exhibiting more scatter, showed a similar trend of consistency between measurement halves. A concave inner raceway geometry was observed with non-symmetrical raceway measurement from left and right edges from both specimens. It was found that the profile height on the left edge is typically smaller than that of the right edge. Measurements from the left edge yielded an average profile height of -2 μm whilst an average profile height of -8 μm was obtained for right edge measurements, which provided an average profile height difference of 6 μm. Measurements taken were relative to the edge of the raceway metallic surface, before the black polymer region visible in Figure 5.4(b).

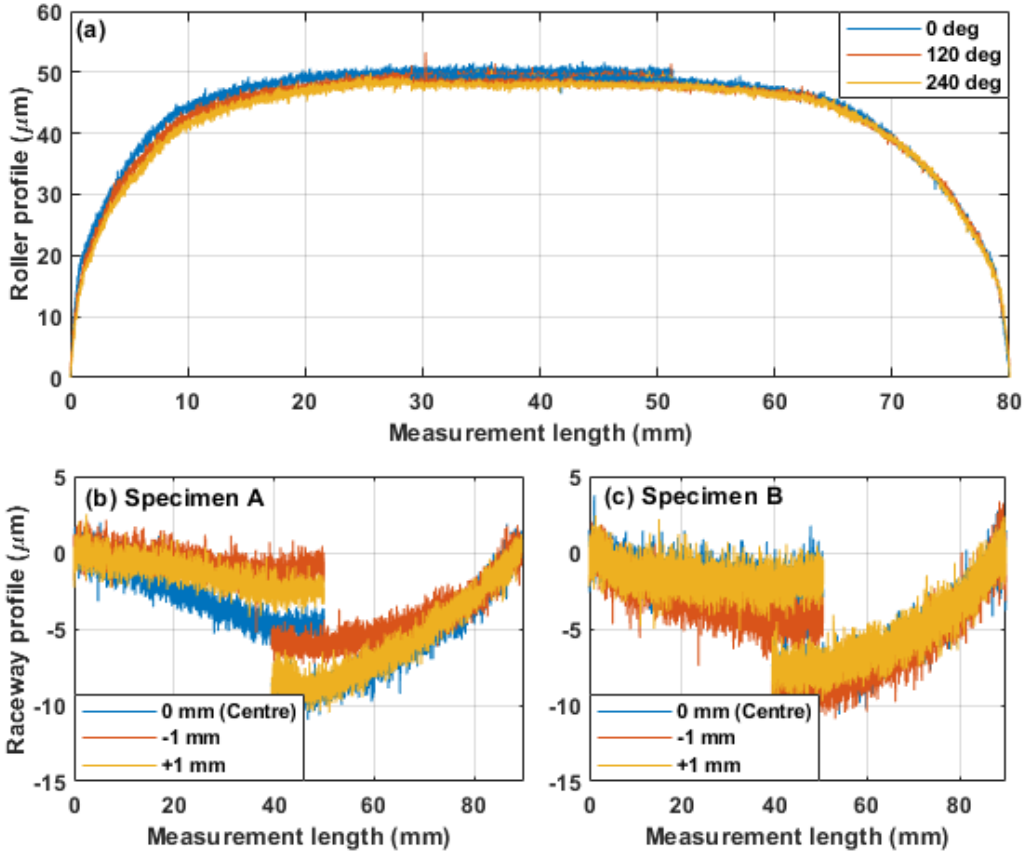

Figure 5.5 – Measurements of (a) roller and (b, c) raceway profiles of NU2244 CRB using Alicona with 50 *mm* range

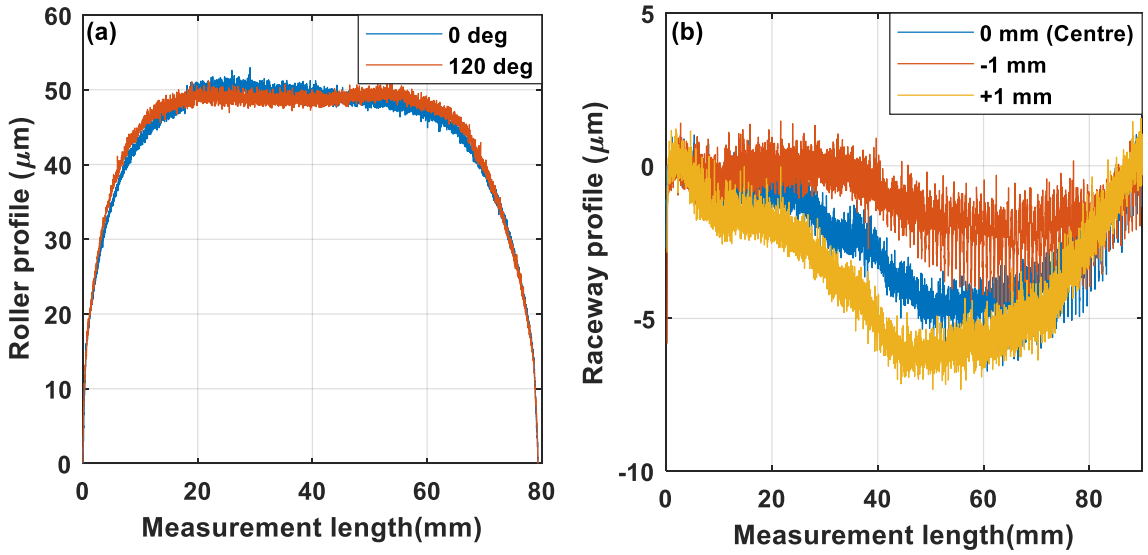

Figure 5.6 – Measurements of (a) roller and (b) raceway profiles for NU2244 CRB using Alicona with 100 *mm* range

Due to the dissatisfactory condition of the data obtained, the measurements were retaken in National Physical Laboratory using a newer Alicona model with twice the range (100 *mm*), eliminating the need for two measurement halves. Figure 5.6(a) shows the roller profile obtained from the measurements. The roller measurements for the 240° portion was overexposed and unusable. Roller measurements were seen to be consistent with that obtained using the 50 *mm* range Alicona where a multi-radius or logarithmic profile exists with a plateau at the centre of the profile. The maximum profile height was found to be 49.5 μm.

On the other hand, Figure 5.6(b) shows the raceway profile measurements obtained. Due to the time restriction in place for the measurement, only one sectioned specimen of the inner raceway was measured. As the scan time increased, the size of the measurement also increased. As the measurement size approaches the processing limitation of the Alicona, the quality of the measurements was seen to decrease. Subsequently, this resulted in the increased scatter for the second half of the raceway measurements. Measurements again were seen to be asymmetrical with an average profile height difference of 5 μm.

32222 TRB

Key and relevant specifications of the 32222 TRB were listed in Table 5.3. These dimensions were inferred from a CAD file of the bearing.

32222 TRB	
Bore diameter, d_i	110 *mm*
Outer diameter, d_o	200 *mm*
Pitch diameter, p_d	154.26 *mm*
Width, b	56 *mm*
Minimum roller diameter, D_e^{min}	21.64 *mm*
Maximum roller diameter, D_e^{max}	24.20 *mm*
Mean roller diameter, D_e^{mean}	22.92 *mm*
Dynamic load rating, C	402 *kN*
Fatigue load limit, C_u	61 *kN*
Number of rollers, Z	20
Roller length, L	37 *mm*
Contact angle for outer race, ϕ	15.64°

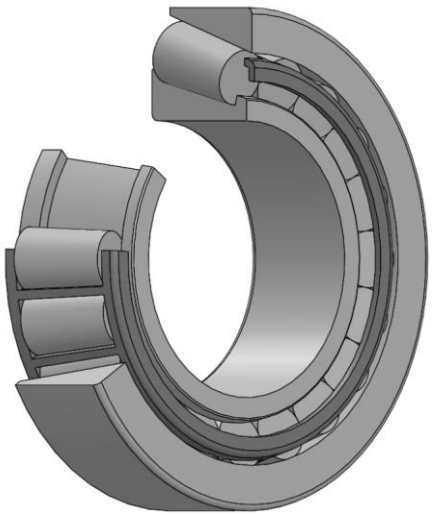

Table 5.3 – Dimensional specification inferred from the 32222 TRB CAD

An additional unit of the 32222 TRB from the same manufacturer, inherited from the OWDIn project detailed in §7 was used for the measurement. The outer raceway however was missing, and the history of the component unknown. Wear and scratch marks exist on the rollers, indicating that the bearing might be in operation before. Despite this, measurements of the roller profiles were still taken. Figure 5.7(a) shows all the 20 rollers removed from the cage of the TRB, whilst Figure 5.7(b) shows the test setup employed for the roller profile measurements. As the roller length (37 *mm*) is within the measurement range of the Alicona (50 *mm*), full measurements can be taken each pass. Apart from that, a new 5x focusing lens was available for this measurement, which vastly improved the measurement speed. Consequently, all 20 rollers were measured.

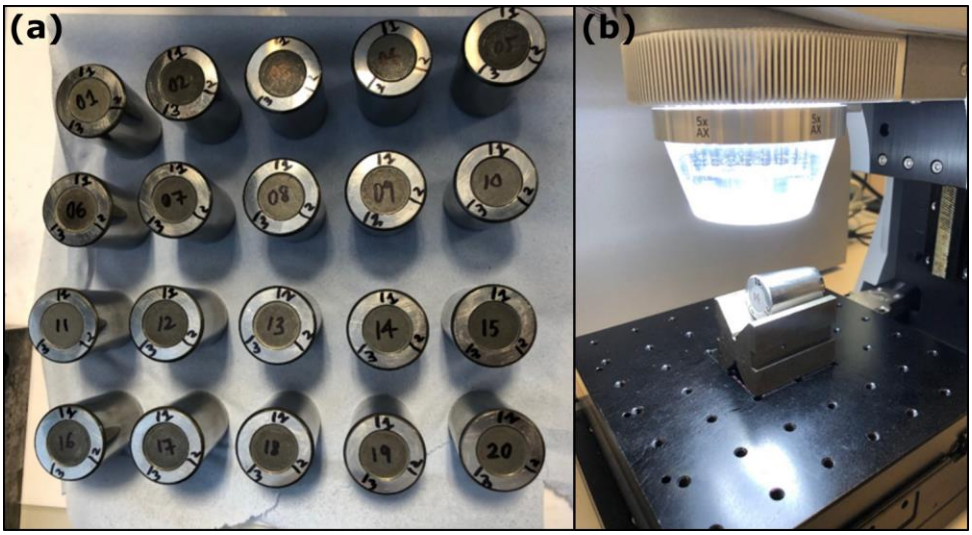

Figure 5.7 – (a) Labelled and marked rollers of the TRB (b) Test setup for roller profile measurement

Figure 5.8(a) shows two of the roller profiles measurement obtained. The roller profiles again exhibit a plateau at the centre with a steeper transition at the sides compared to the NU2244 CRB roller. The centre profile height of Roller 3 seemed to have an average of around 20 μm compared to that of around 16 μm for Roller 13, indicating potential variation in centre profile height among the rollers. This can be visualised through the histogram bivariate plot shown in Figure 5.8(b) where each column represents roller profile measurements for each roller and the colour intensity corresponds to the density or the count of the measurement value. Measurements count within the blue colour domain are noise and measurements from roller fringes and thus omitted. The maximum roller profile height can be seen to vary from 14.03 μm (Roller 11) up to 18.93 μm (Roller 5) with an average of 15.15 μm. This would affect the loading on each roller and subsequently the bearing life.

To further understand the influence of roller profile height on the roller load, a theoretical study was carried out using equations shown in §5.2.2. Variation in roller profile height, z will affect the reduced radius in axis perpendicular to rolling direction, R_y and subsequently the ratio of the equivalent radius, k and the point-contact constant K_{pc}. In the theoretical study, the roller profile design height was assumed to be 15 μm, alongside a tolerance of ± 10 μm.

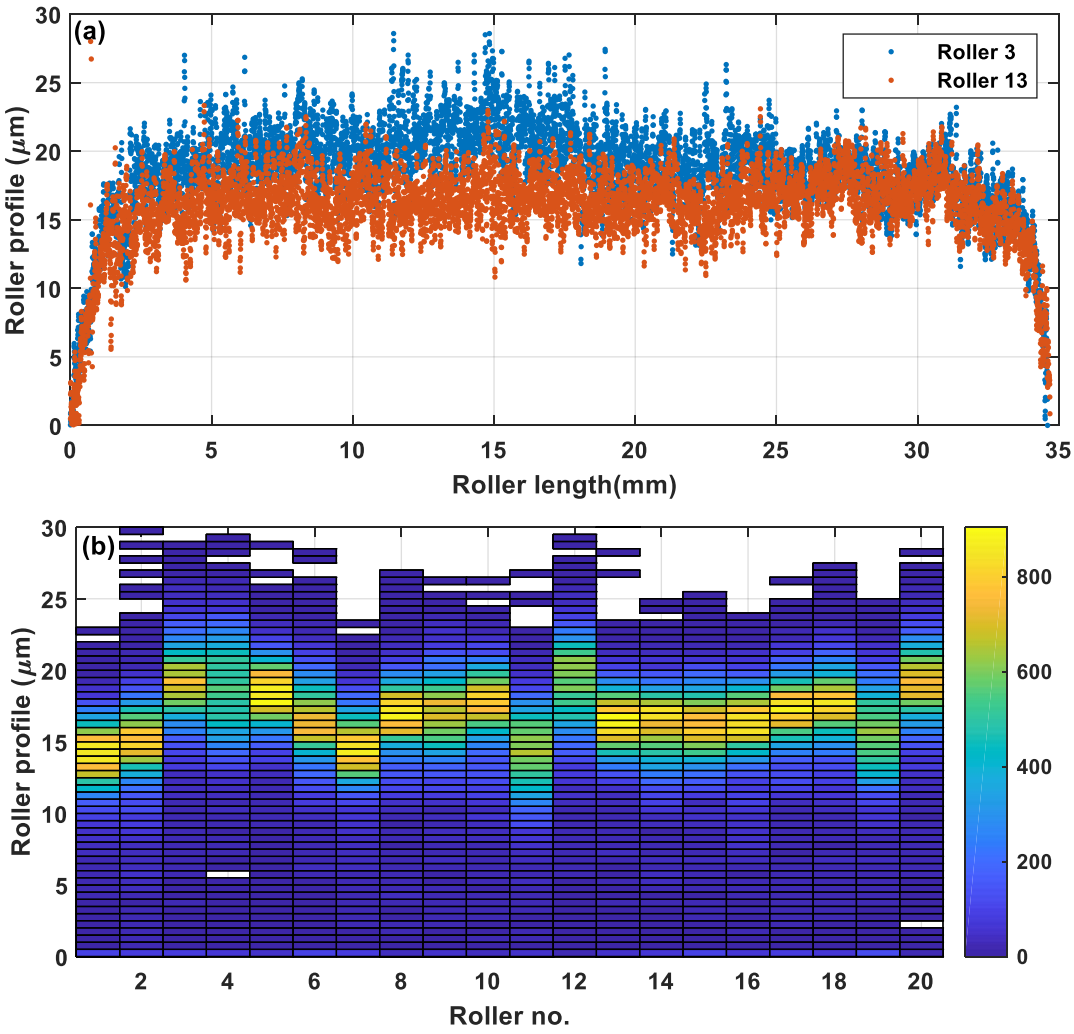

Figure 5.8 - (a) Roller profile measurements for 32222 TRB (b) Histogram bivariate plot for all the 20 measured roller profiles

Table 5.4 shows the results of the theoretical study. For a fixed amount of deflection, a positive variation in roller profile height from its design height will result in a reduction in roller load. However, a reduction in roller profile height will cause the roller load to increase under a greater rate. Since the basic bearing L_{10} life rating is a function of the roller load to the power of 4 for a line contact, and 10/3 for typical roller bearings, any increase in roller load will have a detrimental effect to bearing life [173]. In this case, a -10 μm off design profile height will result in almost 1.6 times increase in roller load and consequently at least 4.5 times reduction in L_{10} basic bearing life rating, accelerating the bearing fatigue failure. For the roller profile variation measured in the 32222 TRB rollers, a ±5% variation in load is expected.

Roller profile height, $h_{profile}$ (μm)	Reduced radius in lateral direction, R_y	Ratio of equivalent radius, k	Constant, K_{pc}	Percentage Difference of Roller Load
5	29.860	2279.432	2.834E+11	1.572
10	14.930	1139.716	2.131E+11	1.182
15	9.953	759.811	1.804E+11	1.000
20	7.465	569.858	1.602E+11	0.888
25	5.972	455.886	1.462E+11	0.810

Table 5.4 – Variation of roller load with roller profile height

5.3.2 Deducing reduced radius and constants from profile measurements

It can be seen from both roller and raceway measurements that the profiles are not of simple shape. To approximate an R_y value, the geometries were assumed to be parabolic and Equation (5.44) was utilised where $h_{profile}$ is the measured profile height, and L_{meas} is the measurement length.

$$R_y = \frac{1}{2 \cdot h_{profile}} \left[{h_{profile}}^2 + \left(\frac{L_{meas}}{2} \right)^2 \right] \quad (5.44)$$

For the NU2244 CRB, R_{y1} (roller) was found to be 17.15 m whilst R_{y2} (raceway) was found to be -198.81 m. The negative value was due to the concave profile of the inner raceway and a z of -5 μm was utilised. This resulted in an R_y of 18.80 and subsequently a k of 841, a small value for a CRB. On the other hand, R_{y1} (roller) for the 32222 TRB was found to be 9.85 m. Since no outer raceway profile measurements exist, the outer raceway is assumed to have no profile. This resulted in a k of 752.28. Constants K_{PC} and K_{LC} for both bearings were subsequently calculated and listed in the table below alongside their k values. Only values relevant to the contact conditions measured in §6 & 7 were computed. These values can then be used in Equation (5.42) and Equation (5.43) to complete the ToF-Load equations.

If one wishes to convert the roller load measurements, Q into bearing radial load, F_r, the following empirical relationship [46] can be used where Z is the number of rollers and ϕ is the roller-raceway contact angle (0° for a CRB).

$$F_r = \frac{1}{4.08} \cdot Q \cdot Z \cos\phi \qquad (5.45)$$

	NU 2244 CRB	32222 TRB
Contact	Inner raceway – roller contact	Outer raceway – roller contact
k	841	752.28
K_{PC}	2.445×10^{11}	1.796×10^{11}
K_{LC}	5.619×10^{9}	3.430×10^{9}

Table 5.5 – Constants calculated for NU2244 CRB and 32222 TRB

5.4 Conclusions

- Equations relating time-of-flight to deflection utilised in the previous chapter were reapplied and rewritten in the context of measuring bearing deflection.
- For conversion of bearing deflection into load, various line contact models were discussed, and the most appropriate model was selected for use.
- Houpert's relationship which consisted of a point contact relationship for low loading conditions and a line contact relationship for high loading conditions was selected and utilised. A transitional deflection was defined where when the deflection exceeds the transitional value, the contact transitions from point to line.
- Measurements of roller and raceway profiles for NU2244 CRB and 32222 TRB were taken to obtain k values and subsequently the K_{PC} and K_{LC} required to convert raceway deflection into roller load.
- Measurements of roller profiles for NU2244 CRB exhibit a logarithmic or multi-radius profile with an average maximum profile height of 49.5 μm, whilst the raceway profile is concave shaped with a height of -5 μm.
- Measurements of roller profiles for 32222 TRB also show a logarithmic shape with an average maximum profile height of 15.15 μm. Profile height of the 32222 TRB was seen to vary from 14.03 μm up to 18.93 μm, potentially resulting in a load variation of ±5%.
- K_{PC} and K_{LC} values for the NU2244 CRB was found to be 2.445×10^{11} and 5.619×10^{9}. For the 32222 TRB these are 1.796×10^{11} and 3.430×10^{9}

respectively. These constants are substituted in the ToF-Load relationship in §5.2.5 and used to obtain roller load from ultrasonic ToF measurements.

6 MEASUREMENTS FROM A FULL-SCALE CRB TEST RIG

6.1 Introduction

This chapter outlines experiments conducted on a cylindrical roller bearing test rig (MultiLife) in which the bearing inner race was instrumented with ultrasonic sensors. Initially, the test rig as well as the experimental setup and procedure are introduced. Measurements are conducted from 20 – 100 *RPM* and with a loading range of 0 – 1000 *kN*. A 20 *RPM* rotational speed step and a 100 *kN* step is utilised. Subsequently, trends in the ultrasonic measurements observed are presented and discussed. Various ultrasonic methods outlined in the previous chapters were applied in this study. This include techniques for ultrasonic sensor instrumentation (§3.2.4), hardware for pulse generation and receiving (§3.6.2), data processing routines (§3.6.4), acoustoelastic constants measurement (§4.3.3), and equations for conversion of measured ToF change to roller load for NU2244 CRB, specified in §5.2.5.

6.2 Experimental setup

6.2.1 Test rig

A rig designed for the testing of wind turbine planetary gearbox bearings called "MultiLife" was utilised for the testing. The rig is owned by *Ricardo plc* and was on loan at the University of Sheffield. Figure 6.1 shows both the schematic and photo of the front-side of the assembled test rig and also a sketch illustrating the location of lubricant inlet and outlet hoses. The rig is capable of rotational speeds between 20 - 100 *RPM* with an applied bearing radial load ranging from 0 – 1500 *kN*. The test bearing inner raceway (NU2244) was held stationary on the instrumentation sleeve which sits at the centre of the rig. Its outer raceway and cage assembly was fitted onto the pulley wheels assembly and was rotated. The bearing has a clearance fit with the instrumentation sleeve and rested on a step within the sleeve. It was then axially pressed against the step to prevent undesired rotation. The rotational speed was supplemented through a motor and pulley belts assembly whilst the radial load is provided by the hydraulic actuator located at the base of the rig. The hydraulic actuator is connected to the static shaft, which sits centrally within the instrumentation sleeve, through two load arms. As the actuator is initialised, the load arms are pulled down which in turn pull the shaft downwards, applying load onto the instrumented static inner raceway. Load cells installed on both sides of the

loading arms provide a measure of the applied load. A Hall effect sensor was installed to measure the bearing rotational speed during testing.

The inner raceway test bearing was lubricated continuously using an assembly of lubrication hoses and pump (not shown in Figure 6.1). A single-phase electric motor acted as a pump. The lubricant was pumped through a 25-micron filter into a cooling radiator before lubricating the bearings through a single inlet port at a radius of $140\ mm$ from the bearing centre axis and 60° from the bearing bottom-dead-centre (BDC), located on the back side of the rig. This is illustrated in Figure 6.1(c). Properties of the lubricants used were shown in Table 6.1. The pressure-viscosity coefficients were calculated using methods detailed in AGMA 925-A03 [192]. A pressure transducer exists at the inlet port to ensure the lubrication is supplied to the rig during testing. Two outlet ports exist at both the front and back side of the rig to draw lubricant back to the reservoir. The rotational speed, load and lubrication of the rig were all controlled through a LabVIEW interface.

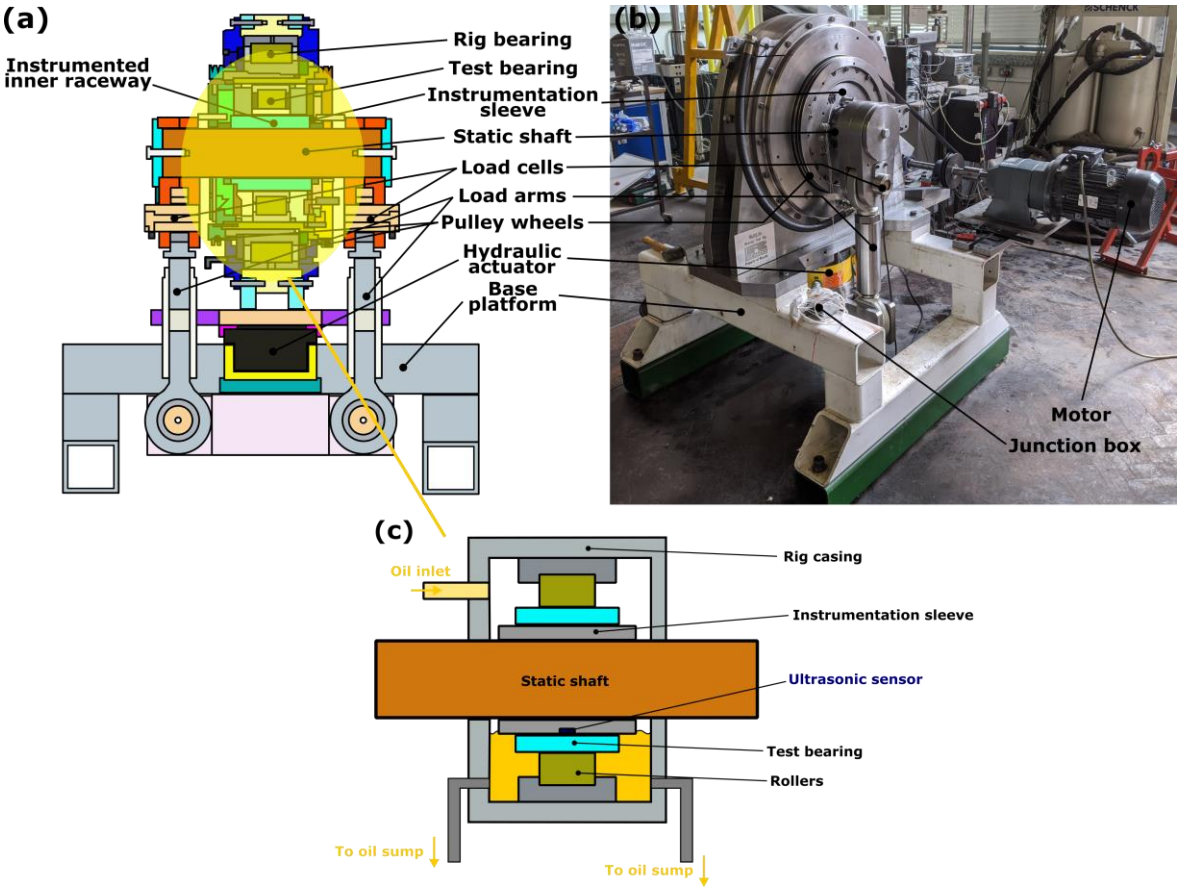

Figure 6.1 – (a) Schematic and (b) photo of the front side of the assembled MultiLife CRB test rig (Schematic adapted from [171]) and (c) sketch illustrating the lubricant inlet and outlet region

Lubricant	Viscosity at 40˚C (cSt)	Viscosity at 100˚C (cSt)	Density at 15˚C (kg/m^3)	Pressure-viscosity coefficient, α (Pa^{-1})
VG 32	32	5.4	870	1.670×10^{-8}
VG 150	150	14.5	890	2.057×10^{-8}
VG 320	320	24.0	900	2.279×10^{-8}

Table 6.1 – Properties of lubricants used for testing

6.2.2 Bearing instrumentation and pulsing system

Sensor instrumentation was carried out on the inner raceway of a NU2244 CRB which was manufactured by PSL. Specifications of the NU2244 CRB are detailed in §5.4. The NU2244 inner raceway was instrumented with 7 longitudinal and 7 shear sensors across the width of the bearing. Figure 6.2(a) and (b) shows the instrumented bearing with the sensors bonded onto the inner bore surface whilst Figure 6.2(c) shows a schematic illustrating the positions of the sensors relative to each other. The sensors were installed with similar procedure as outlined in §3.2.4. Sensors were hand trimmed to approximately $5 \times 1.5\ mm$ rectangular strips and installed at the BDC of the rig which coincide with the maximum loaded region of the bearing. Distance between each row of the sensors was $11\ mm$ whilst distance between the columns were $2\ mm$ apart from the centre point of the sensors.

To allow for all the wiring to fit within the bearing housing, coaxial cables of $0.40\ mm$ in diameter were used. The live terminals were soldered onto the piezo elements whilst the grounds were bonded onto the bearing surface using silver epoxy. Figure 6.3 shows a schematic of the sensor pulsing configuration for the CRB testing.

All 14 coaxial cables were routed from the bearing housing into a junction box. The junction box linked the sensors to cables with SMB connectors attached at the end, all labelled to distinguish the sensors. The desired sensors were then plugged into the data acquisition FMS through the SMB connectors. The reader is referred to §3.6.2 for details and working of the data acquisition system.

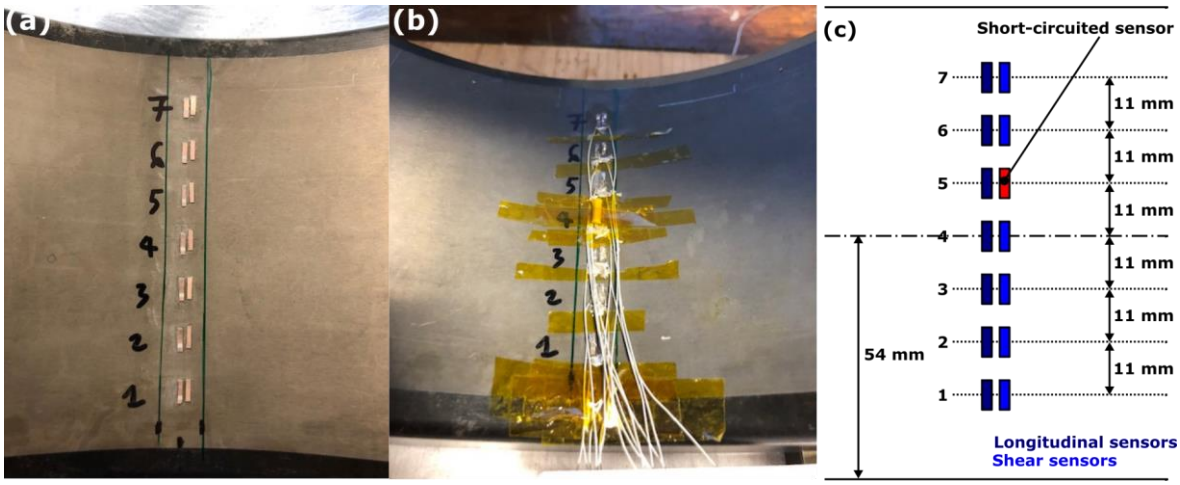

Figure 6.2 – Photo of the instrumented inner raceway showing (a) the bonded piezo elements and (b) the wired-up sensors, (c) schematic of the sensor positions on the raceway

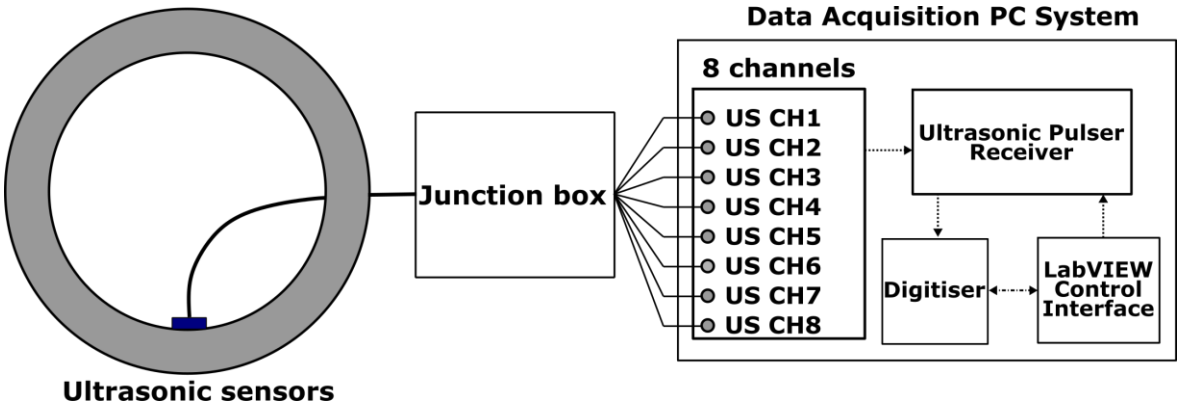

Figure 6.3 – Sensor pulsing configuration for full-scale roller bearing testing

Upon installation of the bearing into the rig, it was discovered that one of the shear sensors (Shear 5) short-circuited and did not register a response. Measurements were subsequently carried out with the remaining 13 functional sensors.

Although the piezo elements were specified at 10 MHz for longitudinal, the actual frequency at which they were operating were observed to be different. The actual values were listed in the table below for each channels.

Sensor CH	1	2	3	4	5	6	7
Longitudinal (*MHz*)	8.1055	8.5938	7.7148	8.0078	8.1055	7.7148	7.6172

Table 6.2 – Actual resonance frequencies of the bonded longitudinal and shear sensors

6.2.3 Test matrix

Testing were separated into 3 different blocks, based on 3 different lubricants of various viscosity (VG32, VG150, VG320). The lubricants used were all from the Castrol Alpha SP range. Each block of testing was then divided again into 3 different sub-blocks as 3 sensor pulsing configuration exist (full longitudinal, fully shear or longitudinal and shear). A minimum of 9,500 pulses per second for each channel exists for all the measurements taken with each dataset consisting of a capture duration of 10 seconds. For each sub-block, measurements at speeds from $20 - 100\ RPM$ and loads of $0 - 1000\ kN$ were taken. A step of $20\ RPM$ and $100\ kN$ were used, resulting in 55 datasets in a sub-block and subsequent 165 datasets for a block. In total, 495 datasets were taken based on the matrix shown in Table 6.3. In this work, only measurements obtained from the longitudinal sensors were presented and discussed as the author considered shear measurements subject of future work and provides no continuity to the longitudinal measurements discussed in the subsequent chapter (§7).

Lubricant	Sensor pulsed	Speed	Load
VG 32	7 Longitudinal	20 – 100 *RPM* (20 *RPM* step)	0 – 1000 *kN* (100 *kN* step)
VG 150	7 Shear		
VG 320	3 Longitudinal, 3 Shear		

Table 6.3 – Lubricant properties and test configuration for the MultiLife Rig

6.3 Trends from a roller pass

6.3.1 General trends

Figure 6.4 shows deflection and reflection coefficient measurements processed from the reflections obtained through the centre longitudinal sensor (row 4). The

data processing routine utilised to obtain ToF and reflection coefficient from raw ultrasonic reflections can be found in §3.6.4 whilst method for conversion of ToF to deflection was detailed in §5.1. Measurements were obtained at 20 *RPM* and 100 *kN* and lubricant used was VG320 mineral oil. Two roller passes were recorded at 2.28 and 2.58 s respectively.

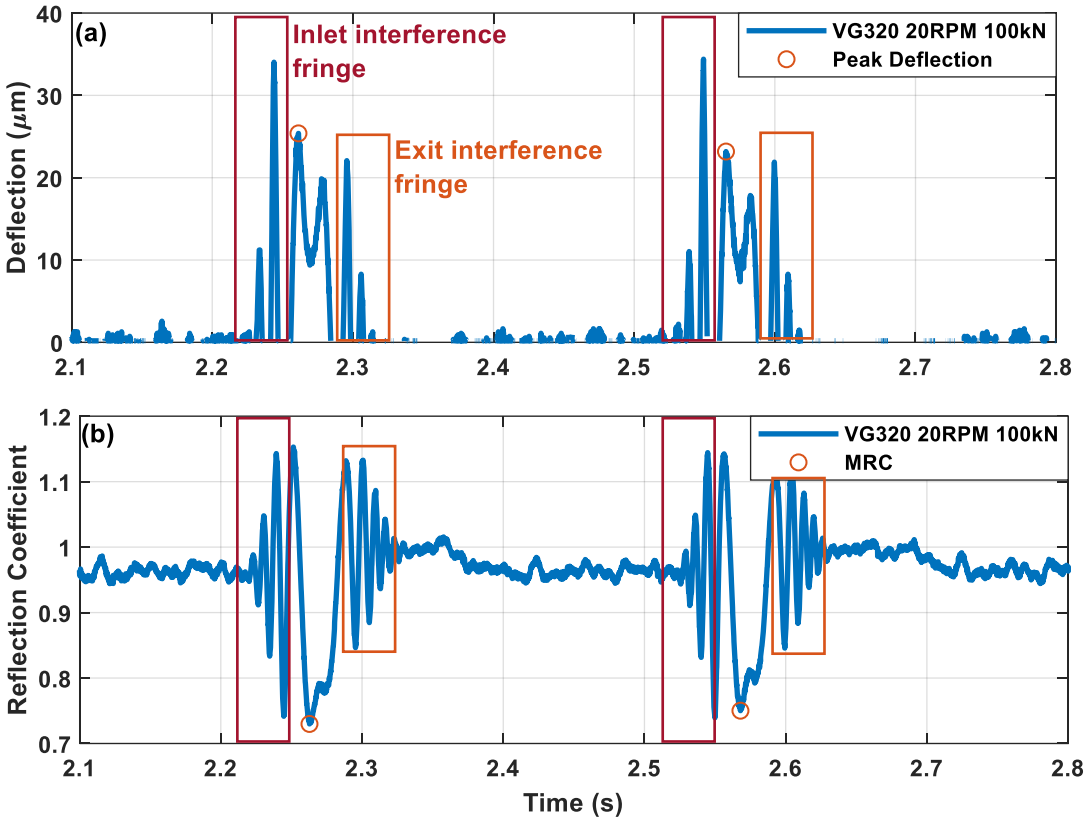

Figure 6.4 – (a) Deflection and (b) reflection coefficient measurements showing two roller passes for VG320 oil at 20 *RPM* and 100 *kN*

The roller passes for deflection measurements resemble a M-shape, with its maximum point located also closer to the inlet region. Conversely, reflection coefficient roller pass resembles a W-shape, with the minimum point also located closer to the inlet region. An interesting observation can be made from the regions highlighted with red and amber rectangles for both deflection and reflection coefficient measurements. These are inlet and outlet region of a roller pass and show oscillations of increasing and decreasing magnitudes. A reflection coefficient exceeding unity means that a surplus of ultrasonic energy is present within the reflected signal. Figure 6.5 attempts to explain the source of this energy surplus. Due to the divergence of the incident sound wave, the ultrasonic energy will be incident across a large segment of the rolling surface. When a rolling element approaches the periphery of the incident wave, small amounts of ultrasonic energy is reflected back

from the roller-raceway interface [171]. These reverberations vary in arrival time depending on the location of the roller with respect to the centre of the sensor as illustrated in Figure 6.5(b). This results in either constructive of destructive interference between the main reflected pulse and the reverberations from the roller, subsequently manifesting as energy fluctuations within the inlet and outlet of the reflection coefficient measurements. These are termed “interference fringes” [171]. Upon entry and exit to the bearing loaded zone, rollers tend to ‘vibrate’ in their cage, which potentially contributes to the interference fringes. This is highly unlikely as static benchtop testing of a roller-flat plate arrangement do still show the presence of interference fringes, eliminating roller ‘vibration’ as the primary cause.

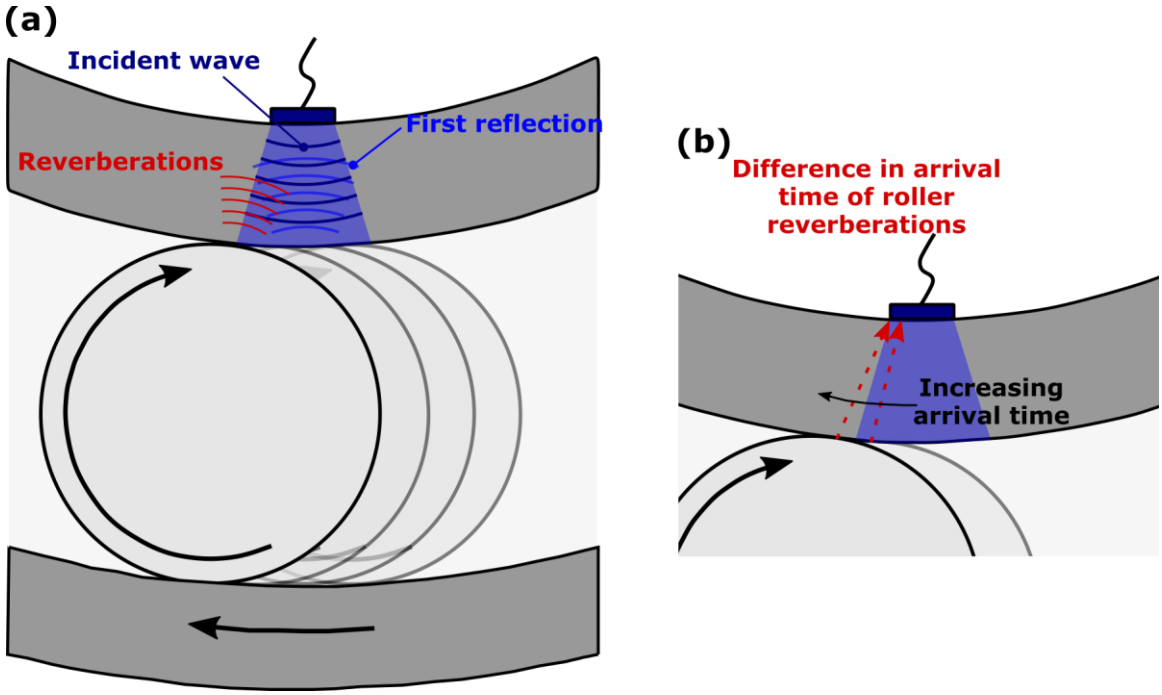

Figure 6.5 – (a) Ultrasonic reflections within the bearing raceway and interference reverberations from a roller-raceway interface, (b) roller position influencing time of arrival of reverberations

For the roller load measurements, the peaks manifesting within these zones are false peaks, despite its higher magnitude at the inlet region at low loads. The roller pass reflection coefficient resembles a W-shape, with the minimum point located closer to the inlet region. The roller load measurements however resemble a M-shape, with the maximum point also located closer to the inlet region.

Outside of the roller pass region, only low amplitude noise was recorded for the deflection measurements. On the other hand, reflection coefficient measurements

varied between unity and 0.95 between roller passes, with 0.95 recorded for the roller inlet region, corresponding to a steel-oil interface and unity measured after a roller pass, corresponding to a steel-air interface.

Figure 6.6 shows the full measurement obtained from a single dataset taken at the same conditions ($20\ RPM$, $100\ kN$, VG320). A higher deflection measurement for a certain roller also registered a lower reflection coefficient and vice versa. An interesting observation can be made where peak deflection and minimum reflection coefficient measurements obtained varied across each roller. This variation or waviness of the peaks and troughs was also observed during previous testing [135, 167]. Figure 6.7 shows the spectral content of the deflection and reflection coefficient measurements. Recurring peaks occurring within both plots correspond to the ball pass frequency of the inner raceway, found to be 13.36 *Hz*. Deduction of bearing rotational speed is thus possible. The frequency content of the reflection coefficient measurements show more noise, which is an effect from the unfiltered interference fringes.

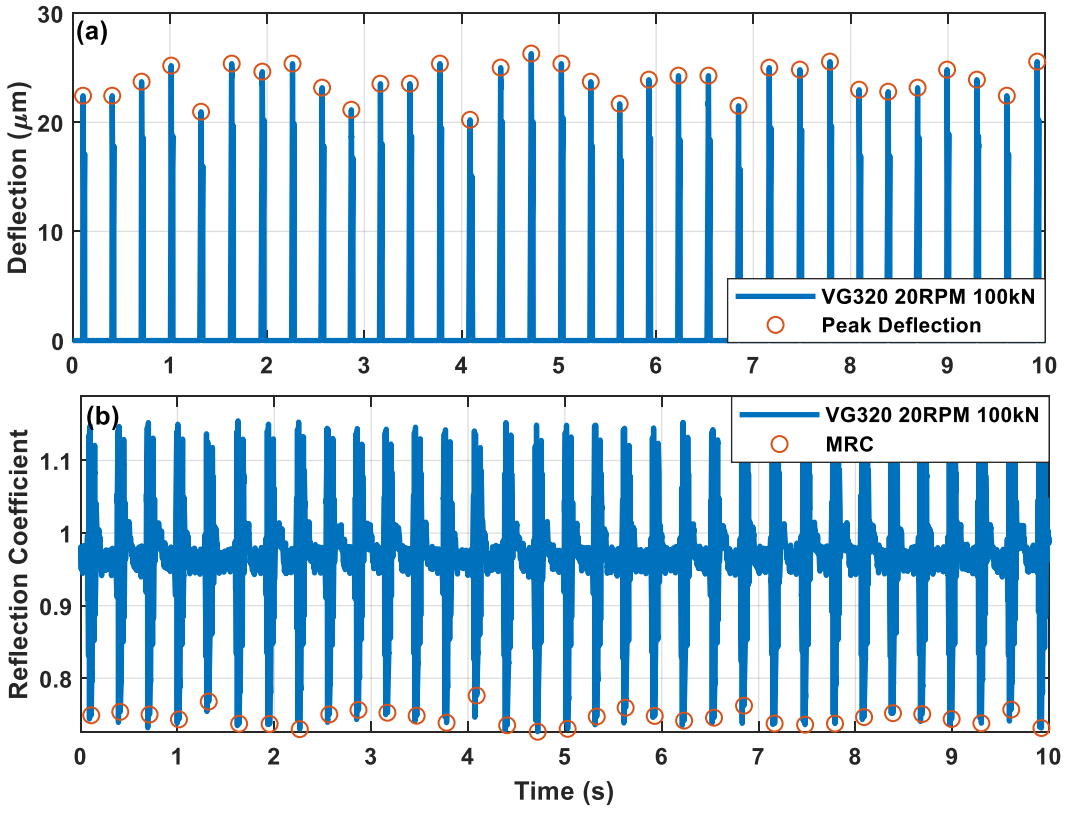

Figure 6.6 – Full (a) filtered deflection and (b) reflection coefficient measurement obtained from a single dataset taken at 20 RPM and 100kN using VG320 oil

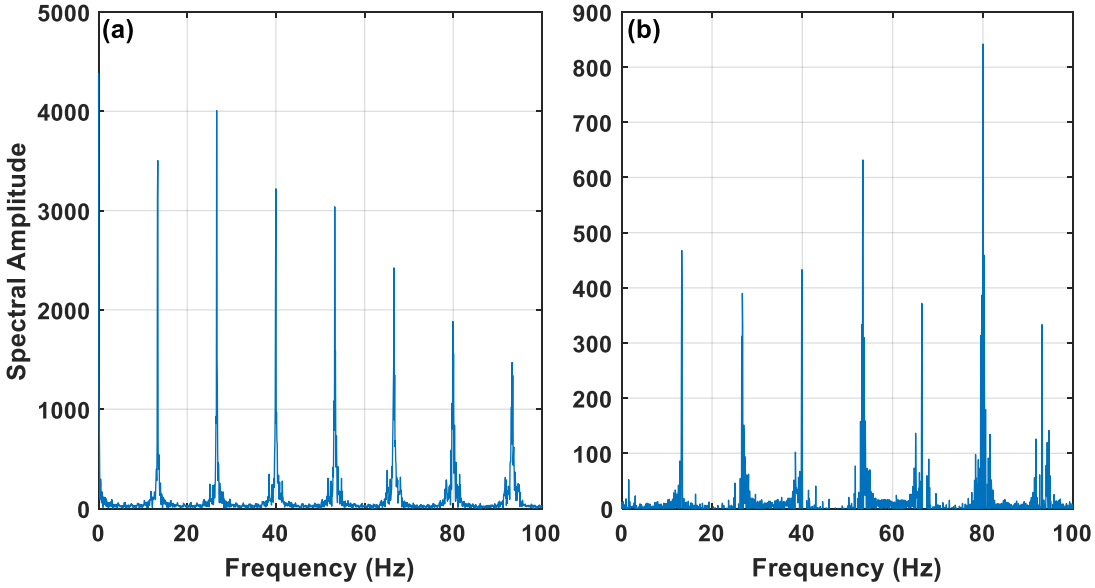

Figure 6.7 – Spectral content of (a) deflection and (b) reflection coefficient measurements

To investigate the periodicity of the peaks and dips of the deflection and reflection coefficient measurements, the peak deflection and minimum reflection coefficient were collated and plotted alongside each other with their respective measured time. This can be seen in Figure 6.8(a) and (b). FFT was subsequently applied to the peak deflection and minimum reflection coefficient to obtain their spectral information as shown in Figure 6.8(c). The frequency content of both measurements seemed to be very similar with a small magnitude peaks visible at 0.15 *Hz* and 0.26 *Hz*. Consequently, torque oscillations due to voltage unbalance from the induction motor [193] can be eliminated as the cause of the variation.

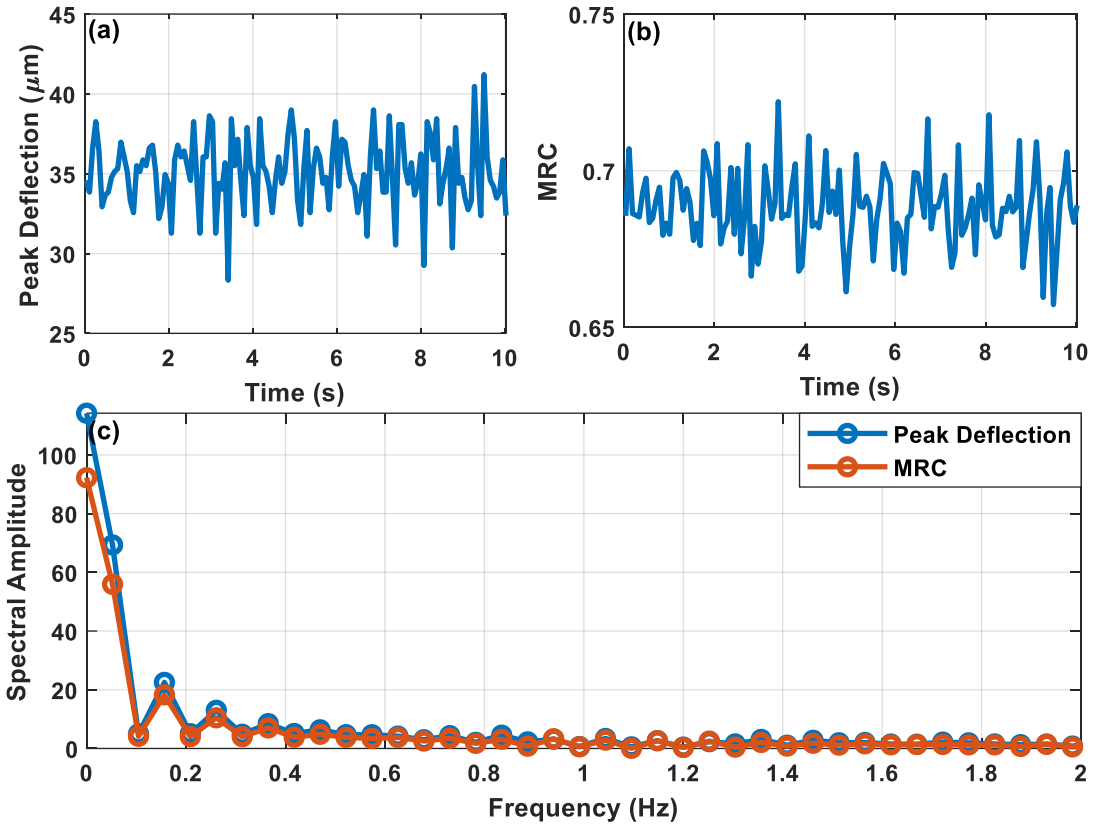

Figure 6.8 – Collated (a) peak deflection and (b) minimum reflection coefficient values and (c) their respective frequency content

Since each measurement point correspond to a single roller and the number of rollers for a full rotation is known, the measurements can be arranged to study the measurement variation between individual rollers and across roller complement. Figure 6.9 shows the range of peak deflection and minimum reflection coefficient values across individual rollers and cycle. Range values for both measurements are slightly higher across a full complement of 15 rollers compared with individual rollers. The interquartile range of both individual roller and full cycle range measurements are very similar, with the rollers having a larger interquartile range for minimum reflection coefficient. A higher interquartile range indicates larger variation in range values, and less consistent measurements. The waviness of peaks and dips is potentially resulted from lack in concentricity of the rotating components (waviness in the bearing rings) and difference in micro-geometry of the rollers. The waviness in the bearing raceways was thought to result in undesired tensile stresses near the raceway which potentially weakens the bearing and result in premature failure [75].

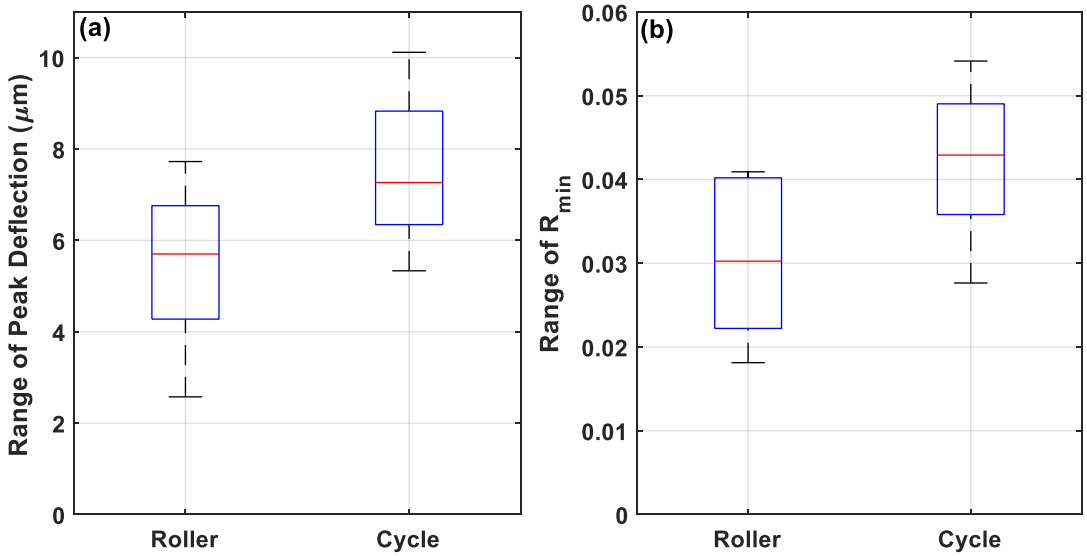

Figure 6.9 – Range of (a) peak deflection and (b) minimum reflection coefficient

6.3.2 Application of spring model on VG320 measurements

Previous testing conducted on MultiLife using VG32 oil [171] concluded that conversion of reflection coefficient measurements to film is not possible due to the contact being within mixed lubrication. The conversion of *R* to *h* was attempted again using the latest measurement taken using VG320 oil, with the hope that the thicker oil sufficiently separates the two contacting surfaces.

Several assumptions were made when converting the reflection coefficient to lubricant film thickness. The speed of sound is assumed to be fixed at $1350\ m/s$, however it is known that it varies with temperature and ideally a calibration curve is required. The acoustic impedance of the bearing raceway and rolling element was also assumed to be constant at $46\ MNs/m^3$. The oil density was calculated using Equation (6.1) with reference density of $860\ kg/m^3$ at reference temperature 15.6 ℃.

$$\rho = \rho_0(1 - 0.00063(T - T_0)) \qquad (6.1)$$

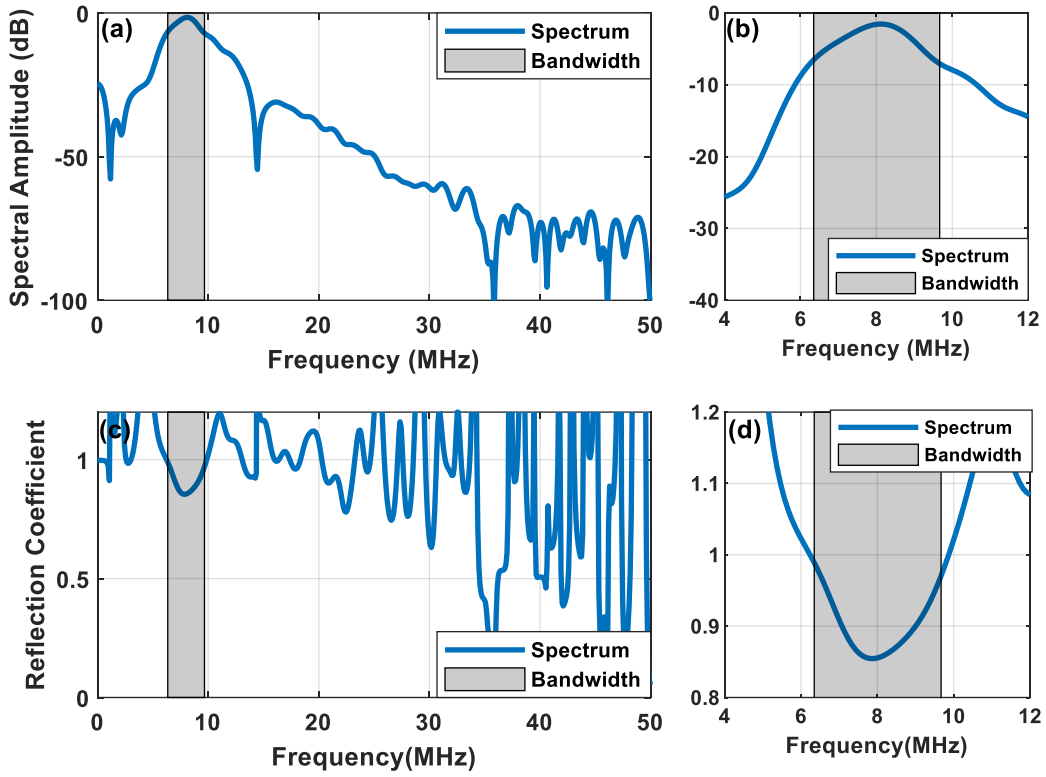

Figure 6.10 – (a) & (b) Spectral amplitude and (c) & (d) reflection coefficient spectra of one of the pulses captured at 100 RPM and 0 kN

Figure 6.10 shows the spectral amplitude and reflection coefficient spectra of the pulse which coincides with one of the minimum reflection coefficient point measured. The data used was captured using the centre sensor at 100 *RPM* and 200 *kN*. The spectral amplitude of the pulse is concentrated within its bandwidth of between 6 - 10 *MHz*. Reflection coefficient measurements should be independent of frequency and thus measurements within the sensor bandwidth should be constant. Measurements however were seen to decrease from 6 – 8 *MHz* before increasing again. Since the data shown was at maximum rotational speed 100 *RPM* and relatively no applied load, it is likely at higher load, the contact would remain mixed and thus conversion from reflection coefficient to film thickness will not be possible across all the datasets.

6.3.3 Filtering of false deflection and reflection coefficient measurements

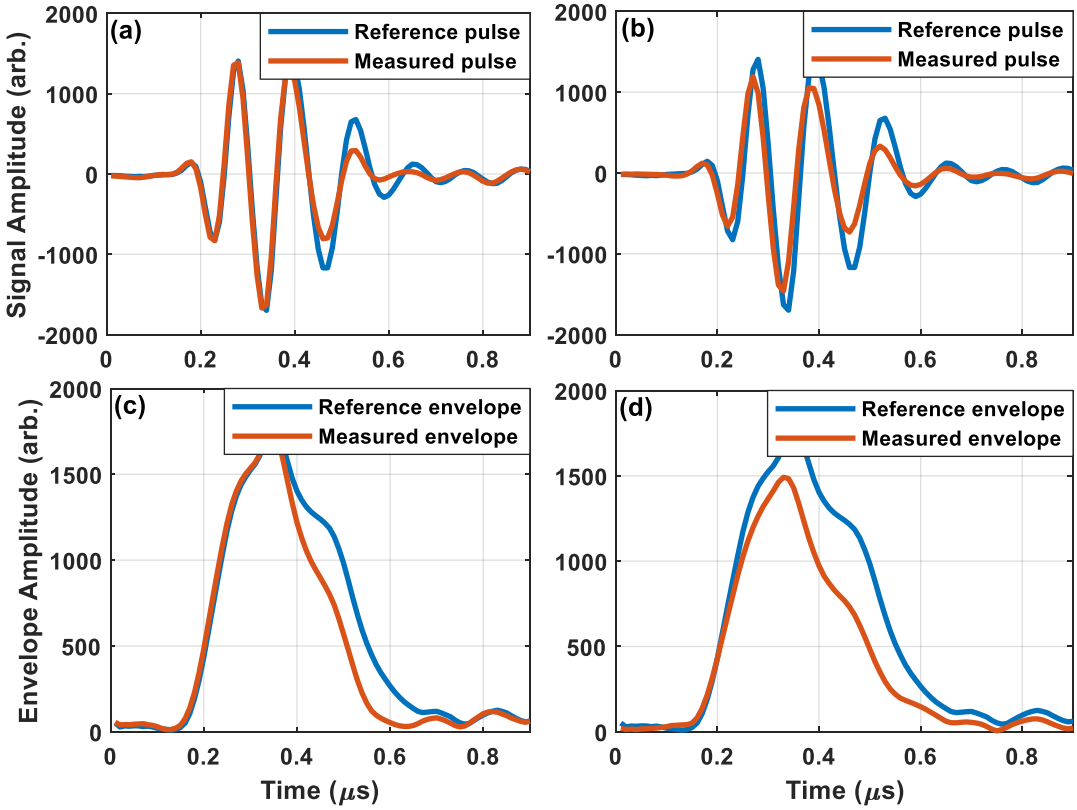

Figure 6.11 – The measured and reference pulses for (a) false and (b) actual peak deflection measurement and the envelopes of the (c) false and (d) actual peak waveform

For deflection measurements at low bearing load (0 – 200 *kN*), the false peak deflection measurement at the roller inlet region is of higher magnitude than the actual peak deflection measurement located within a roller pass. This complicates automation of extraction of actual peak deflection values, and as such an algorithm was developed to remove the false measurements caused by the interference fringes. To further investigate the false load measurements, the reference pulse is plotted alongside the pulse corresponding to the false and actual peaks. Figure 6.11 illustrates the plot. In Figure 6.11(a) and (c), apart from a decrease in amplitude of the loaded pulse after its second oscillation, no change in time-of-flight is apparent. Figure 6.11(b) and (d) on the other hand, show the presence of an actual time shift between the loaded and reference pulse. As such, the false peaks are a result of data processing error where false time-of-flight measurements were recorded due to fringe interference causing cross-correlation errors when correlating the envelopes of the reference and loaded false peak signal.

By contrasting the pulse envelopes of the false and actual *ToF* measurement, it is evident that for the false peak envelope, the amplitude does not vary significantly compared to the reference pulse at its main oscillation between 0.25 – 0.40 *s* whereas measurements from the actual peak do exhibit a variation. This can be used to distinguish between actual and spurious *ToF* measurements. Subsequently, additional codes were incorporated into the *ToF* processing routine for more robust measurements. Figure 6.12 shows the flowchart which the code operates to filter out spurious *ToF* measurements. A HT was initially performed on the measured and reference pulse and the envelopes were normalised against their respective maximum envelope magnitudes. A parameter 'S' was then obtained by finding the difference between the normalised magnitudes of the measured and reference envelope and used to distinguish whether the *ToF* measurement resulted from the pulse is true or false.

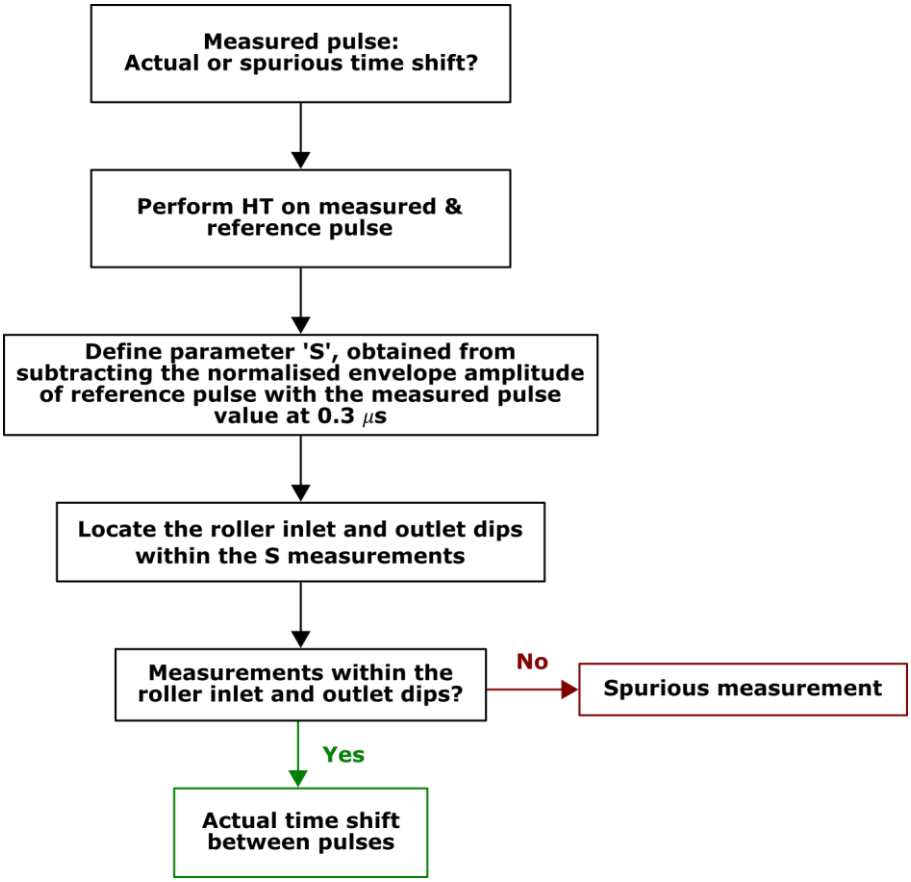

Figure 6.12 – Flowchart of the algorithm for filtering false ToF measurements

Figure 6.13(a) shows the actual roller pass and filtered false deflection measurements whilst Figure 6.13(b) shows the S value for three roller passes. It was observed that recurring dips within the S values occur during each roller pass. These dips correspond to the roller pass inlet and outlet region and consequently can be

used to distinguish between actual and false ToF measurements. The filtered deflection measurements retained the measurements within the roller pass and eliminated the spurious time-of-flight measurements as well as the 'grass' or noise outside the roller-raceway contact region. This is to be expected as without the presence of a roller, there would not be a time shift and subsequently no deflection. Non-contact stresses and stresses from adjacent rollers potentially invalidate reference measurement taken between roller passes. Empirical observations seem to indicate minimal effect from these non-contact stresses, as these would be accounted for when taking the 'live' reference. Further work is necessary to fully validate this. This can be done through varying the hoop stress the raceway experiences and observing its influence on the ToF measurements.

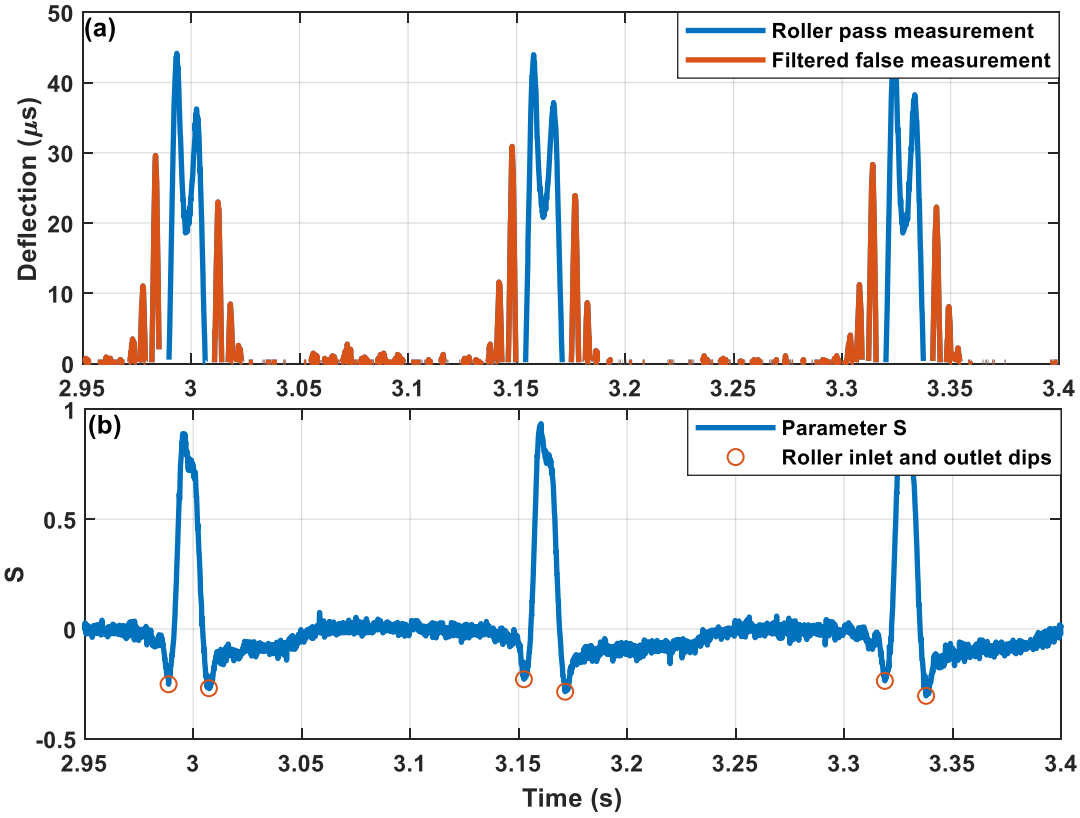

Figure 6.13 – (a) Filtered and unfiltered deflection measurements and (b) the difference between normalised magnitudes of measured and reference envelope for a single roller pass

6.3.4 Variation of deflection and reflection coefficient with load

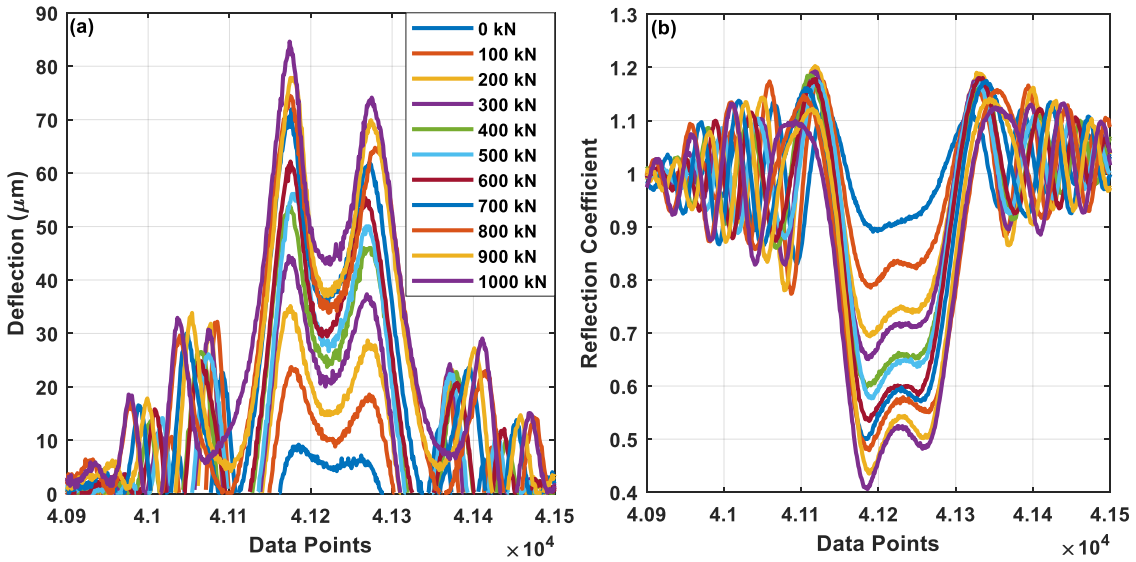

Figure 6.14 – Roller pass patterns for (a) deflection and (b) reflection coefficient measurements with increasing bearing load

Figure 6.14 shows the variation of deflection and reflection coefficient measurements with increasing bearing load for a rotational speed of 40 *RPM*. The measurements shown were for a longitudinal sensor located at the centre of the raceway (row 4). As the bearing loading increases, the deflection measurement alongside the M-shape width also increases, with the peak deflection value consistently increasing. The peaks and trough of the M-shape becomes more prominent as the load increases. The first set of measurements at 0 *kN* show a peak deflection value of just less than 10 μm and minimum reflection coefficient of around 0.9. This was initially thought to be resulted from the weight of the static shaft, loading arms and hydraulic actuator base assembly (approximately 500 *kg* in total), however the cumulative weight would not result in a deflection of 9.2 μm and the matter is subjected to further investigation.

For the reflection coefficient measurements, the minimum reflection coefficient consistently decreases with increasing load. The W-shape pattern also retained across the measurements with the peaks and trough becoming more prominent with increasing load. Interestingly, the interference fringes for both deflection and reflection coefficient measurements do not seem to be influenced by the increasing applied load.

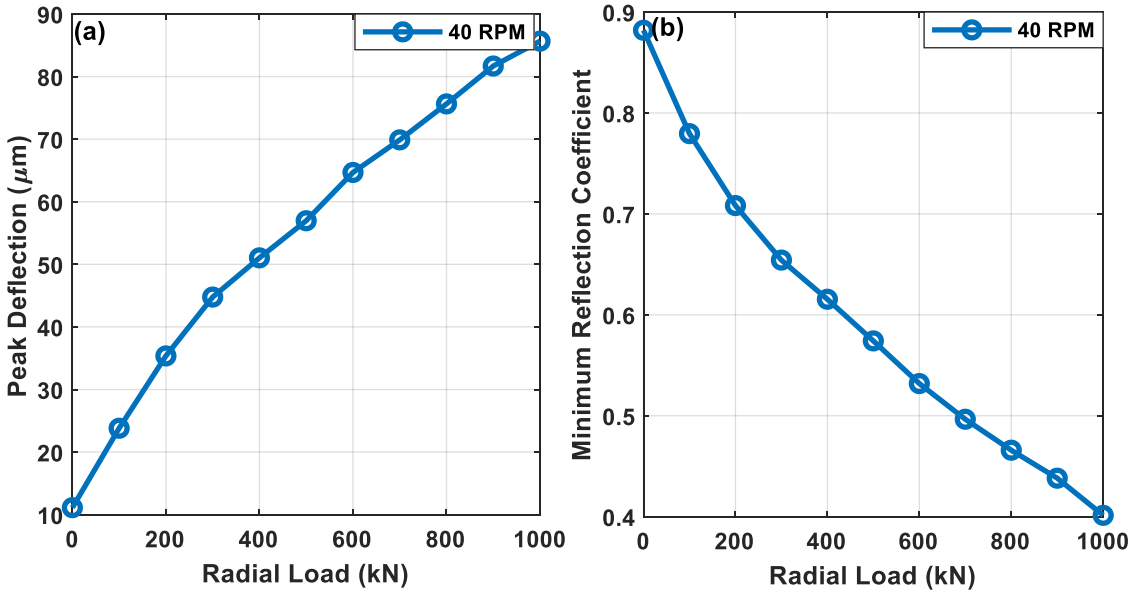

Figure 6.15 – Variation of (a) peak deflection and (b) minimum reflection coefficient with increasing radial load for rotational speed of 40 *RPM*

The averaged peak deflection and minimum reflection coefficient values across the datasets captured at 40 *RPM* were collated and shown in Figure 6.15. A 10 μm deflection was measured at 0 *kN* which gradually increased as the load increased, with a maximum deflection measured at around 85 μm. Conversely, the minimum reflection coefficient decreased with increasing load. Both the plots exhibit an almost linear or slightly parabolic increase with radial load. The peak deflection measurements show signs of having two gradients, between 0 – 300 *kN* and 300 – 1000 *kN*.

6.3.5 Variation of deflection and reflection coefficient with rotational speed

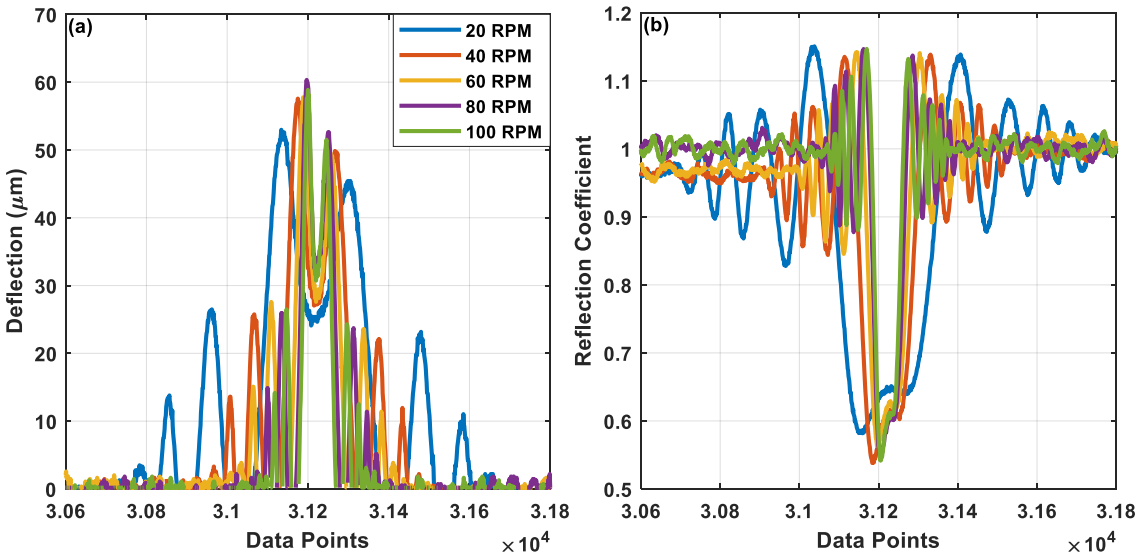

Figure 6.16 – Roller pass patterns for (a) deflection and (b) reflection coefficient measurements with increasing bearing rotational speed

Figure 6.16 shows the variation of deflection and reflection coefficient measurements with increasing bearing rotational speed for a constant load of 500 *kN*. Measurements shown again were for a longitudinal sensor located at the centre of the raceway (row 4). The peak deflection values seem to not vary significantly across the measurements, with the 20 *RPM* data having the largest variation. The same can be said for the reflection coefficient measurements, where the MRC for the measurements are roughly the same except for the 20 *RPM* case. The M-shaped and W-shaped pattern for the measurements become narrower as the rotational speed increases. This is expected since the time which the roller transverses across the sensor reduces as rotational speed increases. Interference fringes for both measurements were not influenced by the rotational speed. Peak deflection and minimum reflection coefficient values were summarised in Figure 6.17. Averaged peak deflection values increased slightly from 20 to 80 *RPM* before dropping at 100 *RPM* whilst the opposite trend is apparent for the minimum reflection coefficient measurements. Deflection measurements drifted by 3%, two-fold less than the variation of minimum reflection coefficient values. The variation at different rotational speeds is potentially attributed to the change in bearing load applied as the rotational speed is varied.

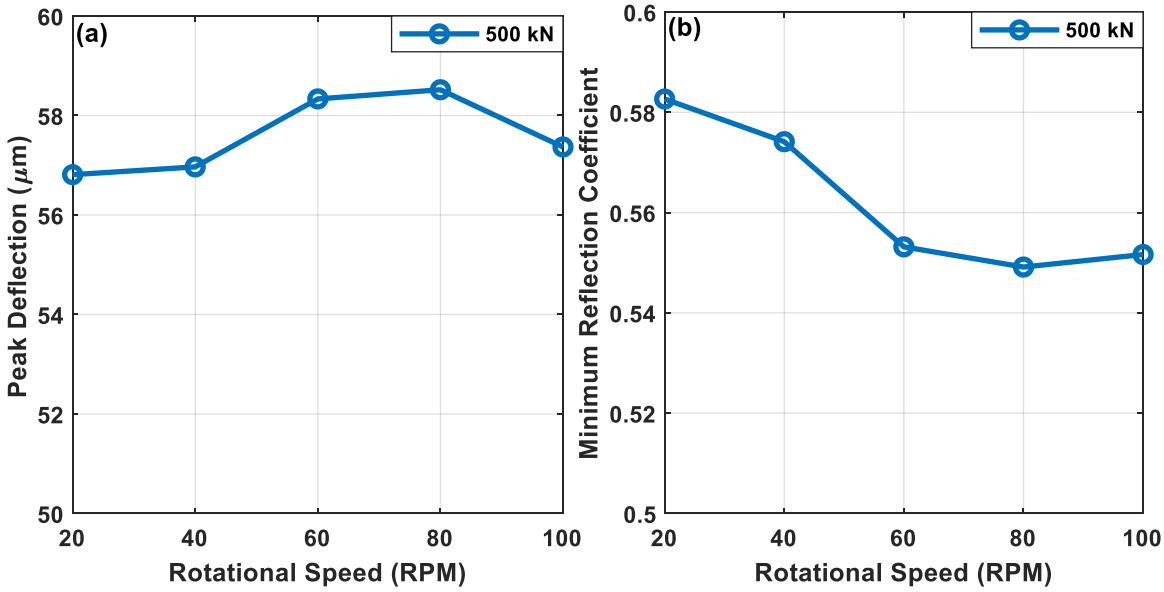

Figure 6.17 – Variation of (a) peak deflection and (b) minimum reflection coefficient measurements with increasing bearing rotational speed at constant load of 500 *kN*

6.3.6 Variation of deflection and reflection coefficient across contact length

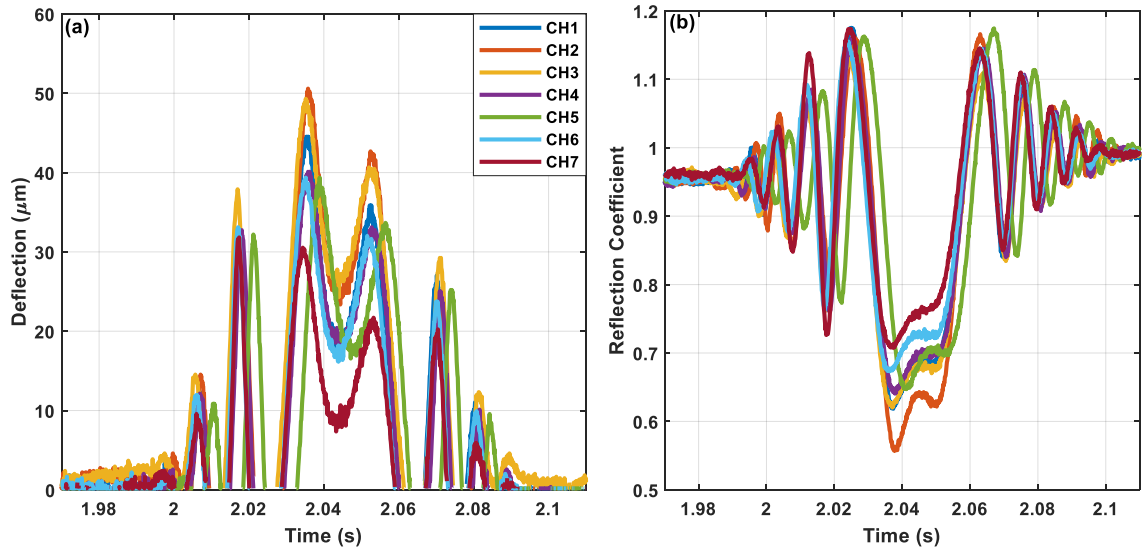

Figure 6.18 – Variation of (a) deflection and (b) reflection coefficient measurements across all 7 longitudinal sensors measured at 20 *RPM* and 300 *kN*

Figure 6.18 shows the variation of deflection and reflection coefficient measurements obtained from all the 7 longitudinal sensors positioned on the inner raceway. The data shown was measured at 20 *RPM* and 300 *kN* using VG320 oil. All the measurement channels seem to be well synchronised except for CH5 (green) which can be seen to lag behind the other measurements. As CH4 and 6 are well synchronised, the lag cannot be resulted from roller skew. Since the lag consistently

manifested on the same channel (CH5) in other measurements, this is most likely due to a constant hardware excitation delay of CH5 from the FMS.

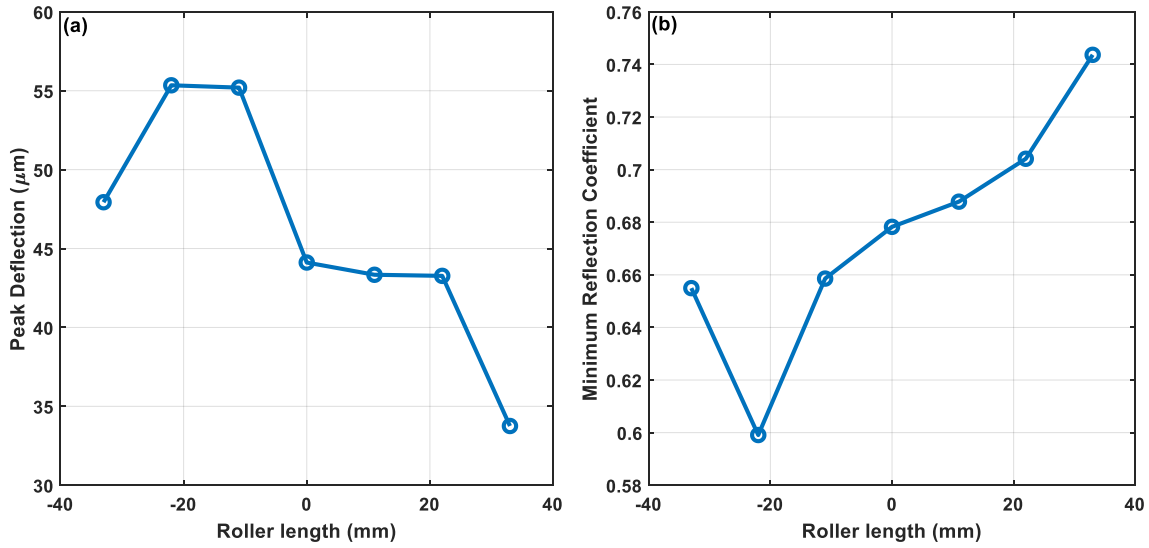

Figure 6.19 – Averaged (a) peak deflection and (b) minimum reflection coefficient measured from the 7 sensors positioned across the roller length

The averaged peak deflection and minimum reflection values for each sensor is shown in Figure 6.19. The averaged peak deflection values can be seen to peak with a value of 55 μm at -22 *mm* and gradually tapers off. The MRC values show a similar trend where the values have a minima at -22 *mm* and gradually increases after. Despite efforts to maintain even loading within the rig, edge loading is still apparent. As such, equations discussed in §5.2.5 cannot be applied and thus deflection measurements were not converted into load.

6.3.7 Variation of reflection coefficient patterns with oil viscosity

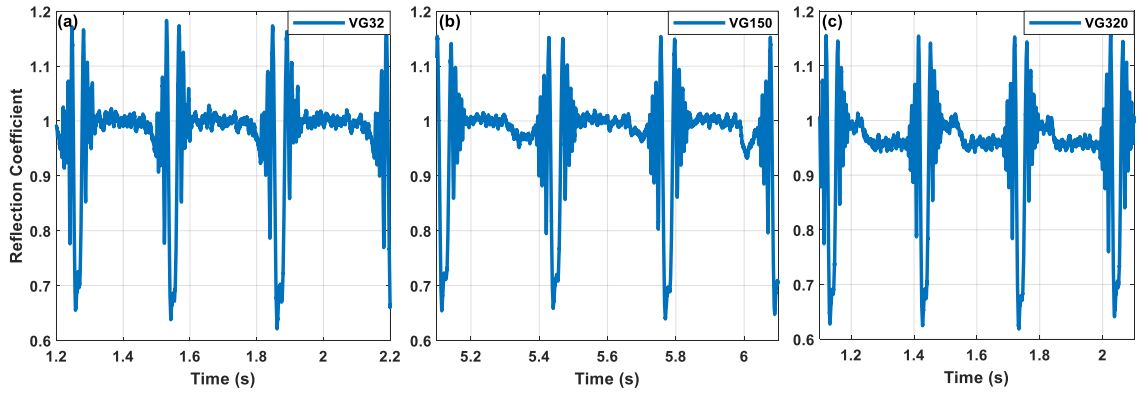

Figure 6.20 – Reflection coefficient patterns for measurements taken at 20 *RPM* and 300 *kN* for (a) VG32, (b) VG150 and (c) VG320 mineral oil

As previously mentioned, measurements between roller passes contain information regarding the lubrication condition of the raceway surface. Figure 6.20 illustrates the patterns of reflection coefficient measurements between roller passes taken from the 3 mineral oil tested, with distinct patterns identifiable among the 3 measurements. For the lowest viscosity oil, the reflection coefficient between roller passes mostly remain at 1, except for the roller inlet region where the measurements transitioned from unity to 0.95. This zig pattern before a roller pass indicates that the roller inlet region and subsequently the roller contact is sufficiently lubricated. Such patterns are also apparent in the VG150 and VG320 oil results. The zig-zag pattern for the two thicker oils manifested much earlier compared to the VG32 oil, with the VG320 oil transitioning from $R = 1$ to 0.95 quickest. As such, the lubricant reflow time would decrease with increasing lubricant viscosity. As the rotational speed increases, the instances where the rollers traverse across the sensor also increases which aids in the distribution of lubricant, resulting in a decrease in reflow time. The viscosity of the lubricant could influence both adversely and favourably on the lubricant reflow time. The more viscous the lubricant, the slower it will flow to refill a voided region. However, a viscous lubricant will have a larger free surface film thickness compared to a less viscous one. Figure 6.21 shows the change in lubricant reflow time with increasing load, rotational speed, and lubricant viscosity. For the load and speed investigation, measurements taken using VG320 oil were utilised. As the applied load increases, a linear increase in small amplitudes of lubricant reflow time can be seen. Conversely, the lubricant reflow time was seen to decrease in an exponential manner with increasing rotational speed. As observed in Figure 6.20, lubricant reflow time also decreased with increasing grade of lubricant viscosity.

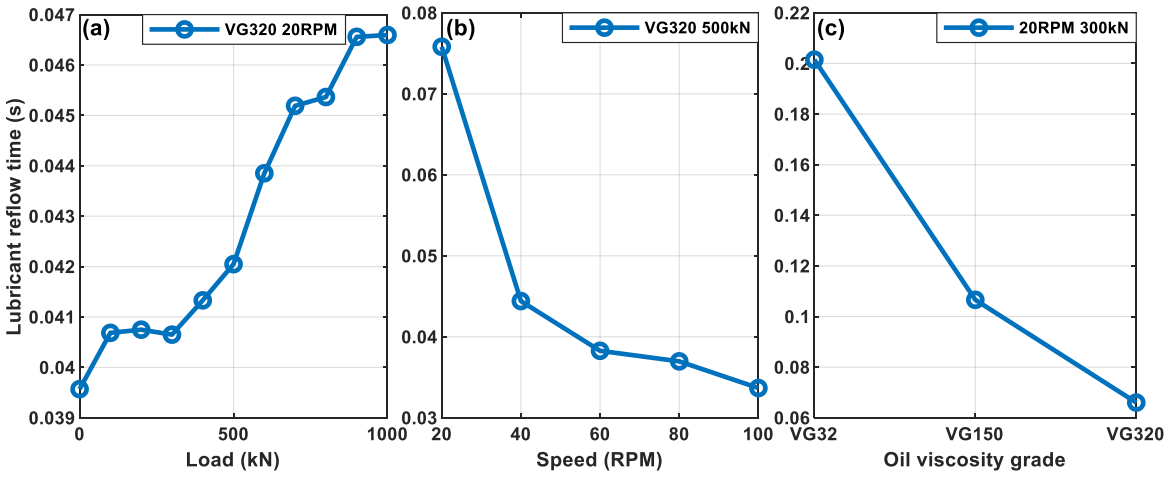

Figure 6.21 – Variation of lubricant reflow time with (a) applied load, (b) rotational speed and (c) lubricant viscosity

6.3.8 Fringe interference investigation

This section aims to have a closer look into the interference fringes. As mentioned before, the interference fringes are theorised to be resulted from reverberations caused by the roller and thus is a function of the roller position. From Figure 6.4, the false peak within the deflection measurements for the inlet interference fringe is always higher than that of the outlet. A similar observation can be made for the reflection coefficient minima in the inlet and outlet region.

To investigate the frequency components within the reflection coefficient plot, empirical mode decomposition was carried out on the signal. The algorithm decomposes the signal into intrinsic mode functions (IMFs) which each cover a certain frequency range and a residual signal through an iterative sifting process. Figure 6.22 shows the reflection coefficient signal, its IMFs and the residual signal which is the signal with the first 3 IMFs removed. With the removal of the initial 3 IMFs, the interference fringes present at the roller inlet and outlet region were also removed. The W-shape manifesting at each roller pass was also smoothened out, leaving a single dip during each roller pass. This indicates that the interference fringes consist of higher frequency components and thus measurements from an ultrasonic sensor operating at a lower central frequency would not contain any interference fringes. This was confirmed experimentally as shown in Figure 6.23. Measurements were taken from a 5.86 *MHz* longitudinal sensor and small amplitude interference fringes were observed at the roller inlet and outlet.

The maxima and minima of the deflection and reflection coefficient measurements located at the roller inlet interference region were selected as parameters to investigate the influence of bearing load and rotational speed on interference fringes. Figure 6.24 shows the variation of the maxima false deflection and minima reflection coefficient amplitudes with increasing bearing load and rotational speed. An increase in bearing speed did not have any visible effect on the maxima false deflection and minima reflection coefficient measurements. Similarly, no clear correlation was also found between the measurements with increasing load, albeit increasing scatter of measurements. Thus, it can be concluded that interference fringes are not a function of bearing load and rotational speed.

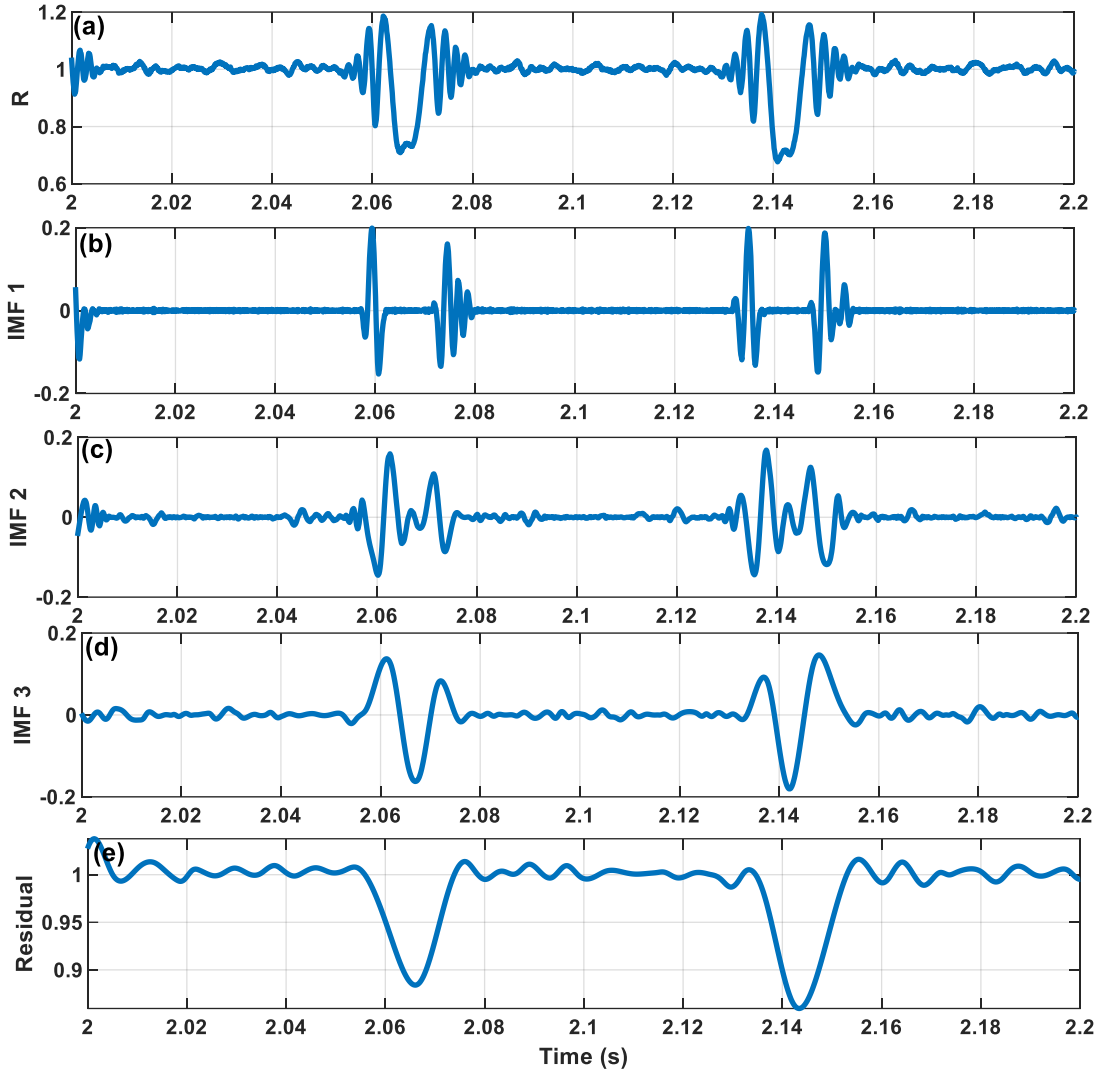

Figure 6.22 – (a) Reflection coefficient signal showing 2 roller passes, (b, c & d) intrinsic mode function 1,2 & 3 and (e) residual reflection coefficient signal

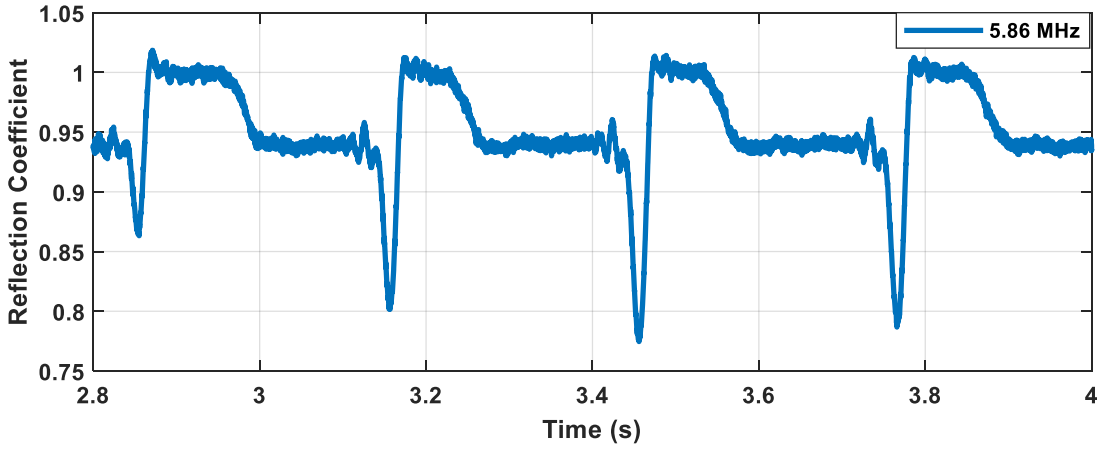

Figure 6.23 – Reflection coefficient showing 3 roller passes for a sensor with central frequency of 5.86 *MHz*

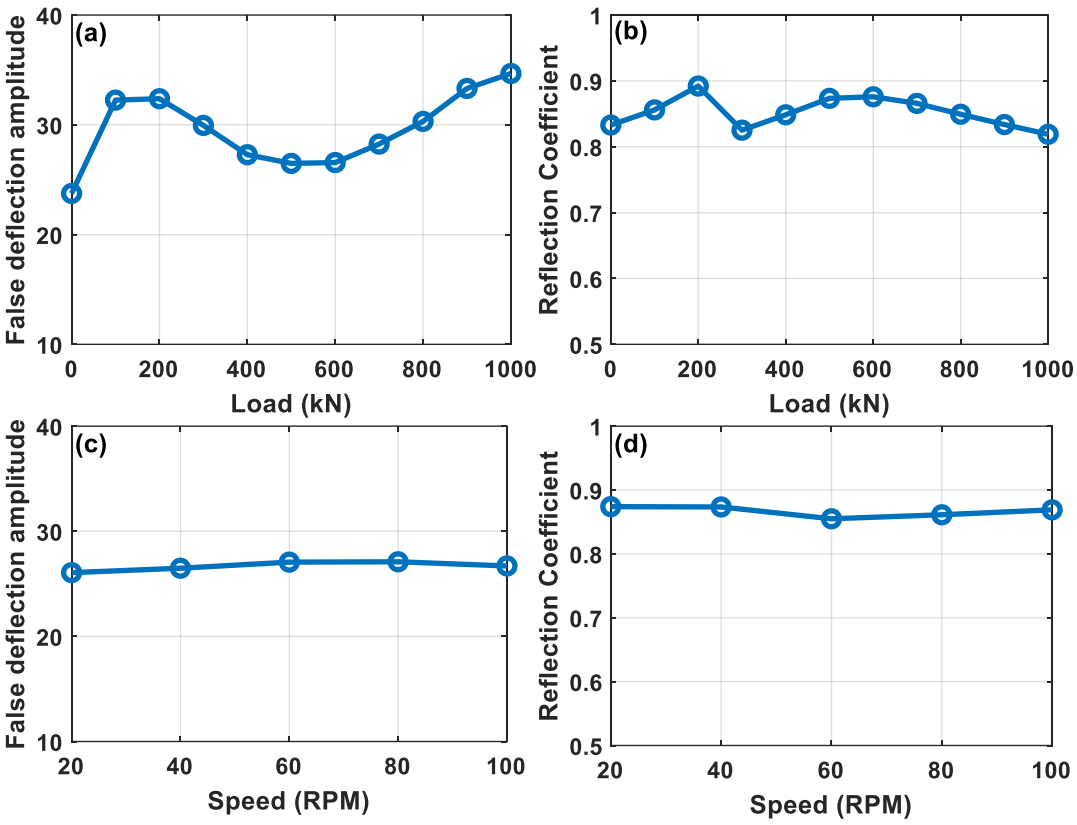

Figure 6.24 – Variation of (a, c) the peak false deflection amplitude and (b, d) reflection coefficient located within the interference inlet region with load and speed

6.3.9 Comparison of ultrasonically inferred rotational speed with demand speed

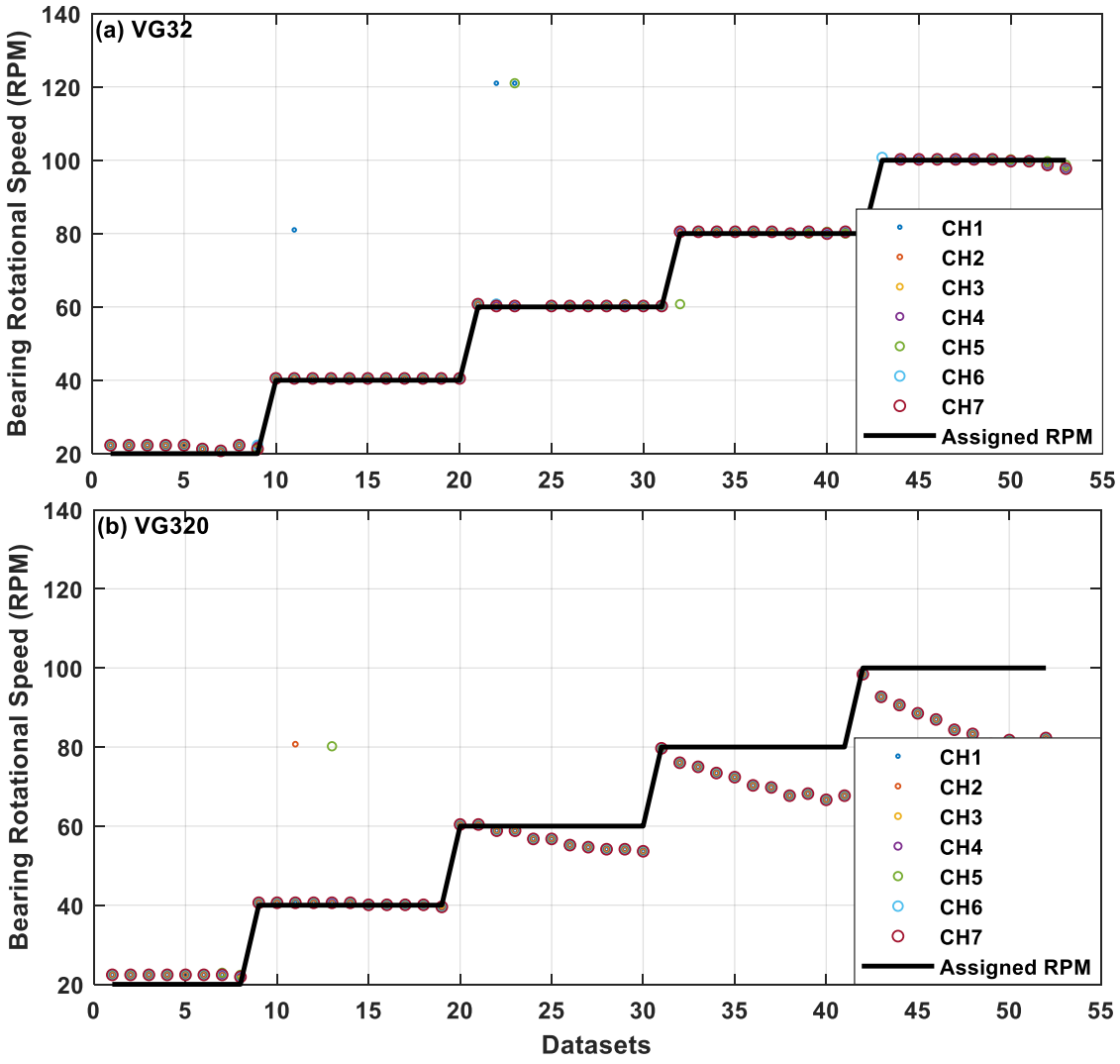

Figure 6.25 – Ultrasonically inferred bearing rotational speed alongside the assigned motor speed for bearing lubricated using (a) VG32 and (b) VG320 mineral oil

Figure 6.25 compares the rotational speed inferred from the ultrasonic measurements against that assigned to the motor across the 52 measured datasets for both VG32 and VG320 mineral oil tests. A Hall Effect sensor exists on the rig to measure the outer raceway rotational speed. At each constant speed step, the points presented correspond to a dataset with different load, arranged in increasing order from left to right.

For VG32 measurements, the rotational speed inferred from each measurement channel for the same dataset is consistent across the measurement, except for 5 instances. Reduced measurement scatter was observed for that of VG320

measurements with only two scatter points detected at 40 *RPM*. Rotational speed measurements for VG32 datasets show very small variation with the assigned speed, with the maximum variation of $3\ RPM$ observed for a dataset recorded at $100\ RPM$. The same cannot be said for the VG320 rotational speed measurements. For the 20 and $40\ RPM$ datasets, bearing rotational speed averaged at $22.39\ RPM$ and $40.62\ RPM$. At higher rotational speeds, the bearing speed gradually drifted from its assigned speed. This was suspected to be a result of increased lubricant viscosity which resulted in increasing torque demand for the motor. As such the rotational speed measured gradually decreased with varying gradient. The gradient was seen to increase with increasing rotational speed demand. The maximum drift for a $60\ RPM$ demand was $5\ RPM$, $12\ RPM$ for a $80\ RPM$ dataset, and finally $21\ RPM$ for a $100\ RPM$ dataset.

6.3.10 Measurements of deflection and reflection coefficient across all sensors

Figure 6.26 and Figure 6.27 shows the variation of measured deflection and minimum reflection coefficient across all the longitudinal sensors for a loading range of 0 – 1000 *kN* at a constant assigned speed of 100 *RPM* taken using VG32 and VG320 mineral oil respectively. The surface plots for the lower speed conditions for both lubrication cases will not be shown as the trends are identical to that of the 100 *RPM*. For both lubrication cases, as the bearing load increases, the measured deflection for all the 7 sensors also increased and vice-versa for the minimum reflection coefficient. The minimum reflection coefficient point was not recorded at the centre (0 *mm*), but however at -22 *mm* from the centre, indicating the presence of roller edge loading. This minima location remained consistent across all the datasets of increasing loads. For the VG32 deflection measurements, the maximum deflection point shifted between -22 *mm* and +22 *mm* and measurements were much more evenly distributed across the sensor. On the other hand, the maximum deflection point for VG320 measurements, shifted from - 22 *mm* at low loading to - 11 *mm* as the load increases.

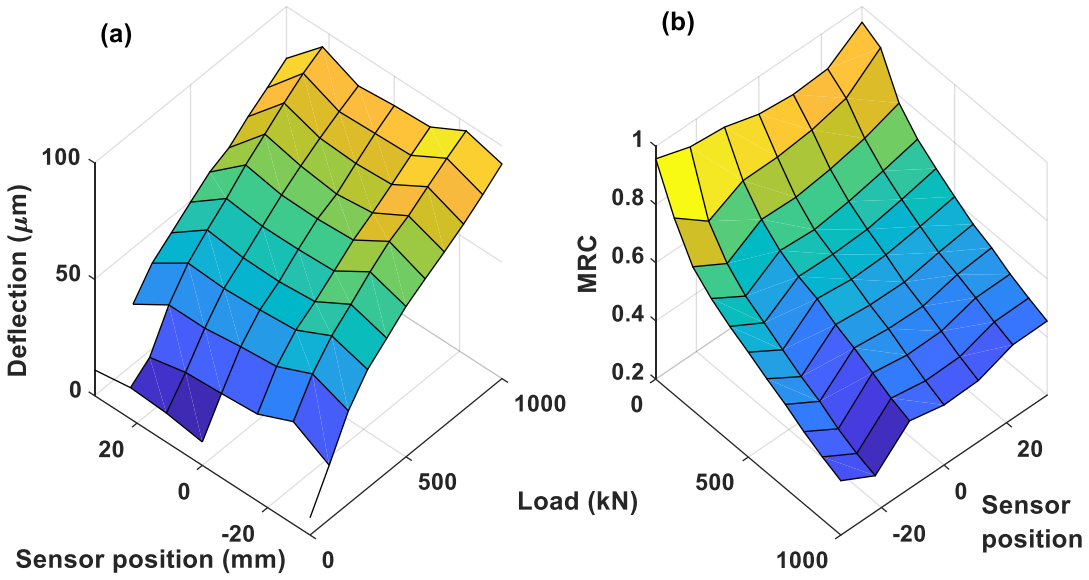

Figure 6.26 – Variation of (a) deflection and (b) minimum reflection coefficient for the 7 longitudinal sensors across 0 – 1000 *kN* bearing load at 100 *RPM* (VG 32)

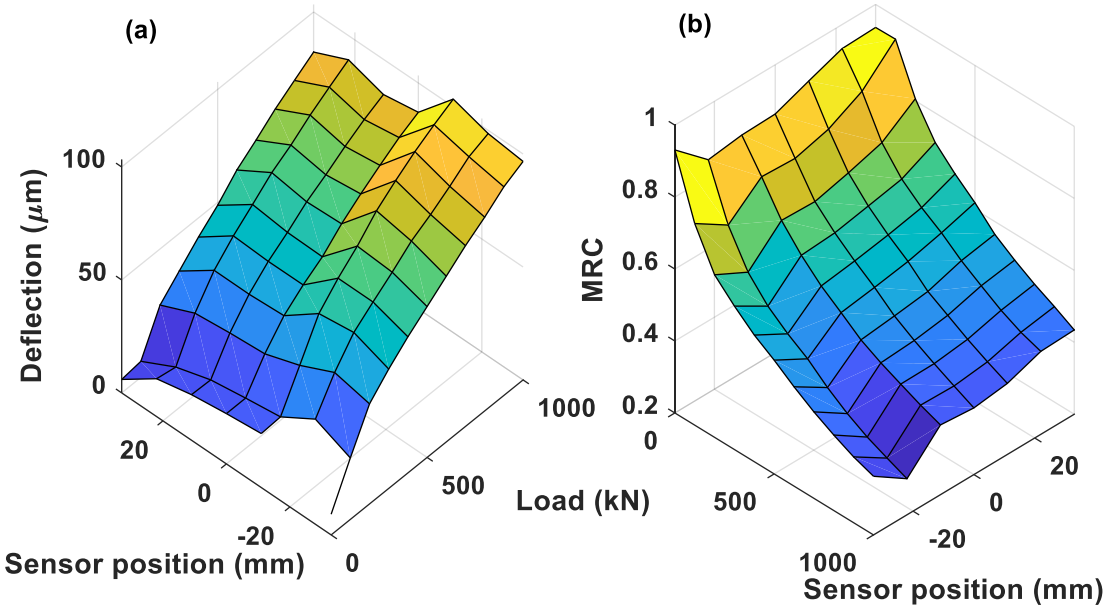

Figure 6.27 – Variation of (a) deflection and (b) minimum reflection coefficient for the 7 longitudinal sensors across 0 – 1000 *kN* bearing load at 100 *RPM* (VG 320)

6.3.11 Comparison of reflection coefficient with theoretical EHL film values

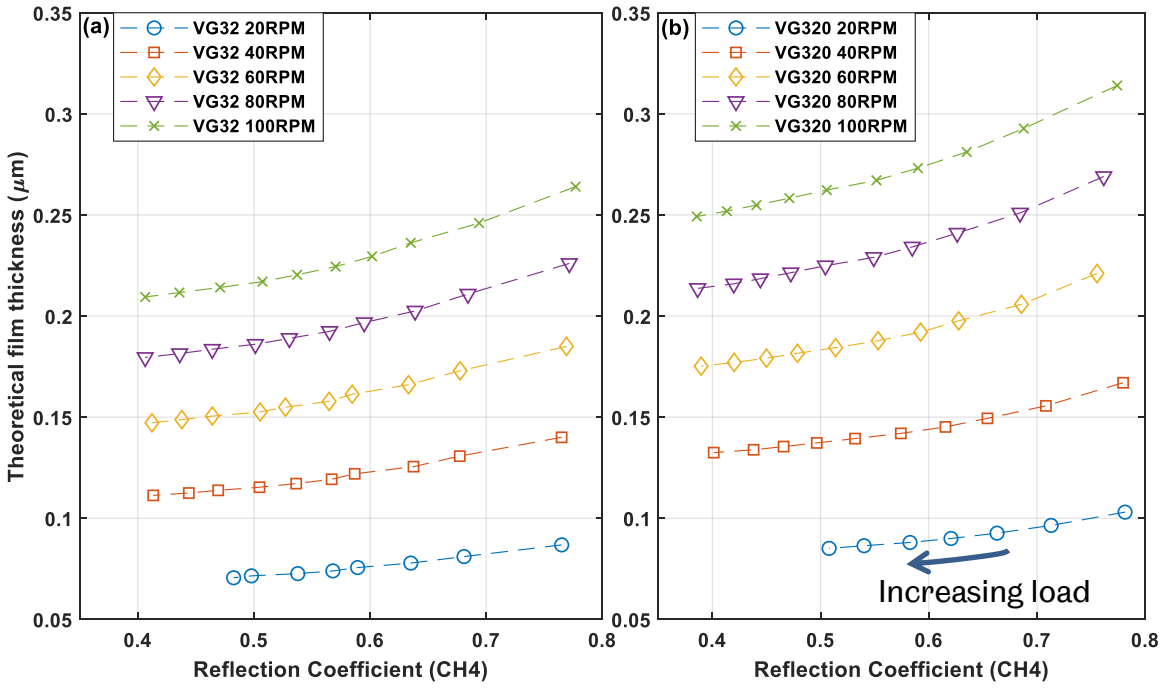

Figure 6.28 – Reflection coefficient measurements obtained from the centre sensor (CH4) plotted against calculated EHL film thickness for (a) VG32 and (b) VG320

Figure 6.28 shows the variation of reflection coefficient measurements with theoretical film thickness for VG32 and VG320 mineral oil, calculated using properties detailed in Table 6.1 for the centre sensor (CH4). For a specific rotational speed, the reflection coefficient measurement for both channels was found to decrease with increasing bearing load applied. The range of reflection coefficient measurement and calculated theoretical film thickness for VG320 was found to be slightly larger compared to VG32.

6.3.12 Comparison of US measured deflection with theoretical values

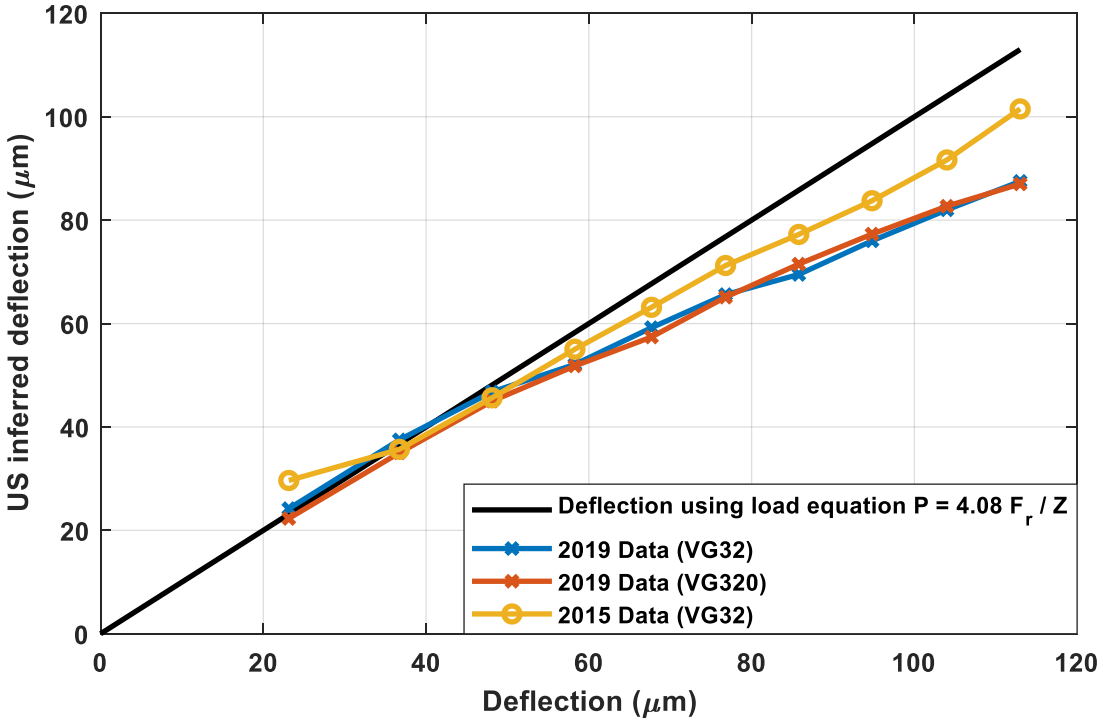

Figure 6.29 – Comparison between ultrasonically inferred deflection (centre sensor, CH4) against that calculated theoretically

Figure 6.29 shows the comparison between the calculated raceway deflection against the ultrasonically inferred deflection measurements for the sensor located at the centre of the raceway (CH4). For the theoretical deflection calculations, the roller load were initially computed from applied bearing load through the relationship specified within the figure. Luc's point-line load-deflection relationship was subsequently used to back calculate the deflection corresponding to each roller load. Three datasets were shown, two taken in 2019 with VG32 and VG320 oil and one taken in 2015 using VG32 oil. The 2019 measurements were shown to have good agreement at low loads, however the error increased gradually as the load increased. This is expected as due to the presence of edge loading, increasingly less load was being sustained at the centre as the load increases. The difference in lubricant viscosity used was also found to not affect the deflection measurements.

Data obtained in 2015 showed better agreement, indicating that less edge loading were present then. This however cannot be proven as only one 10 *MHz* sensor was instrumented at the centre of the raceway. Over this time, a new set of test bearing was installed (bearing rollers and raceway) and the ring which clamped onto the test bearing was ground to reduce the component waviness.

6.4 Discussion

The dynamic and loading capabilities of the full-scale rig allows for replication of bearing operation condition similar to operation under steady condition within a wind turbine gearbox. The rig was constantly troubled with misalignment problems [171] and in 2016, further efforts were taken by *Ricardo plc* to alleviate the issue. The main cause identified was concentricity issues of a ring component, which clamps onto the bearing outer race. This was thought to be remedied through grinding of the component into acceptable tolerance levels. However, from the ultrasonic measurements, it was found that misalignment issues persisted. Deflection measurements were not symmetrical across the roller length and were higher on the front side of the rig. As such, the deflection-load relationship detailed in §5 cannot be used and full validation of the load measurement method cannot be carried out. Comparison of inferred deflection measurements with theoretical un-misaligned values found that at low loading ($< 200\ kN$), measurements seem to agree well with theoretical estimations. As load increases however, the disparity also gradually increased. It is also interesting that the 2015 data taken before modifications to the rig showed less difference and better agreement, potentially indicating the presence of less misalignment. Despite such complications, the results show that it is possible to utilise ultrasonic measurements for identification of misalignments in bearing contacts.

Investigations into interference fringes at the inlet and outlet roller region allow for better understanding of these fringes with the aim of deducing roller-raceway contact width from either the reflection coefficient or deflection measurements. The fringes and subsequently the width of the dips and peaks of reflection coefficient or deflection measurement were proven to be frequency dependant. Thus, there potentially exist a frequency where deduction of roller-raceway contact width is possible. Theoretical comparison of roller contact width is tricky in this case as the contact is misaligned and thus this investigation was not carried out. Apart from that, a dependence on the ratio of roller-raceway contact width and the sensor width is theorised, which require further investigation.

It is interesting to observe the variation of bearing rotational speed with increasing load and rotational speed and the discrepancies between the Hall Effect sensor measurements to the US inferred rotational speed measurements. In this case, for the VG320 measurements, the desired rotational speed at $60, 80$ and $100\ RPM$ were not achieved as the load increased. This is analogous to bearing operation with an unsuitable lubricant (excessively viscous lubricant) where the torque was insufficient to overcome the viscous forces from the lubricant. In this particular case

however, the latter is true as VG320 mineral oil are a commonly used to lubricate wind turbine gearboxes.

The influence of load, rotational speed lubricant viscosity on the patterns of reflection coefficient between roller passes is also particularly intriguing. The influence of bearing load and rotational speed on the lubricant reflow time is as expected where reflow time decreases with rotational speed but increases with bearing load. The latter only has a small dependence and is less intuitive. As the load increases, the amount of residual film present on the raceway after a roller pass reduces. This in turn increases the lubricant reflow time slightly as more lubricant is necessary to reoccupy the surface to achieve a 0.95 reflection coefficient value. On the other hand, the lubricant reflow time was seen to vary inversely with the increase in lubricant viscosity. As such, the reflow time, as well as the patterns of reflection coefficient between roller passes can be used as a parameter for identification of how well the rollers are lubricated.

6.5 Conclusions

- A NU2244 CRB inner raceway was instrumented with 7 longitudinal and 7 shear ultrasonic sensors. The inner raceway was then assembled into the test rig and measurements were subsequently obtained at various bearing load, speed, and lubricant viscosity.
- Dips and peaks manifest within the ultrasonic reflection coefficient and deflection measurements. These correspond to instances where the roller traverses across the sensor.
- The reflection coefficient decreases with bearing load whilst the deflection measurements increase with loading. No visible trend was observed for the reflection coefficient and deflection measurements with increasing rotational speed.
- Recurring patterns in the reflection coefficient measurements can be utilised to infer the lubrication condition of each roller and subsequently the bearing. Lubricant reflow time was found to be influenced by load, rotational speed, and lubricant viscosity. US measurements suggest that an inverse relationship exists for rotational speed and lubricant viscosity whilst an increase in load increase the reflow time slightly.
- Bearing rotational speed inferred through ultrasonic measurements during bearing operation indicate the inability of the motor to supply sufficient torque to obtain desired bearing speed when higher viscosity lubricant

(VG320) was utilised. This specific case demonstrated the capability of ultrasound to detect instances where unsuitable lubricant is utilised, or insufficient motor torque is present albeit not very applicable in wind turbines as no user desired rotational speed exists. Comparison of cage speed with rotational speed measured from hall effect sensor or encoder would help indicate roller slip and is a subject of further investigation.

- Non-symmetrical deflection measurements were obtained across the roller length, indicating the presence of misalignment. This demonstrates the capability of ultrasonic deflection measurements to detect misalignments in contact within bearings. Comparison of the deflection measurements with theoretical un-misaligned values show good correlation at loads lower than $200\ kN$ but increasing disparity as the bearing load increases.

7 FIELD MEASUREMENTS FROM AN OPERATIONAL WIND TURBINE

This chapter presents a case study demonstrating the capabilities of the ultrasonic load measurement techniques to provide information on bearing condition, from a field operational wind turbine gearbox bearing. The methods utilised in this chapter include techniques for ultrasonic sensor instrumentation (§3.2.4), hardware for pulse generation and receiving (§3.6.2), data processing routines (§3.6.4), acoustoelastic constants measurement (§4.3.3), and equations for conversion of measured ToF change to roller load for 32222 TRB, specified in §5.2.5.

Background information regarding the project is initially explained, followed by the measurements of turbine operating parameters and subsequently measurements and trends observed from the ultrasonic measurements. It is prudent to note that the author is only involved in the data processing and analysis of the acquired measurements and takes no credit in the design, planning (sensor positioning) and installation of the condition monitoring systems within the wind turbine.

7.1 Background

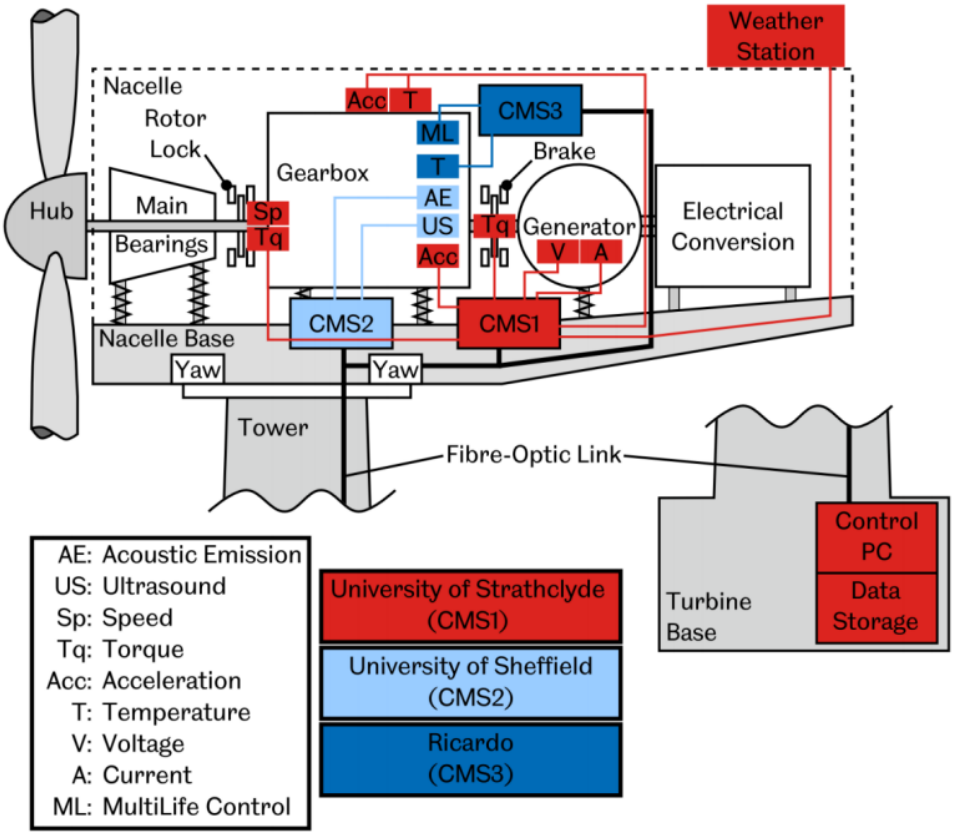

Figure 7.1 – Schematic of sensors instrumented within the WT by all parties [171]

The background information presented in §7.1 and 7.2 aims to brief the reader with information essential for understanding the measurements obtained and discussed in the subsequent sections.

As part of a project, called OWDIn (Offshore Wind Drivetrain Innovation) which was funded by the Department of Energy and Climate Change (DECC) UK, a combined Wind Turbine Condition Monitoring System (CMS) was developed between three collaborative partners, namely The University of Sheffield, University of Strathclyde and Ricardo. Figure 7.1 shows an overview of all the sensors installed and their locations within the WT by all parties.

The University of Strathclyde installed sensors for measuring overall turbine operational parameters (CMS1) such as generator voltage and current, temperature and gearbox torque whilst Ricardo's system would be largely focused on monitoring the performance of their MultiLife actuation system (CMS3), a system designed to improve the life of planetary gearbox bearings. Further information on MultiLife can be found in [171]. On the other hand, the University of Sheffield installed an advanced sensor system for bearing monitoring within the gearbox, utilizing ultrasound (US) and acoustic emission (AE) sensors (CMS2). The author was not involved in the design and installation of CMS2, however gathered and processed data from the system. As ultrasound is the primary focus of this study, subsequent sections will focus predominantly on the design, installation, and data acquisition as well as analysis of the ultrasonic measurements only.

7.1.1 Wind turbine specification

A Vestas V42 (600kW) wind turbine located within the Barnesmore wind farm in Donegal, Ireland was selected to be instrumented. The wind turbine, named 'Barnesmore T2' was chosen due to its exposure to the harshest wind conditions among all the other turbines across the wind farm, and subsequently the highest bearing load whilst also having an increased chance of bearing failure. The wind farm is operated by Scottish Power Renewables.

7.1.2 Gearbox bearing specification

It was initially planned by the personnel involved in the design and installation of the condition monitoring system to have one of the planetary gearbox bearings instrumented with US and AE sensors, however due to the extreme complexity of the instrumentation involved, the idea was abandoned and one of the bearings situated on the High-Speed Shaft (HSS) was retrofitted instead. Figure 7.2 shows a schematic of the bearing configuration for the HSS. At the rotor side, a pair of

tapered roller bearing (TRB) labelled A & B was employed to support the shaft, bearing both axial and radial load whilst at the output end, a cylindrical roller bearing labelled C is used to support only the radial load.

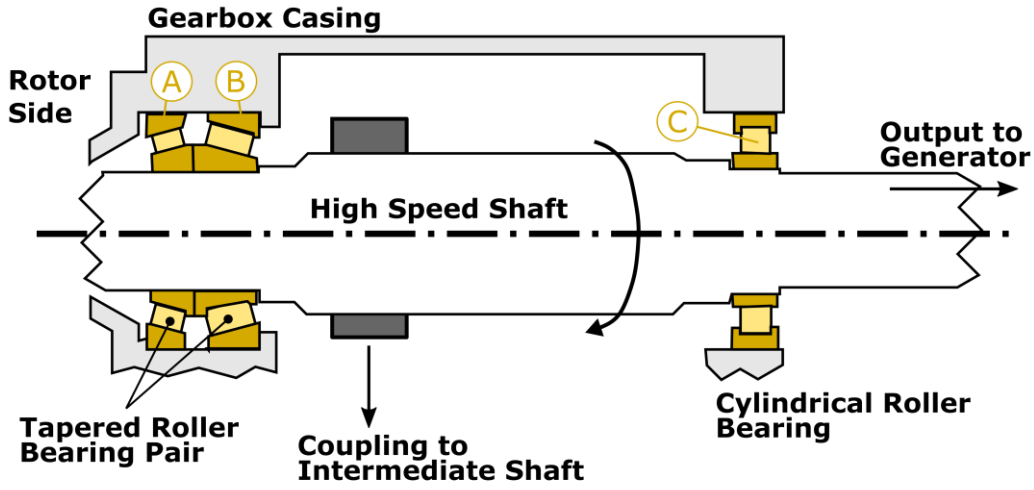

Figure 7.2 – HSS bearing configuration (adapted from [171])

It is desired to instrument the highest loaded TRB bearing on the HSS. To gain an insight on the loading conditions of the gearbox and subsequently the bearings, a multibody analysis was carried out by Ricardo engineers using an in-house multibody software called "SABR". The model was based on the maximum rated torque applied to the gearbox during maximum rated power and maximum rated speed of 600kW and 30RPM respectively. From the modelling results, it was discovered that **Bearing B** would have the highest equivalent radial load ($P = 45.8kN$) between the two TRB bearings within the HSS assembly. The selected bearing was a 32222 Tapered Roller Bearing, with specifications detailed previously in §5.3.1.

7.2 Methodology

7.2.1 Bearing instrumentation

After identifying the bearing to be instrumented, the SABR model was further used to better understand the circumferential load distribution of the TRB. This was to decide on the circumferential location of the bearing at which the ultrasonic sensors would be placed. Figure 7.3(a) illustrates the map of the normalised stress distribution around the circumference of the TRB. Using this information, the position of two ultrasonic sensors were selected, as illustrated with vertical break lines within the figure. The ultrasonic sensors were bonded onto the static outer

raceway of the TRB, specifically at the centre of the maximum loaded zone, 201° from the bearing TDC **(Location 2)** and at 241° from TDC, at the edge of the maximum loaded zone **(Location 1)**. Figure 7.3(b) shows the inferred distribution of internal roller load, Q_φ through the centre of the outer raceway, obtained by taking a horizontal slice across the normalized stress distribution map. This was used to approximate the expected loading at the sensor locations and generate relationships shown in Equation (7.1) for the roller load at sensor locations 1 and 2 (Q_{US1} & Q_{US2}), where Q_{max} is established from using the Palmgren relationship (Equation 5.45) [46], considering that the bearing load, F_r would equal to 45.8 *kN* at gearbox rated power.

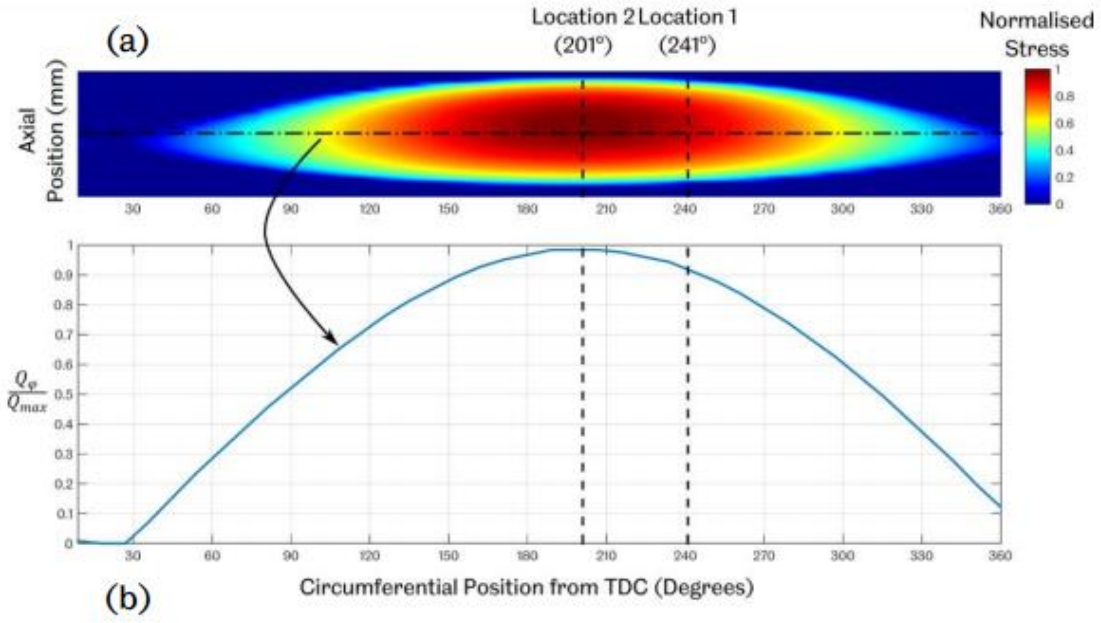

Figure 7.3 – (a) Normalised circumferential stress distribution map around the maximum loaded HSS TRB bearing (Bearing B, Figure 7.2) (b) Normalised circumferential distribution of internal load Q_φ through the centre of the outer raceway, inferred from a cross-section of the stress distribution of map in (a) [171]

$$Q_{US1\ or\ US2} = 0.92Q_{max}\ or\ 0.98Q_{max} \qquad (7.1)$$

Figure 7.4 illustrates the arrangement of the ultrasonic sensors installed onto the bearing outer raceway. The instrumentation process carried out on the bearing outer raceway is similar to those outlined in §3.6.2 and two 10 MHz longitudinal sensors ($5\,mm \times 1\,mm$) were utilised. To accommodate the sensors, a shallow, tapered groove that is parallel with the outer raceway-roller surface was machined along the circumference. This ensures that the sensors can be operated in pulse-echo mode, where the same piezo-element acts as both a transmitter and receiver.

This meant that only a single piezo element is required at each sensor location, thus effectively halving the total number of sensors, and considerably reducing and simplifying the instrumentation process. Platinum RTD thermocouples were also installed directly adjacent to the ultrasonic sensors to give the closest estimation of the temperatures occurring at the contact under the ultrasonic sensors beam path.

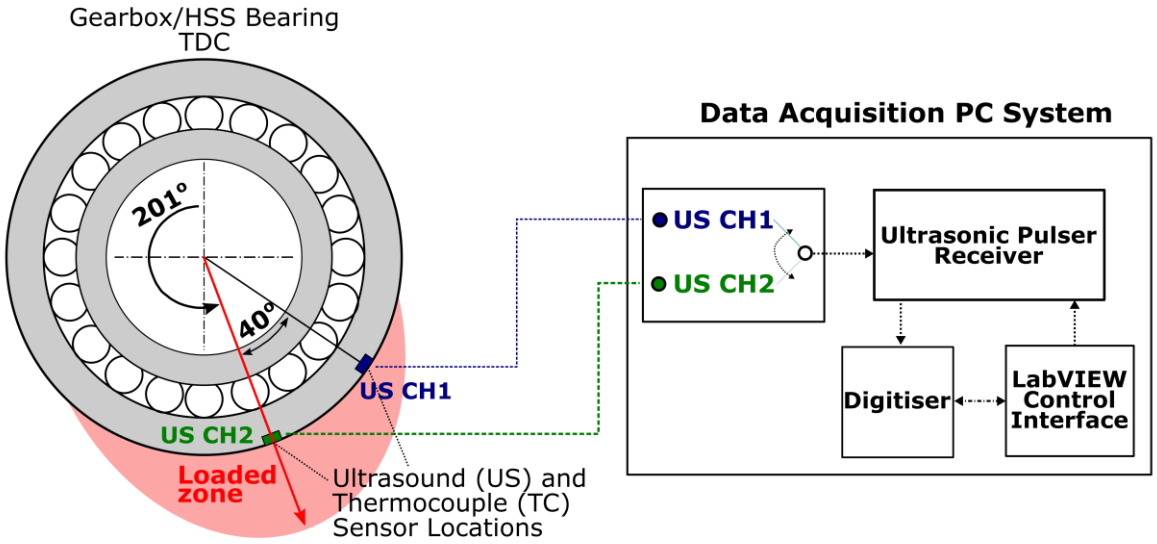

Figure 7.4 – Location of ultrasonic sensors installed on the bearing outer raceway and schematic of the data acquisition system

7.2.2 Hardware acquisition

Due to the high maximum rotational speed of the HSS bearing (1500 *RPM*), a high pulse repetition rate is necessary to ensure adequate data points were captured within the raceway-roller contact region. Therefore, an FMS system is used, which subsequently dictated that the CMS2 system will be PC based.

The minimum footprint of the ultrasonic acquisition system was approximately 500 x 430 x 175 *mm*, based on the outer dimensions of the PC casing. Due to the limited space within the nacelle, the system was installed in a vertical orientation and an outer casing was designed to ensure that the acquisition PC was appropriately protected from the harsh nacelle environment. Figure 7.5 shows the assembled FMS system with its casing.

The PC system is particularly susceptible to vibration, moisture and heat. Consequently, extra measures were taken to avoid or lower the possibility of known issues from occurring. These include:

- Reduction of vibration transmission from the nacelle to the PC through anti-vibration feet.

- Ensuring all the acquisition PCI cards are secured in place and preventing them from disconnecting using an internal bracket, installed across the motherboard.
- Utilizing a solid-state drive instead of conventional hard drives to prevent hard drive malfunction due to vibration.
- Reduction of moisture exposure to the PC using an outer casing
- Louvered air vents to provide air circulation whilst restricting moisture ingress

The sensitive US and AE cables situated on the bottom side of the CMS2 system were protected using jump leads which connects the internal wiring to reliable BNC and BNO connectors.

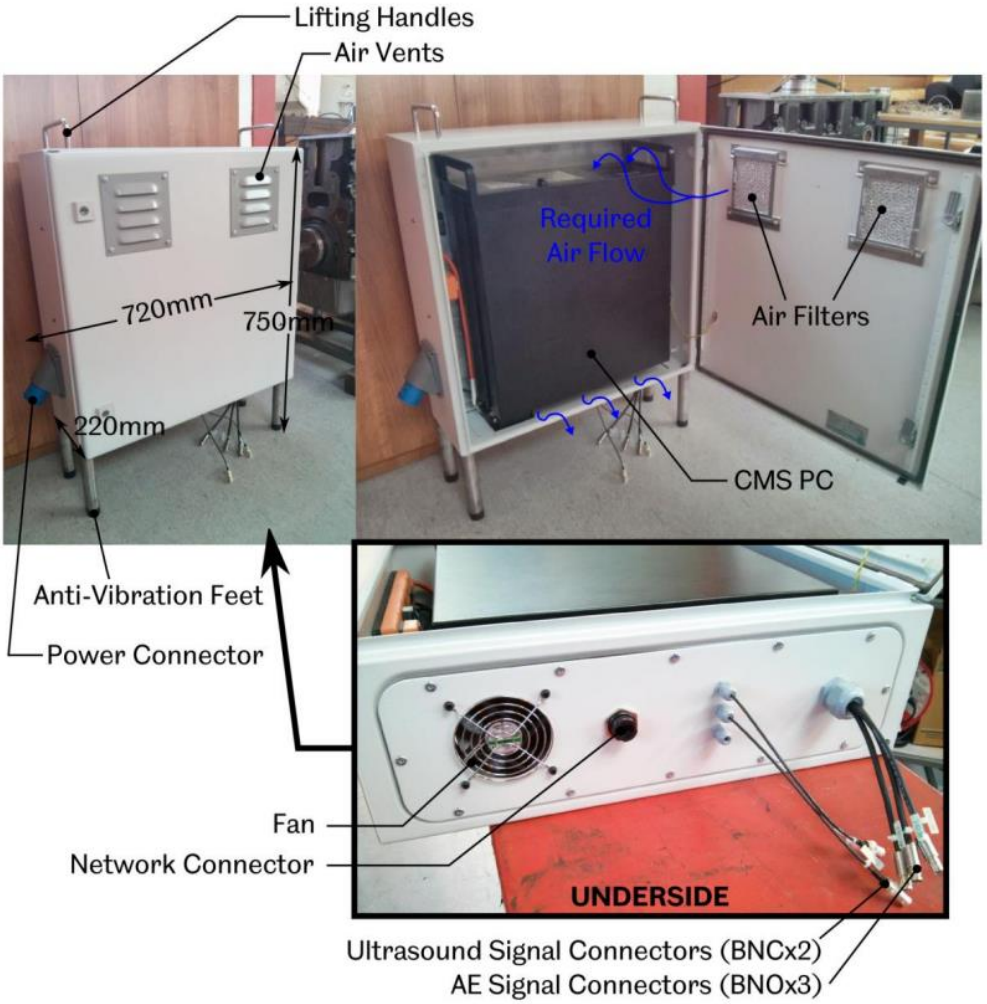

Figure 7.5 – The CMS2 Acquisition PC system [171]

7.2.3 Acquisition software

To allow for minimal human input, the software was written to automatically execute whenever the system is active. Figure 7.6 shows a flow diagram of the general operating sequence of the acquisition PC.

Initially on start-up, the US acquisition PCI cards was activated. The system was then configured based upon settings pre-defined in the configuration file. A list of configurable settings can be found in Figure 7.7. After this, a LabVIEW binary file format (.tdms) was created for the acquisition and storage of US & AE data. The current date and time, and the metadata was then written in the form of a header to the save file to include all the current system settings assigned within the configuration file.

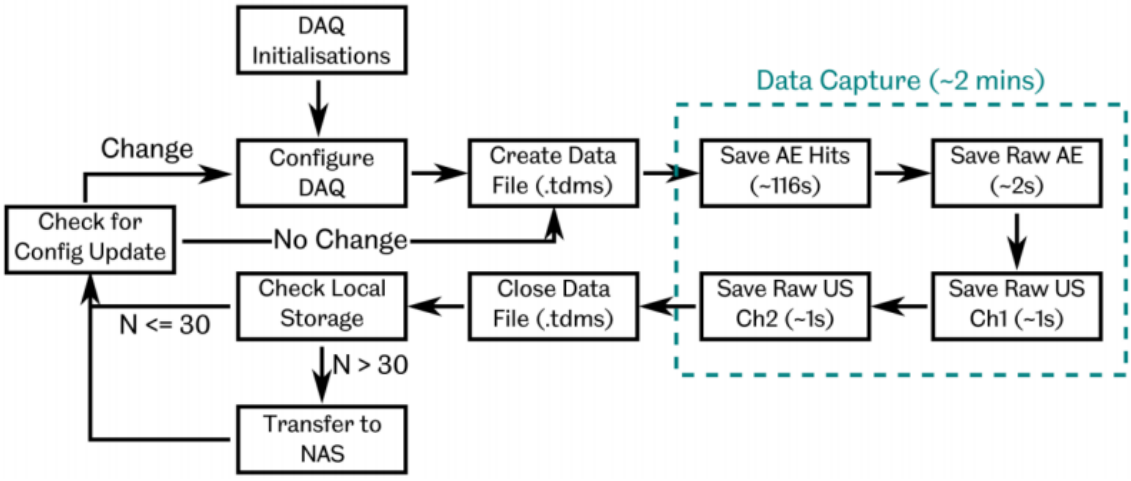

Figure 7.6 – General operating sequence for CMS2 [171]

Ultrasound Settings	Acoustic Emissions Settings	Capture Settings
Excitation Voltage	Full Scale Range	AE raw data capture duration
Pulser Repetition Rate	Hit threshold	AE hit capture duration
Signal Range	Sampling Rate	US raw data capture duration
Gain	DC Offsets	
Pulse Width	Data capture segments	
Delay		
Signal Filters		

Figure 7.7 – Configurable settings in the acquisition software [171]

The system would then enter its data acquisition loop. It was identified that when an excitation voltage was applied to the piezo-elements, considerable levels of noise was observed on AE measurements. As a result, US and AE measurements cannot be captured simultaneously and thus the different capture regimes/sequences within the data acquisition loop.

It was desirable to capture measurements from both US and AE sensors in their raw unprocessed, unfiltered digitised form to retain the most information. However, given the high sampling rates of the US and AE sensors ($100MHz$ and $2MHz$ respectively), there would be issues with the storage size of the data file. Consequently, for US measurements, a capture duration of 1 second for each sensor was employed with a time delay of 20 minutes between each capture instance to minimise data volumes, generating a data file of $50MB$ each instance.

As illustrated in Figure 7.6, ultrasonic measurements on each channel were captured in sequence rather than simultaneously. This was due to the desire of acquiring the data at the highest applicable pulse repetition rate of $80\ kHz$ which was essential due to the high rotational speed of the bearing ($1500\ RPM$) and subsequently the speed at which each rolling element would traverse across the ultrasonic beam path. If measurements were obtained simultaneously, the pulse repetition rate would be halved between the two sensor channels, as a result measurement were captured sequentially instead. This however meant that the two ultrasonic measurement channels were not synchronised and a further detailed look into the measurements revealed issues related to non-optimized pulse repetition rate causing the PC data buffer to fill up and subsequently resulting in data loss. This will be discussed further in the subsequent sections.

The data file will be closed once the data acquisition loop is completed, and the system then checks the total number of files present within the local hard drive. If the number of datafiles exceeded the pre-defined threshold, amounting to approximately 1 hours' worth of data, a data transfer sequence would be initialised where all the local data would be emptied to a $2TB$ NAS drive located at the base of the turbine. In the event where no NAS drive could be detected by the system, data captured by the CMS2 PC will be temporarily stored within a secondary $2TB$ hard drive installed within the PC to free up storage space on the main SSD.

Through altering the relevant values within the system configuration file, the system settings can be altered. The changes are applied prior to re-entering the data acquisition loop, after the system performed local storage checks and data transfer if required.

7.3 Data availability for CMS1 & 2

As reiterated previously, the author is not involved in the design and installation of the condition monitoring system, presented in the previous two sections (§7.1 & 7.2) which was done by past colleagues. The author's work on gathering, processing, and analysing the measurements obtained is presented from this section (§7.3) and onwards.

Figure 7.8 shows an overview of the available TDMS files for the 3 condition monitoring systems. Data processing priority was assigned to datasets which CMS1 & 2 overlap in availability. This was to allow for trend identification of ultrasonic measurements with turbine operating parameters (CMS1). Disparity in data availability between systems is a result of code error in the respective systems and full memory in NAS drive due to prolonged capture. The months which CMS1 & 2 overlap in data availability are June, July, September, and October in 2015 and January for 2016. Due to the vast amount of data present and the limited time available for data processing, it is not possible to process all the available measurements. Consequently, only datasets from June, September and October 2015 were processed to allow correlation of ultrasonic load and reflection coefficient measurements with turbine operating conditions.

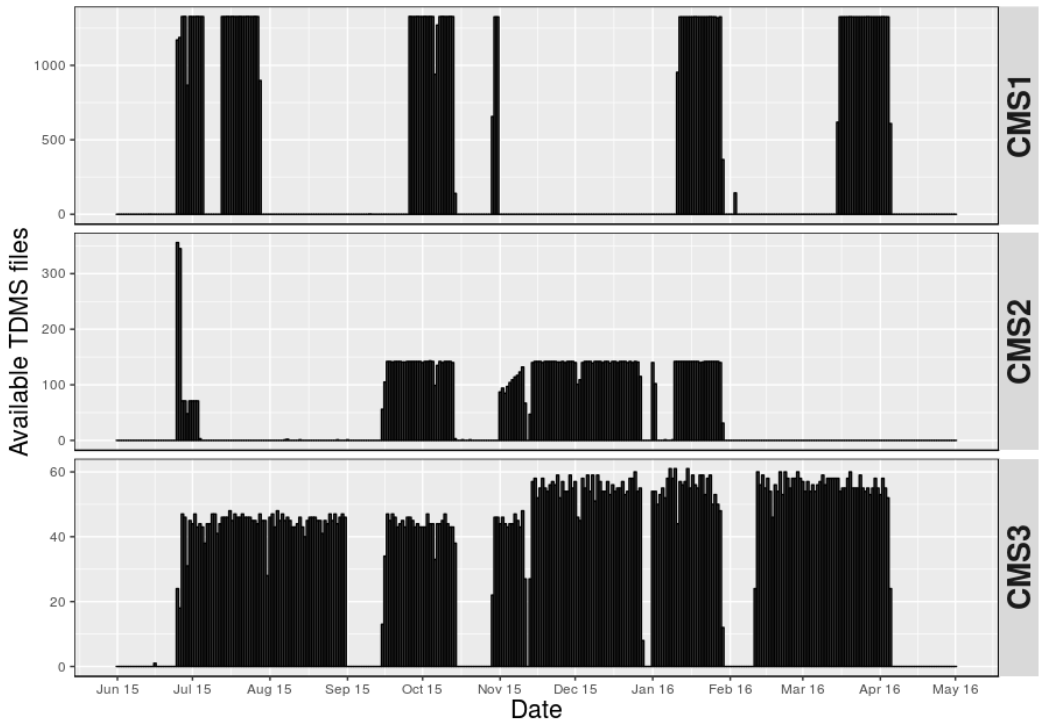

Figure 7.8 – Availability of data for the 3 CMS systems

7.4 CMS1 measurements

CMS1 measurements were captured independently through a system setup and programmed by the University of Strathclyde. The measurements are comprised of data collected from various sensors, all collated into a single tdms file of $20\ MB$. Table 7.1 details all the wind turbine operational parameters captured by CMS1 and the sensing method employed. It was intended for measurements to be captured every minute; however, this was not executed consistently. Each of the 3 phases of generator current and voltage is measured using Rogowski coil-based sensors and voltage sensors respectively. Accelerometers and PT100 resistance thermocouple detectors (RTD) were fitted onto the main bearing, gearbox and generator casings to measure both vibration and temperature fluctuations. A measurement tower fitted on the roof of the nacelle consisting of an anemometer, a wind vane, PT100 RTD, and humidity sensors measured wind speed, wind direction, ambient temperature and humidity. A Hall effect sensor fitted on a bracket measured low speed shaft speed and gearbox reaction torque was measured by two load cells positioned on each side of the gearbox. A pressure sensor also existed which measures hydraulic brake pressure. Generator current, voltage, wind speed and vibration measurements were captured at a higher sampling rate of 10240 samples/s whilst the remaining measurements were captured at 50 samples/s. The capture duration was assigned to 60 seconds. Accelerometer, wind direction and humidity measurements were omitted as they are of the least interest.

Measurement	Sensing method	Data Acquisition
Generator Current	Rogowski coil	NI-9220
Generator Voltage	Voltage sensor	NI-9220
Main bearing, gearbox and generator vibration	Accelerometer	NI-9234
Main bearing, gearbox and generator temperature	PT100 RTD	NI-9217
Wind speed	Anemometer	NI-9401
Wind direction & humidity	Wind vane & humidity sensors	NI-9220
External air temperature	PT100 RTD	NI-9217
Low-speed shaft speed	Hall effect sensor	NI-9401
Gearbox reaction torque	Load cell	NI-9220
Hydraulic brake pressure	Pressure sensor	NI-9220

Table 7.1 – CMS1 Measurement [194]

It was found that the tdms file is broken when saved and the file was required to be repaired to enable access. To repair the CMS1 tdms file, the file was opened and then closed. The sequence of opening and closing the broken tdms file fixes it, however, increases the size of the file by nearly 4-fold. The following section showed data extracted from a single CMS1 dataset (20150626_163522.tdms).

7.4.1 Generator current and voltage

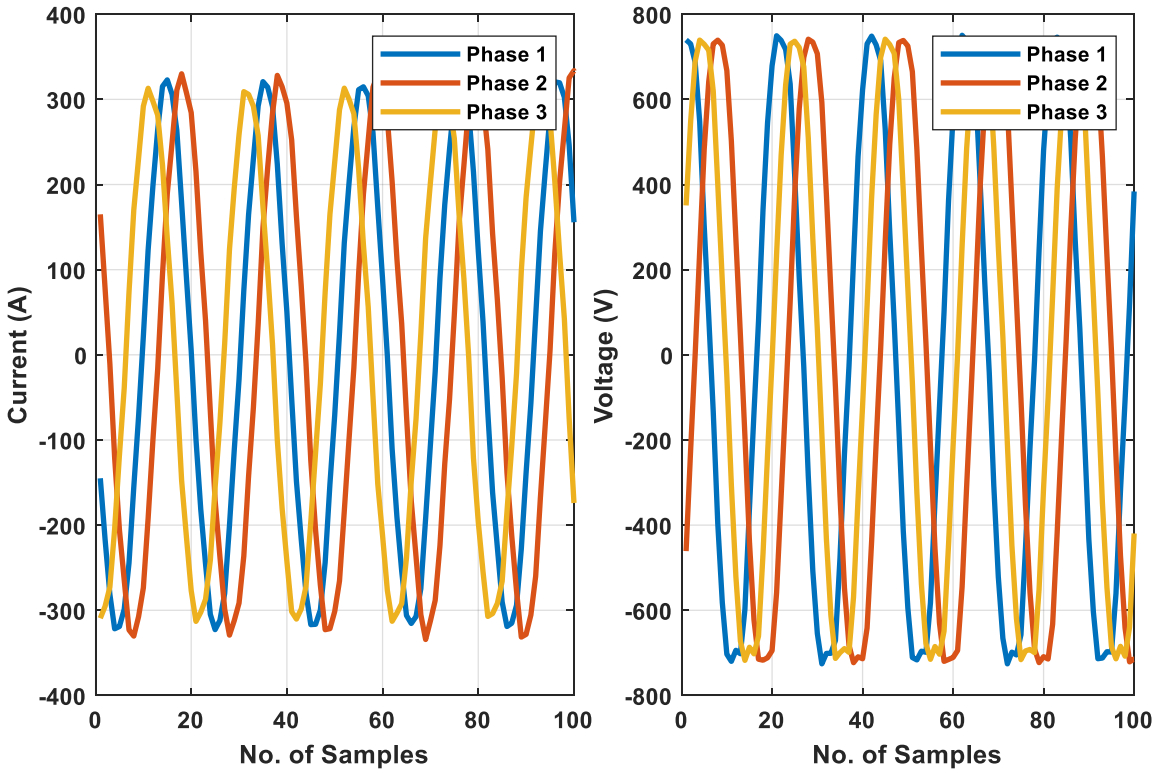

Figure 7.9 – Current and voltage measurements for all 3 phases

Figure 7.9 shows the current and voltage measurements for all 3 phases. The generator is an asynchronous 690V ABB Motors M2CG_400XL_4_B3, 3-phase generator with a current of $567\ A$ and a power factor $(\cos \emptyset)$ of 0.89. These values were derived from the generator's identification plate shown in Figure 7.10

Current measurements for all 3 phases appear normal however, hard clipping of voltage measurements can be seen for the negative-cycle portion. This is a result of incorrect assignment of voltage range across the 16-bit resolution. This results in calculation of turbine power to be inaccurate during instances of clipping, which happen when turbine is operating near to rated power.

The measured voltage and current are alternating values and root mean squared (r.m.s.) values were used when calculating the rated power. Conversion of

measured voltage and current to r.m.s. values was carried out using the equations below.

$$V_{r.m.s.} = 0.7071\tilde{V}_{peak} \quad (7.2)$$

$$I_{r.m.s.} = 0.7071\tilde{I}_{peak} \quad (7.3)$$

Figure 7.10 – Generator identification plate

The power for each phase, P_{phase} was computed using Equation (7.4) where V_p and I_p are voltage and current values for the phase and $cos\emptyset$ is the power factor of the generator, fixed at 0.89. The total power, P_{total} then was computed by summing up the power of all three phases.

$$P_{phase} = V_{p.}I_p cos\emptyset \quad (7.4)$$

$$P_{total} = \sum_{i=1}^{3} P_{phase\ i} = \left(V_p I_p cos\emptyset\right)_{phase\ 1} + \left(V_p I_p cos\emptyset\right)_{phase\ 2} + \left(V_p I_p cos\emptyset\right)_{phase\ 3}$$

$$= \left[\left(V_p I_p\right)_{phase\ 1} + \left(V_p I_p\right)_{phase\ 2} + \left(V_p I_p\right)_{phase\ 3}\right] \times cos\emptyset \quad (7.5)$$

7.4.2 Temperature

Temperature measurements were taken using RTD sensors at 6 different locations, specifically at the main bearing casing, the low-speed (LS) and high-speed (HS) gearbox casing and front and back of the generator and also external air temperature, obtained from a sensor mounted on the bracket alongside the anemometer at the nacelle roof. Figure 7.11 shows the temperature measurements extracted from one dataset, captured at $50\ samples/s$ with a resolution of $0.05\ ^{\circ}C$. It was expected that temperature at the HSS gearbox section would be the highest, following that would be the LSS gearbox section temperature as the rotational speeds differ by a factor of 50. However, this was not the case with the LSS thermocouple measuring $1\ ^{\circ}C$ higher. The second highest would be the generator, followed by the main bearing and finally the external air temperature. For trend identification between US and temperature measurements, only temperature measurements located closest to the HSS bearing will be of interest.

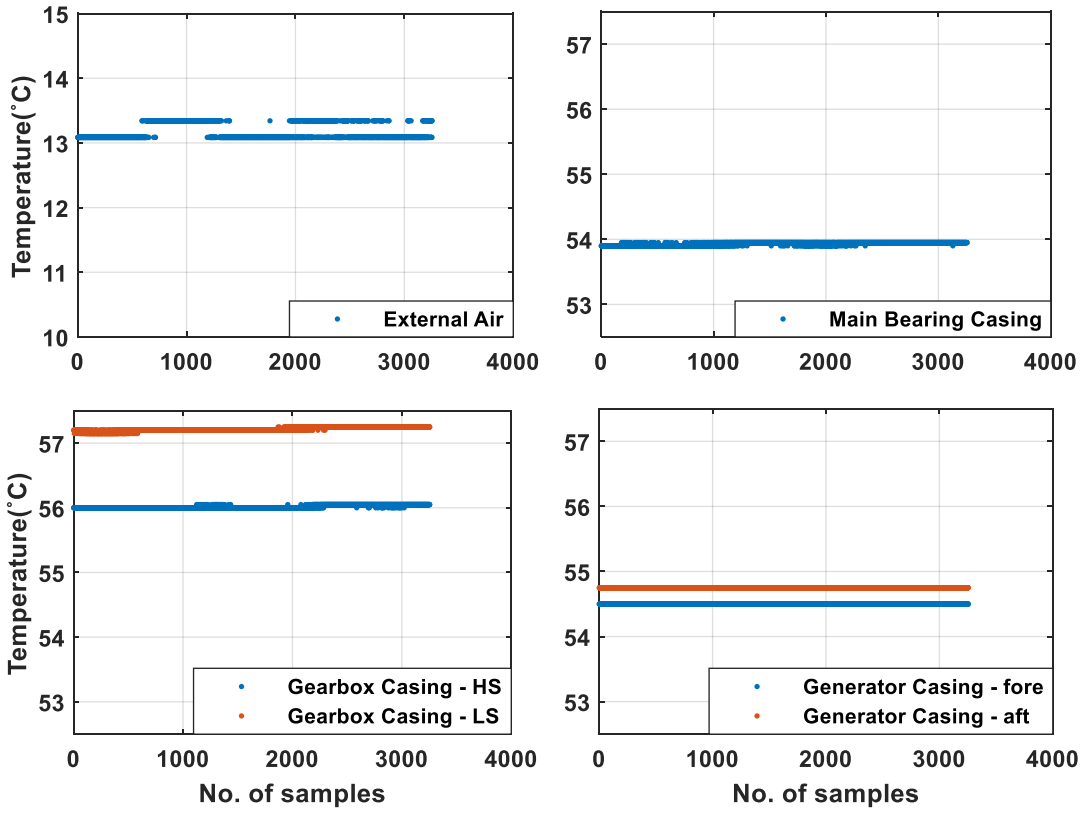

Figure 7.11 – Measurement from RTD sensors

7.4.3 Wind and LSS speed

Wind speed measurements shown in Figure 7.12, were captured through an anemometer fitted on the nacelle roof, at a sampling speed of $10240\ samples/s$ and

resolution of $0.1\ m/s$. Measurements seem to have a range of $8.5 - 13\ m/s$ within the 65 seconds capture window, demonstrating the variability of wind. The resolution of $0.1\ m/s$ was seen to be insufficient to capture the variation of wind speed as the measurements seem to be 'blocky'. It is also prudent to note that the wind speed measurements captured will be different to the wind speed which the turbine experiences as the anemometer was positioned on top of the nacelle and there would be differences between the wind fields at the top of the nacelle and at the wind turbine blade.

The low-speed shaft (LSS) speed measurements plotted alongside the wind speed measurements were obtained from a hall effect sensor at $50\ samples/s$. As the gear ratio between the low-speed and high-speed shaft is known (1:50), the hall effect sensor measurements can be converted to show high-speed shaft speed. From the plot, the maximum LSS speed was found to be around $30\ RPM$, which translates to a maximum HSS speed of $1500\ RPM$.

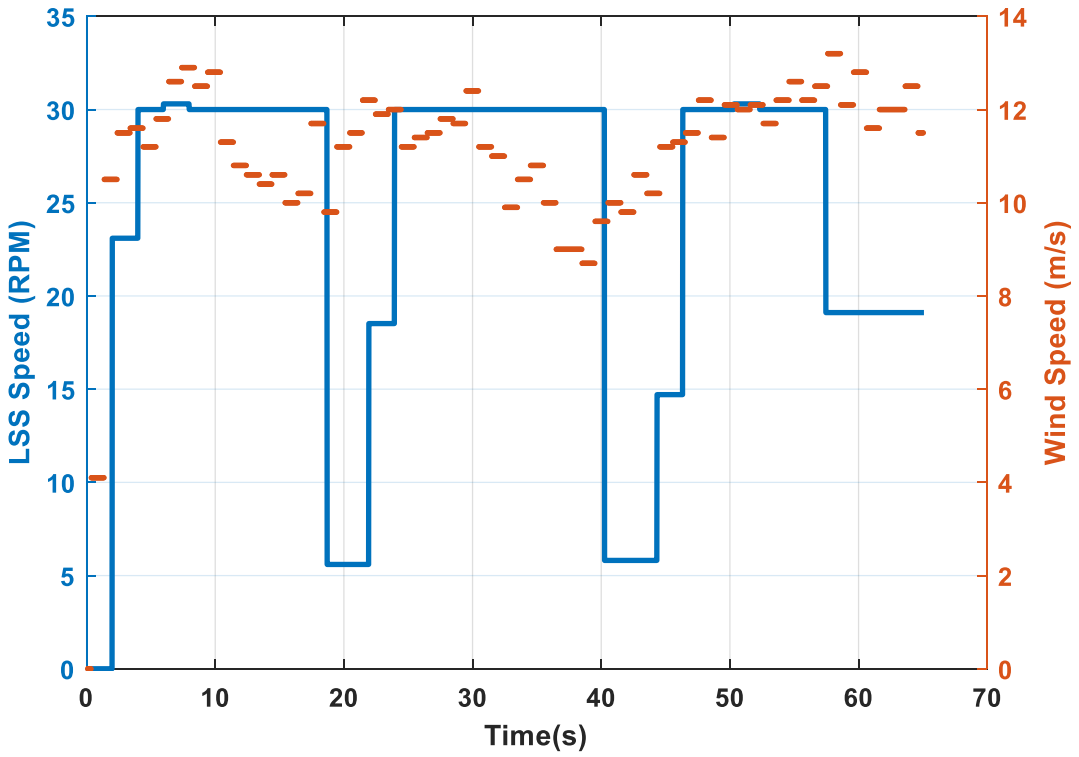

Figure 7.12 – LSS and wind speed measurements within a dataset

7.4.4 Gearbox input torque

Load pins were employed to measure the gearbox input torque. The positions of the load pins are detailed in Figure 7.13. With knowledge of the distance and positions of the load pins, the gearbox input torque can be calculated. However, it was made

known to the author that there is a reaction support which its exact location is unknown, reacting a portion of the input moment. Additionally, there were uncertainties towards whether the load cells were calibrated across their $0 - 10V$ output. Despite this, conversion from voltage to load and subsequently gearbox torque was still carried out for relative comparison.

Ignoring the additional reaction support, the load pin measurements can be used to provide an estimation of the gearbox input torque, T_{in} where *LC1* & *LC2* are measurements from Load Cell 1 and 2 respectively and d_{pin} is $850\ mm$ which is the distance of the load pins from the centre of the gearbox input shaft.

$$T_{in} = (LC1 - LC2) \cdot d_{pin} \tag{7.6}$$

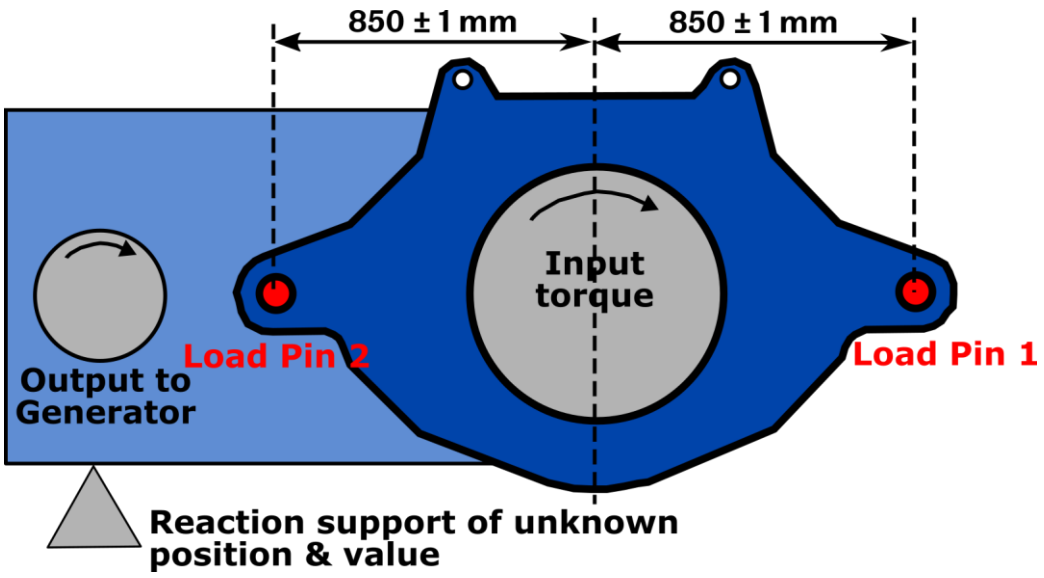

Figure 7.13 – Locations of the load cells on the gearbox

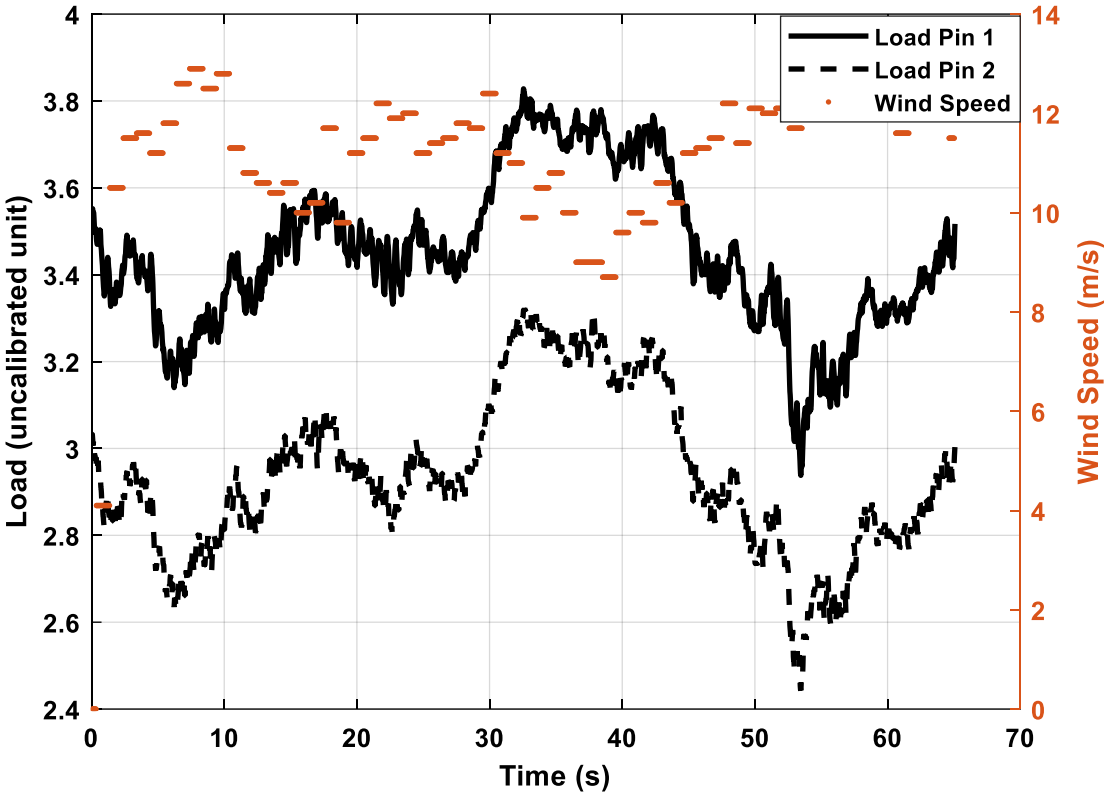

Figure 7.14 – Load pin measurements alongside wind speed

7.4.5 Hydraulic brake pressure

Figure 7.15 shows the variation of hydraulic brake pressure across the measurement period, taken at $50\ samples/s$. Most of the datapoints were concentrated at 0 bar, however some portion within the dataset showed fluctuations of brake pressure from 0 to $120\ bar$. Judging by how the wind speed does not exceed cut-out values, it is puzzling to observe that pressure measurements were fluctuating erratically. More likely this is measurement noise than actual pressure measurement fluctuations as there should be a gradual, steady increase in pressure as observable within Figure 7.16, when the emergency brake is applied. As such brake pressure measurements were deemed unreliable and will not be used in correlation between US measurements.

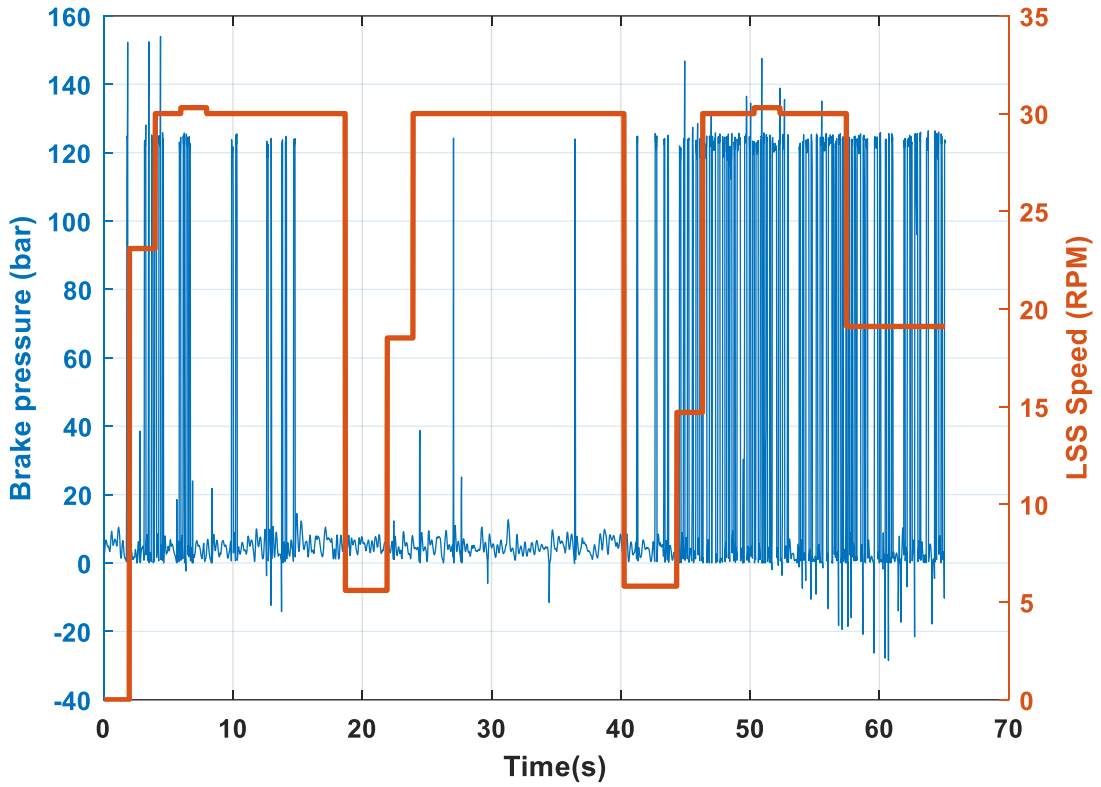

Figure 7.15 – Brake pressure and LSS Speed

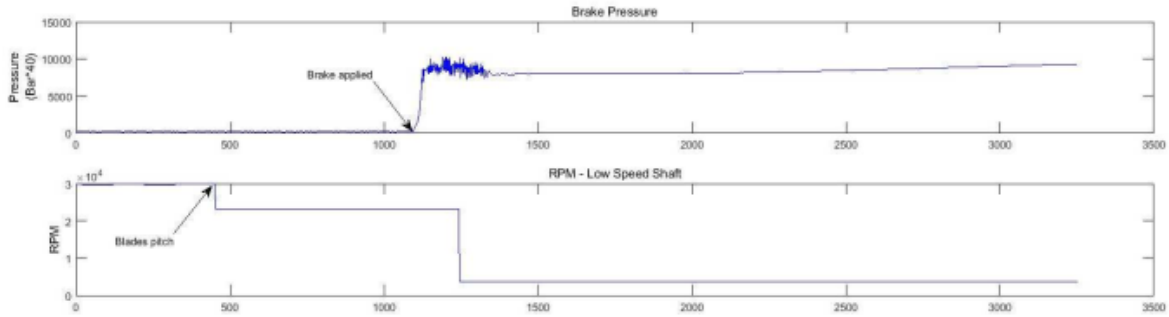

Figure 7.16 – Variation of brake pressure during an emergency stop event [195]

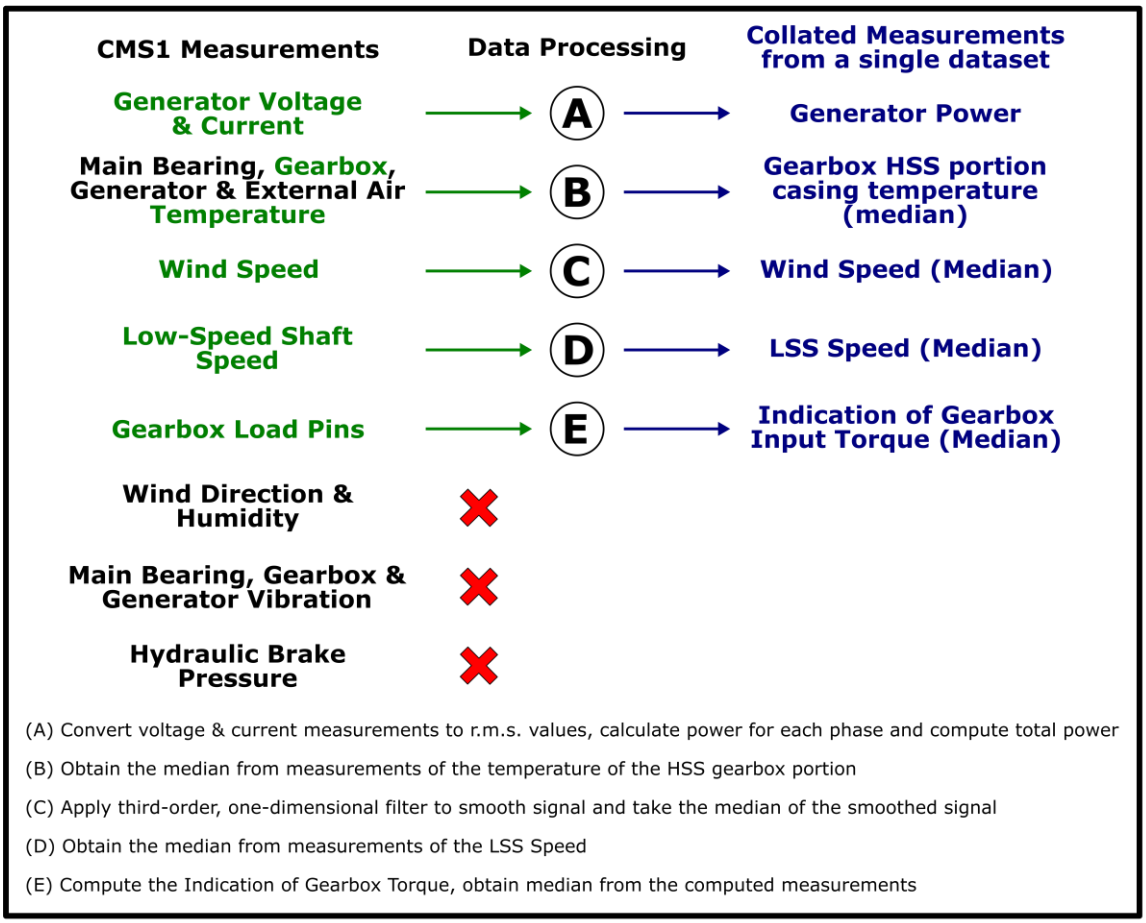

Figure 7.17 – Summary of the data processing routine on CMS1 measurements

Figure 7.17 shows an overview of the data processing routine carried out on each of the CMS1 datasets and the collated measurements from a single dataset using the procedures explained previously. These collated measurements from a single dataset were subsequently gathered and plotted alongside all the other datasets collected within the investigation period (June, September & October 2015). The measurements were then correlated with each other to identify trends within the datasets.

Figure 7.18 shows the variation of CMS1 measurements across June 2015. Trends of wind speed, gearbox input torque and HSS temperature can be identified within the plots with the HSS temperature varying in a lesser extent compared with the wind speed and gearbox input torque. Generator power was seen to be clipping at just below $600\ kW$ and this is most likely due to clipping of the voltage measurements. Measurements of LSS speed however showed intermittently erroneous readings. This was due poor alignment of the hall effect sensor with the holes on the rotor locking disc resulting from mounting issues and turbine vibration [194].

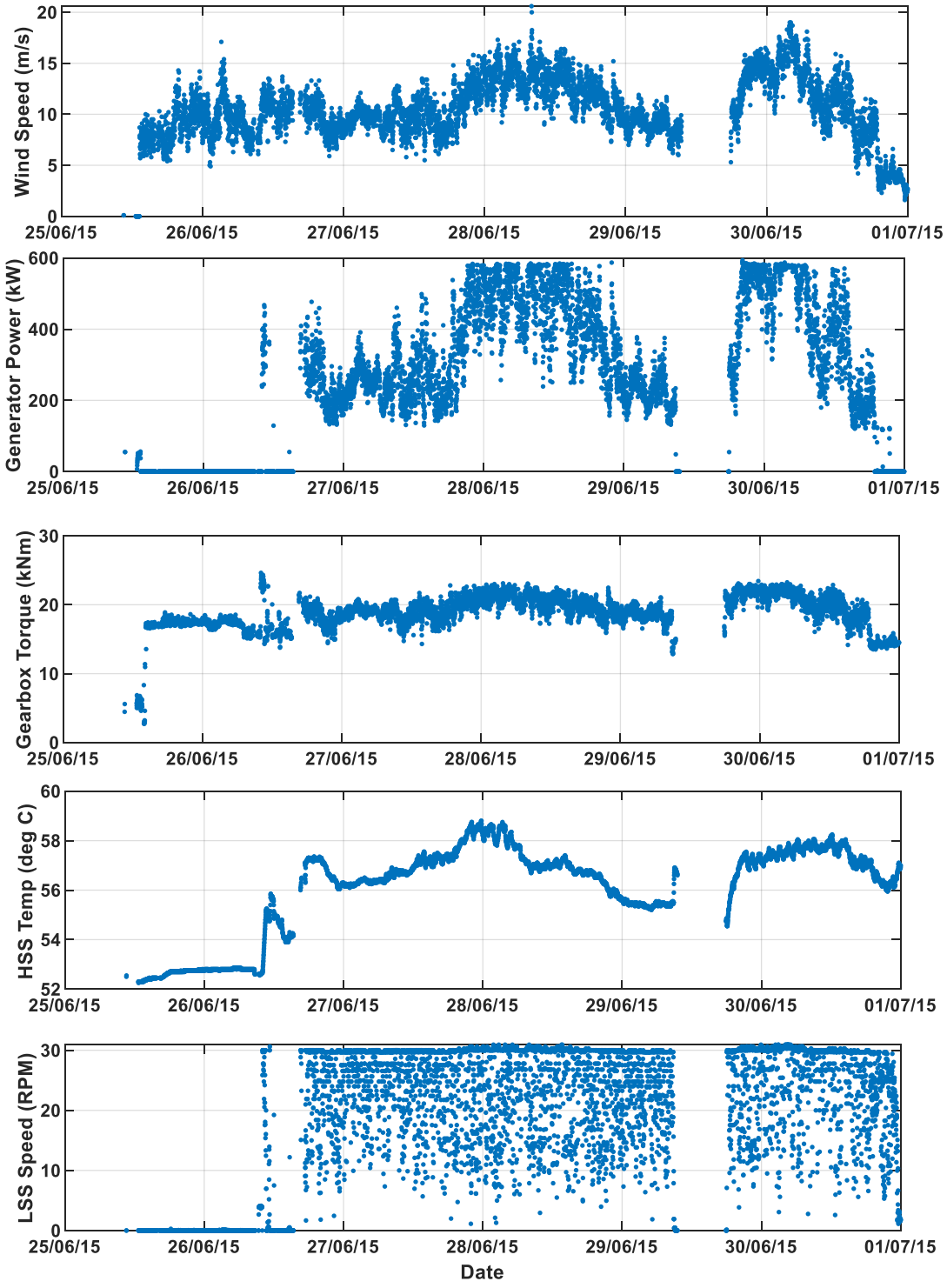

Figure 7.18 – CMS1 measurements for June 2015

7.4.6 Trends between CMS1 measurements

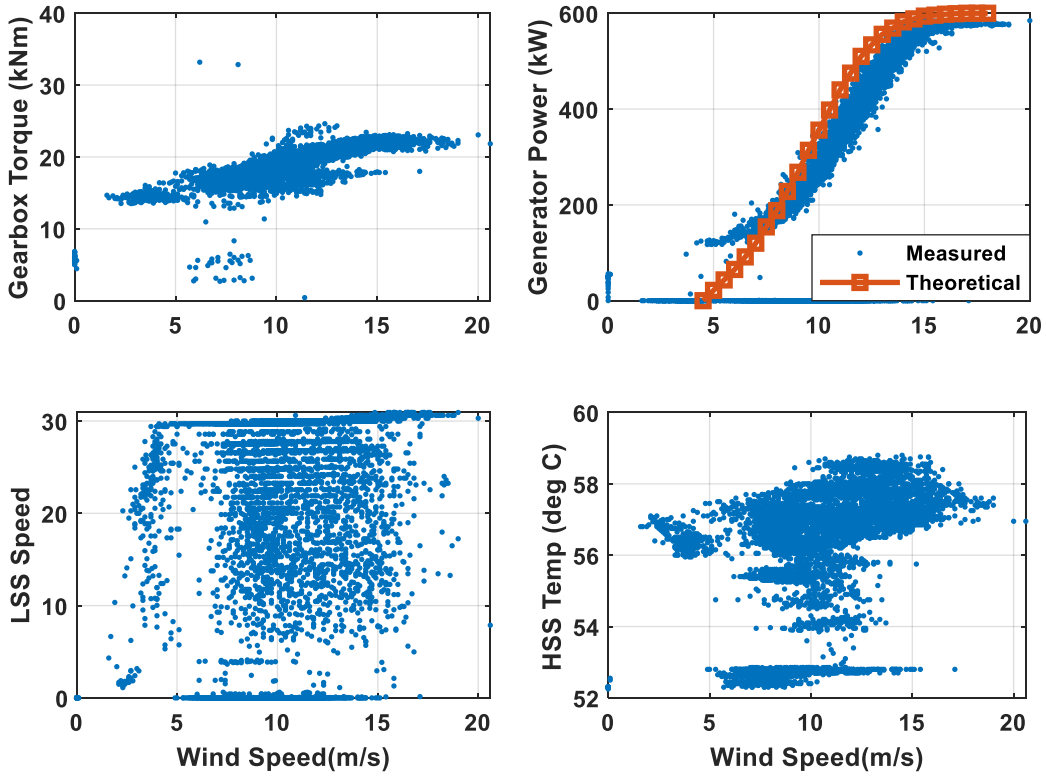

Figure 7.19 – Correlation of wind speed with other turbine operating parameters

Figure 7.19 shows the correlation of wind speed with other turbine operating parameters. The generator power measured was also compared with its theoretical values obtained from [38]. No sensible trend can be identified for the plot against the LSS speed and HSS temperature, the former resulted from erroneous measurements. Gearbox input torque was seen increasing in a linear pattern with wind speed as expected whilst the common S-curve was observed for the correlation against generator power. The measured S-curve was seen to be offset to the right of the theoretical turbine curve and starts at $100\ kW$ as opposed to 0 for the theoretical power curve. Typically, measured turbine curve would be offset to the left of the theoretical power curve. This is because the wind speed measured is behind the rotor, thus measurement is marginally less compared to the wind speed the rotor experiences. However, in this case, the plot indicates that the wind speed measured is more than that of what the rotor experiences. The offset is potentially resulted from power being supplied by the grid into the generator to start turbine operation. Upon initiation, the turbine rotor speed increases from 0 up to rated speed.

7.5 CMS2 measurements

Having explored the turbine operating parameters obtainable from a single dataset of CMS1, the subsequent section delves into the ultrasonic measurements obtained from the CMS2 system.

7.5.1 Ultrasonic measurements – single dataset analysis

General Data Analysis

In this section, a single dataset was selected and processed in detail to extract as much information out of one dataset as possible. The dataset selected was CMS2_20150626_163526.tdms, one of the earliest data captured by the acquisition PC, thus rendering it free from any acquisition hardware and sensor degradation. In some sections, only measurements from CH1 were shown to avoid repetition of similar features across the two channels.

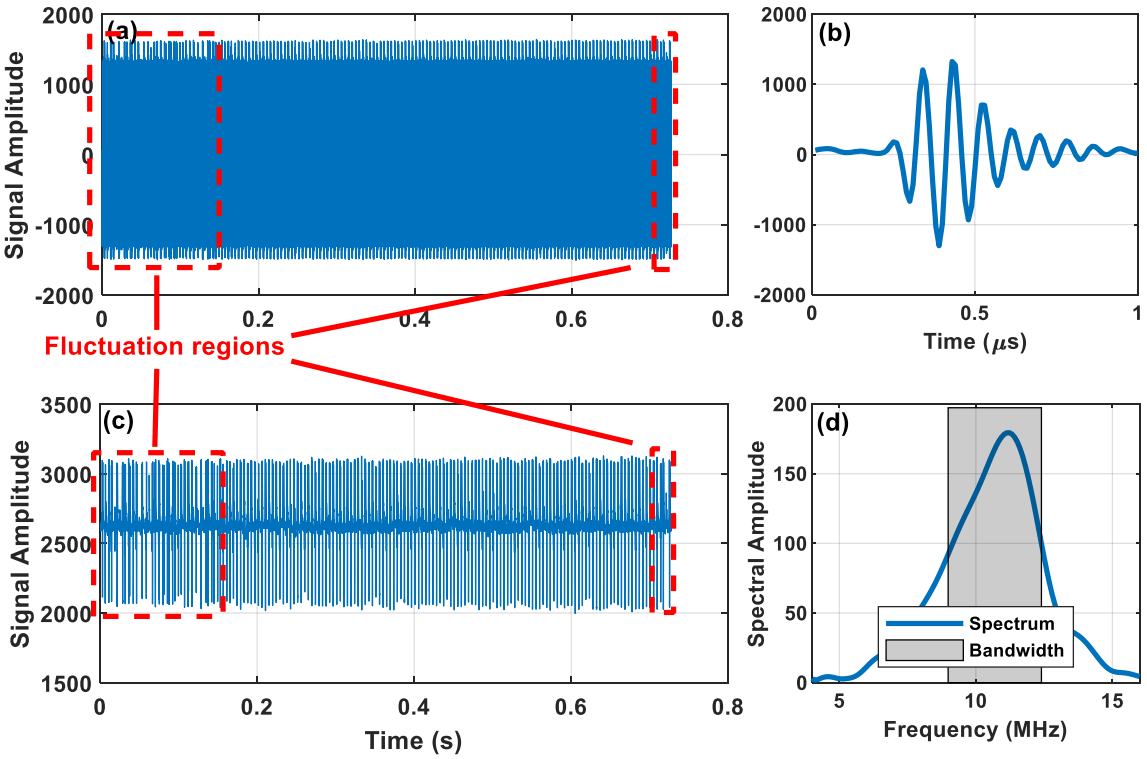

Figure 7.20 – Ultrasonic measurements from CH1: (a) Raw ultrasonic data stream (b) Reference pulse (c) Peak-to-peak amplitude (d) Frequency domain of reference pulse

Figure 7.20 shows various features of the ultrasound data obtained from the sensor positioned at the edge of the maximum loaded region (CH1). Figure 7.20(a) shows the raw ultrasonic data stream obtained from CH1 which consists of an assembly of

captured pulses, plotted along their captured time, whilst Figure 7.20(c) shows the peak-to-peak amplitude of the raw ultrasonic data stream. Figure 7.20(b) shows the reference pulse of the sensor in time domain whilst Figure 7.20(d) shows the response in frequency domain.

An initial look at the raw ultrasonic data stream and the peak-to-peak plot indicate some variability in the distances between the energy dips within the first $0.15\ s$ and also towards the end of the capture window. These two windows are termed fluctuation regions. The energy dips again correspond to each roller pass as more ultrasonic energy is lost when there is contact between the rolling element and raceway. Outside of the fluctuation region, the distances between the energy dips or roller passes remain roughly constant, indicating constant bearing speed and constant separation distance between the rollers within the bearing. The fluctuation region might be initially mistaken as regions of unstable bearing rotation, however upon investigations in other datasets, it was discovered that the fluctuation regions were consistently present within the same capture period (the first 0.15 s and towards the tail end of the dataset) and occasionally outside of these. This was subsequently discovered to be as a result of hardware limitations of the FMS. Even though the FMS can pulse at a maximum pulse repetition rate of $80\ kHz$, the processing speed of the PC might not be able to cope with the sudden influx of data. When data is captured, it is temporarily stored within the buffer. The PC then empties the buffer and stores the captured data in the file. Pulsing at high PRR overloads the buffer's storage capacity. As additional data is streamed into the PC, there is insufficient storage space in the buffer and thus these data are lost. There is thus an optimum PRR which it is high enough to not incur aliasing issues in the measurements whilst also allowing the PC to cope with the data influx. Another convincing evidence which solidifies this claim would be that the total captured data time, around $0.73\ s$ in this case, is always less than the pre-defined one second capture time.

The reference pulse waveform, as expected, exhibit a smooth bell-shaped curve, indicating that it is well damped, whilst its frequency spectrum shows a central frequency of $11.23\ MHz$ with a bandwidth $(-6\ dB)$ between $8.98 - 12.40\ MHz$.

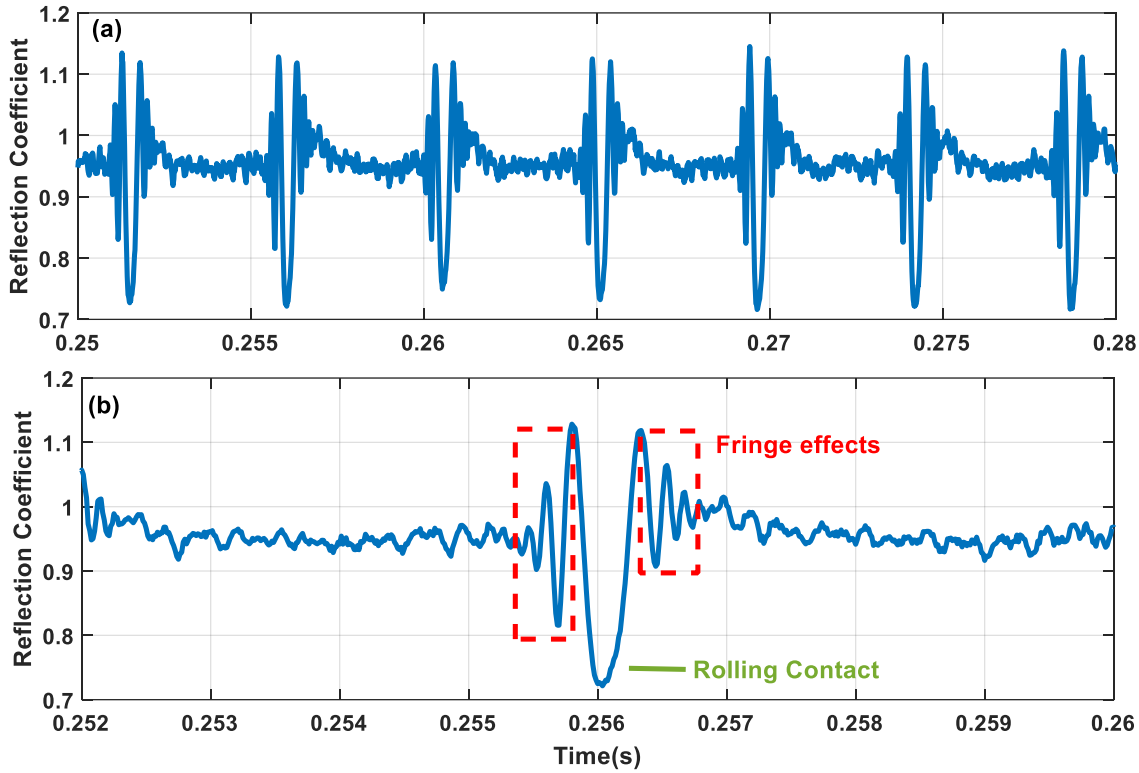

Figure 7.21 – Reflection coefficient measurements for: (a) 7 successive roller passes (b) a single roller pass

Figure 7.21(a) shows part of the reflection coefficient plot obtained at the central frequency ($11.23\,MHz$) of the ultrasonic transducer. Seven dips in reflection coefficient measurements are visible, with each corresponds to a roller pass and the minimum reflection coefficient per roller pass would be around 0.72, with each roller distinctly having different minimum reflection coefficient values.

Figure 7.21(b) focuses onto an individual roller pass, analysing the shape and distinct features of a roller pass. The reflection coefficient was seen to reduce to a minimum which corresponds to the peak contact pressure as opposed to the "W-shaped" profile seen in §6.3.1 The subsequent pressure peak corresponding to the constriction of oil film was also not observed in the measurements. This may be attributed to aliasing effect as very few data points (~3 points) exist within the roller pass region, however this was disproven in the subsequent section.

A more plausible explanation would again be due to an averaging effect of the ultrasonic response as the sensor beam path is much larger than the raceway-roller contact dimensions. The interference fringes were again observed at either side of the rolling contact as a result of divergence of ultrasonic energy through the bearing raceway.

Lubrication patterns between roller passes, as observed in §6.3.7 was also evident in the dataset. At the rolling contact entry region, the reflection coefficient remained at 0.95 before the fringe region. After the roller pass, the reflection coefficient initially at unity, gradually decrease back to 0.95. This indicates that the raceway is swept clean of oil briefly after the roller pass despite being flooded. The lubricant subsequently flows back to the raceway surface thereafter which causes the reflection coefficient to decrease and plateaus around 0.95. This will be discussed in detail in the subsequent sections.

Variability in bearing rotational speed, individual roller ultrasonic measurements can be further investigated through superimposing the reflection coefficient curve. Figure 7.22(a) shows the superimposed reflection coefficient plots for the first two revolutions. Measurements shown are for a full bearing complement, consisting of 20 rollers. Attempt was taken to match the roller pass of each revolution however to no avail, as can be seen in Figure 7.22(b) and (c). There are periods within the dataset of the 1st and 2nd revolution which matches; however, majority of the roller passes do not match up. This is due to fluctuations in measurement resulted from hardware limitations due to buffer overload as explained previously on page 183.

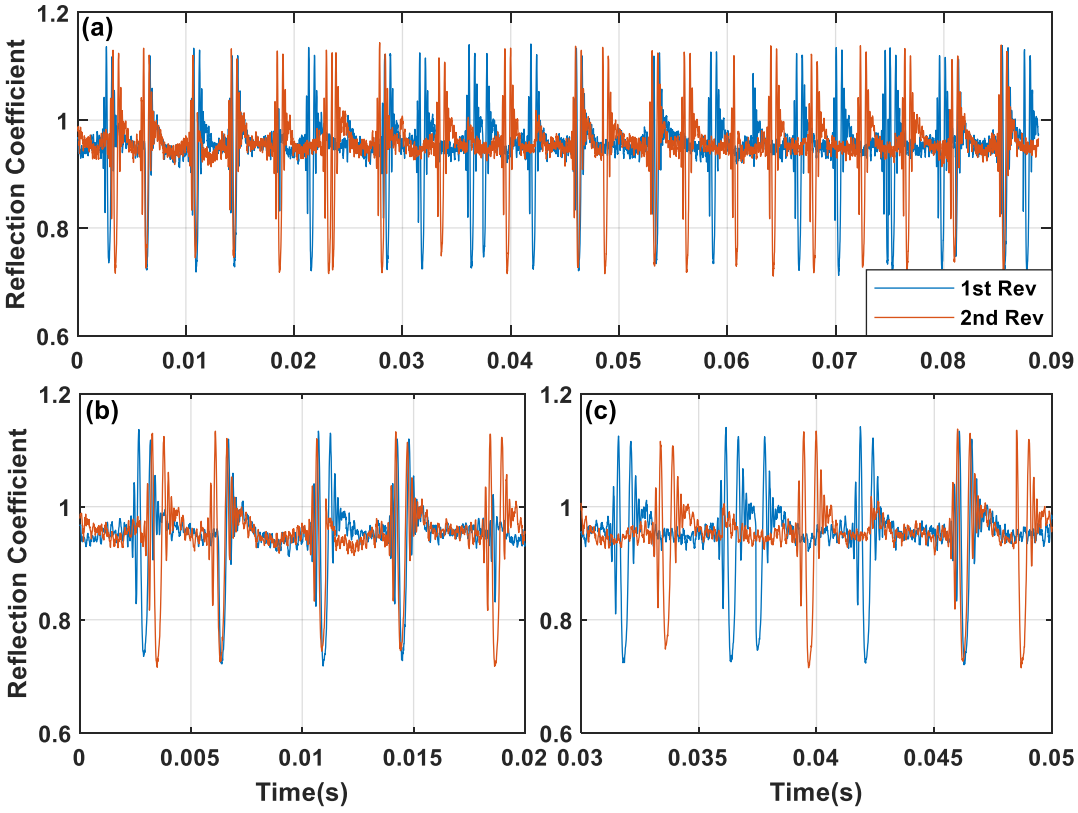

Figure 7.22 – (a) Superimposed reflection coefficient measurements (1st and 2nd revolution) (b) Matching portion and (c) Non-matching portion within the plot

If measurements from the first two revolutions were omitted as shown in Figure 7.23, it can be seen that near perfect match can be obtained, demonstrating constant bearing speed and consistent ultrasonic acquisition performance within the stabilised data capture period.

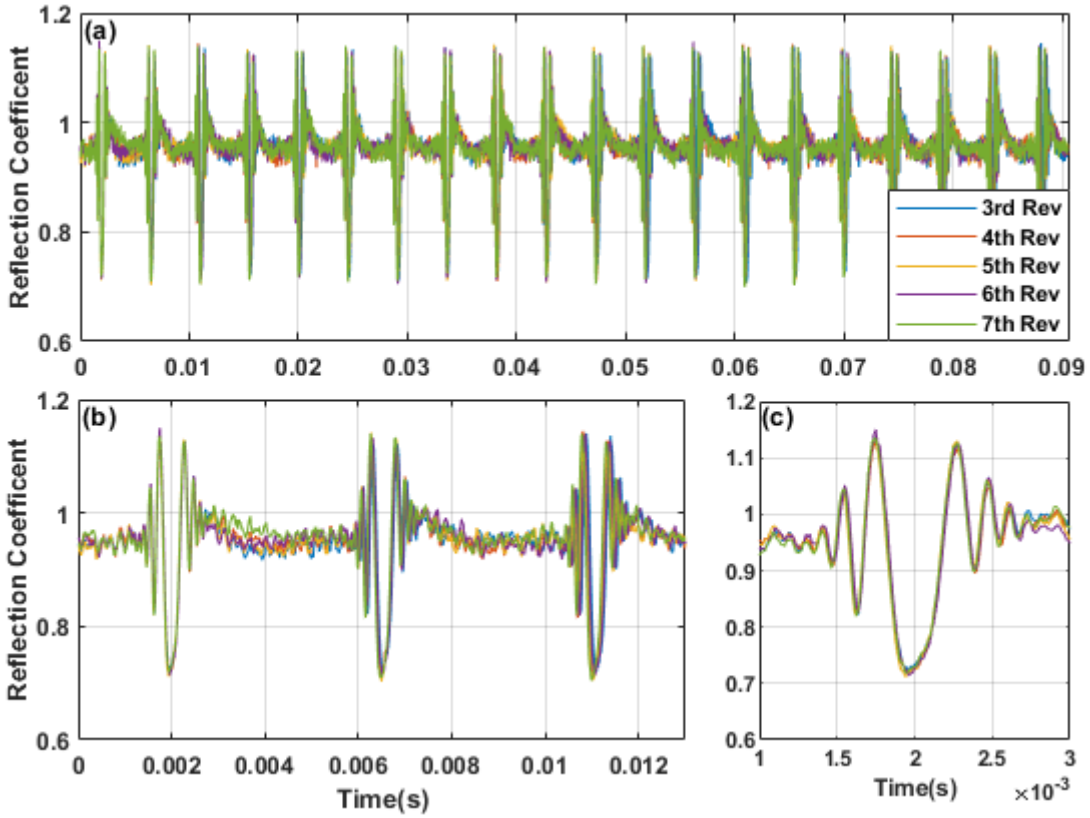

Figure 7.23 – (a) Superimposed reflection coefficient plot (3rd – 7th revolution) (b) First three recorded roller passes (c) First recorded roller pass

The "profile" or "width" of energy dips for each individual roller pass for each revolution was found to be very similar and consistent, however the minimum reflection coefficient for the same roller does vary slightly with revolution as can be seen in Figure 7.24(b) for the first roller. There are also slight differences in each of the roller's minimum reflection coefficient across the bearing complement, indicating load experienced on each roller is slightly different, such phenomenon also observed in §6.3.1.

This is again unusual as they should experience similar loading since the rollers are of same dimensions, unless the load within the bearing changes slightly between successive roller passes ($\sim 5\ ms$). An alternative explanation for this would be that there is misalignment of the rolling elements or differences in clearance between the rolling elements.

Although near perfect match in reflection coefficient dips was obtained for the third to seventh recorded revolutions, complete match would require manual tweaking of the reflection coefficient curves for each revolution. This indicates that the rotational speed of the bearing is not perfectly constant as per actual operation, with the maximum lag or lead of a rolling contact curve found to be 20 pulses or $0.25\ ms$. This coincides with the width of the peak within the power spectral density (PSD) of the reflection coefficient curve shown in §3.6.4.

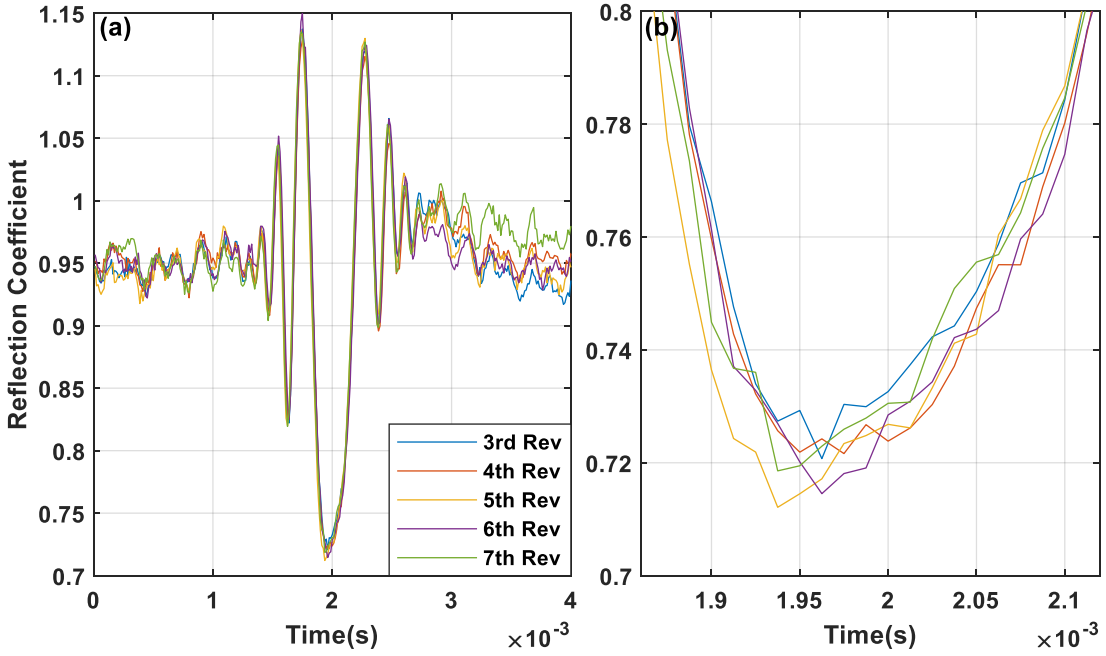

Figure 7.24 – (a) Superimposed reflection coefficient for the first recorded roller (3rd to 7th revolution) (b) Magnified view of the reflection coefficient dip

Attempt was taken again to convert the reflection coefficient measurements to lubricant film thickness using the spring model. Since the lubricant viscosity used is the same as the previous chapter, previously made assumptions for film thickness calculations were also applied in this case.

Figure 7.25 shows the spectral amplitude, the reflection coefficient spectra and the lubricant film thickness for CH1. The reflection coefficient spectrum was computed at the sensor's central frequency of $11.23\ MHz$. For each frequency, an average value of the minimum reflection coefficient for each roller pass was computed. From Figure 7.25(d), the reflection coefficient values slowly reduced within the bandwidth of the ultrasonic sensor. The reflection coefficient at transducer central frequency was found to be 0.73 which corresponds to a film thickness of $1.02\ \mu m$, indicating that the bearing is operating within the elasto-hydrodynamic regime.

The reducing slope in the lubricant film thickness plot of Figure 7.25(f) was observed to be much steeper compared to the reflection coefficient plot. As a result of the dependency of R with frequency, the lubricant film thickness measurements are again invalid. This is again caused by the beam width of the ultrasound being bigger than the contact width of the raceway-rolling element interface.

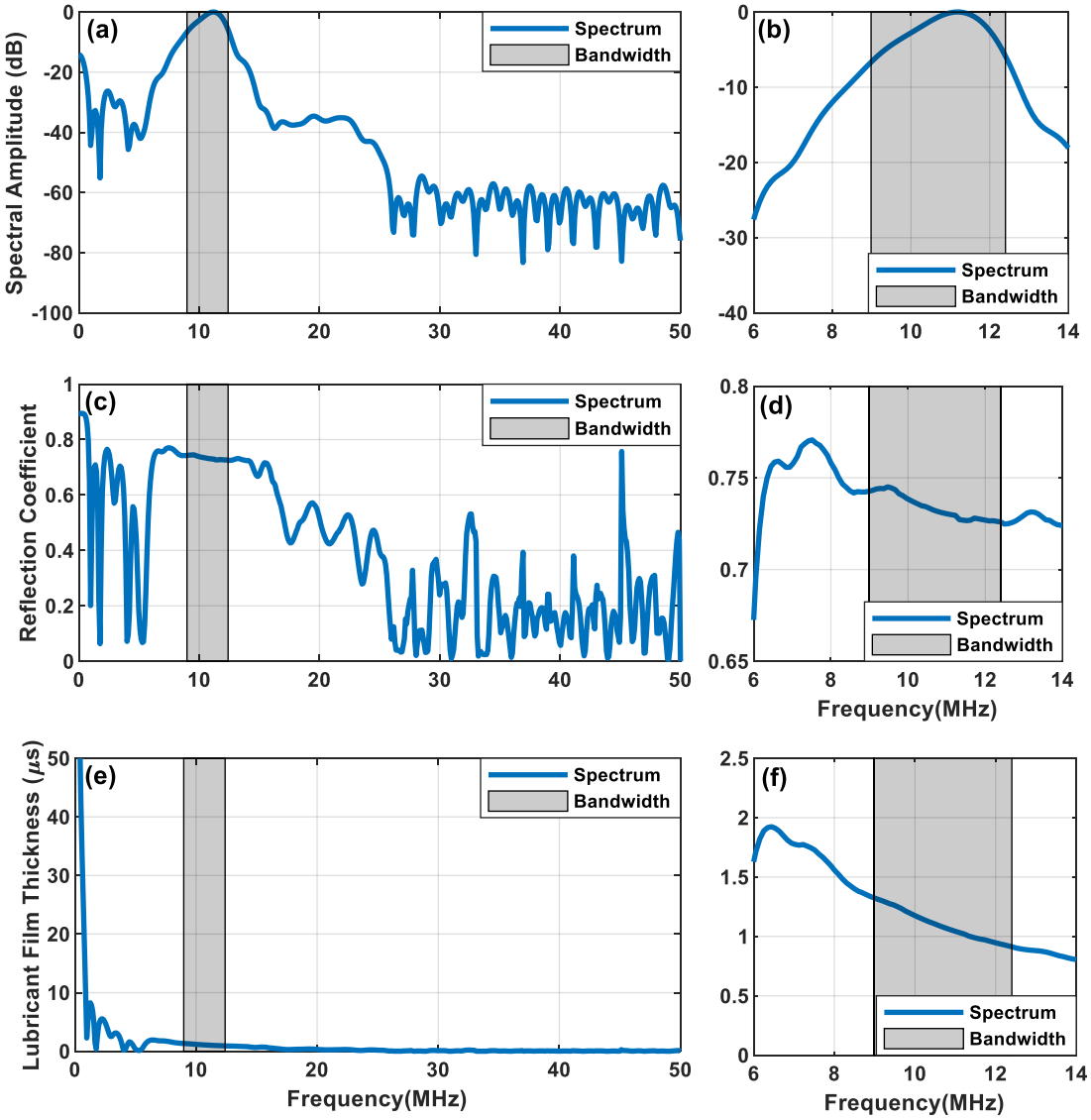

Figure 7.25 - (a) Spectral amplitude of the reflection coefficient (b) a magnified view of the spectral amplitude bandwidth region (c) reflection coefficient spectrum (d) a magnified view of the reflection coefficient spectral bandwidth region (e) lubricant film thickness (f) a magnified view of the lubricant film thickness bandwidth region

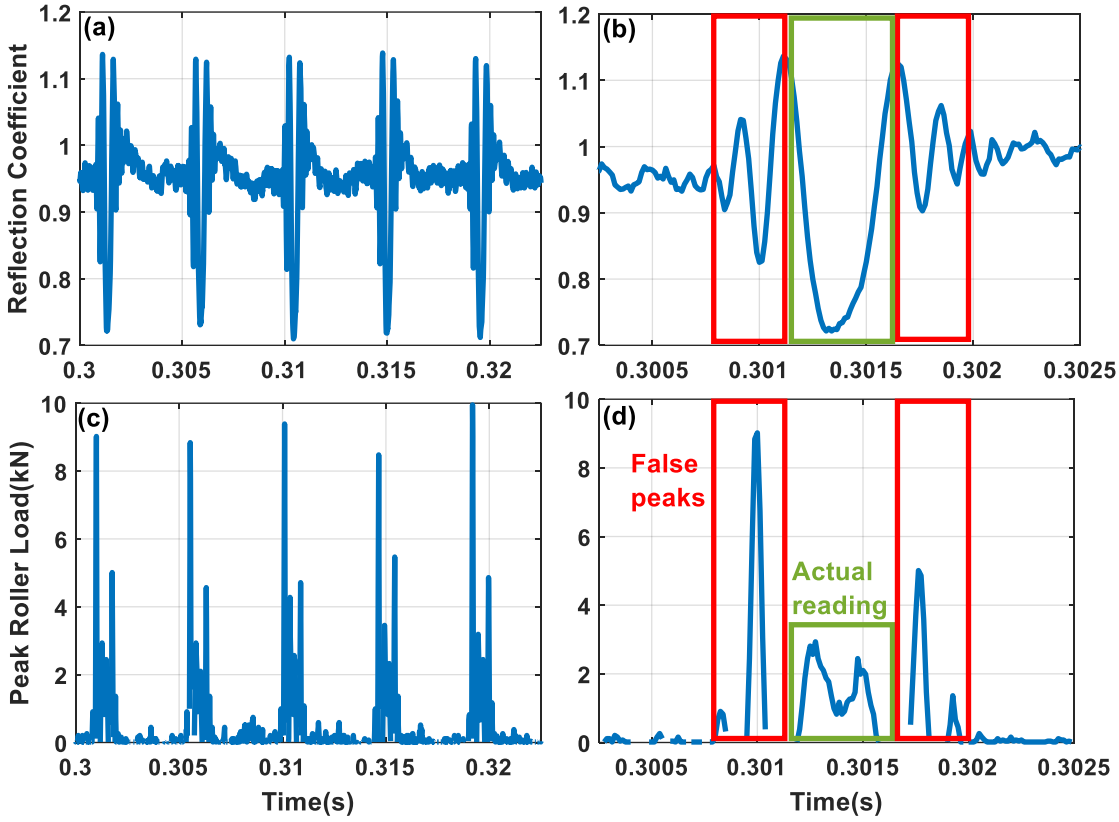

Figure 7.26 – Reflection coefficient measurements showing (a) 5 consecutive roller passes and (b) one single roller and peak roller load measurements showing (c) 5 consecutive roller passes and (d) one single roller from CH1 sensor

Figure 7.26 shows the reflection coefficient and peak roller load measurements obtained from CH1. Looking solely on Figure 7.26(c), the peak roller load might be mistaken to be around $8 - 10\ kN$. This was however not the case as shown in Figure 7.26(d). It was expected that the minimum reflection coefficient for each roller to be corresponding to the maximum measured load, however the maximum load measured corresponds to the contact fringes. This is usually not an issue if the load on the bearing is sufficiently high ($> 300\ kN$ for measurements shown in §6), however due to the low loading the bearing experiences, the false peaks have a significantly higher value compared to the actual contact measurements. The actual roller contact load measured again resembles a "M-shape" where the load increases to a maximum before reducing to a minimum at the centre of the contact and then gradually increases thereafter. These features were also observed from the measurements presented in §6.3.1 and is theorised to be resulted from the constructive and destructive interference due to reverberations from the incoming and outgoing rollers, also explained in §6.3.1. Through application of the filtering algorithm developed in §6.3.3, false ToF measurements as a result of fringe effect

were successfully filtered. Figure 7.27 shows the filtered peak roller load measurements for a full rotation consisting of 20 rollers.

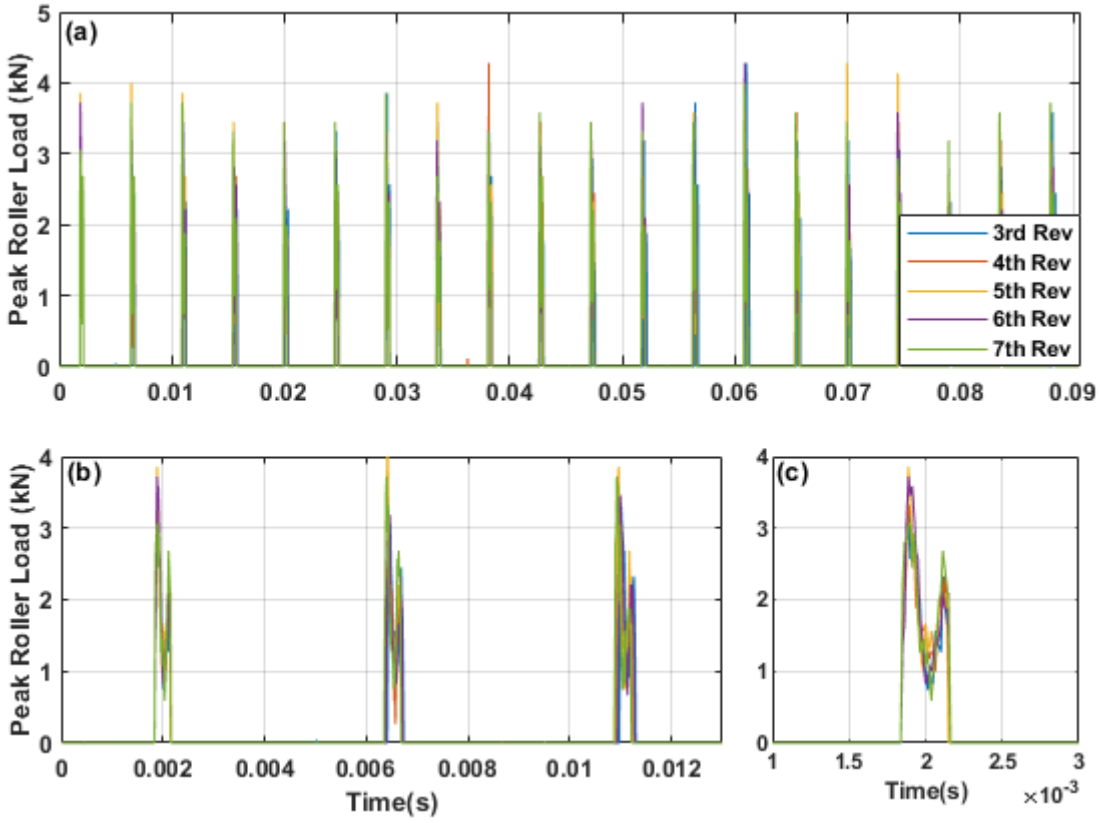

Figure 7.27 - (a) Superimposed Peak Roller Load plot (3rd – 7th revolution) (b) First three recorded roller passes (c) First recorded roller pass from CH1 sensor

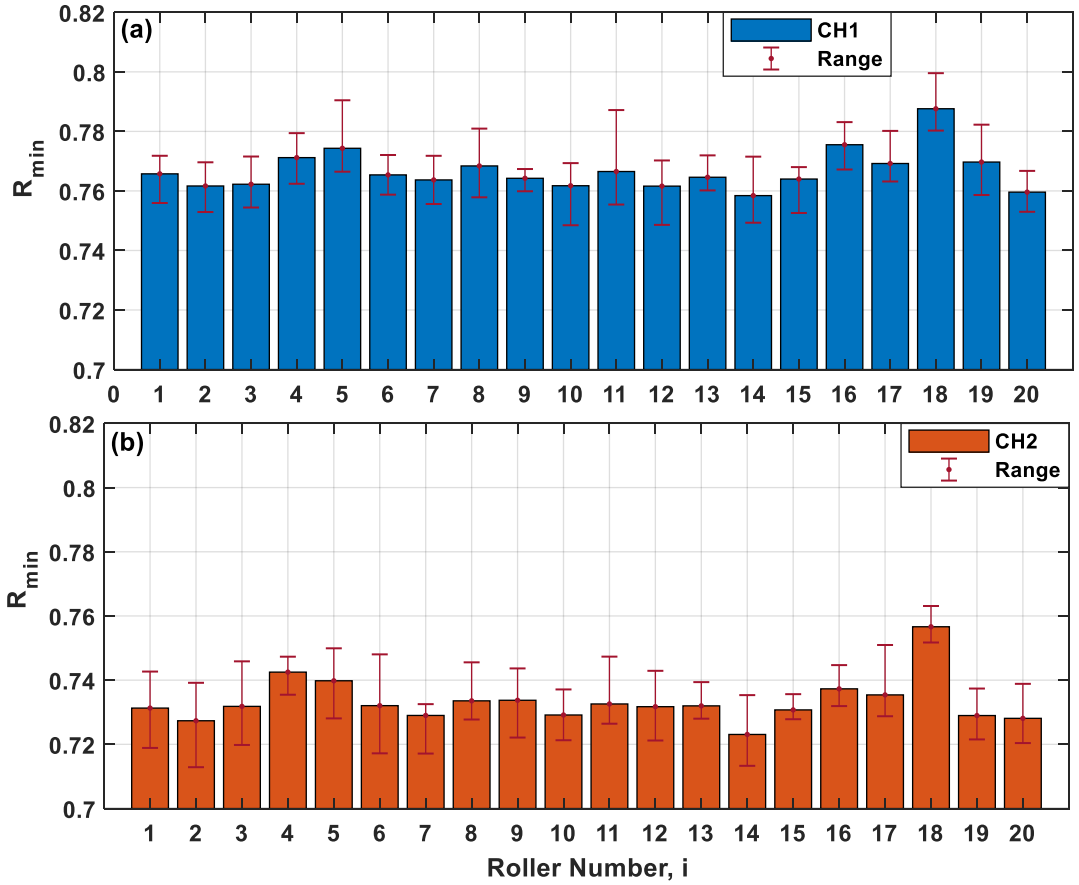

Figure 7.28 – Average minimum reflection coefficient values of each roller for (a) sensor located at the edge (CH1) and (b) centre of the maximum loaded region (CH2)

Figure 7.28 illustrates the minimum reflection coefficient values averaged across each rotation for all 20 rollers, captured from both sensor channels. The range (maximum and minimum values) for each roller were represented through the error bars. Each individual roller had at least 5 measurements since the bearing completes 5 full revolutions within the 1 second acquisition period. The range measurement was further discussed in the following sections.

Recurring patterns, ie. increasing and decreasing trends of individual roller measurements across the two sensor channels can also be seen within the bar plots. This is particularly evident for Roller 18 (i=18) which had the highest R_{min} values for both sensor channels. These patterns, analogous to Caesar cipher, were subsequently used to align or synchronise measurements between the two sensor channels, as the measurements taken lack information on the rollers' angular position.

Reflection coefficient measurements from CH1, as expected, are higher, with an average of 0.767 compared to 0.733 of CH2. This is because CH1 experiences less loading and subsequently is expected to have a thicker oil film and smaller contact.

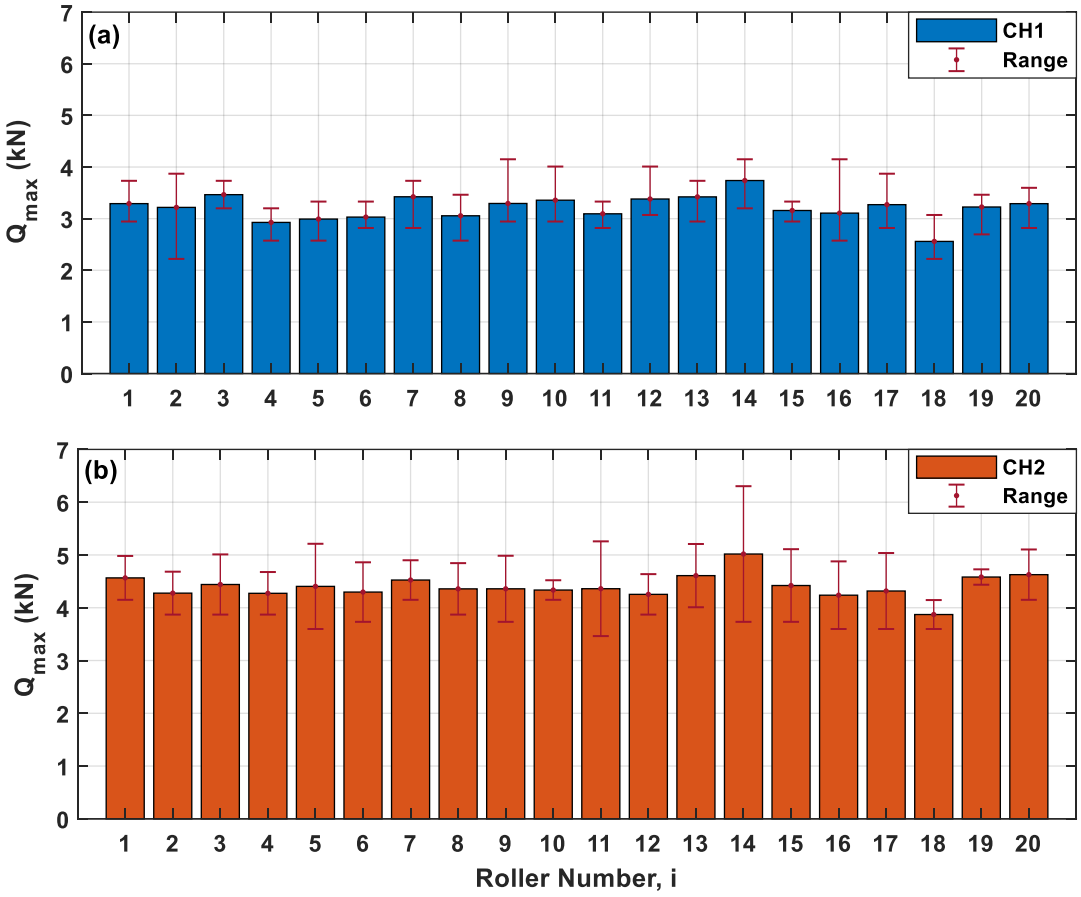

Figure 7.29 – Average maximum roller load measurements of each roller for (a) sensor positioned at the edge (CH1) and (b) centre of the maximum loaded region (CH2)

Figure 7.29 illustrates the peak roller load, Q_{max} measurements averaged across each rotation for all 20 rollers, computed through Equation (5.45) alongside its range for both sensor channels. Again, data from a full bearing complement were shown within the plot, corresponding to 20 rolling elements. Measurements from the sensor positioned directly within the maximum loaded region (CH2) are evidently higher with an average of $4.406\ kN$ across the complement, compared to that of $3.215\ kN$ (CH1). This varied by 39% (CH1) and 17% (CH2) compared with the theoretical roller load computed through multi-body SABR modelling [171] (5.30 kN for CH1 and 5.64 kN for CH2). Despite suffering from more variation (higher range values) within the load measurements, recurring patterns analogous to that observed within Figure 7.28 are still seen. Expected trends between the R_{min} and

Q_{max} measurements for each roller are also apparent. As an example, Roller 18 registered the lowest Q_{max} for both channels and had the highest R_{min} values across the complement.

Figure 7.30(a) and (b) shows the range measurements of R_{min} and Q_{max} which were gathered and converted into boxplots. For each sensor channel, two range data were compared, the range for individual roller, i and the range for a full bearing complement data (cycle), n. The range for individual roller, i consists of 20 range values for rollers 1 to 20 whilst the range for the cycle, n consist of 5 range values for full bearing revolution 1 to 5.

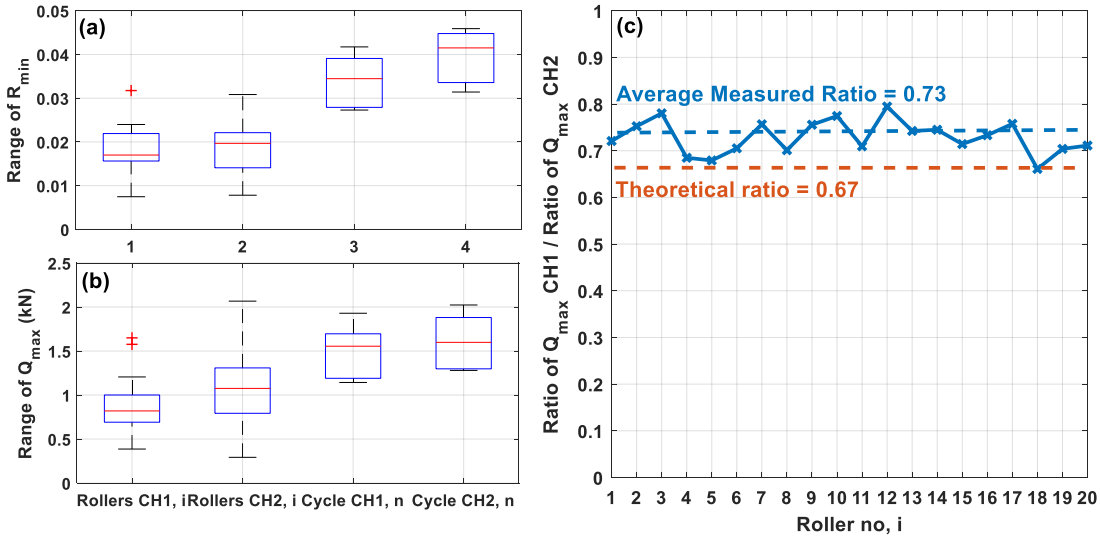

Figure 7.30 – Variation of (a) minimum reflection coefficient and (b) peak roller load and (c) ratio of peak roller load of CH1 against CH2

The reflection coefficient measurements for a single individual roller across 5 cycles ($n = 1$ to 5), i.e. Measurement of roller 18 ($i = 18$) for rotational data, $n = 1$ to 5, do not vary significantly, with an average range of recorded values (max-min values) of around 0.018 for both sensor channels. Measurements across a full bearing rotation, i.e. $n = 1$ comparing the measurement of roller $i = 1$ up to $i = 20$, however show a higher range value of 0.034 (CH1) and 0.039 (CH2). These measurements indicate that there seem to be small variation in measurements for the same roller within a compliment but a higher variability in measurements obtained from each roller across a cycle within a complement for both channels.

The average range of load measured for the individual rollers ($i = 1$ to 20) was discovered to be 0.88 kN (CH1) and 1.08 kN (CH2) whilst the average range of load measured across cycles (n=1 to 5) was at 1.51 kN (CH1) and 1.60 kN (CH2). The result again indicate that there is less variation in the load carried by the same roller

within a full bearing complement compared to measurements from each roller across a full bearing complement, ie. Measurements for roller 18 ($i = 18$) across 5 cycles ($n = 1$ to 5) does not vary as much as measurements across roller 1 to 20 ($i = 1$ to 20) across a cycle ($n = 1$ or $n = 2$ and so on). The variation in measured load on an individual roller is potentially a result of the lack of concentricity between the rotating parts and also differences in micro geometries of roller profiles resulting in differences in load sustained by each roller. This is further supported by the fact that the variation of Q_{max} across the complement (the peak and trough across $i = 1$ to 20 for a cycle $n = 1, 2, 3..$) matches up across CH1 and 2 after aligning the two channels, indicating that the same roller passing through CH1 resulting in a peak measurement is also registering a peak measurement as it passes through CH2.

Since there exist two ultrasonic sensors placed along the circumference of the bearing, information on the circumferential load distribution can be obtained partially (partial as there is only two datapoints across the circumference). Figure 7.30(c) shows the ratio of peak roller load of CH1 & 2. The theoretical ratio was computed using Equation (7.7) where φ is the angular distance from the maximum loaded roller, Q_φ and Q_{max} are the roller load at angular distance and maximum roller load respectively, and ϵ is related to the bearing axial and radial ring shift which was assumed to be 0.5 due to lack of information.

$$\frac{Q_\varphi}{Q_{max}} = \left[1 - \frac{1}{2\epsilon}(1 - \cos\varphi)\right]^{1.5} \quad (7.7)$$

The theoretical ratio was found to be around 0.67 whilst the measured ratio around 0.73, both having a variation of around 9%.

Comparison of roller load with literature

Two published studies [176, 196] have attempted to measure and model the loads experienced by the HSS gearbox bearings during normal turbine operation. Both studies were conducted on a $750\ kW$ NREL drivetrain gearbox. The NREL gearbox differs from the gearbox in the present study through two aspects, the power rating and shaft layout. It has a $750\ kW$ power rating (compared to the $600\ kW$ used in this study) and the shaft layout differs slightly as the single cylindrical roller bearing (CRB) and TRB pair are located on opposite sides of the pinion. Despite these differences, we shall draw some broad comparisons with the load measurements obtained in this work.

In Bruce et al. [176], to simulate the $750\ kW$ NREL turbine drivetrain, a multibody dynamic WT gearbox model was developed using Ricardo's VALDYN software. Input parameters for the model include the dimensions, damping, inertia, and material properties of the gearbox components. The outputs of the model were limited to torque, reaction forces of the gearbox components, including bearings internal stresses and strains and the model fails to simulate rotor and generator off-axis loads, gearbox component's internal deflections and load sharing between the planetary gear bearing pairs. Table 7.2 summarizes the resultant forces of the HSS bearings computed by the model.

On the other hand, Guo and Keller [196] utilised three models of increasing complexity (semi-analytical, SIMPACK multi-body, and Transmission 3D finite element models) to determine bearing loads on the same $750\ kW$ NREL drivetrain. Results from the three models were then compared with a dynamometer test, where strain gauges were instrumented onto the HSS TRB pair for bearing load measurement. Results from the experiment and models agreed well with each other, except for measurements during the transitional operation. As the generator power is increased, HSS bearing load also increased in a linear pattern. Table 7.2 shows the radial load of the HSS bearings at full power. The radial load for each individual TRBs was not stated in the paper, however the authors did specify that the downwind TRB experienced higher loading as most axial loading was supported by it.

Since the CRB can only support radial loading and the two studies were simulating the same NREL drivetrain, measurements of load for the CRB should be similar across the two studies. It was found however that measurements vary by $16\ kN$. As the modelling results from Guo and Keller [196] agreed with their experimentally measured load from the dynamometer test, the measurements bear higher confidence. The discrepancy between the two modelling results is potentially resulted from the limitations in the VALDYN model mentioned previously.

For this current research, a $20.6\ kN$ bearing load was measured through the ultrasonic sensors at $356\ kW$ from the downwind HSS TRB. The value seems sensible compared with the two other previously mentioned studies. As only the downwind bearing of the TRB pair was instrumented, comparison across the HSS bearing was not possible for the current study.

Present study	**Bearing**	**Bearing Radial Load (kN) at 356 kW**
	TRB-Downwind	20.6
Bruce et al. [176]	**Bearing**	**Total Bearing Load (kN) at 750 kW**
	CRB	63.0
	TRB-Downwind	79.0
	TRB-Upwind	15.0
Guo & Keller [196]	**Bearing**	**Bearing Radial Load (kN) at 750 kW**
	CRB	47.0
	TRB-Pair (Down & Upwind)	31.0

Table 7.2 - Comparison of ultrasonically field measured HSS bearing load with theoretical and laboratory-based experimental investigations

B-Scans

An ultrasonic B-Scan refers to a two-dimensional image generated when the ultrasonic measurements are plotted across the cross section of the instrumented component. As such, each vertical slice of the B-Scan is a single ultrasonic pulse and the z-axis (axis going into the paper) corresponds to the amplitude of the ultrasonic response. The letter 'B' corresponds to brightness. Figure 7.31 shows the time and frequency domain B-Scans of the ultrasonic response as one of the rollers traverses across the sensor. Amplitude of the ultrasonic response in time domain which were less than 0 were clipped to produce a clearer, much focused plot. Similar amplitude clipping was conducted on the frequency plot where the amplitude below 0.4 was set to 0.4.

Three main horizontal intensity strips can be observed within the time domain B-Scan and these correspond to the three main peak oscillation of the pulse. Fringes in the form of ripples again are observed within the time domain B-Scan and is a result of ultrasonic interference. The interference of the fringes however is less apparent on the higher intensity strips and more apparent during the final few oscillations of the pulse $(0.6 - 1.0\ \mu s)$. This is most likely due to the low loading the bearing experiences, resulting in a high reflected signal amplitude which is less prone to the effects of interference waves.

The frequency domain B-Scan shows that majority of the ultrasonic energy is concentrated within the sensor's bandwidth $(-6\ dB)$ of 4 to 16 MHz. Within the region where the roller is directly beneath the sensor, the ultrasonic energy is the lowest. Ultrasonic interference manifests itself as vertically angled lines on each side of the main energy void where the roller is at the centre of the sensor. A clear

transition can be seen at 15 *MHz* where the measurements seem to divide into two portions. Measurements are extremely blurred beyond the roller pass region.

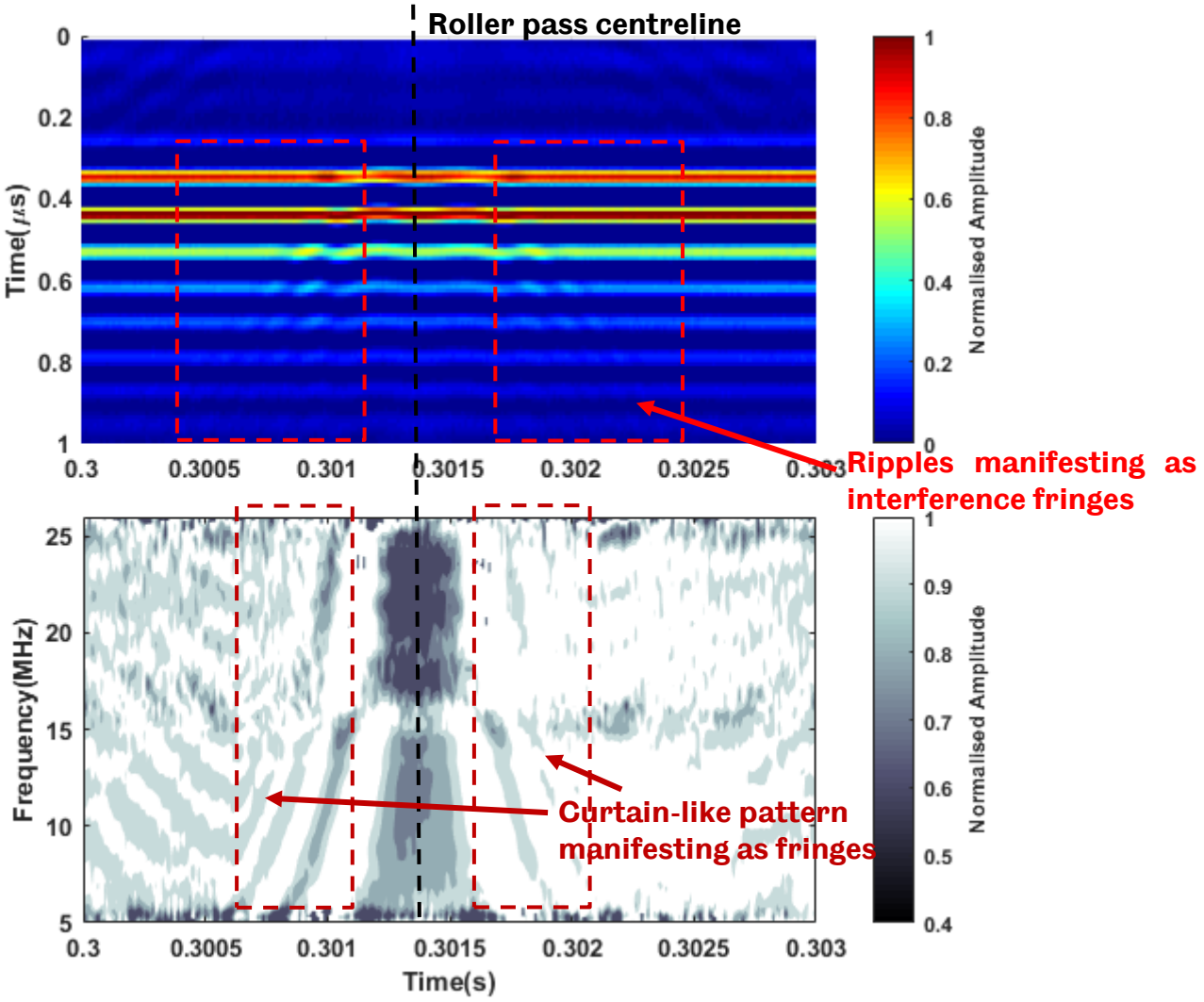

Figure 7.31 – Time domain (Top) and frequency domain (bottom) intensity plot

Caesar shift[1] repeatability study

With information on the rotational speed of the bearing and the delay time of capture initialisation between the two ultrasonic measurements, prediction of the roller shift can be carried out. This would however require the exact capture initialisation delay time to be known. The nominal delay time between captures based on Figure 7.6 is 1 second, however an additional delay time from software

[1] The Caeser shift cypher is where each letter is replaced by a letter a fixed number of places along in the alphabet. Here, we shift the roller position by a fixed number of places between CH1 and CH2.

initialisation will also need to be added and this is predicted to take between 0.01 to 0.20 s. Figure 7.32 shows the roller shift number plotted against its delay time for various bearing rotational speeds. As the bearing rotational speed increases, the gradient of change of the roller shift number also increases and the different possible roller shift options also increase. Unfortunately, due to the delay time being an unknown, the roller shift option is not limited to a certain range.

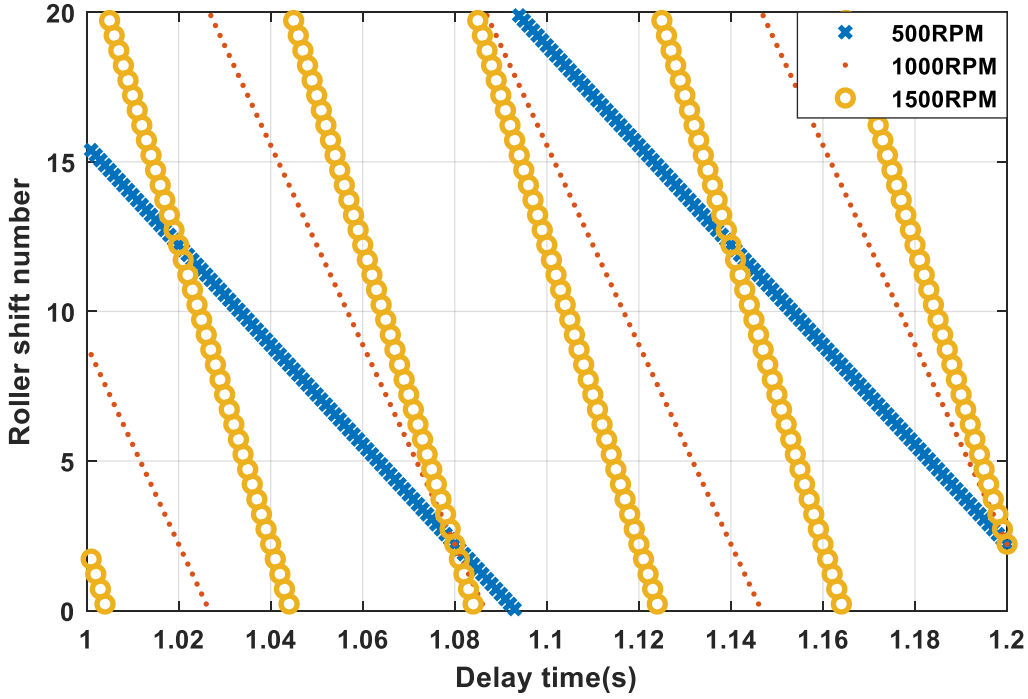

Figure 7.32 – Prediction of roller shift number with delay time

To investigate the repeatability of the Caesar shift phenomenon across the two ultrasonic measurement channels, 7 datasets were randomly selected with the only selection criteria being data collected when the bearing is rotating at maximum speed of 1500 RPM. This is to maximise the number of full cycles collected within the data. The procedure for alignment of the two measurement channels are illustrated in Figure 7.33. The datasets were initially processed to obtain the minimum reflection coefficient and peak roller load measurements. Ignoring the first 0.18 s and the final 0.05 s of the data, the minimum reflection coefficient and peak roller load measurements for each individual roller for both measurement channels (CH1 & 2) were collected and compiled. Care was taken to ensure no peaks or dips were omitted as this would incur errors within the measurement and the sequence of the data which correspond to specific rollers within the complement. The average R_{min} and Q_{max} measurement across the cycles for each roller were subsequently computed for and the measurements of CH2 were correlated against

CH1 to obtain the shift number. This generated two shift numbers, one from correlating the average R_{min} and the other from the average Q_{max} measurements. After synchronisation through shifting CH2 measurements to match that of CH1, the data were then aligned with the initial dataset shown in Figure 7.28 (CMS2_20150626_163526) for ease of comparison and completeness.

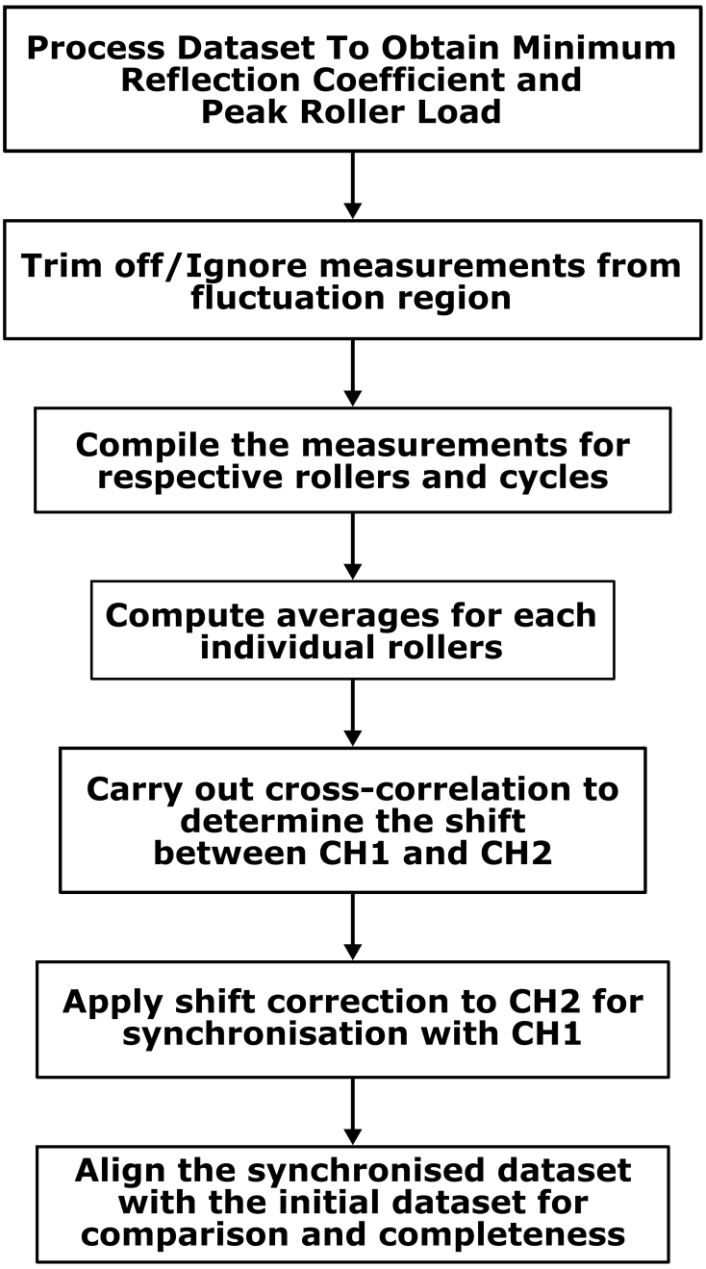

Figure 7.33 – Shift correction procedure for CH2 US measurements

The results of the shifted measurements can be seen in Figure 7.34 and Figure 7.35. To avoid duplication of the plots, only two of the measurements (CMS2_20150626_234145 and CMS2_20151013_230007) were shown.

For measurements shown in Figure 7.34, the shift number of 8, obtained from either R_{min} or Q_{max} does not contradict each other. The R_{min} measurements also correlate well with the Q_{max} measurements; as R_{min} increases, Q_{max} decreases (Roller 18). In Figure 7.35 however, two different shift values (9 & 16) were obtained. Upon manual inspection, it was discovered that the shift value computed by using the average R_{min} values was the correct shift. The error was due to low signal-noise ratio of the average Q_{max} measurements, especially on the less loaded measurement channel (CH1), causing trends across the roller complement to be diminished and thus resulting in difficulty of the code to register a correct shift value. As a result, shift computed using average R_{min} values attain higher confidence and were chosen instead of their counterpart.

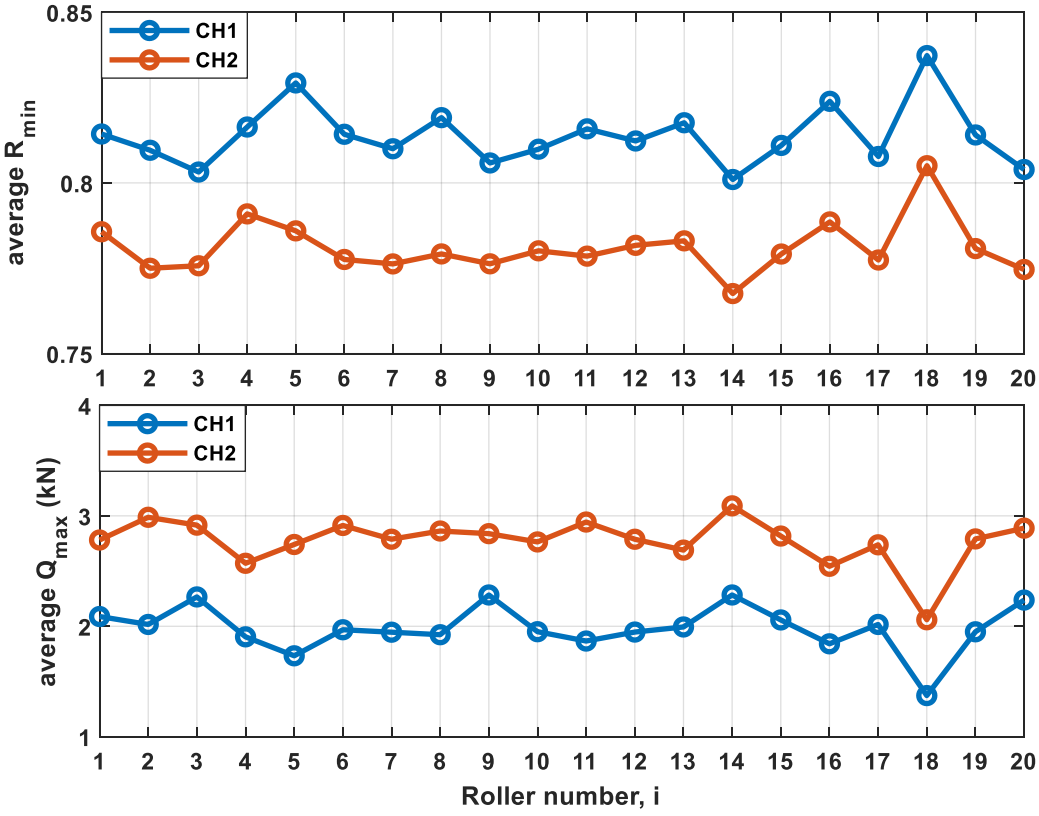

Figure 7.34 – Average minimum reflection coefficient and Peak Roller Load of individual rollers for dataset CMS2_20150626_234145

Another interesting observation was that the trend of the R_{min} and Q_{max} measurements seem to be very apparent and consistent across different datasets (ie. Roller 18 always exhibits higher R_{min} and lower Q_{max} values. As elaborated in the previous sections, this is potentially resulted from geometrical differences between the rollers due to manufacturing tolerances. Q_{max} measurements however were

more erratic, and trends are less visible due to the lower signal-to-noise ratio within the measurements.

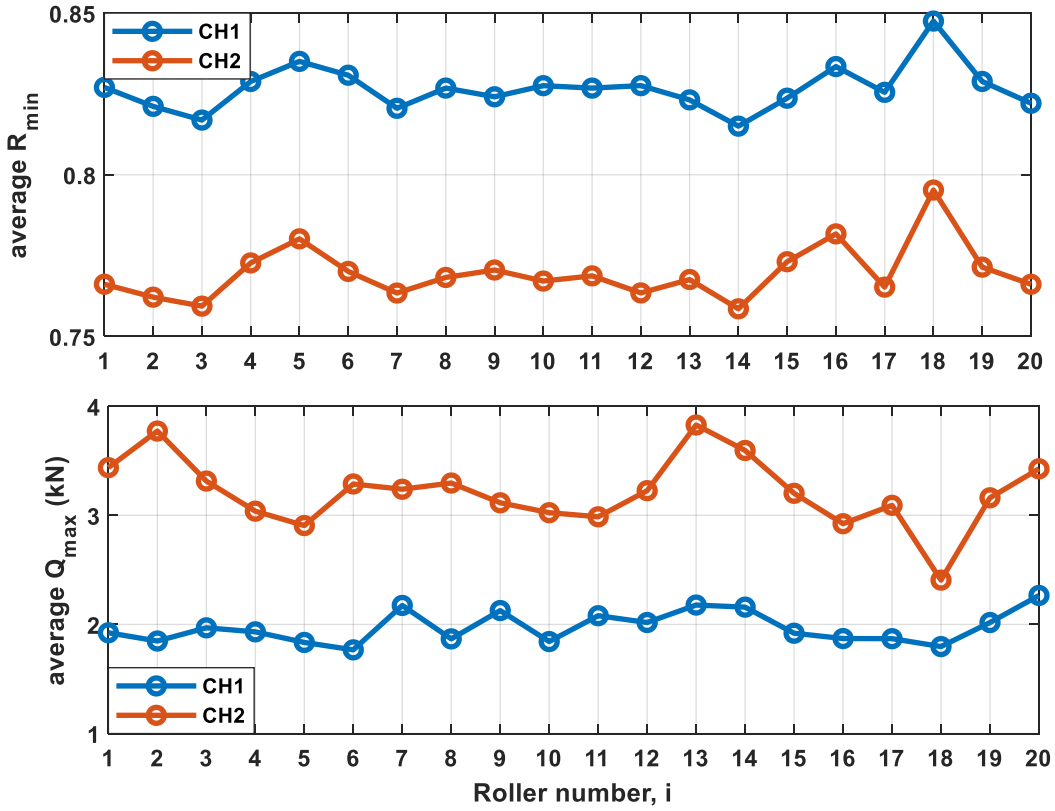

Figure 7.35 – Average minimum reflection coefficient and peak roller load of individual rollers for dataset CMS2_20151013_230007

Shift values of all the 7 investigated datasets were shown in Table 7.3. A wide range of shift values exist from the minimum shift value of 8 to a maximum of 17 with a mode of 8. This agrees well with the roller shift prediction model in Figure 7.32 as the roller shift number is dependent on the delay time which varies with each dataset, resulting in a range of shift values observed.

Data Filename	Shift no.	
	Average R_{min} shift	Average Q_{max} shift
CMS2_20150626_234145	8	8
CMS2_20150627_030457	17	18
CMS2_20150627_044529	11	11
CMS2_20150627_125207	9	9

CMS2_20150627_201828	13	13
CMS2_20150930_225933	8	20
CMS2_20151013_230007	9	16

Table 7.3 – Shift correction for randomly selected US measurements

Aliasing-Free Verification

A dataset obtained at extremely slow HSS rotational speed, showing only one roller pass was used to verify that the reflection coefficient profile at maximum bearing rotational speed is free of aliasing problems. Figure 7.36 shows the dataset where each reflection coefficient measurement was plotted as points to illustrate the density of data points within the 2 second dataset where a single roller pass was recorded.

The reflection coefficient values decrease gradually at the roller inlet region until it reached a minimum. R values then gradually increase as the roller passes through the sensor. A minimum value corresponding to the EHL constriction at the exit region was not observed due to the fringe effect and sensor response averaging. The profile of reflection coefficient at low rotation speed (high number of samples for a roller pass) is similar to that obtained at bearing maximum rotational speed ($1500\ RPM$) and thus verifying that all the datasets do not experience aliasing.

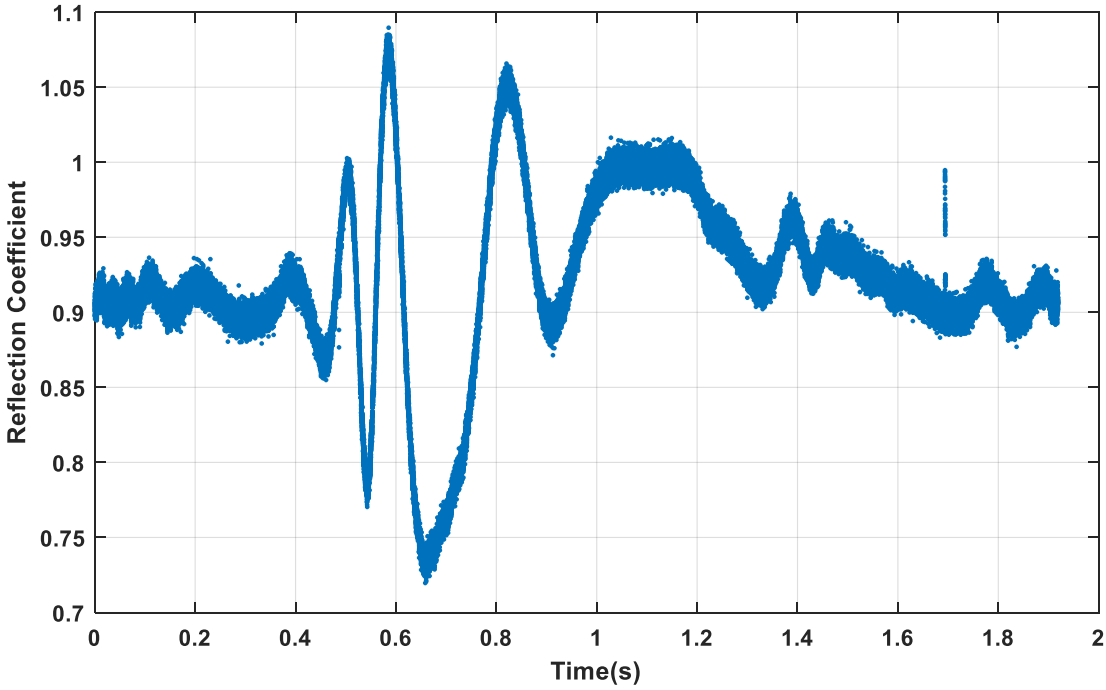

Figure 7.36 – Anti-aliasing dataset

Indication of roller lubrication

As mentioned in §3.6.4, reflection coefficient measurements between roller passes can be used as indication of roller lubrication as reduction in reflection coefficient is caused by the presence of lubricant on a bearing raceway. This included the two lubrication patterns identified at low and high bearing rotational speeds.

In the previous chapter, the relationship between lubricant reflow time and rotational speed was shown for $0 - 100\ RPM$. Figure 7.37 shows the relationship between lubricant reflow time and bearing rotational speed for $0 - 1550\ RPM$. 8 datasets of varying rotational speeds were used. The lubricant reflow time of each datasets were initially manually compiled, and an average reflow time was computed for each of the datasets. Similar to the trend observed from the previous chapter, the reflow time decreased exponentially as the bearing rotational speed increases. It is apparent that as a result of the lubricant reflow mechanism at low rotational speed, the reflow time differed considerably compared to that computed at higher bearing rotational speed. During instances of low bearing rotation, the lubricant has adequate time to replenish the region previously swept clean by a rolling element before the incoming roller traverses across. At higher speeds, the decrease of lubricant reflow time is a result of an increase in rotational speed, as the roller forces the oil into the starved raceway region ahead of its passage and potentially the increase in operating temperature reduces the lubricant's viscosity, allowing for quicker replenishment of the raceway surface.

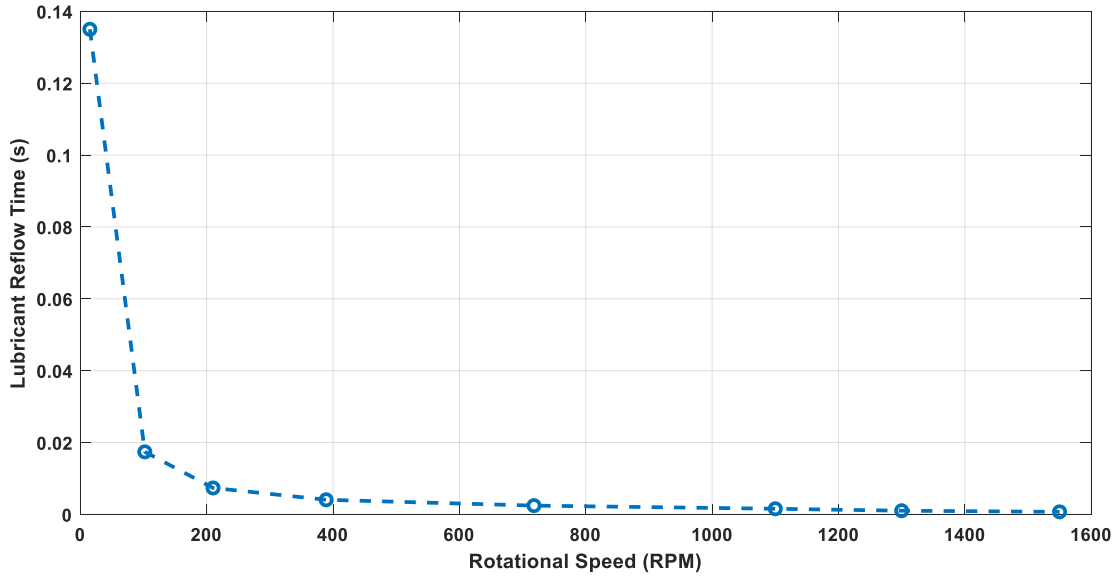

Figure 7.37 - Variation in lubricant reflow time with rotational speed

Figure 7.38 illustrates one specific set of data which captures two distinct lubrication phenomena within a single revolution. For the first 5 roller passes, reflection

coefficient measurements between roller passes remains at unity, indicating insufficient lubrication. For the subsequent 5 roller passes, the reflection coefficient exhibits the recurring pattern where after a roller pass, it transitions from insufficient $(R = 1)$ to adequately lubricated $(R = 0.95)$. In this gearbox design, lubricant is supplied into the gearbox from the top and is reliant on the rotating parts to distribute it throughout the gearbox bearings. It is apparent that the process is non-stationary and susceptible to intermittent lubrication.

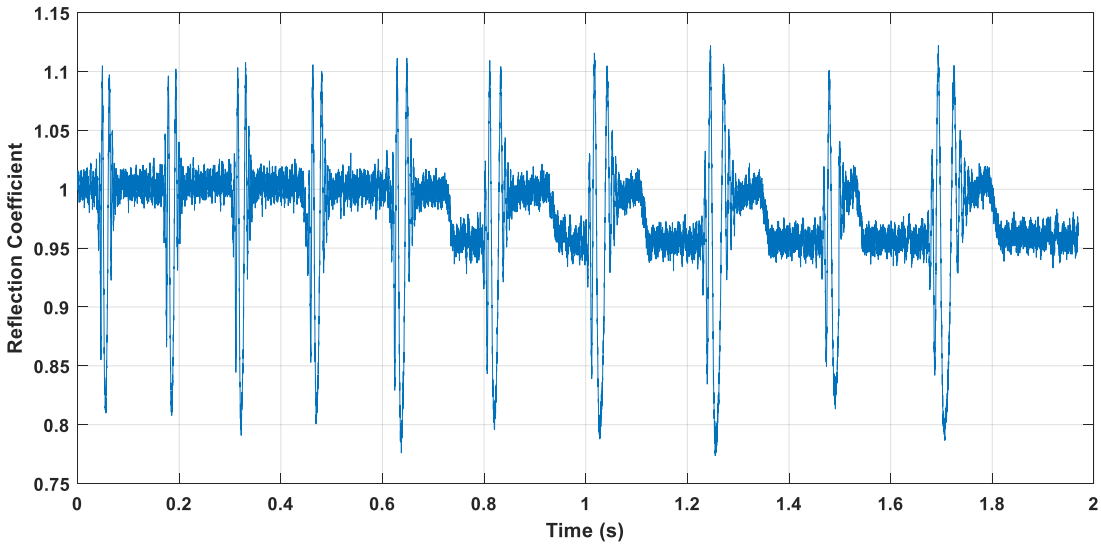

Figure 7.38 – An indication of roller lubrication; a single dataset where the first 5 roller passes sweep out oil and are not replenished. For the next 5 roller passes, replenishment occurs

Automation for detection of bearing lubrication condition

The following section discusses an algorithm written to detect and categorise the lubrication condition of each dataset. It was found in the previous section that reflection coefficient measurements contain information on the lubrication condition of the raceway and the roller. Through analysing the histograms of the reflection coefficient measurements, it was discovered that datasets with distinct lubrication condition differ in their histogram patterns and thus can be categorised automatically. Each dataset was sorted into the following categories:

- No rotation/Bearing Idle
- Partially lubricated
- Fully lubricated – slow rotation
- Fully lubricated – fast rotation

- Fully unlubricated/insufficiently lubricated

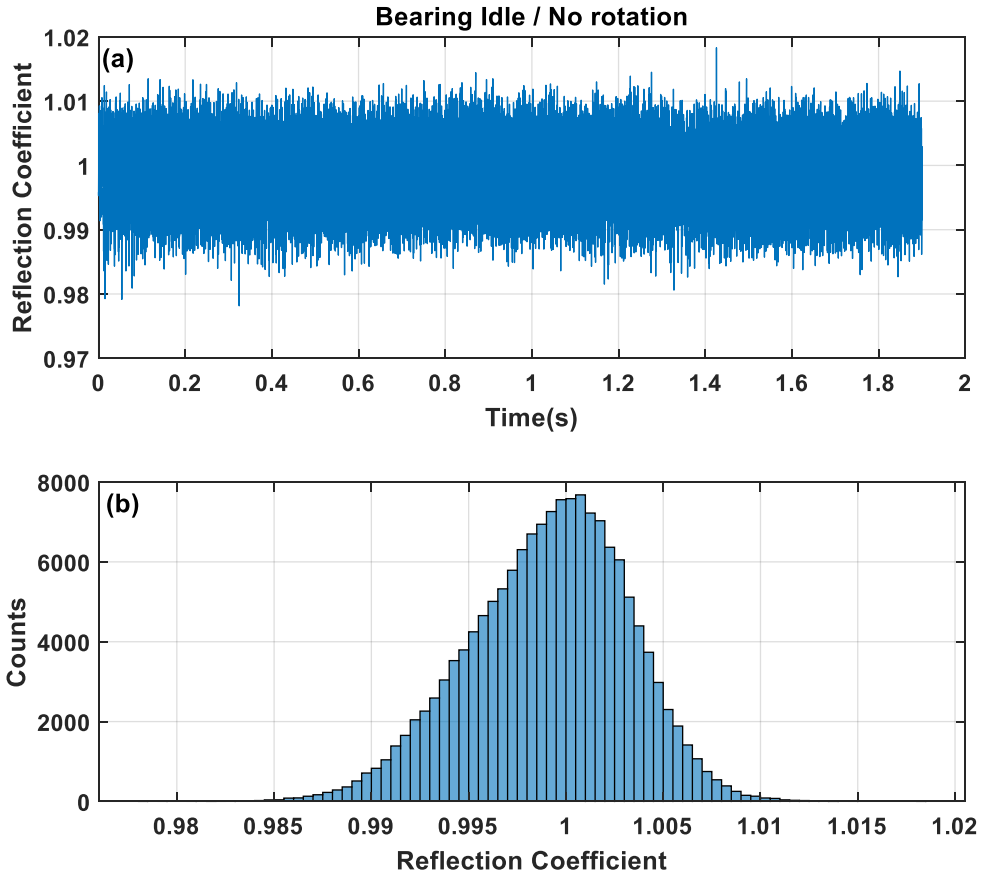

Figure 7.39 – (a) Reflection coefficient and (b) histogram of reflection coefficient data, captured when bearing is idle

Figure 7.39(a) shows a dataset's reflection coefficient where the bearing is idle and below it, its histogram. The histogram resembles an asymmetric normal distribution with its peak centred around unity. Range values of reflection coefficient of 20 datasets captured randomly selected in June 2015 was computed to obtain statistical information on the deviation of range values for datasets captured when the bearing is idle. This can then be used to distinguish idle datasets from non-idle ones using the range of reflection coefficient as the deciding parameter. The range values of the 20 datasets are shown in Figure 7.40 with a mean of 0.0476. This however will not filter out datasets where the bearing is rotating extremely slow and the roller is passing through the bearing sensing region as the range values will be different. This is one of the odd datasets which is difficult to categorise automatically.

Figure 7.41 shows the reflection coefficient pattern for a fully lubricated, slow rotation and partially lubricated dataset alongside their histogram plots. Two distinct peaks can be observed within the histogram at 0.95 and 1.00 respectively. For the fully lubricated dataset under slow rotation, the dominant peak is located at 0.95 whilst for the partially lubricated dataset, the dominant peak is located at 1.00. The ratio of the peak counts at 0.95 and 1.00 contains information on the duration when the raceway is insufficiently lubricated ($R = 1.00$) and adequately lubricated ($R = 0.95$).

Figure 7.42 shows the reflection coefficient plots for a fully lubricated, fast rotation and fully unlubricated dataset alongside their histogram plots. A single peak is apparent for both datasets, at 0.95 for the fully lubricated dataset under fast rotation ($> 500\ RPM$) and at 1.00 for a fully unlubricated dataset.

It is apparent that through observing distinct histogram features, it is possible to categorize each dataset into their respective lubrication condition. An automation code was subsequently written based on distinguishing different patterns in the histogram of the Reflection Coefficient to categorize the datasets.

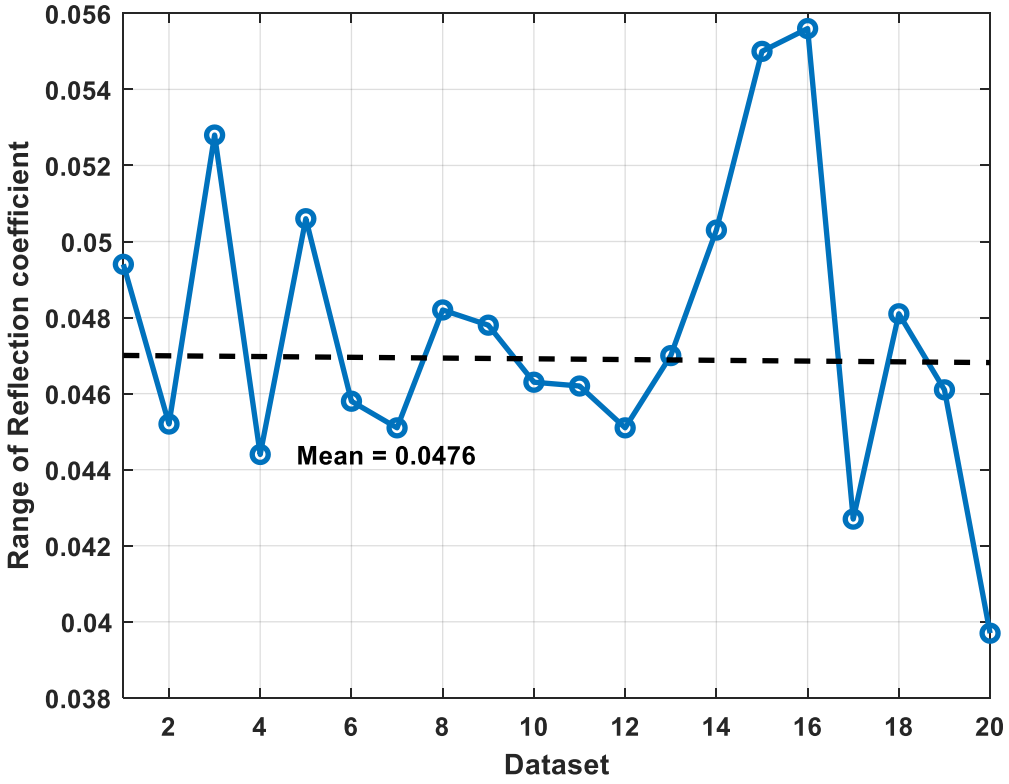

Figure 7.40 – Range of reflection coefficient values for non-rotating datasets

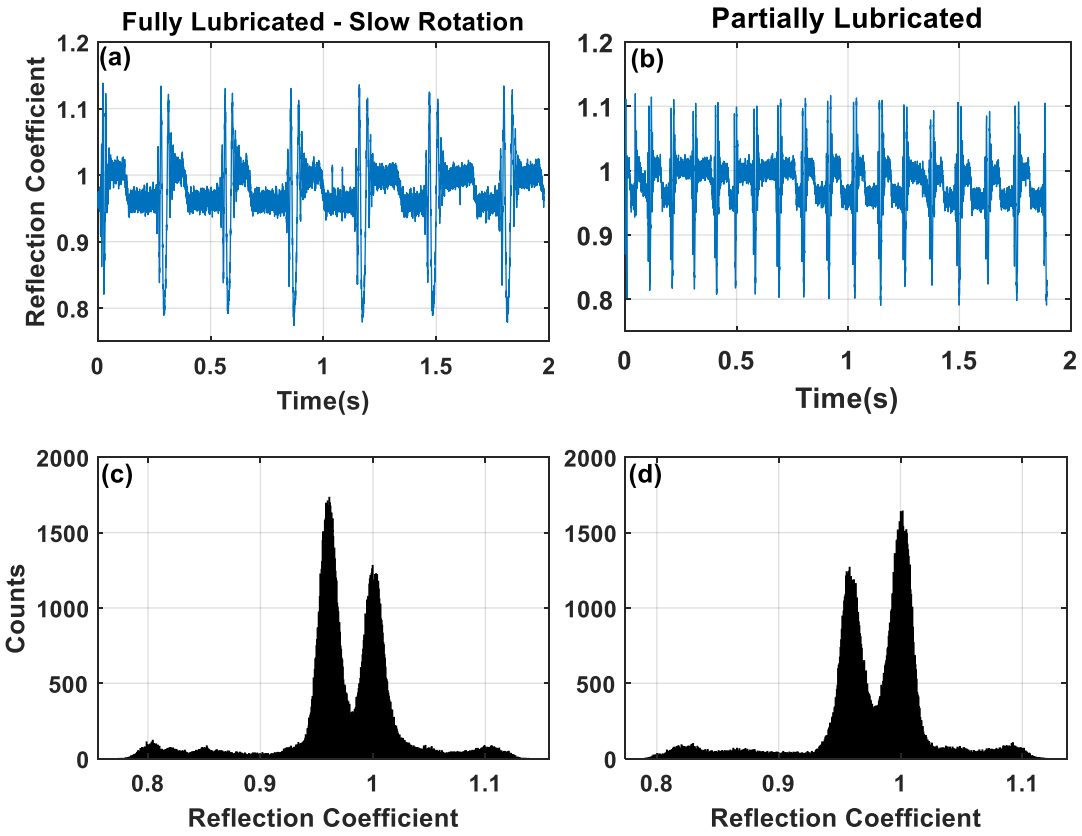

Figure 7.41 – Reflection coefficient plots in time domain and histogram plots for (a) fully lubricated, slow rotation and (b) partially lubricated conditions

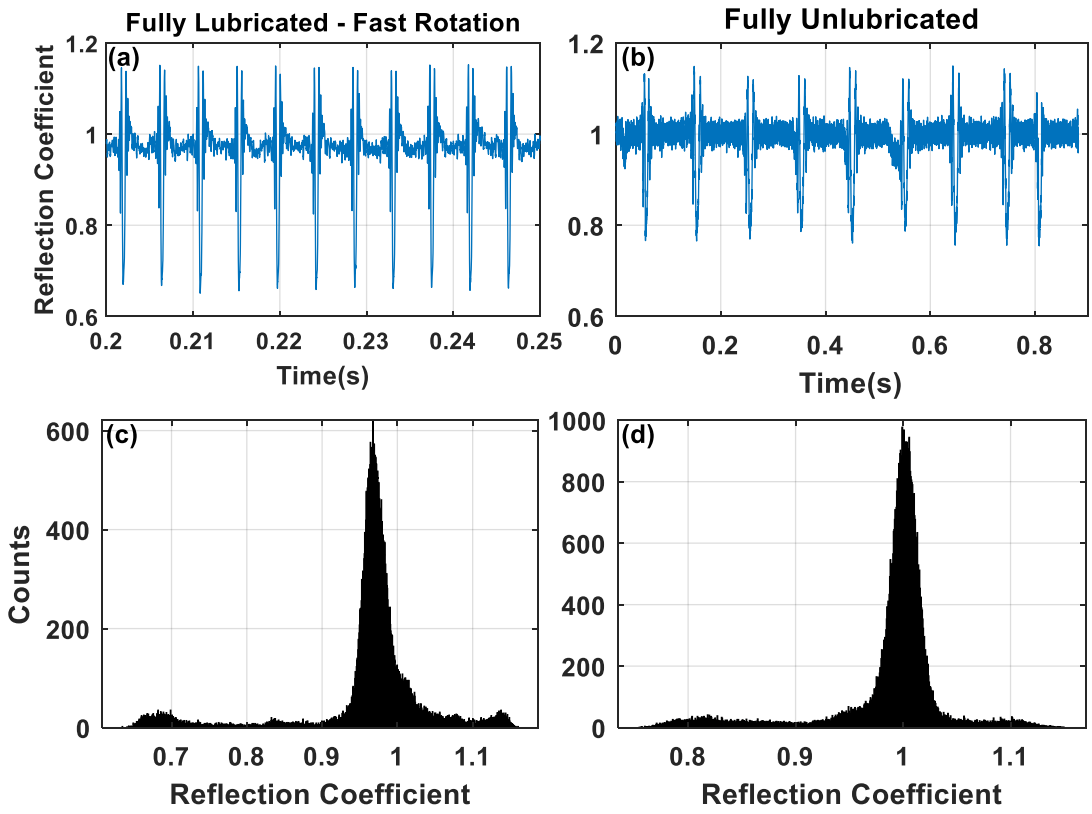

Figure 7.42 - Reflection coefficient plots in time domain and histogram plots for fully lubricated, fast rotation and fully unlubricated

Automation code design & optimisation

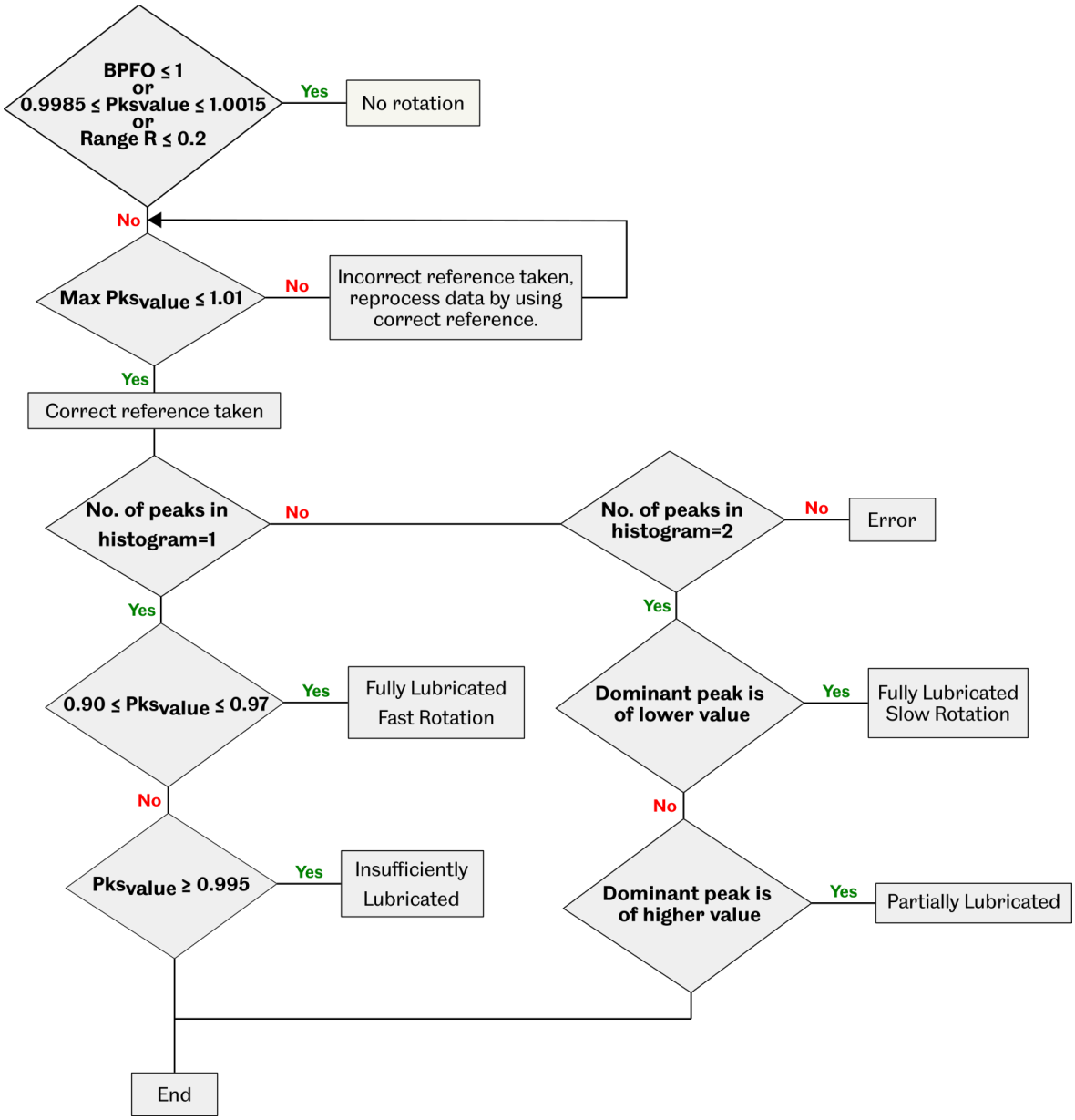

Figure 7.43 – Lubrication condition automation flowchart

Figure 7.43 shows the data processing routine carried out in attempt to categorize datasets based on their lubrication condition. 3 parameters were initially set to filter out data that is captured when the bearing is idle or rotating at extremely slow speeds ($BPFO \leq 1$). Attempt was then taken to try to correct the error arising from obtaining a reference at a steel-oil interface. The datasets were then subsequently categorised based on their distinct histogram pattern shown in the previous section.

If only a single peak exists within the histogram, depending on the value of the peak, the dataset is either fully lubricated (fast rotation) or insufficiently lubricated. If two peaks exist and the peak consisting of a higher count (dominant peak) is of lower value, then the data will be categorised as fully lubricated (slow rotation) else, it would be partially lubricated.

Since the accuracy of the algorithm is unknown, an assessment was carried out using datasets collected in June 2015. 50 random datasets were selected, and both manually and automatically categorised based on their lubrication condition. The accuracy of the algorithm was then subsequently determined. It was found that 44 out of 50 of the datasets were correctly categorised for CH1 measurements, resulting in an 88% automation accuracy. Accuracy for CH2 measurements were found to be 86% and these were deemed acceptable.

The wrongly categorised datasets arose due to the datasets not fitting into the typical histogram pattern shown in the previous section and due to narrow distinction between partially lubricated and fully lubricated datasets. Datasets captured at extremely slow rotational datasets particularly, presents a challenge to tweak the code to include and enable accurate categorisation of these datasets.

The lubrication condition was then contrasted between CH1 and CH2 measurements to determine whether there exist, concurrently, any difference in the lubrication status at different locations within the bearing.

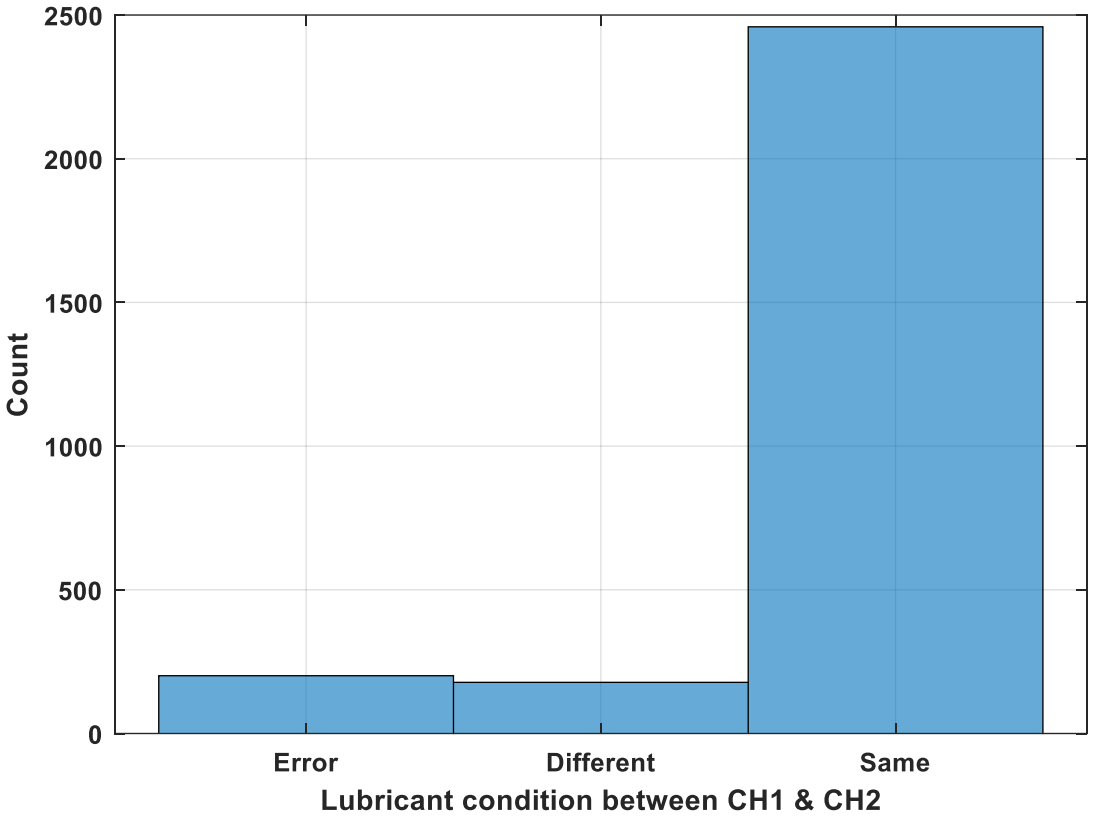

Figure 7.44 – Difference in lubrication behaviours between CH1 & CH2 ultrasonic measurements within the same dataset

Only around 6% out of the 2,838 datasets exhibited different patterns of reflection coefficient between roller passes, and subsequently varying bearing lubrication conditions for CH1 and CH2 measurements. Over half of these datasets (55%) recorded either partial lubrication or full lubrication, followed by 24% for insufficient and fully lubrication and finally 21% measured insufficient and partially lubricated conditions. As most of the partially lubricated and insufficiently lubricated measurements occur under transient operation ($0 - 1499\ RPM$), it can be deduced that under such operation, varying regions within the bearing loaded zone can experience a difference in lubrication. It is however prudent to note that part of this is potentially be attributed to the brief lag in data acquisition between the two measurement channels which could potentially cause the lubricant behaviour to change, albeit extremely unlikely within such a short instance. Error from categorisation of datasets, recorded at 7% was a result of measurements taken at rotational speeds less than $10\ RPM$, resulting in insufficient measurements between roller passes as a large portion of the measurement fall within the roller pass region. This is an inherent weakness of the automation algorithm and can be alleviated through assigning a minimum rotational speed threshold for data captured.

Figure 7.45 illustrates a measurement captured at varying lubrication condition between CH1 and CH2. CH1 shows that the bearing raceway is partially lubricated whilst CH2 measurements are that of a fully lubricated condition.

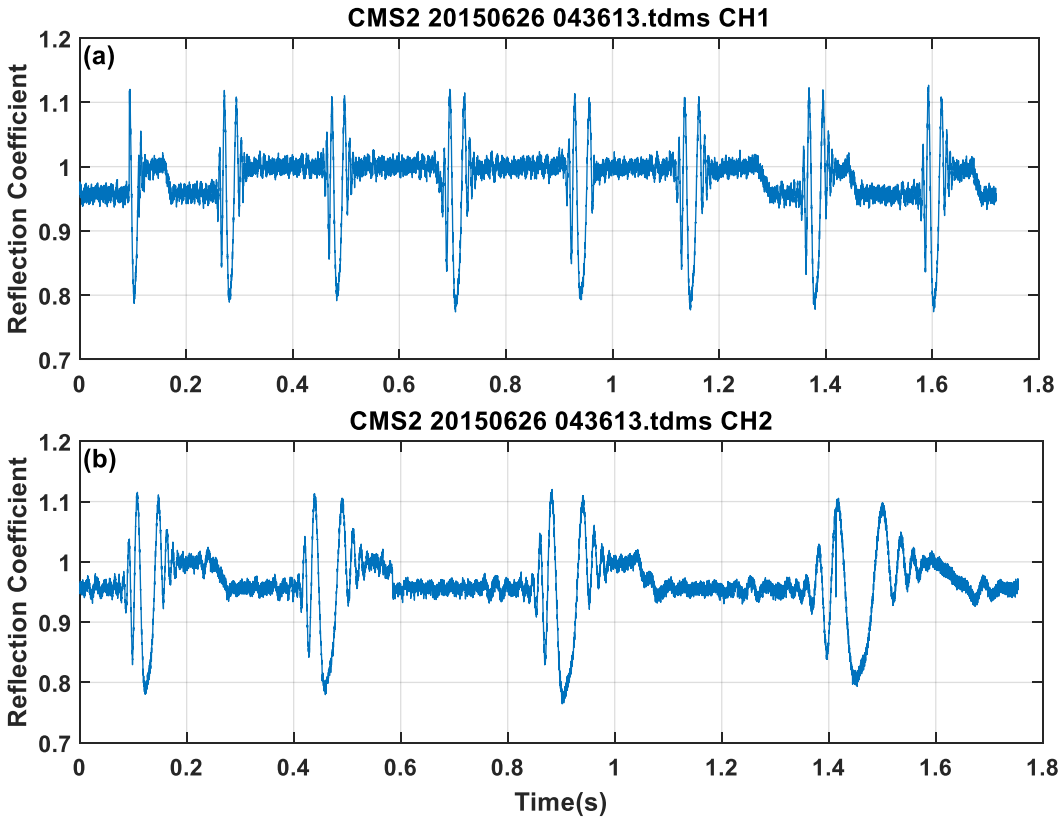

Figure 7.45 – Difference in lubrication condition between (a) CH1 and (b) CH2 of the same dataset

7.5.2 Trends across CMS2 measurements

The previous section highlights key trends that are available within a single ultrasonic dataset. This section explores the variation of reflection coefficient and roller load across all the measurements. For a single dataset and for each measurement channel, the measurements were summarised into 3 parameters, averages of roller reflection coefficient and peak roller load and bearing rotational speed inferred using ball pass frequency.

June 2015 Data

Figure 7.46 shows the variation of reflection coefficient, peak roller load and rotational speed measurements from CH1 across June 2015. The measurements were subcategorised into three distinct sections namely low speed and high-speed

measurements as well as clipped data. Ultrasonic pulses captured within the 'clipped data' region exhibited amplitudes higher than the maximum range the 12-bit FMS can sample (±2048) and was a consequence of excessive amount of excitation being applied to the sensor.

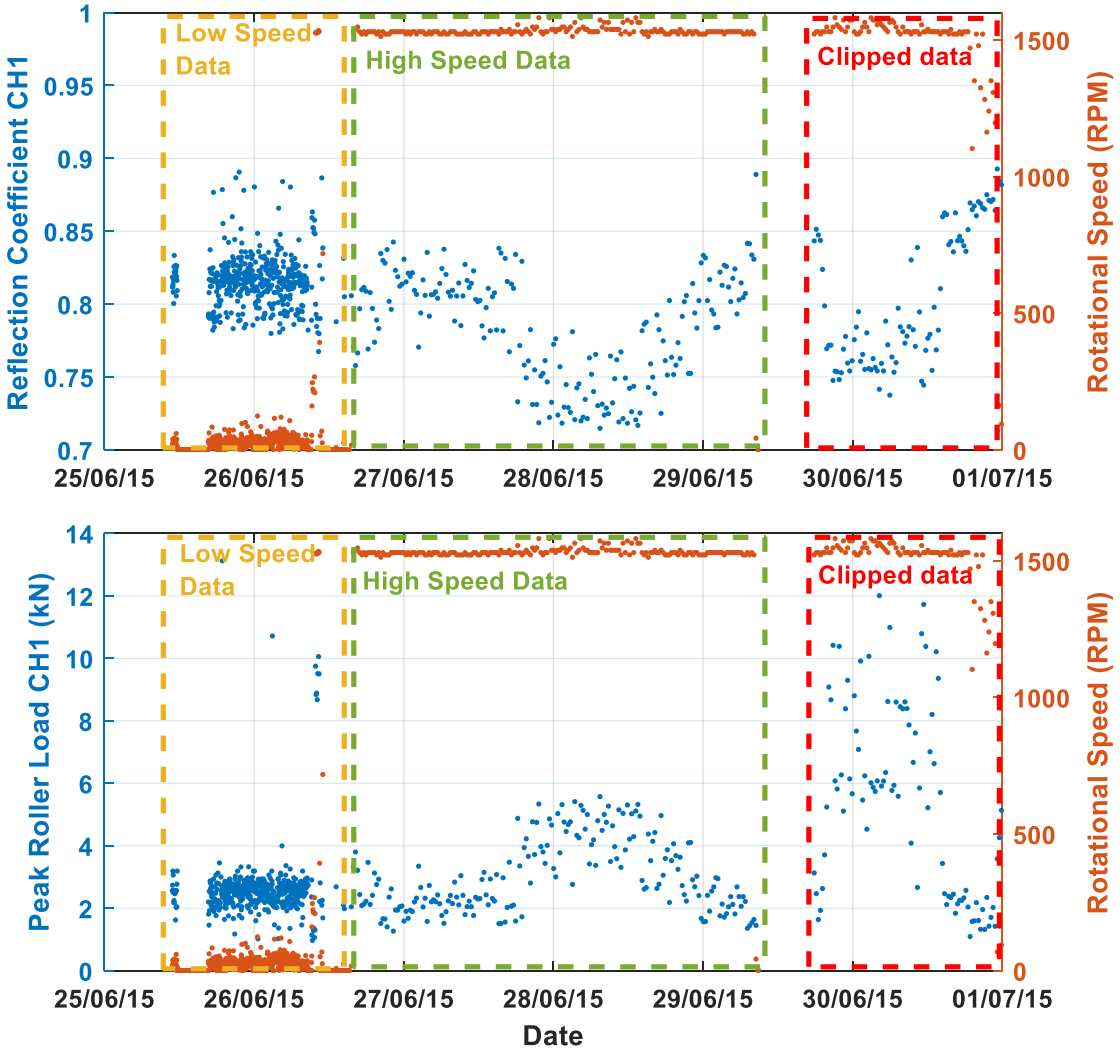

Figure 7.46 – Variation of roller minimum reflection coefficient, peak roller load and rotational speed for CH1 across June 2015

CH1 and CH2 measurements of reflection coefficient, peak roller load and rotational speed measurements within these subcategories were then correlated to identify trends within their respective subcategories. Figure 7.47 illustrates this with the Pearson Correlation (PC) values shown in the titles within the plots.

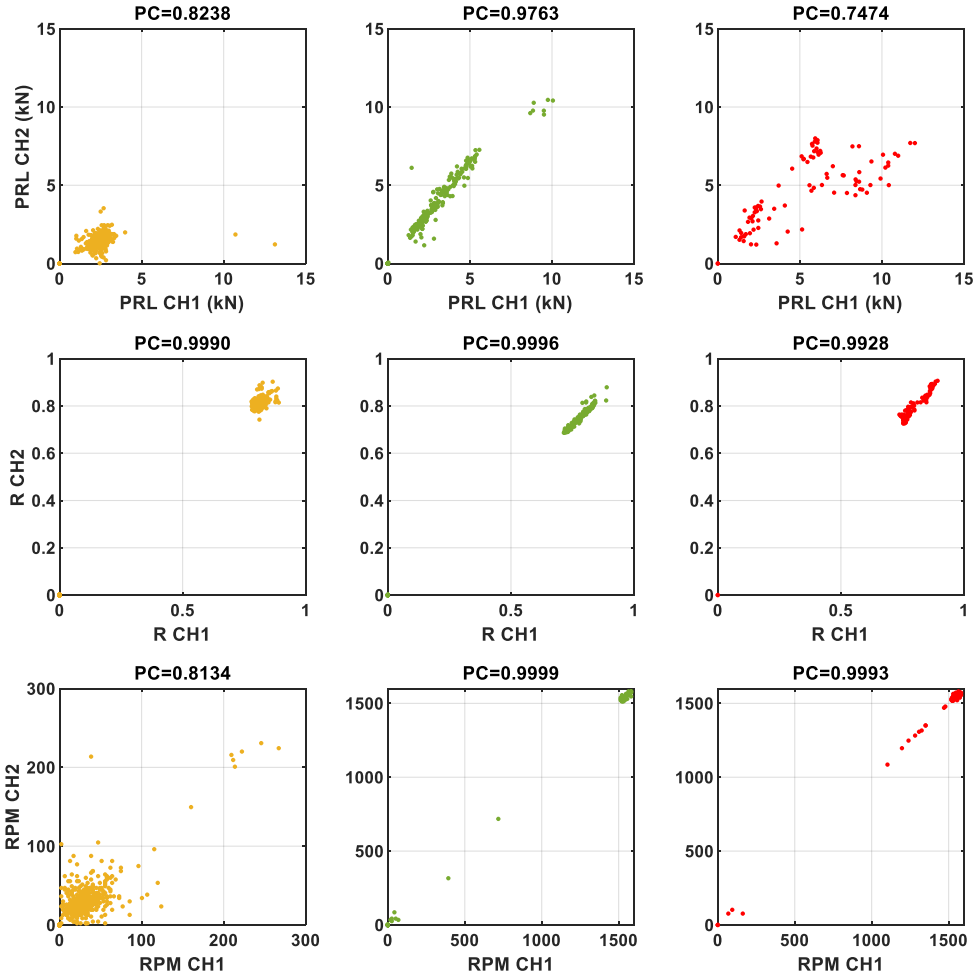

Figure 7.47 - Pearson correlation for 3 portions of measurement obtained from June 2015: low speed (yellow), normal (green) and clipped data (red)

For the low-speed measurements, correlation of peak roller load and rotational speed between CH1 & CH2 was poor ($PC < 0.9$) whilst correlation of reflection coefficient was much better with a PC of around 0.9. For high-speed measurements, peak roller load, reflection coefficient and rotational speed measurements between CH1 & 2 all showed good PC values. This indicated that roller load and rotational speed measurements at low speed were unreliable with reflection coefficient values being most reliable out of the three. Reliability of rotational speed measurements were dictated by the ball pass detection algorithm, which was less reliable at low speeds, and thus resulting in a low PC value. At low rotational speed, the turbine is in transient operational mode and it is expected that the gearbox input torque is low and subsequently the bearing load. A low roller load measurement will be more

susceptible to noise and this is potentially the reason for the low PC values for roller load.

For datasets 870 and 871, the captured ultrasonic pulse information was missing within the data. This indicated that there were issues with the data capture sequence of the pulsing computer. For datasets 872 to 961, the pulses captured show signs of clipping (amplitude exceeding ± 2048) despite no change in signal pulse voltage and gain configuration. This combined with the previous missing data occurrences indicated some problems associated with the ultrasonic pulsing card and possibly an unknown source contributing to this sudden surge in pulse amplitude (ie. stray voltage, current from lightning strikes).

To better understand what information can be extracted from the clipped measurements, a single clipped dataset was manually processed and analysed. Figure 7.48 shows the raw ultrasonic data stream, its peak-to-peak values, and the clipped reference pulse in its time and frequency domain. A glimpse of the peak-to-peak amplitude plot suggests that no useable information can be obtained from the dataset, however reflection coefficient and load measurements were still able to be extracted from the dataset as shown in the subsequent figure. The reflection coefficient however does not include information on the real part as the measurements were clipped.

As shown in the PC plots, the magnitude of the load and reflection coefficient measurements are inaccurate as they were affected by the clipping of pulse. PC values for reflection coefficient is 0.99 which indicates that CH1 and CH2 measurements are very similar. This should not be the case as CH2 is located at the centre of the maximum loaded region and thus should observe lower reflection coefficient values than CH2. Clearly the clipping of the pulse jeopardized the sensitivity of the reflection coefficient measurements with load. Despite not being able to distinguish energy loss from roller passes using signal amplitude within the raw ultrasonic dataset, this can still be done through the reflection coefficient measurements obtained from the frequency domain of the captured pulses. Subsequently, ball pass frequency can be inferred through the reflection coefficient measurements. The dataset seemed to be clean and roller passes can be distinguished clearly. This was verified by the PC values for the rotational speed measurements showing a PC value of 0.95. The magnitude of reflection coefficient however will not be accurate due to loss of information from the clipped pulses.

The profile of roller load for each roller pass still resembles an M-shape, thus it is still also possible to distinguish roller passes within the roller load measurements. The accuracy of the measurements however is also affected by the clipping of pulses

as the time-of-flight computational method relies on the envelope of the pulses and the maximum location of the reference and measurement envelopes. PC values for peak roller load indicates the unreliability of the measurement. As such, for clipped measurements, only rotational speed measurements are reliable. For June 2015, only measurements falling within the high-speed data portion were collated to be subsequently correlated against turbine operating parameters.

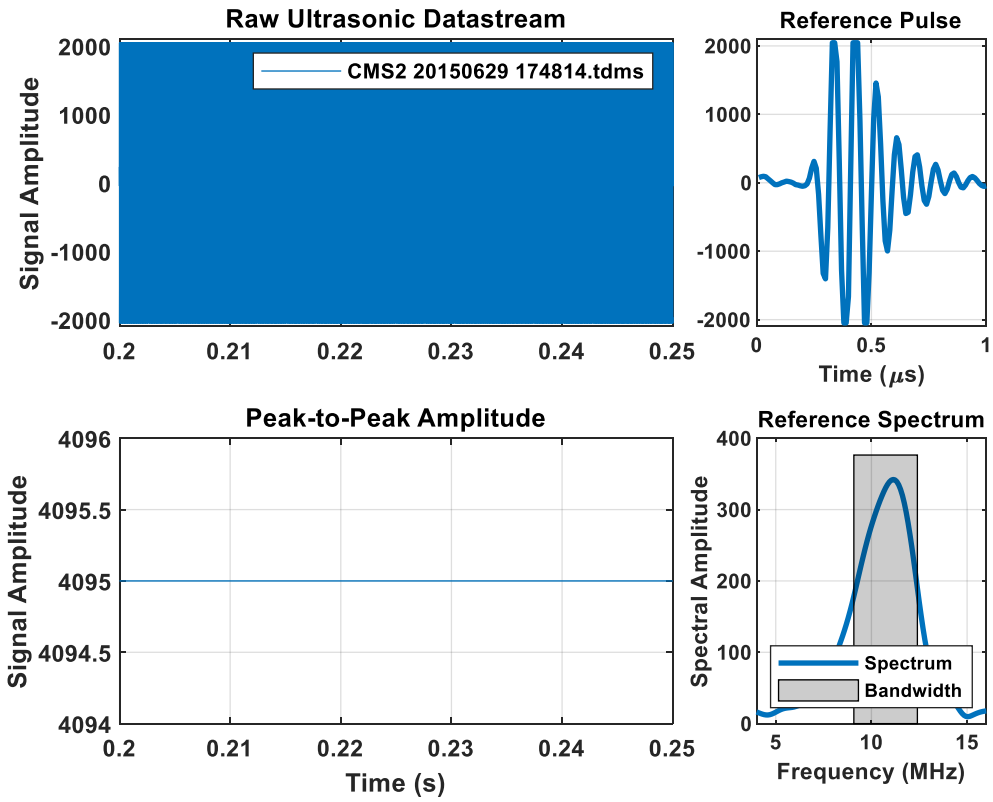

Figure 7.48 – Ultrasonic CH1 data features of a clipped dataset

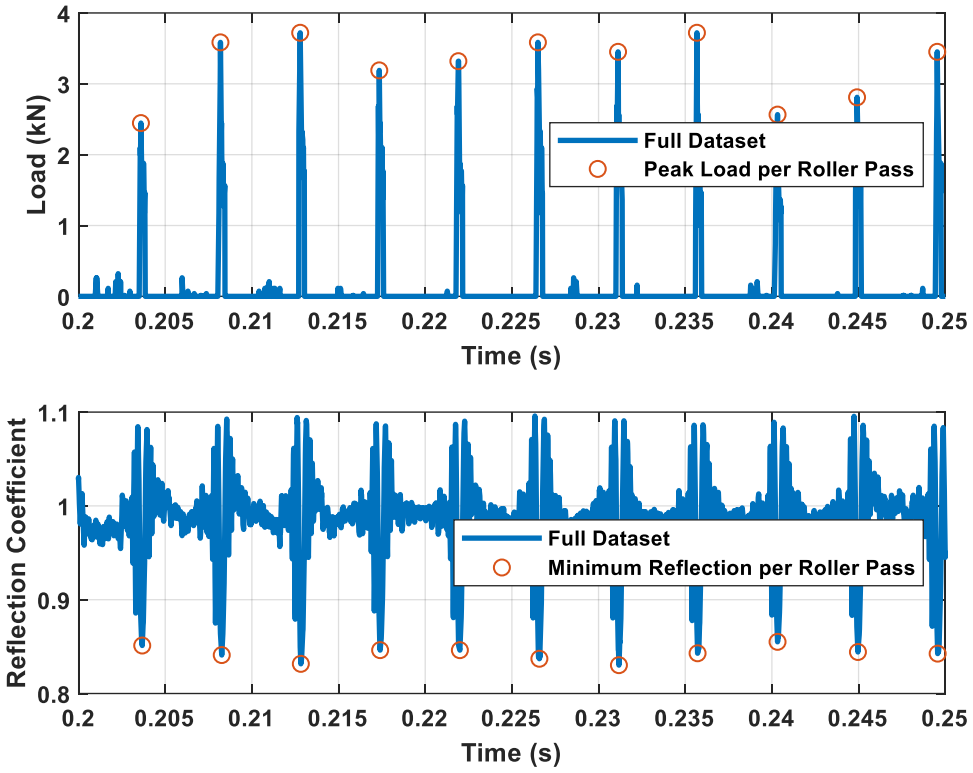

Figure 7.49 – CH1 Peak roller load and reflection coefficient measurements for the clipped dataset

Sept & Oct 2015 Data

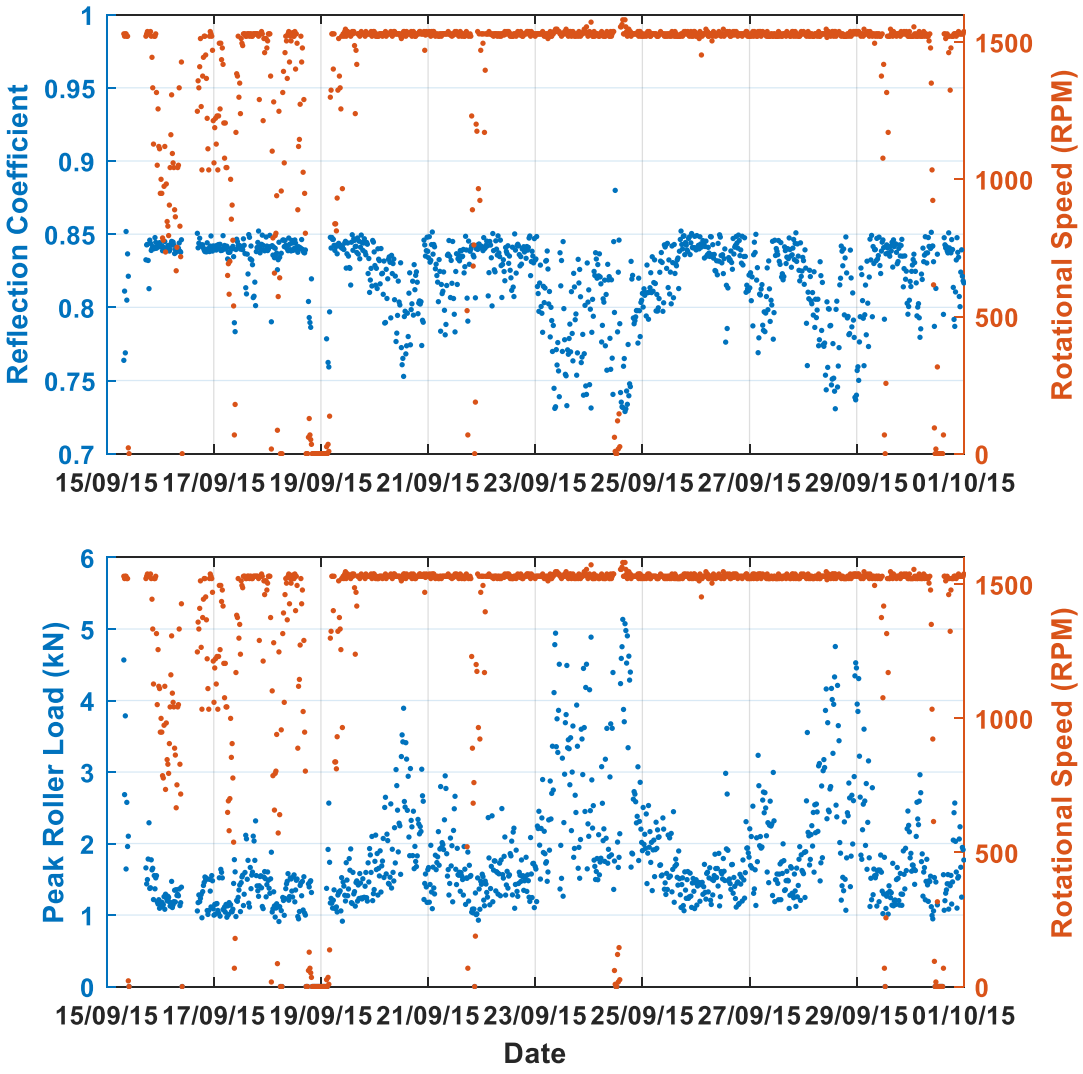

Figure 7.50 - Variation of roller minimum reflection coefficient, peak roller load and rotational speed across Sept 2015

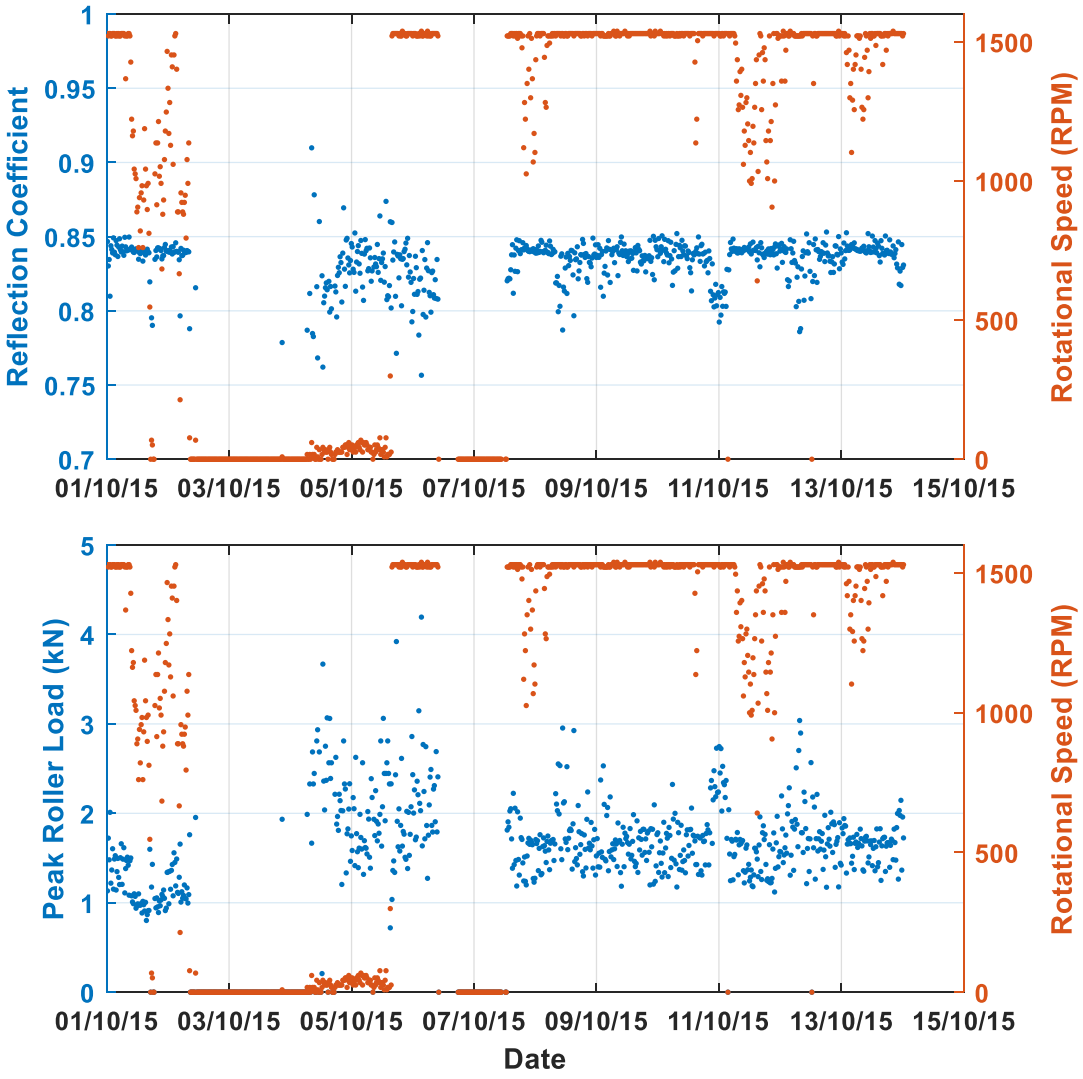

Figure 7.51 - Variation of roller minimum reflection coefficient, peak roller load and rotational speed across Oct 2015

Figure 7.50 and Figure 7.51 illustrates the variation of minimum reflection coefficient and peak roller load for measurements collected in Sept and Oct 2015. Contrasting to measurements in June 2015, no distinct low speed data portions can be identified and most of the measurements were captured at maximum HSS speed where the turbine is generating power. As such, measurements from Sept and Oct 2015 were all included to be correlated with turbine operating parameters.

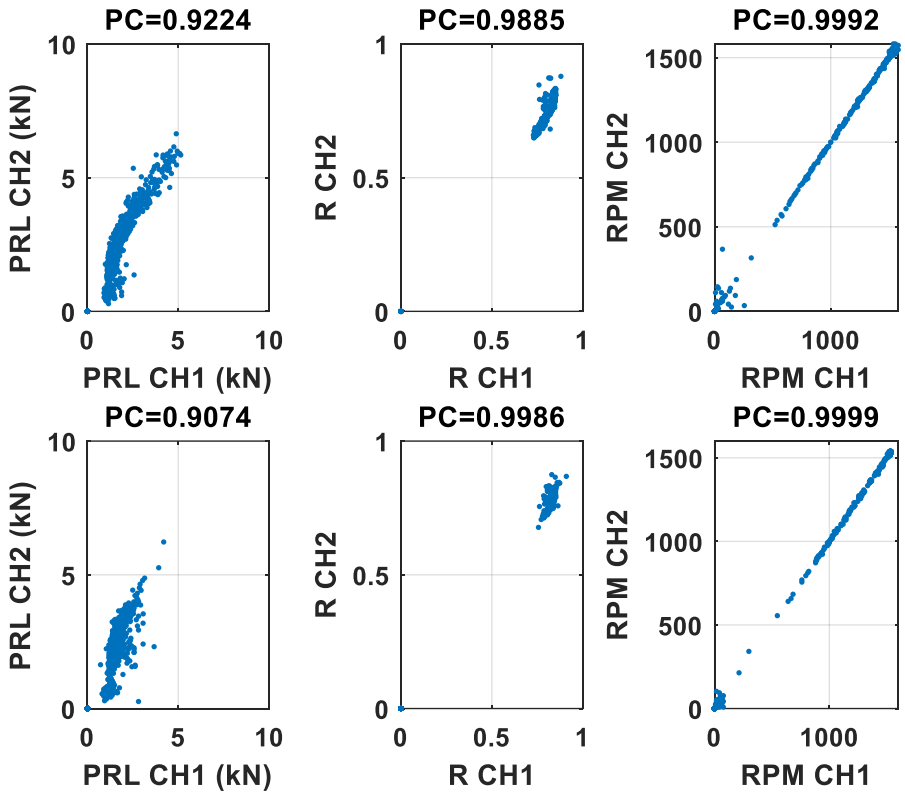

Figure 7.52 – Pearson correlation plots for Sept & Oct 2015

Figure 7.52 shows the PC plots for the Sept and Oct datasets respectively. The PC values for PRL is 0.9224 and 0.9074 whereas for reflection coefficient, it is 0.9885 and 0.9986 for Sept and Oct datasets. The PC values for RPM is greater than 0.999 for both months.

It is interesting to note that the PRL correlation plots resemble the positive portion of the hysteresis loop whilst the R correlation plots, albeit less apparently, resemble the negative portion of the hysteresis loop. This demonstrated the juxtaposition between the peak roller load and reflection coefficient measurements.

Trends across all measurements

CMS2 measurements from all 3 months were compiled and collated to produce the following plot. Figure 7.46 depicts the variation of minimum reflection coefficient and peak roller load with the rotational speed for both sensor CH1 & CH2. 1,900 datasets captured at rotational speeds between $0 - 1550\,RPM$ were collated to show an overview of the trends of the minimum reflection coefficient and peak roller load across the varying rotational speeds.

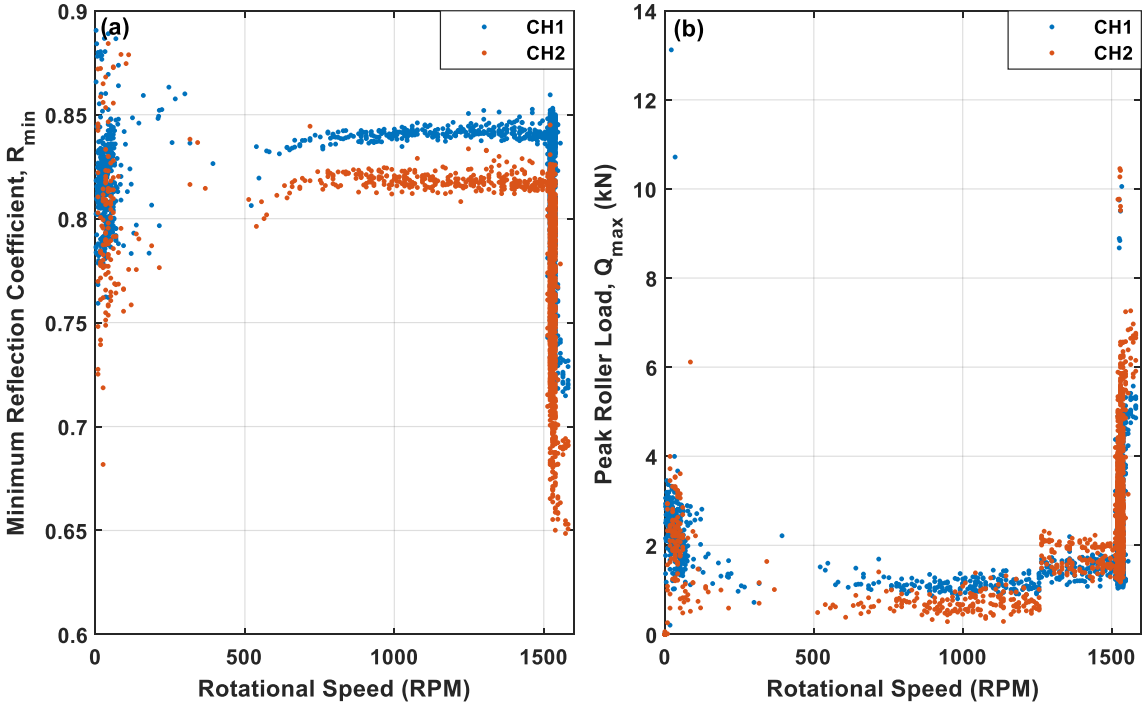

Figure 7.53 – Variation of minimum reflection coefficient and peak roller load with rotational speed

In general, as the rotational speed increase (and the load remained constant) it is expected that the reflection coefficient would increase as a thicker lubricant film is generated. This can broadly be observed within Figure 7.53(a). However, during normal operation, the bearing load rarely remain the same when turbine shaft speed increases. Two turbine operational regimes can be observed:

i) **Transitional (0 – 1499 RPM)** where the wind speed is less than the rated speed and the wind turbine is still ramping up.

ii) **Steady state (1500 RPM)** where the wind turbine has achieved its rated rotor speed and the generator is producing power.

For the minimum reflection coefficient plot (which can be viewed as an indication of lubricant film thickness) the trend is analogous to a Stribeck curve despite the

Stribeck curve plotting friction as opposed to film thickness. At low bearing speeds, *R* increases briefly before decreasing and finally increasing constantly until achieving the rated rotor speed of $1500\,RPM$. The minimum reflection coefficient then exhibits a range of values at $1500\,RPM$; this is resulted from an increase in bearing loading as the generator begins producing power. This increase in load is seen within the maximum roller load measurements at $1500\,RPM$. The increasing trend of R_{min} is also consistent for both sensor channels across the rotational speed, with an offset between the two channels due to the positions of the sensor within the bearing loaded zone.

The load measurements, Q_{max}, depicts an interesting feature; at low speed $(0 - 1300\,RPM)$ measurements from CH1 is higher than CH2, despite the fact that CH1 is nominally located within the less loaded region of the bearing. At around $1300\,RPM$, both CH1 & CH2 exhibit a step increase, with measurements from CH2 exceeding CH1. This is potentially a result of high measurement error at $< 1300\,RPM$ as the load on the bearing is small, and the proportion of error reduces as the bearing load increases. If the load measurements were accurate, this phenomenon will also manifest within the reflection coefficient plot, showing a step decrease around $1300\,RPM$ as the lubricant film decreases due to an increase in roller load. Evidently within the reflection coefficient plot, this is missing and thus roller load measurements $< 1300\,RPM$ are most likely inaccurate.

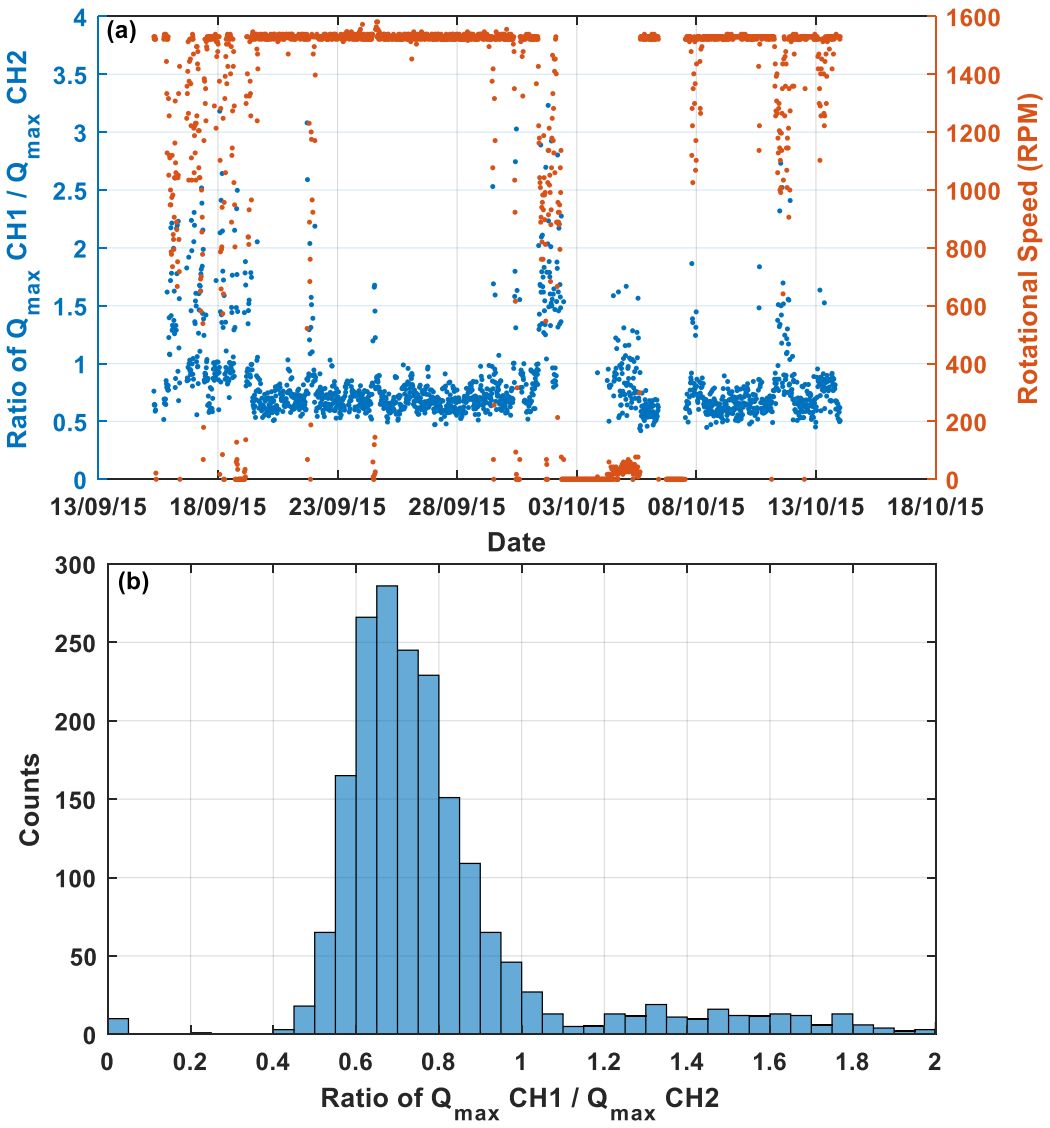

Figure 7.54 – (a) Ratio of peak roller load CH1 against CH2 across Sept and Oct 2015 and (b) histogram of the ratio

Figure 7.54 shows the ratio of peak roller load of CH1 against peak roller load of CH2 and the histogram of the ratio. The mean of the ratio was found to be 0.8442 whilst the median was found to be 0.7283. The peak count of the ratio however was found to be for values between $0.65 - 0.70$, which coincides with the theoretical value of 0.67.

Ratio values were seen to fluctuate excessively during transient rotational speeds ($< 1500\ RPM$), indicating that measurements captured during transient periods were more susceptible to noise.

7.6 Trends between ultrasonic measurements and turbine operating parameters

Due to the two condition monitoring systems (CMS1 and CMS2) acquiring data at different sampling intervals, the datasets need to be synchronised for any comparison to be drawn. CMS1 was captured at a higher rate than CMS2, and thus it was sensible to resample CMS1 measurements to the acquisition period of CMS2. To achieve this, interpolation of the CMS1 measurements was carried out. This would be fine for CMS1 parameters that are less volatile, such as HSS temperature however, interpolation on parameters such as wind speed and gearbox input torque might potentially introduce additional errors into the measurements.

7.6.1 LSS speed

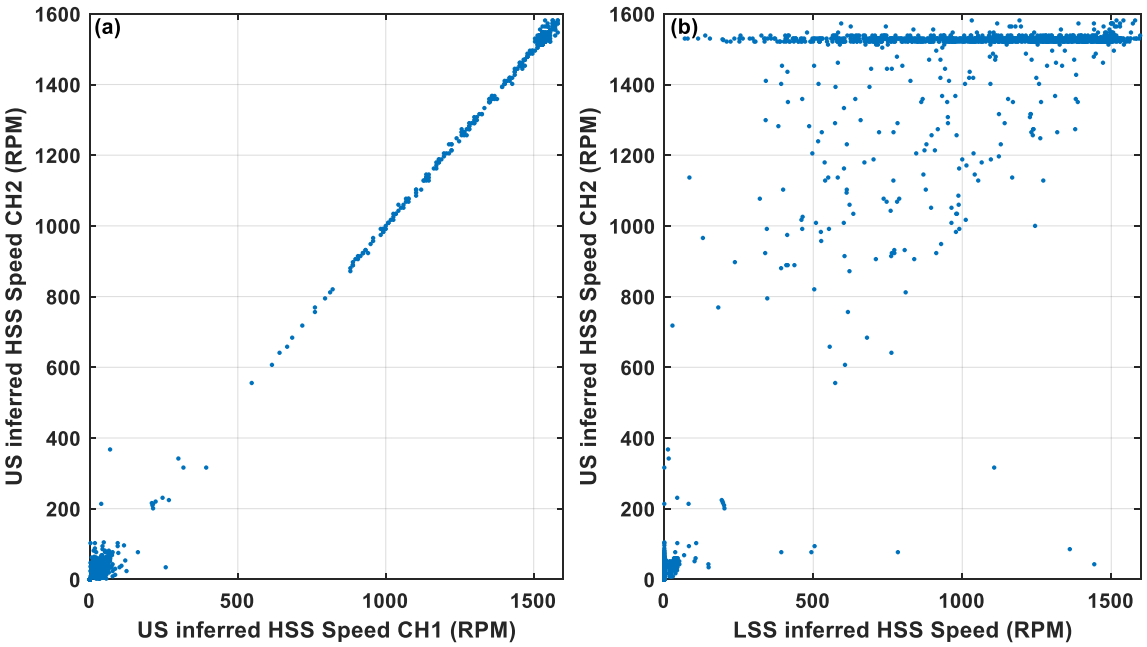

Figure 7.55 – Correlation between a) the ultrasonically inferred HSS speed of the two channels and b) the LSS and ultrasonically inferred HSS speed

Figure 7.55 illustrates the correlation between the ultrasonically inferred HSS speed of the two US channels and the correlation between the HSS speed measured from the hall effect sensor with the US inferred HSS speed. The two plots contrasted how well the two channels of ultrasonic measurement inferred the HSS speed and further confirmed the unreliable rotational speed measurement obtained from the hall effect sensor.

7.6.2 HSS temperature

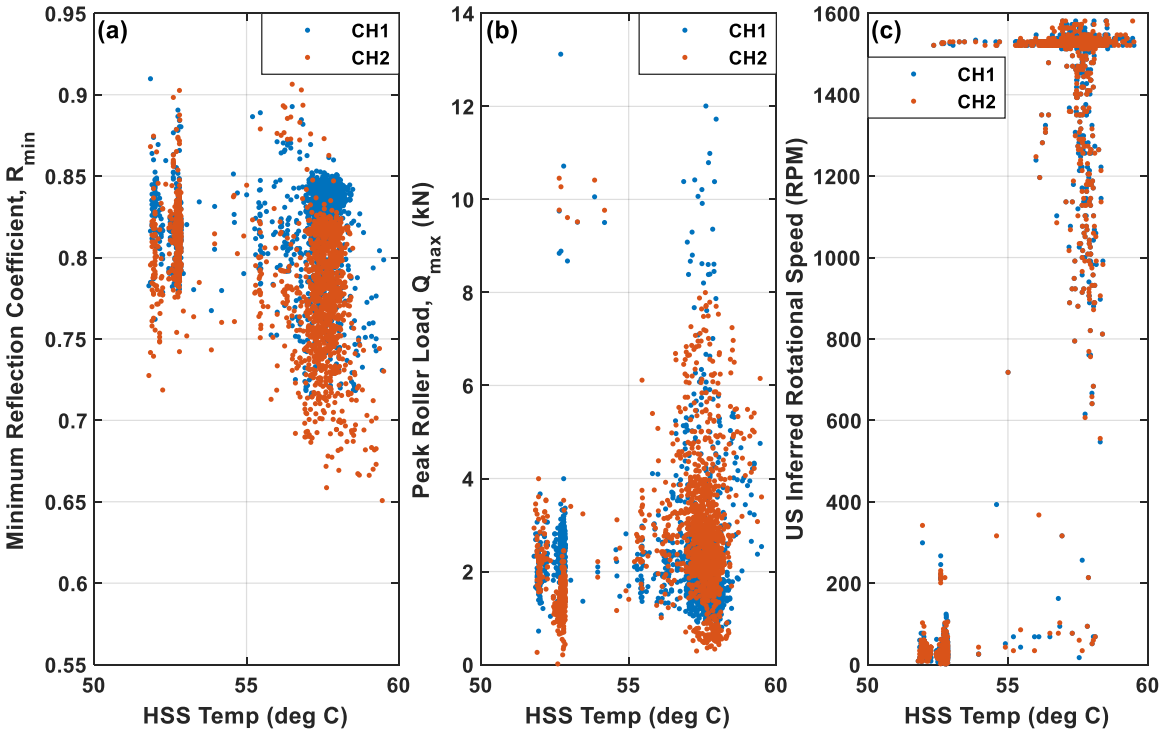

Figure 7.56 – Correlation of a) minimum reflection coefficient, b) peak roller load and c) ultrasonically inferred rotational speed with HSS Temperature

Figure 7.56 shows the minimum reflection coefficient, peak roller load and ultrasonically inferred HSS speed with the HSS temperature. Majority of the data were captured between the $55 - 60\,^{\circ}C$ region. No visible trend can be observed between the ultrasonic parameters and the HSS temperature, which is to be expected. The minimum reflection coefficient, albeit temperature dependant, considered the variation of temperature through acquisition of 'live reference' and the peak roller load measurements should be independent of temperature. In normal operating conditions without a defect in any components of the HSS, the HSS temperature would gradually increase with its rotational speed until it achieves an equilibrium and plateaus out, which can be seen in Figure 7.56(c). The range of temperature measurements observed reflect the status of operation of the turbine, whether the turbine was operating actively or just idling due to wind speed not reaching cut-in values. The low spectrum of the measurement $(50 - 55\,^{\circ}C)$ would be captured when the turbine is not actively operating whilst for the high spectrum, the turbine would be operating mostly beyond cut-in wind speed.

7.6.3 Gearbox input torque

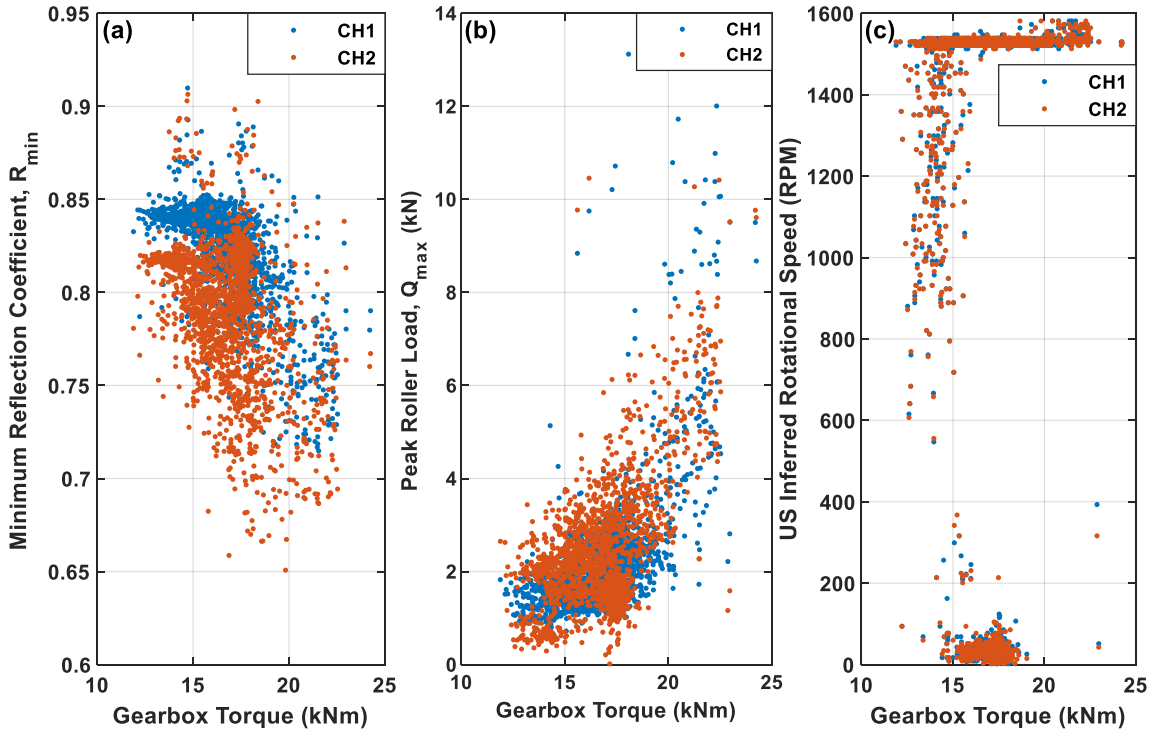

Figure 7.57 – Correlation of a) minimum reflection coefficient, b) peak roller load and c) ultrasonically inferred rotational speed with gearbox torque

Figure 7.57 shows the minimum reflection coefficient, peak roller load and US inferred HSS speed plotted alongside gearbox input torque. Despite the measurement having considerable amount of scatter, trends can still be observed for the minimum reflection coefficient and peak roller load measurements as the minimum reflection coefficient for both US channels decreases as the gearbox torque increases whilst the peak roller load increases with increasing input torque. Minimum reflection coefficient for CH1 is seen to be higher than CH2 and the opposite is true for peak roller load measurements. No visible trend can be observed between gearbox torque and HSS rotational speed. The majority of the dataset is concentrated at maximum HSS speed of $1550\ RPM$ whilst there is also a portion of data captured when the HSS speed is $< 200\ RPM$.

7.6.4 Wind speed

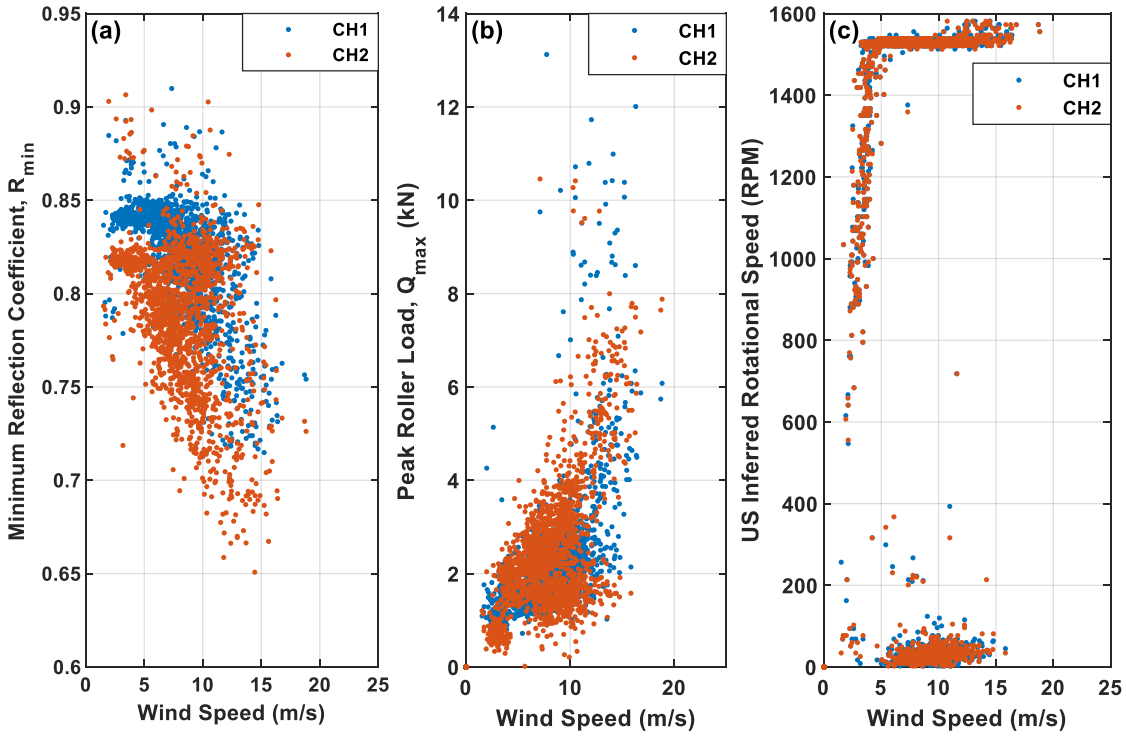

Figure 7.58 - Correlation of a) minimum reflection coefficient, b) peak roller load and c) ultrasonically inferred rotational speed with wind speed

Figure 7.58 shows the minimum reflection coefficient, maximum roller load and US inferred HSS speed with wind speed. As with gearbox torque, the minimum reflection coefficient will decrease with increasing wind speed. On the other hand, the peak roller load will increase as wind speed increases. Similar amount of a scatter can be observed for the data, potentially due to error in wind speed measurements as the wind field exposed to the anemometer is much different from that experienced by the wind turbine rotor blades. As wind speed increases and approaches cut-in wind speed of $3.5\ m/s$, the turbine begins rotating from idle and this can be observed in Figure 7.58(c). The HSS speed will continue to increase until it reaches max rotational speed at $1550\ RPM$. The measurements where the rotational speed is $< 200\ RPM$ and the wind speed is greater than $5\ m/s$ was potentially captured when the turbine was forcibly configured to not rotate either through application of hydraulic brake or the pitching of the rotor blades.

7.6.5 Generator power

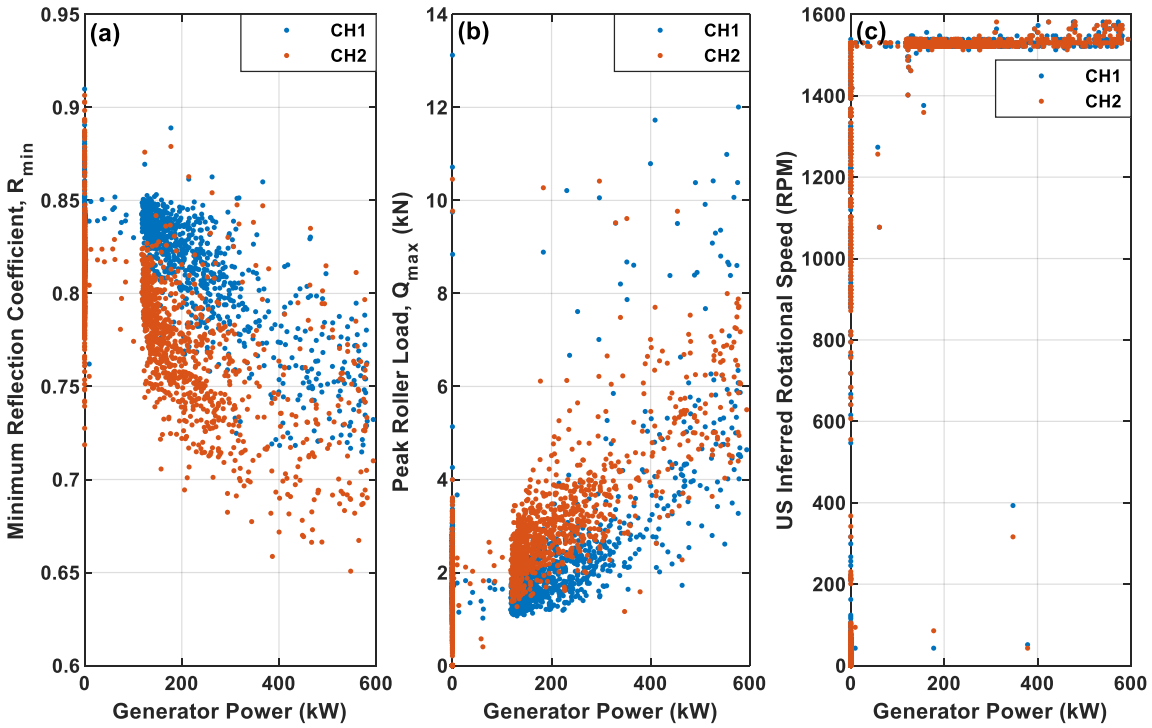

Figure 7.59 - Correlation of a) minimum reflection coefficient, b) maximum roller load and c) ultrasonically inferred rotational speed with generator power

Figure 7.59 shows the minimum reflection coefficient, maximum roller load and US inferred HSS speed plotted against generator power. Clear trends between minimum reflection coefficient and maximum roller load can be observed with increasing generator power. As the generator power increases, the minimum reflection coefficient decreases whilst the peak roller load increases for both US channels. Minimum reflection coefficient measurements from CH1 is clearly and more consistently higher than CH2 across the range of generator power. Distinct differences between CH1 & CH2 peak roller load measurements are also clearly visible with CH2 exhibiting higher values than CH1. The generator as expected will only start generating power when it achieves max rotational speed of $1550\ RPM$. This explains the trend in Figure 7.59(c). Between $0 - 1550\ RPM$, the wind turbine is operating in transient mode, as the rotational speed is increasing, and no power is generated. Upon reaching maximum rotational speed, the generator will begin generating power and its output will vary between $0 - 600\ kW$, depending on the wind speed and consequently the torque.

7.6.6 Minimum reflection coefficient with theoretical EHL film values

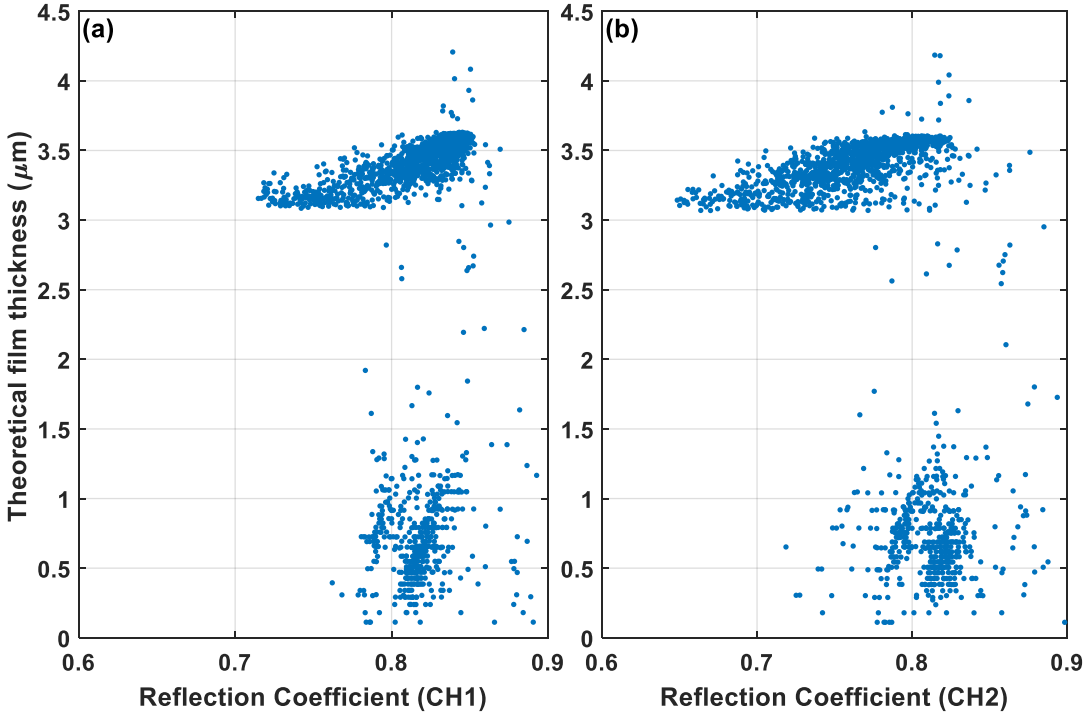

Figure 7.60 – Relationship between reflection coefficient and theoretical film thickness for (a) CH1 and (b) CH2 measurements

Figure 7.60 shows the relationship between the reflection coefficient measurements and theoretical EHL film thickness calculated using lubricant properties detailed in Table 6.1. For both CH1 and CH2 measurements, two distinct clusters of measurement were visible, concentrated at theoretical films greater than 3 μm and less than 1.5 μm. The former is associated with measurements captured at maximum bearing rotational speed of 1550 *RPM* whilst the latter is comprised of measurements <1000 *RPM*. As observed in §6.3.11, the reflection coefficient reduces with decreasing theoretical film thickness. Such a trend is more prominent in the higher rotational speed data cluster. A slightly greater range of reflection coefficient is evident in CH2 measurements due to the higher load the bearing experiences.

7.6.7 Bearing lubrication condition with HSS temperature & speed

In the "Automation for detection of bearing lubrication condition" section (page 204-208), attempt was made to categorise each dataset based on its lubrication condition. The current section aims to investigate whether there exist relationships between bearing lubrication condition and the temperature as well as the rotational speed of the HSS.

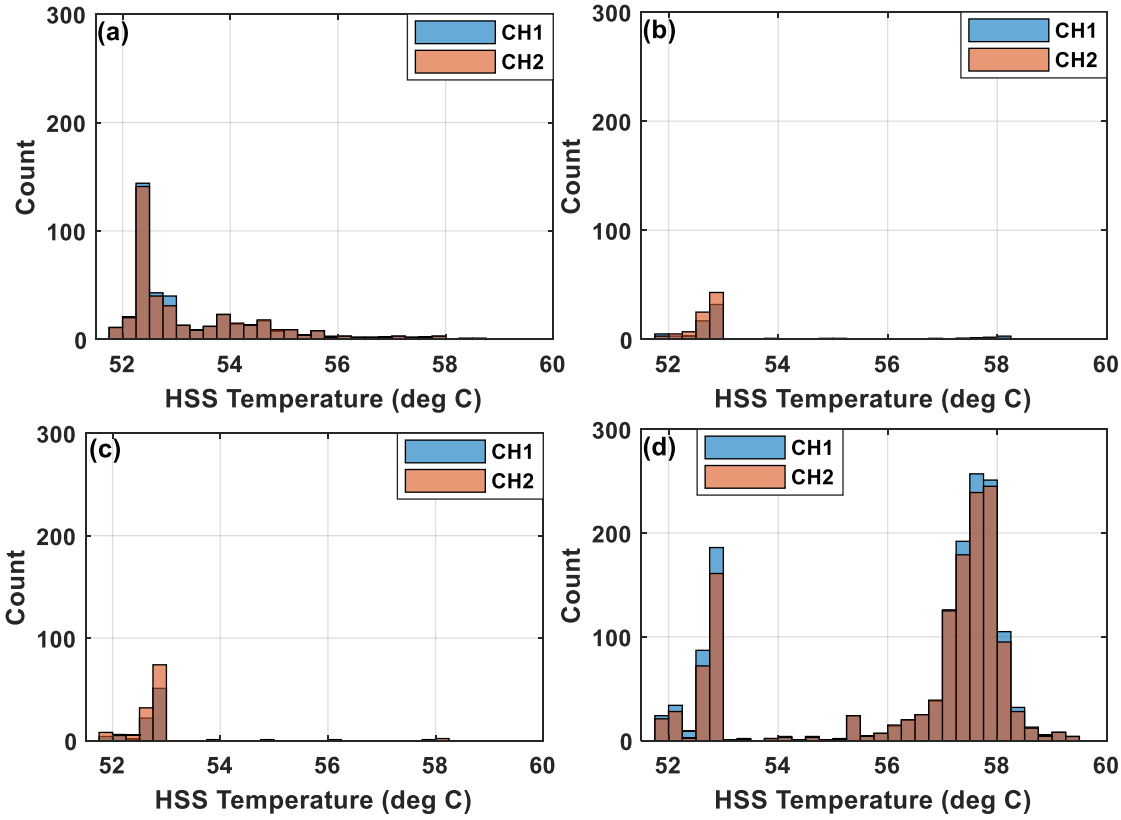

Figure 7.61 – Histogram of HSS temperature for datasets where bearing is (a) idle (b) insufficiently lubricated (c) partially lubricated (d) fully lubricated

Figure 7.61 shows the histogram plots for the HSS temperatures for both CH1 & CH2 datasets when (a) the bearing is idle, (b) the bearing is insufficiently lubricated, (c) partially lubricated and (d) fully lubricated. Temperatures are concentrated around $52.5\ ^{\circ}C$ for idle datasets as there is less heat generated from the HSS rotating. Interestingly, datasets exhibiting insufficient and partial lubrication are also concentrated in the lower temperature region, around $53\ ^{\circ}C$. This indicates that these datasets mostly occur during transient turbine operation where the turbine is either ramping up or slowing down depending on the availability of wind. For fully lubricated datasets, most of the data are concentrated between $57.0\ to\ 58.5\ ^{\circ}C$ with a minor peak of concentration around $53\ ^{\circ}C$. The higher temperature is a result of constant bearing operation at maximum rotational speed of 1550 *RPM*.

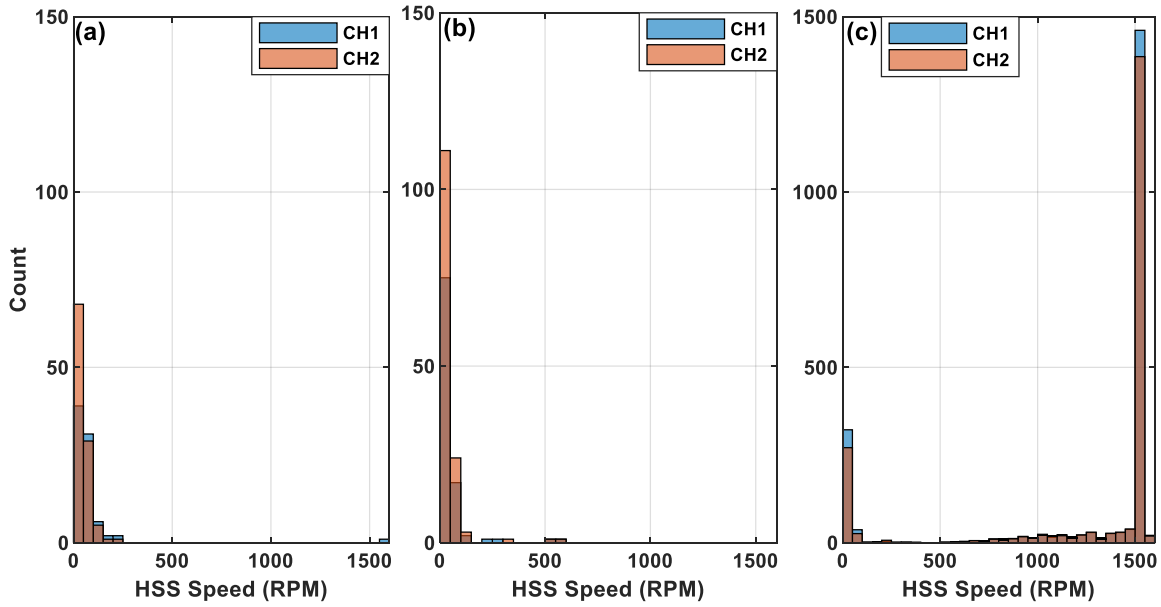

Figure 7.62 – Histogram of HSS speed for datasets where bearing is (a) insufficiently lubricated (b) partially lubricated and (c) fully lubricated

Figure 7.62 shows the distribution of datasets across the range of HSS speed for datasets which exhibited (a) insufficient lubrication, (b) partial lubrication and (c) full lubrication. Note that the scale between the 3 y-axes are different to show the data clearly. Datasets categorised as insufficiently or partially lubricated are mostly of low rotational speed ($< 500\ RPM$), adding proof to the theory that these are captured during transient operation. For the fully lubricated dataset, the measurements are mostly concentrated at the maximum speed of $1550\ RPM$ with a small portion concentrated at $< 50\ RPM$. The speed measurements coincide well with the temperature measurements and indicate that HSS temperatures at steady operating conditions of $1550\ RPM$ are much higher than that during transient operation. During transient operation, the bearing can be insufficiently, partially, or fully lubricated. Potentially this is due to low HSS temperature influencing lubricant viscosity and subsequently distribution of lubricant in the gearbox. At low-speed conditions, the lubricant behaviour is highly dependent on its own ability to reoccupy the region previously swept clean of lubricant by the roller and this is dependent on lubricant viscosity which in turn is dependent on temperature.

7.7 Discussion

7.7.1 Inferences

For measurements of each individual roller load, it was unexpected and interesting to observe that different rollers within a complement carry different load and subsequently have varying film thicknesses between them. This highlights a very interesting issue where the dimensional tolerance of the rollers potentially influences the bearing life. Rollers might vary in diameter or/and roller profile. In Chapter 4, attempt was made to quantify each contribution. Numerous literatures exist [197, 198, 199] studying the effects of off-sized rolling elements on bearing performance and also effects of varying roller profiles on bearing performance [200, 201]. An increase in roller profile height will result in the reduction in contact dimensions. This in turn will increase the load imparted on the roller and subsequently result in a decrease in bearing life. This agrees with findings of [201].

It is interesting to be able to observe and detect flow of lubricant within a bearing. This was demonstrated first time within an operational environment. What was interesting was the distinct lubricant behaviours at slow and fast rotational speed observed for an oil lubricated bearing. The lubrication behaviour for oil was found to be distinct from that of a grease lubricated bearing [202]. This provided insight into how oil is circulated within a bearing and serves as a method of evaluating the effectiveness of a lubrication system.

Insight towards how lubrication differs between transient and steady state potentially points towards most of the damage occurring during transient operation as more metal-to-metal contact would occur during this phase. Contrary to this, the measurements show that at low rotational speed or under transient operation, the bearing can be either insufficiently, partially, or fully lubricated whilst at high rotational speeds, the bearing is mostly fully lubricated. This finding is worrying for bearings located at the LSS portion of the wind turbines as they typically rotate at very low speeds.

7.7.2 Assumptions and limitations

Measurement of roller load

The ultrasonic load measurement technique converts change in time-of-flight into raceway deformation. Conversion of raceway deflection into roller load would require the use of contact models. Selection of appropriate contact model is relatively straight forward for simple geometries, i.e. cylinder on flat surface. This

however becomes much more complicated when involving raceway and roller with profiles in addition to their major radii. Elliptical contact will exist at low loading which would transition into line at higher loading. The main difficulty here would be to determine the profiles of roller and raceway, usually in microns, and subsequently determine an equivalent reduced radius for the two profiles. As bearing manufacturers are reluctant to provide this sensitive information, this typically would require measurements using a coordinate measurement machine or a surface profilometer.

Prior to analysis of the measurements, it was thought that the load imparted on the HSS bearing would be too low to exhibit a large enough change in time-of-flight to be detectable. This was however proven wrong as measurements of deflection and subsequently load was possible. Subsequently, this provided confidence that the method can be applied in a low load case and the lower bound of the load measurement method defined to be 1.70 *ns* (1 *kN*), with a smallest measurable raceway deflection of 0.02 *μm*, captured using a 100 *MHz* (10 *ns*) digitizer.

With the existing sensor measurement acquisition method, a reference pulse is obtained when a roller is not directly present under the sensor. It is subsequently assumed that no load is imparted on the raceway. This method of reference acquisition is only valid provided that no residual stresses are present within the bearing raceway. By comparing the unstressed speed of sound measurements of two sensors, at two locations, around the circumference of the bearing, the presence of residual stresses within the bearing raceway can be roughly determined. If a difference in sound speed greater than 5% exists between the two measurements, residual stress would be present within either one or both of the measured locations.

Currently, the effect of sensor averaging on the roller load measurements is a subject of continued investigations. It is theorised that the load measurement is an averaged value, measured across the piezo element's sensing region, however laboratory validation testing of a cylindrical roller loaded uniaxially between two plates appear to indicate that this does not influence the accuracy of the roller load measurement technique.

Since only two ultrasonic sensors were bonded onto the bearing outer raceway, the circumferential load resolution of the bearing is limited to only these two points. For bearing instrumentation involving a stationary raceway, a larger number of sensors bonded corresponds to a better circumferential load resolution. Alternatively, the circumferential load resolution can be improved with less instrumentation work

through instrumentation of the rotating raceway, i.e. the inner raceway. A single piezo element would be enough to map out the bearing circumferential load. However, this would also introduce additional complexities involving the use of slip rings as the wires will be rotating alongside the raceway.

Similar to any other measurement techniques, the accuracy of the load measurement technique is influenced by the lateral and vertical sampling resolutions; the former referring to the time resolution and the latter voltage resolution or signal amplitude. The higher the two sampling resolutions, the better the accuracy. Signal-to-noise ratio also influences the accuracy, at low loading, the change in ToF is very small and thus susceptible to larger errors. As the load gradually increases, the ToF change also increases, improving the signal-to-noise ratio and subsequently measurement accuracy.

Measurement of bearing lubrication condition

When taking a reference pulse from a dataset, there typically exist two raceway lubrication conditions. When a reference pulse is selected as the raceway is un-lubricated, i.e. steel-air interface, the reflection coefficient measurements will be true, whereas when a reference is taken when the raceway is lubricated, the reflection coefficient values will require an offset to be valid. The reflection coefficient value requires multiplication by 0.95 from unity as the R value for a steel-oil interface is 0.95. Often enough, recurring patterns within the reflection coefficient measurements will exhibit clues to which whether offsetting of the reflection coefficient measurements is required.

The amount of free surface oil film thickness necessary to produce a reflection coefficient of 0.95 is currently less understood. It is theorized that as the free surface oil film thickness reduces, the reflection coefficient will gradually rise from 0.95 to 1. In principle, a free surface oil film with a thickness less than the wavelength of the ultrasonic signal will be undetectable by the sensor and subsequently registers a reflection coefficient of unity.

Instrumentation and data acquisition

There exist multiple complexities accompanied with the installation of the CMS2 measurement system. The sensors are required to be oriented normal to the rolling surface to ensure sound waves propagate and strike the interface perpendicularly. For a tapered roller contact, as utilised in this study, this necessitates machining of the bearing raceway to accommodate the sensors; an alternative would have been the use of an angled boss. The intricacies associated with bonding of sensors onto the bearing raceway is further complicated by the difficulty in accessing key

strategic locations within the bearing. The presence of a bearing housing and the limited space within the wind turbine nacelle limit available options for positioning of sensors and routing of cables. As a consequence, retrofitting of ultrasonic sensors is highly unlikely without adequate access to a bearing. In this study, as a consequence of the complexity and access limitations in instrumenting a higher loaded bearing, such as a planetary bearing, a more accessible and easier, low loaded HSS bearing was instrumented instead.

For optimised sensor signal response and wiring requirements, the minimum width of the piezo-electric crystals is constrained to around $1\ mm$. Accounting for beam spread, the sensing region of the piezo crystals would be in the region of $3\ mm$. This is still large relative to the contact dimensions of the raceway-roller interface of less than $0.5\ mm$ and as measurements obtained are averaged across all the pulses captured within the sensing region, detailed features of the contact region, such as the EHL constriction region is currently not possible.

Although attempt was taken to limit the volume of data produced through capturing one second of data every 20 minutes, huge amounts of data were still accumulated. This is partially caused by the high PRR required, producing a $50\ MB$ size data for each capture. However, the measurements were often recorded when the turbine was idle, resulting in redundant measurements. It would be better if data capture can be concentrated during occurrences of turbine transient events, as these are thought to be most detrimental to bearing life. This could potentially be implemented through measuring turbine operating parameters such as wind speed or generator/gearbox torque and executing data capture when these parameters are fluctuating excessively.

Notwithstanding the above, the approach has demonstrated its capability, for the first time in measuring the load directly imparted by each rolling element on the bearing raceway and indicated how this is very likely to be resulted from the geometry of the rolling element. The flow of lubricant around the bearing has also been measured qualitatively and various interesting phenomenon were shown. Above all, the use of relatively low cost piezo-electric crystals for ultrasonic pulsing and receiving, partially alleviates any economic considerations and facilitates instrumentation of array of sensors onto the bearing raceway.

7.8 Conclusions

- Ultrasonic measurements of load and lubrication were successfully obtained from an operational HSS gearbox bearing within the wind turbine in the field

- Lubricant film generated by the same roller within the complement does not vary much between revolutions and more variation is observed across the complement
- Load imparted by the same roller within the complement varied less between revolutions compared to that of all the rollers across the complement. The variation in load between different rollers is theorized to be resulted from slight variation in roller profile dimensions, stronger evidence is necessary to further validate this. This can be done through testing a bespoke bearing with known varying roller profiles across its complement.
- The trend of reflection coefficient and roller load across two measurements are consistent, a high roller load resulting in a lower reflection coefficient, indicating a thinner oil film and potentially metal-metal contact and vice versa.
- Two regimes of bearing operation, transient and steady state, were identified when roller load and reflection coefficient were plotted alongside bearing speed. As the bearing starts rotating from idle up to its rated speed, the minimum reflection coefficient gradually rises as more oil is entrained into the contact. No visible trend was seen for the peak roller load during this phase. The minimum reflection coefficient and peak roller load then exhibit a range of values at rated speed once the generator begins producing power.
- Two distinct lubrication reflow behaviours were identified, and this was observed to be influenced by bearing rotational speed. At low bearing rotational speeds, the lubricant is allowed adequate time to fill the raceway region previously voided in lubricant by the outgoing roller. At higher rotational speeds, the lubricant is forced into the region by the incoming roller. There were instances within the measurement datasets where some rollers did not show a fully flooded inlet, whilst near neighbours did. This shows the stochastic nature of the bearing lubrication.

8 DISCUSSION

The discussion chapter is separated into two sections. The first section discusses the significance and novelty of the ultrasonic measurement system. The subsequent section discusses its limitations and ideas for further work to address these limitations and for the continued development of the ultrasonic measurement method and monitoring system.

8.1 General discussion

The implementation of a bearing ultrasonic load and lubrication system for monitoring wind turbine bearings would help improve the durability of WT bearings. Direct roller and bearing load field data would prove invaluable in understanding the magnitude and propensity of transient overloading and load reversal events the bearing experiences. These events were thought to be the main factors which result in premature bearing failure through RCF and WECs. Such data and general bearing operational load measurements would also allow for alternative bearing life calculation methods which would account for these premature failures, facilitating modelling studies on the effect of these loading with bearing durability and subsequently the design of more durable bearings. These data alongside the bearing lubrication measurements can also be used as parameters for general condition monitoring of the bearing and better maintenance scheduling.

The field bearing lubrication condition would allow for better understanding of the variation in lubrication condition during turbine operation and the effectiveness of lubrication for all the bearings present in the drivetrain, allowing for improved designs of lubricating systems or quick remedy of insufficiently lubricated bearings to ensure the bearings operated under optimally lubricated conditions.

8.2 Further Work

8.2.1 Validation of the ultrasonic load measurement

Due to the presence of misalignment on the full-scale test rig, the platform was not suitable for validation testing of the load measurement method. A new platform which incorporated a flat plate-roller-flat plate arrangement is suggested where roller load can be applied hydraulically, and these can be compared directly without the use of empirical relationship to convert bearing load into roller load. The jig also serves as a good platform for understanding the beam spread problem of the ultrasonic sensor. This can be achieved through varying the distance of the ultrasonic sensor from the roller-flat plate contact. Apart from that, validation and

comparison of the existing load-deflection equations can be carried out. A study to which the effect of roller profiles on edge loading and misalignment is also possible on the jig.

A study to confirm the effect of non-contact stresses such as multi-axial stresses, hoop stresses in bearing rings and macro deflections on the accuracy of the ultrasonic deflection measurement is also necessary. It is theorised that if the reference is taken with such stresses, then the measurements will 'account' for these effects, but data is required to confirm this and also study the significance of these effects on the deflection measurement.

The effect of varying roller profiles on the roller load also requires further validation tests. This can be done by measuring the roller load from a bespoke test bearing with rollers of known varying profile height. The roller profile height could be varied consecutively (one high, one low) across the complement to determine whether such a trend across the roller complement would also be visible in the roller load measurements.

8.2.2 Alternative methods for deflection-load conversion

The current work used a simple Hertzian point-line contact equation to convert raceway deflection into load. This limits the applicability of the method to only conversion of maximum raceway deflection measurements taken at the centre of the raceway and roller. To overcome this, slicing techniques [187, 203] or even simple FEA modelling utilising the measured raceway and roller profiles can be used. This however would increase the complexity of the load-deflection calculations but allows for load profile measurements across the raceway and roller.

Measurement of raceway and roller profiles were conducted using an optical profilometer which has limited measurement length. An alternative would be a Talysurf stylus profilometer which has a range of 120 *mm*, however for this work the author did not have access to one.

8.2.3 Measurement of transient load events

Unfortunately, the measurements obtained from Barnesmore do not contain any datasets which indicate the presence of transient load events. This was somewhat expected as the bearing is located on the HSS and load fluctuations and reversals are being "filtered" by bearings located closer to the rotor blade such as the main bearings or the planetary bearings. Consequently, it will be interesting to be able to validate the capability of ultrasound in measuring these events. This can be done

through instrumenting the main bearing of a WT or one of the inner raceways of the planetary gear. Measurements taken during the application of turbine hydraulic brake, pitching of blades would also be interesting. It is also interesting if collaborative work can be conducted with parties such as NREL or SKF which own a gearbox test facility or a large bearing test rig. The ultrasonic load measurement methods can subsequently be compared with other load measurement techniques such as measurements from strain gauge and film measurements from capacitance sensors.

8.2.4 Measurement of EHL lubricant film thickness and free surface lubricant on raceway

Currently, due to the large sensor beam width compared to the EHL film contact region, measurements of reflection coefficient cannot be converted to film thickness through the spring model. Methods of focusing potentially could reduce the beam width and alleviate this problem. These include utilisation of physical lenses to focus the beam, data processing methods utilising an array of sensors termed total focusing method and phased array systems.

The thickness of the free surface lubricant which corresponds to a reflection coefficient of 0.95 is still a subject of further investigation. This can be conducted through instrumenting an array of sensors of various frequency bandwidths and measuring the free surface film thickness through resonance dip method. This would confirm the theory that as the reflection coefficient increases from 0.95 to 1, the free surface lubricant film thickness would decrease. This would allow for a table for conversion of reflection coefficient to free surface lubricant film for a given sensor frequency.

The effect of the lubricant inlet position to the lubrication condition of the raceway requires further investigation. Through dry testing, recurring patterns between the roller passes were confirmed to be resulted from the flow of lubricant on the raceway surface. Positioning of the lubricant inlet closer to the sensing region would validate the fully lubricated reflection coefficient pattern and perhaps limiting the flow of lubricant would allow for validation of partially and insufficiently lubricated reflection coefficient patterns. Investigating the effect of reflow time with different bearing geometries such as a longer roller would also be interesting. In theory, if the sensor sensing region is kept constant, the reflow time would potentially not vary significantly to measurements taken using a shorter roller.

8.2.5 Recommendations for improvements for an US WT-CMS

Despite not participating in the design, instrumentation and implementation stages for the wind turbine ultrasonic monitoring system, there were plenty of lessons that were learnt from gathering, processing and analysing the data obtained.

It is desirable for future instrumentation that the CMS which captured turbine operating conditions is to be synchronised with the US CMS. This would allow direct comparison between the two measurements, eliminating the error arising from having to interpolate between datapoints to synchronise the two datasets.

Although bearing rotational speed can be inferred through ultrasonic measurements, it is also desirable that reliable measurements of bearing rotational speed be obtained. This can be easily achievable through installation of an encoder. The installation of an encoder also allows for the position of the rotating raceway to be known, facilitating comparison and synchronization across datasets.

Ultrasonic measurements were triggered to capture every 20 minutes which at numerous instances captured data when the bearing is idle. The datasets were useful for statistical error analysis however, this does not justify capturing hundreds of idle datasets and a better method of triggering data capture is required since each ultrasonic dataset occupy a considerable amount of storage space (~250 MB). A better alternative would be triggering data capture through bearing rotational speed measurement. Data acquisition may be halted when bearing is idle and resumed during transient and steady state operation. Another interesting alternative would be to focus measurements during transient loading events where it is theorised to cause the most damage to the bearing, but this is difficult to achieve as the onset of these event would need to be predicted to allow for the initialisation of the data acquisition routine. Potential triggers would include the hydraulic pressure during emergency braking and pitching of the rotor blades.

Although the current hardware setup has been successfully operating throughout the commissioning period, it is far from the ideal setup. It is not ideal to locate the PC-based FMS system in the nacelle as the system is extremely sensitive to mechanical vibrations, however this had to be done as long cables between the FMS and sensors would result in poor measurements. It was found that at the end of Jan 2016, the system failed to boot up. Upon removal and inspection of the system, the PC was found to be defective, however all the ultrasonic acquisition cards were functioning well. Alternatives for the system are under trial and these systems would also have to cope with the requirement of withstanding the harsh nacelle environment.

On the issue of large data size, it was proposed that data acquired can be stored in a hard drive which is then uploaded to cloud to be processed readily and deleted thereafter. This can only be implemented if a robust data processing routine is designed and the system is utilised as a 'condition monitoring' system.

Above all, the use of custom, relatively low cost piezoceramic sensors for ultrasonic pulsing and receiving and in-situ monitoring of a HSS gearbox bearing has been a success. Limitations however currently rest on the hardware aspect of the system to accommodate more sensing channels without sacrificing pulsing rate, to be sufficiently robust to withstand the harsh conditions within a wind turbine nacelle, and to allow for cloud capabilities for data storage and processing.

9 CONCLUSIONS

As a closure to this thesis, the original contributions and main findings of this study will be presented which included results from the investigation on second and third order elastic constants of EN31 bearing steel and also measurements from both lab based full-scale cylindrical roller bearing and field based HSS tapered roller bearing testing.

9.1 Original contribution of research

Throughout the research conducted within this thesis, several novel techniques were developed which widened the field of knowledge. These are summarised below:

- Measurements of second and third-order elastic constants of EN31 has been successfully carried out for the first time.
- A novel method for inferring the lubrication condition of the inlet region of each rolling element for rolling element bearings has been developed.
- For conversion of ultrasonic deflection measurements to roller load, a new relationship which is better representative of the contact conditions at both low and high bearing load has been used.
- The ultrasonic measurement techniques have been successfully implemented onto an operational wind turbine high-speed shaft bearing for the first time.
- Unprecedented real time, in-situ measurements of bearing load and lubrication have been successfully obtained from the field instrumented bearing.
- Features observed include variation of roller load across different rollers within a bearing complement, variation of roller load and lubrication along with turbine operation, and various bearing lubrication condition.
- For laboratory-based full scale CRB testing, raceway deflection alongside bearing lubrication condition have been successfully obtained across an array of 7 longitudinal sensors for the first time.
- Raceway deflection measurements provided insight into the alignment condition of the bearing assembly, allowing for successful diagnosis of bearing edge loading and misalignment.

9.2 Key findings

9.2.1 Understanding the effect of stress on ultrasound

An experiment was designed to better understand the effect of stress of ultrasonic waves and subsequently quantify the second and third order acoustoelastic constants of EN31 bearing steel. Three experiments were conducted with varying loading range and steps and also test component geometry. The EN31 bearing steel samples were instrumented with ultrasonic sensors on the side and placed onto a base plate which has a groove machined at the bottom with ultrasonic sensors instrumented within the groove.

Measurements of acoustoelastic constants of EN31 bearing steel

It was found that plastic flow within the EN31 sample was able to be detected in the measurements. This was typically recorded during the first couple of loading and unloading cycles which affected the time-of-flight measurement. An exponential shape also exists for the acoustoelastic constant measurements with increasing applied stress. As the compressional stress increases, the variation in acoustoelastic measurements decrease. The geometry of the test component was also found to influence the measurements. The shape of the puck specimen resulted in uneven stress distribution and subsequently erratic, non-linear measurements from the sensors instrumented on the side of the specimen, which were perpendicular to the applied stress. The linear measurements obtained from the square column verified this. Measurements of acoustoelastic constant for EN31 bearing steel was found to be similar to that of rail and Hecla steel reported in literature. This is also true for the second and third-order elastic constants measured. It was also found that the longitudinal acoustoelastic constant measured in this work (-2.26) only differed by less than 1 % compared with the previous value obtained (-2.24). Measurements of shear acoustoelastic constant (-0.25) indicated much less influence of stress on the change in time-of-flight values compared with the influence from deflection and potentially better applicability for roller load measurement.

Quantification of ToF errors arising from data processing

The compression testing measurements also allowed investigations into the data processing methods used to compute the pulse time-of-flight. These include the optimum number of interpolation points and also the effects of different methods of processing (Hilbert transform vs pulse cross-correlation) on the time-of-flight measurements. An optimum number of interpolation point of 5×10^5 was identified, providing a time resolution greater than $3.98 \times 10^{-6}\ \mu s$, and keeping the

error in the 10^{-12} magnitude whilst not utilising excessive computational power. The Hilbert transform cross-correlation method incurred an error of $\pm 0.01\ \mu s$ due to slight differences in the pulse envelopes of the first and second reflection. However, this is only valid for a reasonable bell-shaped pulse and for pulses with more erratic waveform, it would be expected that a higher error exists.

9.2.2 Influence of roller and raceway profiles on roller load

The load-deflection relationship

The ultrasonic reflectometry measurements compute raceway deflection which requires contact models to be applied to obtain roller and subsequently bearing load. Previous model utilised only accounted for line-contact. Due to the utilisation of raceway and roller profiles in rolling element bearings for reduction of edge loading, contact in bearings are often elliptical which gradually transitioned into line with increasing load. A new model which accounted for the curvatures of raceway and roller and also the transition from elliptical to line contact was identified and used. The method requires information on the raceway and roller geometries including profiles which subsequently can be replaced with constants to facilitate the use of the equation.

Variation of roller profiles

A study was subsequently carried out to investigate the variation of roller profile height across a full complement of 20 rollers. Rollers from a used 32222 TRB were utilised. The roller profiles were measured using a non-contact optical profilometer. It was discovered that the profile height of the 32222 TRB rollers was seen to vary from $14.03\ \mu m$ up to $18.93\ \mu m$. Theoretical calculations found that this could potentially result in a load fluctuations of $\pm 5\ \%$ during bearing operation.

9.2.3 Lab-based, full-scale CRB testing

A test rig on loan from *Ricardo plc* was utilised for full-scale laboratory testing of NU2244 CRB bearings. These bearings were utilised in the planetary gear stage of an epicyclic wind turbine gearbox. The NU2244 inner raceway was instrumented with an array 7 longitudinal and 7 shear sensors across the width. The rig was driven with an electric motor and bearing load was provided through a hydraulic power pack. The loading and rotational speed of the bearing was varied between $0 - 1000\ kN$ and $20 - 100\ RPM$. Lubricant viscosity utilised during testing was also varied to observe the effects of varying lubrication on the ultrasonic measurements.

Trends from roller pass

Consistent patterns were produced in deflection and reflection coefficient measurements as the roller traversed across the sensor. These manifest as peaks and dips within the deflection and reflection coefficient measurements. At the inlet and outlet of a roller pass, interference fringes exist where reflection coefficient was seen to rise above 1. These resulted in clear distinction of the contact inlet and outlet to be impossible and subsequently, inferring contact size through deflection and reflection coefficient measurements was not possible. Investigations into these fringes found that they were frequency dependant and independent of bearing operation (bearing load and rotational speed).

With an increase in bearing load, the peak deflection values were observed to also increase whilst the minimum reflection coefficient values decreased. Trends associated with increasing bearing rotational speed was less obvious. A slight increase was noticed for peak deflection values and a slight decrease for the minimum reflection coefficient as the rotational speed increases. This was attributed to slight variation in bearing load as the rotational speed increases.

Periodicity in the peak deflection values and minimum reflection coefficient values was also observed. An investigation into the frequency of the periodicity yielded no additional information. The variation of deflection and reflection coefficient for each individual rollers were found to be less compared to the variation across the full rolling element complement. These might be resulted from the lack of concentricity of the rotating component or micro geometrical differences in the profiles of the roller and raceways.

Measurement of bearing load/deflection

Through comparing deflection and reflection coefficient measurement across all the sensors instrumented along the width of the raceway, it was found that the peak deflection location was not located at the centre of the raceway, indicating the presence of edge loading. As such, the equations which convert deflection to roller load were not valid and cannot be applied. Deflection measurements were shown subsequently, rather than roller load. Despite the weakness of the deflection-load relationship, the findings demonstrate the capability of an array of ultrasonic sensors in detecting edge loading.

The deflection measurements obtained for the 3 different lubricants used were compared with that calculated theoretically. Measurements obtained from 2015 were also included in the investigation. It was found that lubricant viscosity, as expected, do not influence the deflection measurements. Measurements taken in

2020 showed good agreement at low loading but gradually deviate from theoretical values at higher load. Measurements taken in 2015 showed a similar trend, however with less deviation at higher loading. This indicated that in 2015, the rig was much better aligned compared to in 2020.

Measurement of bearing rotational speed

Due to the manifestation of peaks and dips as roller passes within the measurements, it is possible to infer bearing rotational speed. This was successful as ball pass measurements and subsequently bearing rotational speed for each dataset was computed. Comparison between ultrasonically inferred roller speed with demand speed was carried out for VG32 and VG320 datasets. It was found that for the VG32 measurements, the bearing rotational speed only deviated by $\pm 5\ RPM$ whilst a maximum drift of $21\ RPM$ was observed for the VG320 datasets. This was suspected to be a result of the inability of the motor to rotate at designated speed of 80 and $100\ RPM$ when using lubricant with higher viscosity under increasing bearing loading. This specific case demonstrated the capability of ultrasound to detect when unsuitable lubricant is utilised, or insufficient motor torque is present albeit not very applicable in wind turbines as no "user-desired" rotational speed exists.

Measurement of bearing lubrication

The use of the spring model for measurement of lubricant film thickness was not possible due to various reasons. This was a result of a mixture of high contact loads, low lubricant viscosity, low entrainment speed and the averaging effect of the sensor. The operational conditions of the bearing resulted in boundary and mixed lubrication which caused lubricant film measurements to not be meaningful. An alternative method for detection of lubrication was utilised instead. This involved the use of reflection coefficient measurements between roller passes and the identification between a steel-air interface where the reflection coefficient is unity and a steel-oil interface where the reflection coefficient is 0.95. Subsequently, patterns within the roller passes can be utilised to determine the lubrication condition of a bearing.

A parameter termed the "lubricant reflow time" was defined, which is the time taken for the reflection coefficient after a roller pass to return to 0.95. The lubricant reflow time was found to be influenced by bearing rotational speed, lubricant viscosity and also slightly by bearing load. The reflow time was found to increase slightly with bearing loading, decrease with both increasing rotational speed and lubricant viscosity.

9.2.4 Field measurements of an HSS TRB from an operational wind turbine

As part of a previous collaboration project involving The University of Sheffield, The University of Strathclyde and *Ricardo plc*, a HSS gearbox bearing within an operational wind turbine was instrumented with ultrasonic sensors to monitor the bearing condition. The bearing instrumented was a 32222 TRB and two sensors were installed on the outer raceway. They were located at the centre and the edge of the bearing maximum loaded region. Apart from ultrasonic sensors, wind turbine operating parameters were also recorded, allowing correlation between the two measurements.

Trends from roller pass

Trends similar to those observed during laboratory testing on a CRB were also observed in the measurements taken from an operational HSS gearbox bearing. The periodicity in peaks and dips of the roller load and reflection coefficient measurements was observed, again potentially attributing to micro geometrical differences between rolling elements or concentricity issues in the rotating components.

Since no encoder was installed on the bearing, synchronisation of the ultrasonic measurements was carried out through matching the trends within the measurements for the two measurement channels. The peaks and dips for each roller pass were able to provide sufficient clue to which the dataset can be rearranged.

Measurement of bearing lubrication

The variation in lubricant reflow time with bearing rotational speed was found to be an exponential relationship. This was found to be a result of two different lubricant reflow patterns, at low and high rotational speed. At low rotational speed, the lubricant was seen to be able to freely flow back into the region previously swept clean by the roller. At high rotational speed, the incoming roller was seen to force the lubricant into the void.

Due to the varying patterns of reflection coefficient measurements between roller passes and subsequently the distinct patterns manifesting in histograms, it was possible to distinguish the lubrication condition of each dataset into various categories such as partially, fully, or insufficiently lubricated. An automation algorithm was also successfully developed to sort the datasets into their respective categories.

Correlation of ultrasonic measurement with wind turbine parameters

Two regimes of turbine operation were identified through correlating the rotational speed measurements with minimum reflection coefficient and peak roller load of the bearing. These were transitional where the wind speed is below rated speed and the turbine was ramping up and steady state, where the turbine has achieved its rated speed and generating power.

Correlation between ultrasonically inferred bearing rotational speed and LSS calculated speed found that the LSS measurements were intermittent due to poor mounting conditions of the Hall effect sensor. No apparent trend was found between minimum reflection coefficient and peak roller load against HSS temperature. The trends of ultrasonic roller load and reflection coefficient measurements with increasing wind speed, generator power and gearbox input torque were found to be similar. As the wind speed, generator power and gearbox input torque increases, the minimum reflection coefficient was seen to decrease whilst the peak roller load increased. Insufficiently lubricated and partially lubricated datasets were found to be of low rotational speed (< 500 *RPM*). For fully lubricated datasets, a wide range of rotational speed was found.

REFERENCES

[1] The Meteorological Office [Met Office]. *What is climate change?* Available from: http://tiny.cc/tgoksz

[2] The National Aeronautics and Space Administration [NASA]. *Climate Change: How Do We Know?* Available from: http://tiny.cc/2hoksz

[3] The National Oceanic and Atmospheric Administration [NOAA]. *NOAA Merged Land Ocean Global Surface Temperature Analysis (NOAAGlobalTemp).* Available from: http://tiny.cc/jhoksz

[4] Le Treut, H. et al., *Historical Overview of Climate Change*. In: Climate Change 2007: The Physical Science Basis. Contribution of Working Group I to the Fourth Assessment Report of the Intergovernmental Panel on Climate Change [Solomon, S., D. Qin, M. Manning, Z. Chen, M. Marquis, K.B. Averyt, M. Tignor and H.L. Miller (eds.)]. 2007: Cambridge University Press, Cambridge, United Kingdom and New York, NY, USA.

[5] The Meteorological Office [Met Office]. *Global surface temperatures in 2017.* Available from: http://tiny.cc/ljoksz

[6] Forster, P. et al., *Changes in Atmospheric Constituents and in Radiative Forcing*. In: Climate Change 2007: The Physical Science Basis. Contribution of Working Group I to the Fourth Assessment Report of the Intergovernmental Panel on Climate Change [Solomon, S., D. Qin, M. Manning, Z. Chen, M. Marquis, K.B. Averyt, M.Tignor and H.L. Miller (eds.)]. 2007: Cambridge University Press, Cambridge, United Kingdom and New York, NY, USA.

[7] The National Oceanic and Atmospheric Administration [NOAA]. *El Niño & La Niña (El Niño-Southern Oscillation)*. Available from: http://tiny.cc/qkoksz

[8] The Intergovernmental Panel on Climate Change [IPCC], *Climate Change 2007: The Physical Science Basis*, Available from: https://bit.ly/3nQxfVf.

[9] BBC News. *What does Trump actually believe on climate change?* Available from: http://tiny.cc/ytarsz

[10] Department for Business, Energy & Industrial Strategy. *2016 Greenhouse Gas Emissions.* Available from: http://tiny.cc/fmoksz

[11] Myllyvirta, L., *Analysis: Coronavirus temporarily reduced China's CO2 emissions by a quarter*, 2020. Available from: http://tiny.cc/2noksz

[12] Ruixiong, Z. et al., *NOx Emission Reduction and Recovery during COVID-19 in East China*, Atmosphere, 2020. **11**(4): Article 433

[13] Myllyvirta, L. and H. Thieriot. *11,000 air pollution-related deaths avoided in Europe as coal, oil consumption plummet,* 2020. Available from: http://bit.ly/39DGW4m

[14] Global Food, Environment and Economic Dynamics. *COVID-19 reduces economic activity, which reduces pollution, which saves lives,* 2020. Available from: http://bit.ly/393AMuk

[15] Department for Business, Energy & Industrial Strategy. *Energy Trends March 2020.* Available from: http://tiny.cc/rooksz

[16] Wind Europe. *Wind energy in Europe in 2018: Trends and statistics,* 2019. Available from: http://tiny.cc/zooksz

[17] Foxon, T.J. et al., *UK innovation systems for new and renewable energy technologies: drivers, barriers and systems failures*. Energy Policy, 2005. **33**(16): p 2123-2137.
[18] Shockley, W., and H. Queisser. *Detailed balance limit of efficiency of pn junction solar cells.* Journal of Applied Physics, 1961. **32**(510): p 510-519.
[19] Kotzalas M. and G. Doll, *Tribological advancements for reliable wind turbine performance*. Philosophical Transactions of Royal Society A, 2010. **368**(1929): p 4829-4850.
[20] Faulstich, S., B. Hahn, H. Jung, and K. Rafik, *Suitable failure statistics as a key for improving availability.* Proceedings of the EWEC, 2009.
[21] Musial, W., S. Butterfield, and B. McNiff, *Improving Wind Turbine Gearbox Reliability*. European Wind Energy Conference, 2007.
[22] Shuangwen, S., *Report on Wind Turbine Subsystem Reliability – A survey of various databases*. National Renewable Energy Laboratory, 2013.
[23] Spectrum Energy Systems. *V42 Wind Turbine.* Available from: http://bit.ly/38hdRMS
[24] Froese, M., *Why integrated bearing designs reduce wind-turbine gearbox failures*, 2018. Available at: http://tiny.cc/wqoksz
[25] Schaeffler, *Bearing solutions and services for wind turbine gearboxes*, 2013. Available at: http://tiny.cc/81q7tz
[26] Ciprian, R., *The most common causes of bearing failure and the importance of bearing lubrication*, RKB Technical Review – February 2010, 2010. Available at: http://tiny.cc/91q7tz
[27] Scott, K. and D. Infield, *Effects of extreme and transient loads on wind turbine drive trains.* 50th AIAA Aerospace Sciences Meeting including the New Horizons Forum and Aerospace Exposition, 2012.
[28] Evans, M., *White structure flaking (WSF) in wind turbine gearbox bearings: effects of 'butterflies' and white etching cracks (WECs)*. Journal of Materials Science and Technology, 2011. **7**(2): p 3-22
[29] Evans, M., A. Richardson, L. Wang and R. Wood, *Serial sectioning investigation of butterfly and white etching crack (WEC) formation in wind turbine gearbox bearings.* Wear, 2013. **302**(1-2): p 1573-1582.
[30] NTN corporation. *Care and maintenance of bearings*. Available from: https://bit.ly/3s7HQij
[31] ISO 15243:2004(E). Rolling bearings – damage and failures – terms, characteristics and causes. (International Organisation for Standardisation, 2004)
[32] Widner, R. and W. Littmann, *Bearing damage analysis*. Proceedings of the 20th Meeting of the Mechanical Failures Prevention Group, 1974.
[33] Barden Precision Bearings. *Bearing failure: causes and cures*, 1992. Available from: https://bit.ly/3hN3dk1
[34] Hamilton, G. and S. Moore, *A modified gauge for investigating an elastohydrodynamic contact*. Proceedings of Institution of Mechanical Engineers, 1967. **182**: p 251.
[35] Spikes H. and P. Cann, *The development and application of the spacer layer imaging method for measuring lubricant film thickness*. Proceedings of the Institution of Mechanical Engineers Part J, 2001. **215**: p 261-277.

[36] Manwell, J., J. Mcgowan and A. Rogers, *Wind Energy Explained – Theory, Design and Application*. 2nd Edition. 2009: John Wiley & Sons Ltd.
[37] Casey, T. (2018), *Why the energy storage problem won't be a problem for long*, Available from: http://tiny.cc/3hpksz
[38] The Wind Power (2020), *Vestas V42*. Available from: http://bit.ly/35fanIN
[39] Datkhile, S., P. Tapre, and C. Veeresh, *A Comparative Study of Constant Speed and Variable Speed Wind Energy Conversion Systems,* Global Research and Development Journal for Engineering, 2016. **1**(10): p 19-24.
[40] Rashad, A., S. Kamel, F. Jurado and K. Mahmoud, *Performance Improvement of Various Types of Induction-based Wind Farms Using Center-node Unified Power Flow Controller*, International Journal of Control, Automation and Systems, 2018. **16**: p 2644-2655.
[41] Lars, H. and F. Blaabjerg (2002), *Wind turbine systems*. Available from: http://bit.ly/2LWPriL.
[42] The Royal Academy of Engineering (2010), *Wind Turbine Power Calculations*. Available from: https://bit.ly/3nMYYX8
[43] Evolution – the business and technology magazine from SKF, *Premature bearing failures in wind gearboxes and white etching cracks (WEC)*, Available from: http://bit.ly/3ssJefl.
[44] Liu, Z. and L. Zhang, A review of failure modes, condition monitoring and fault diagnosis methods for large-scale wind turbine bearings, Measurement, 2020. **149**: Article 107002.
[45] The TIMKEN Company (2020), *Engineered Bearings*. Available from: http://bit.ly/2XKwmD7
[46] Harris, T., *Rolling bearing analysis*. 4th Edition. 2001: John Wiley & Sons.
[47] Wei, Y., Y. Qin, R. Balendra and Q. Jiang, *FE analysis of a novel roller form: a deep end-cavity roller for roller-type bearings*, Journal of Material Processing Technology, 2004. **145**(2): p 233-241.
[48] Houpert, L., *Miscellaneous Engineering Approaches to Contact Elasticity Calculations*, Bearing World, 2018.
[49] Windpower Engineering & Development (2018), *2018 Renewable Energy Guidebook*. Available from: http://bit.ly/39xmYIF
[50] Evans, A., and R. Rawlings, The thermally activated deformation of crystalline materials, Physica Status Solidi (b), 1969. **34**(1): p 9-31.
[51] Schaeffler Technologies AG & Co. KG (2001), *INA Bearing failure mode archive*. Available from: https://bit.ly/35HqXkT
[52] He, Z., J. Zhang, W. Xie, Z. Li, and G. Zhang. *Misalignment analysis of journal bearing influenced by asymmetric deflection, based on a stepped shaft model*, Journal of Zhejiang University Science A, 2012. **13**: p 647-664.
[53] Whittle, M., W. Shin, J. Trevelyan and J. Wu, *A parametric study of the effect of generator misalignment on bearing fatigue life,* Proceedings of EWEC, 2011.
[54] Detweiler, W., (2011), *Common causes and cures for roller bearing overheating*. Available from: https://bit.ly/3bGkk60.
[55] FAG (2003), *Rolling bearing damage: recognition of damage and bearing inspection*. Available from: https://bit.ly/2XIO7D6.

[56] Schwack, F., N. Bader, J. Leckner, C. Demaille and G. Poll. *A study of grease lubricants under wind turbine pitch bearing conditions*, Wear, 2020. **454-455**: Article 203335.
[57] Tallian, T., *Failure atlas for Hertz contact machine elements*. 2nd Edition. 1999: American Society of Mechanical Engineers.
[58] Maleque, M., and M. Salit, *Materials Selection and Design*. 1st Edition. 2013: Springer Singapore.
[59] SKF (2017), *Bearing damage and failure analysis*. Available from: https://bit.ly/2XHsgM3.
[60] Zaretsky, E. (2010), *In search of a fatigue limit: A critique of ISO Standard 281:2007*. Available from: http://bit.ly/3oOZoxp.
[61] Martin, J. and A. Eberhardt, *Identification of potential failure nuclei in rolling contact fatigue*, Journal of Fluids Engineering, 1967. **89**(4): p 932-942.
[62] Luyckx, J. *Hammering wear impact fatigue hypothesis*, Wind turbine tribology seminar, 2011.
[63] Evans, M., *An updated review: white etching cracks (WECs) and axial cracks in wind turbine gearbox bearings*, Journal of Materials Science and Technology, 2016. **32**(11): p 1133-1169.
[64] Scott, D., B. Loy, and G. Mills, *Paper 10: Metallurgical Aspects of Rolling Contact Fatigue,* Proceedings of the Institution of Mechanical Engineers, 1966. **181**(15): p 94-103.
[65] Tamada, K., and H. Tanaka, *Occurrence of brittle flaking on bearings used for automotive electrical instruments and auxiliary devices*, Wear, 1996. 199(2): p 245-252.
[66] Gegner, J., *Tribological Aspects of Rolling Bearing Failures*, Tribology - Lubricants and Lubrication, 2011: IntechOpen.
[67] Uyama, H., H. Yamada, H. Hidaka, and N. Mitamura, *The Effects of Hydrogen on Microstructural Change and Surface Originated Flaking in Rolling Contact Fatigue*, Tribology Online, 2011. **6**(2): p 123–132.
[68] Holweger, W., *Influence on bearing life by new material phenomena*, Wind Turbine Tribology Seminar, 2011.
[69] Ruellan, A. *Tribological analysis of white etching crack (WEC) failures in rolling element bearings*, 2015, PhD thesis, INSA de Lyon.
[70] Grabulov, A., R. Petrov, and H. Zandbergen, *EBSD investigation of the crack initiation and TEM/FIB analyses of the microstructural changes around the cracks formed under Rolling Contact Fatigue (RCF)*, International Journal of Fatigue, 2010. **32**(3): p 576-583.
[71] Lamagnere, P., D. Girodin, P. Meynaud, F. Vergne and A. Vincent, *Study of elasto-plastic properties of microheterogeneities by means of nano-indentation measurements: Application to bearing steels*, Material Science and Engineering: A, 1996. **215**(1-2), p 134–142.
[72] Murakami, Y. and S. Beretta, *Small defects and inhomogeneities in fatigue strength: experiments, models and statistical implications*, Extremes, 1999. 2: p 123–147.
[73] Tricot, R., *Influence of metallurgical parameters on the phenomena of contact fatigue in rolling-sliding bearings and gears*, Rev. Met. Paris., 1976. **73**(4): p 385–411.

[74] Manieri, F., K. Stadler, G. Morales-Espejel, and A. Kadiric, *The origins of white etching cracks and their significance to rolling bearing failures*, International Journal of Fatigue, 2019. **120**: p 107-133
[75] Lai, J., and K. Stadler, *Investigation on the mechanisms of white etching crack (WEC) formation in rolling contact fatigue and identification of a root cause for bearing premature failure*, Wear, 2016. **364-365**: p 244-256.
[76] Holweger, W., et al., *White etching crack root cause investigation*, Tribology Transactions, 2015. **58**(1): p 59-69.
[77] Ruellan, A., X. Kleber, F. Ville, J. Cavoret and B. Liatard, *Understanding white etching cracks in rolling element bearings: Formation mechanisms and influent tribochemical drivers*, Proceedings of the Institution of Mechanical Engineers, Part J: Journal of Engineering Tribology, 2014. **229**(8): p 886-901.
[78] Uyama, H. and H. Yamada (2014), *White structure flaking in rolling bearings for wind turbine gearboxes*. Available from: https://bit.ly/35JQsll.
[79] Newlands, C., A. Olver, and N. Brandon, *Gaseous evolution of hydrogen from hydrocarbon oil and grease lubricated contacts*, Tribology Series, 2003. **41**: p 719-726.
[80] Kohara, M, T. Kawamura, and M. Egami, *Study on mechanism of hydrogen generation from lubricants*. Triblogy Transactions, 2006. **49**(1): p 53–60.
[81] Holweger W, *Progresses in solving white etching crack phenomena*, NREL - Gearbox reliability collaborative, 2014.
[82] Mikami, H. and T. Kawamura, *Influence of electrical current on bearing flaking life*, SAE World Congress & Exhibition, 2007.
[83] Evans, M., A. Richardson, L. Wang, R. Wood, W. Anderson, *Confirming subsurface initiation at non-metallic inclusions as one mechanism for white etching crack (WEC) formation*, Tribology International, 2014. **75**: p 87-97.
[84] Bruce, T., H. Long, T. Slatter and R. Dwyer-Joyce, *Formation of white etching cracks at manganese sulfide (MnS) inclusions in bearing steel due to hammering impact loading*, Wind Energy, 2016. **19**(10): p 1903-1915.
[85] Williams, J., *Engineering tribology*. 2005: Cambridge University Press.
[86] Stachowiak, G. and A. Batchelor, *Engineering tribology*. 4th Edition, 2013: Butterworth-Heinemann.
[87] Tribology: lubrication, friction, and wear [tribos] (2016), *Film Thickness Ratio or Lambda Ratio*, Available from: http://bit.ly/35Gl71K.
[88] The Torrington Company (2012), *Bearing failure prevention guide*, Available from: https://bit.ly/2LQcjk4.
[89] The Timken company (2014), *Timken bearing damage analysis with lubrication reference guide*, Available from: https://bit.ly/3bG0oQC.
[90] Evans, R., T. Barr, L. Houpert and S. Boyd, *Prevention of smearing damage in cylindrical roller bearings*, Tribology Transactions, 2013. **56**(5): p 703-716.
[91] Errichello, R., *Morphology of Micropitting*, Gear Technology, 2012. p 74-81.
[92] Machinery Lubrication (2003), *Predicting oil and grease life*, Available from: http://bit.ly/3srpWac.
[93] Raadnui, S. and S. Kleesuwan, *Electrical pitting wear debris analysis of grease-lubricated rolling element bearings*, Wear, 2011. **271**(9-10): p 1707-1718.

[94] Motion Control Tips (2017), *Electric motor fluting: What is it and what causes it?*, Available from: https://bit.ly/3idjAGS.
[95] Onyx Insight, *Electrical pitting – Bearing failure*, Available from: http://bit.ly/2XEHeCy.
[96] Onyx Insight, *Corrosion – Bearing failure*, Available from: http://bit.ly/39xTCK5.
[97] NTN Global, *Rust and Corrosion*, Available from: http://bit.ly/39x64df.
[98] Sheng, S., J. Keller and C. Glinsky, *Gearbox reliability collaborative update*, Sandia Reliability Workshop, 2013.
[99] Kim, K., G. Parthasarathy, O. Uluyol, W. Foslien, S. Sheng and P. Fleming, *Use of SCADA Data for Failure Detection in Wind Turbines*, ASME 2011 5th International Conference on Energy Sustainability, 2011.
[100] Yang, W., P. Tavner, C. Crabtree, Y. Feng and Y. Qiu, *Wind turbine condition monitoring: technical and commercial challenges,* Wind Energy, 2012. **17**(5): p 673-693.
[101] Wang, K., V. Sharma and Z. Zhang, *SCADA data based condition monitoring of wind turbines*, Advances in Manufacturing, 2014. **2**: p 61-69.
[102] Tonks, O. and Q. Wang, *The detection of wind turbine shaft misalignment using temperature monitoring*, CIRP Journal of Manufacturing Science and Technology, 2017. **17**: p 71-79.
[103] Terasaki, I., *Introduction to thermoelectricity*, Materials for Energy Conversion Devices, 2005. p 339-357.
[104] Omega, *Temperature probes*, Available from: http://bit.ly/2LT9FKw.
[105] Hameed Z., Y. Hong, Y. Cho, S. Ahn, C. Song, *Condition Monitoring and Fault Detection of Wind Turbines and Related Algorithms: A Review*. Renewable and Sustainable Energy Reviews, 2009. **13**(1): p 1-39.
[106] Gear Technology (2013), *Understanding Oil Analysis: How It Can Improve the Reliability of Wind Turbine Gearboxes*, Available from: http://bit.ly/3nLp78J.
[107] Hamilton, A. and F. Quail, *Detailed State of the Art Review for the different Online/Inline Oil Analysis Techniques in Context of Wind Turbine Gearboxes*, Journal of Tribology, 2011. **133**(4): Article 044001.
[108] Tchakoua, P., R. Wamkeue, M. Ouhrouche, F. Slaoui-Hasnaoui, T. Tameghe and G. Ekemb, *Wind Turbine Condition Monitoring: State-of-the-Art Review, New Trends, and Future Challenges*, Energies, 2014. **7**: p 2595-2630.
[109] Dupuis, R, *Application of oil debris monitoring for wind turbine gearbox prognostics and health management*, Annual Conference of the Prognostics and Health Management Society, 2010.
[110] Powrie, H, R. Wood, T. Harvey, L. Wang and S. Morris, *Electrostatic charge generation associated with machinery component deterioration*, Proceedings in IEEE Aerospace Conference, 2002.
[111] Liu, R., H. Zuo, J. Sun, L. Wang, *Electrostatic monitoring of wind turbine gearbox on oil-lubricated system*, Proceedings of the Institution of Mechanical Engineers, Part C: Journal of Mechanical Engineering Science, 2016. **231**(19): p 3649-3664.
[112] Harvey, T., R. Wood and H. Powrie, *Electrostatic wear monitoring of rolling element bearings*, Wear, 2007. **263**(7-12): p 1492-1501.

[113] Pawlak, Z., *Tribochemistry of Lubricating Oils*, 1st Edition. 2003: Elsevier Science.
[114] Sheng, S. and P. Veers, *Wind Turbine Drivetrain Condition Monitoring—An Overview*, Mechanical Failures Prevention Group: Applied Systems Health Management Conference, 2011.
[115] Madsen, B., *Condition Monitoring of Wind Turbines by Electric Signature Analysis*, 2011, Master's Thesis, Technical University of Denmark.
[116] Marquez, F., A. Tobias, J. Perez and M. Papaelias, *Condition monitoring of wind turbines: Techniques and methods*, Renewable Energy, 2012. **46**: p 169-178.
[117] Gupta, P. and M. Pradhan, *Fault detection analysis in rolling element bearing: A review*, 5th International Conference of Materials Processing and Characterization, 2017. **4**(2): p 2085-2094.
[118] ISO 10816-8:2018. Mechanical vibration – Evaluation of machine vibration by measurements on non-rotating parts – Part 8: Reciprocating compressor systems. (International Organisation for Standardisation, 2018)
[119] Dyer, D. and R. Stewart, *Detection of rolling element bearing damage by statistical vibration analysis*, Journal of Mechanical Design, 1978. **100**(2): p 229-235.
[120] Shanbr, S., F. Elasha, M. Elforjani, J. Teixeira, *Detection of natural crack in wind turbine gearbox*, Renewable Energy, 2018. **118**: p 172-179.
[121] Yang, Z., U. Merrild, M. Runge, G. Pedersen and H. Borsting, *A study of rolling element bearing fault diagnosis using motor's vibration and current signatures*, IFAC Proceedings Volumes, 2009. **42**(8): p 354-359.
[122] Soresen, B., et al., *Fundamentals for remote structural health monitoring of wind turbine blades -a Preproject*, Riso National Laboratory, 2002.
[123] Schubel, P., R. Crossley, E. Boateng and J. Hutchinson, *Review of structural health and cure monitoring techniques for large wind turbine blades*, Renewable Energy, 2013. **51**: p 113–123.
[124] Hyers, R., J. McGowan, K. Sullivan, J. Manwell and B. Syrett, *Condition monitoring and prognosis of utility scale wind turbines*, Energy Materials, 2006. **1**(3): p 187–203.
[125] Tan, C., P. Irving and D. Mba, *A comparative experimental study on the diagnostic and prognostic capabilities of acoustics emission, vibration and spectrometric oil analysis for spur gears*, Mechanical Systems and Signal Processing, 2007. **21**(1): p 208–233.
[126] Li, C. and S. Li, *Acoustic emission analysis for bearing condition Monitoring*, Wear, 1995. **185**(1): p 67-74.
[127] Mba, D. and R. Rao, *Development of Acoustic Emission Technology for Condition Monitoring and Diagnosis of Rotating Machines: Bearings, Pumps, Gearboxes, Engines and Rotating Structures*, Shock Vibration Digest, 2006. **37**(5): p 3-16.
[128] Kundu, T., *Acoustic source localization*, Ultrasonics, 2014. **54**(1): p 25-38.
[129] Al-Jumaili, S., M. Pearson, K. Holford, M. Eaton and R. Pullin, *Acoustic emission source location in complex structures using full automatic delta T mapping technique*, Mechanical Systems and Signal Processing, 2016. **72-73**: p 513-524.

[130] Lu, B., Y. Li, X. Wu and Z. Yang, *A review of recent advances in wind turbine condition monitoring and fault diagnosis*, Proceedings of IEEE Power Electronics and Machines in Wind Applications, 2009.
[131] Chakrapani, S., V. Dayal, R. Krafka and A. Eldal, *Ultrasonic testing of adhesive bonds of thick composites with applications to wind turbine blades*, AIP Conference Proceedings, 2012. **1430**: p 1284-1290.
[132] Li, S., K. Shi, K. Yang and J. Xu, *Research on the defect types judgment in wind turbine blades using ultrasonic NDT*, IOP Conference Series: Material Science and Engineering, 2015. **87**: Article 012056.
[133] Dwyer-Joyce R., B. Drinkwater, and C. Donohoe, *The measurement of lubricant-film thickness using ultrasound*, Proceedings of the Royal Society A, 2003. **459**(2032): p 957-976.
[134] Dwyer-Joyce R., T. Reddyhoff, and B. Drinkwater, *Operating Limits for Acoustic Measurement of Rolling Bearing Oil Film Thickness*, Tribology Transactions, 2004. **47**(3): p 366-375.
[135] Chen W., R. Mills, and R. Dwyer-Joyce, *Direct Load Monitoring of Rolling Bearing Contacts using Ultrasonic Time of Flight*, Proceedings of the Royal Society A, 2015. **471**(2180): p 1-21.
[136] Sensorland, *how they work: The Strain gauge*, Available from: https://bit.ly/35GOxxY.
[137] Omega, *Linear Strain Gauges - SGD-1.5/120-LY11*, Available from: http://bit.ly/2LQeggz
[138] Keller, J. and B. McNiff, *Gearbox reliability collaborative high-speed shaft calibration,* NREL Technical Report, 2014.
[139] Omega, *Introduction to Strain gauges*, Available from: http://bit.ly/3stgRhi.
[140] Engineering fundamentals, *Sensitivity of strain gage wire materials*, Available from: http://bit.ly/35JRqOv.
[141] Guo, Y. and J. Keller, *Investigation of high-speed shaft bearing loads in wind turbine gearbox through dynamometer testing*, Wind Energy, 2018. **21**(2): p 139–150.
[142] Camp, V., *From "condition monitoring" to "reliable rotation" – how technology enables industrial revolutions, and how people turn technology into business value*, Bearing World Conference, 2018.
[143] Dantec Dynamics, *Measurement Principles of DIC*, Available from: http://bit.ly/38JixLG.
[144] Pan, B., K. Qian, H. Xie and A. Asundi, *Two-dimensional digital image correlation for in-plane displacement and strain measurement: A review*, Measurement Science and Technology, 2009. **20**: Article 062001.
[145] Instron, *An Introduction to Digital Image Correlation (DIC)*, Available from: http://bit.ly/3idlvdr.
[146] McCormick, N. and J. Lord, *Digital Image correlation*, Materials Today, 2010. **13**(12): p 52-54.
[147] Krautkramer, H., and J. Krautkramer, *Ultrasonic Testing of Materials*, 4th Edition, 1990: Springer-Verlag.
[148] Morgner, W., K. Schiebold and H. Krause, *Ultrasonic high-temperature materials evaluation – a solved problem?,* Material Evaluation, 1987. **45**: p 569-571.

[149] Manbachi, A. and R. Cobbold, *Development and Application of Piezoelectric Materials for Ultrasound Generation and Detection*, Ultrasound, 2011. **19**(4): p 187–196.
[150] Olympus, *Conventional Transducer Construction*, Available from: http://bit.ly/3nNRCm0.
[151] Kažys R., A. Voleišis and B. Voleišienė, *High temperature ultrasonic transducers: review*, Ultragarsas, 2008. 63(2): p 7-17.
[152] BS EN 50324-2:2002. Piezoelectric properties of ceramic materials and components. Methods of measurement. Low power. (British Standards, 2002)
[153] Piezo systems, *Material Properties*, Available from: http://bit.ly/2LPVaHo.
[154] Meggitt A/S, Pz27 (Navy II) Soft relaxor type PZT, Available from: https://bit.ly/3igSe2t.
[155] American Piezo Ceramics International, Piezo Electrode Patterns, Available from: http://bit.ly/3bNNErv.
[156] Dwyer-Joyce, R., T. Reddyhoff and J. Zhu, *Ultrasonic measurement for film thickness and solid contact in Elastohydrodynamic lubrication*, Journal of Tribology, 2011. **133**(3): Article 031501.
[157] Gonzalez-Valadez, M., R. Dwyer-Joyce and R. Lewis, *Ultrasonic reflection from mixed liquid-solid contacts and the determination of interface stiffness*, Tribology and Interface Engineering Series, 2005. **48**: p 313-320.
[158] Hunter, A., *Ultrasonic Measurements of the strip thickness, lubricant film thickness, roll deflection and roll stress in a roll bite in the cold rolling of steel*, 2018, PhD Thesis, University of Sheffield.
[159] El-Sisi S. and G. Shawki, *Measurement of oil-film thickness between disks by electrical conductivity*. Journal of Fluids Engineering, 1960. **82**(1): p 12-16.
[160] Astridge D. and M. Longfield, *Capacitance measurement and oil film thickness in a large radius disc and ring machine*. Proceedings of the Institution of Mechanical Engineers, 1967. **182**: p 89-96.
[161] Glavatskih, S., O. Uusitalo and D. Spohn, *Simultaneous monitoring of oil film thickness and temperature in fluid film bearings*. Tribology International, 2001. **34**(12): p 853-857.
[162] Pialucha, T. and P. Cawley, *The detection of thin embedded layers using normal incidence ultrasound*, Ultrasonics, 1994. **32**(6): p 431-440.
[163] Zhang, K., Q. Meng and W. Zhao, *Measurement of oil film thickness in cylindrical roller bearing by ultrasound*, ASME 2014 12th Biennial Conference on Engineering Systems Design and Analysis, 2014.
[164] Li, M., H. Liu, C. Xu, M. Jing and G. Dong, *Ultrasonic measurement of cylindrical roller-bearing lubricant film distribution with two juxtaposed transducers*, Tribology Transactions, 2017. **60**(1): p 79-86.
[165] Zhang, K., Q. Meng, W. Chen, J. Li, P. Harper, *Ultrasonic measurement of oil film thickness between the roller and the inner raceway in a roller bearing*, Industrial Lubrication and Tribology, 2015. **67**(6): p 531-537.
[166] Li, M., M. Jing, Z. Chen and H. Liu, *An improved ultrasonic method for lubricant-film thickness measurement in cylindrical roller bearings under light radial load*, Tribology International, 2014. **78**: p 35-40.

[167] Reddyhoff, T., S. Kasolang, R. Dwyer-Joyce and B. Drinkwater, *The phase shift of an ultrasonic pulse at an oil layer and determination of film thickness*, Proceedings of the Institution of Mechanical Engineers Part J: Journal of Engineering Tribology, 2005. **219**(6): p 387-400.
[168] Lindner, G., C. Bruckner and M. Schmitt, *Online bearing lubricant sensing by mode conversion of surface acoustic waves*, Sensor+Test Conferences, 2011.
[169] Takeuchi, A., *Detection of Operational Abnormality of Ball Bearing with Ultrasonic Technique*, Key Engineering Materials, 2004. **270-273**: p 252-257.
[170] Pao, Y., *Theory of Acoustoelasticity and Acoustoplasticity*, Solid mechanics research for quantitative non-destructive evaluation, 1987. p 257-273.
[171] Howard, T., *Development of a novel bearing concept for improved wind turbine gearbox reliability*, 2016, PhD Thesis, University of Sheffield.
[172] BS EN 61400-4:2013. Wind turbines, Part 4: Design requirements for wind turbine gearboxes. (British Standards, 2013)
[173] LaCava, W., Y. Xing, C. Marks, Y. Guo and T. Moan, *Three-dimensional bearing load share behaviour in the planetary stage of a wind turbine gearbox*, IET Renewable Power Generation, 2013. **7**(4): p 359-369.
[174] Guo, Y., J. Keller and W. LaCava, *Combined effects of gravity, bending moments, bearing clearance and input torque on wind turbine planetary gear load sharing*, American Gear Manufacturers Association (AGMA) Fall Technical Meeting, 2012.
[175] LaCava, W., J. Keller and B. McNiff, *Gearbox reliability collaborative: Test and model investigation of sun orbit & planet load share in a wind turbine gearbox*, 53rd AIAA/ASME/ASCE/AHS/ASC Structures, Structural Dynamics and Materials Conference, 2012.
[176] Bruce T., H. Long, and R. Dwyer-Joyce, *Dynamic modelling of wind turbine gearbox bearing loading during transient events*. IET Renewable Power Energy, 2015. **9**(7): p 821-830
[177] ISO 281:2007. Rolling bearings – Dynamic load ratings and rating life. (International Organisation for Standardisation, 2007)
[178] Massachusetts Institute of Technology [MIT], *Module 3: Constitutive Equations*, Available from: https://bit.ly/35KnMZv.
[179] Egle, D. and D. Bray, Measurement of acoustoelastic and third-order elastic constants for rail steel, The Journal of the Acoustical Society of America, 1976. **60**(3): p 741-744.
[180] Afzalul, K. and H. Zhang, *Measurement of non-linear elastic constants of rail steel*, Conference Proceedings of SPIE, 2012.
[181] Dubuc, B., A. Ebrahimkhanlou and S. Salamone, *Higher order longitudinal guided wave modes in axially stressed seven-wire strands*, Ultrasonics, 2018. **84**: p 382-391.
[182] Takahashi, S., *Measurement of third-order elastic constants and stress dependent coefficients for steels*, Mechanics of Advanced Materials and Modern Processes, **4**: Article 2.
[183] Takahashi, S. and K. Takahashi, *Third order elastic constants of semi-continuous casting ingot A3004 aluminium alloy and measurement of stress*, Journal of Material Science, 2007. **42**: p 2070-2075.

[184] Stobbe, D., *Acoustoelasticity in 7075-T651 Aluminium and Dependence of Third Order Elastic Constants on Fatigue Damage*, 2005, PhD Thesis, Georgia Institute of Technology.
[185] Crecraft, D., *Ultrasonic wave velocities in stressed nickel steel*, Nature, 1962. **195**: p 1193-1194.
[186] Johnson, K., *One Hundred years of Hertz Contact*, Proceedings of the Institution of Mechanical Engineers, 1982. **196**(1): p 363-378.
[187] Teutsch, R. and B. Sauer, *An Alternative Slicing Technique to consider pressure concentrations in non-hertzian line contacts*, ASME Journal of Tribology, 2004. **126**(3): p 436-442.
[188] Tripp, J., *Hertzian contact in two and three dimensions*, NASA Technical Paper 2473, 1985.
[189] Zantopulos, H., *An alternate solution of the deformation of a cylinder between two flat plates*, ASME Journal of Tribology, 1988. **110**(4): p 727-729.
[190] Houpert, L., *An engineering approach to Hertzian contact elasticity – Part I*, ASME Journal of Tribology, 2001. **123**(3): p 582-588.
[191] Houpert, L., *Hydrodynamic load calculation in rolling element bearings*, Tribology Transactions, 2016. **59**(3): p 538-559.
[192] AGMA 925-A03. Effect of lubrication on gear surface distress. (American Gear Manufacturers Association, 2013)
[193] Donolo, P., G. Bossio, C. Angelo, G. Garcia and M. Donolo, *Voltage unbalance and harmonic distortion effects on induction motor power, torque and vibrations*, Electric Power Systems Research, 2016. **140**: p 866-873.
[194] Ferguson, D., *Installation of Wind Turbine Condition Monitoring Equipment at Barnesmore Wind Farm*, Internal Report, 2015.
[195] Howard, T., R. Fuentes, D. Ferguson, J. Feuchtwang, D. Benchebra, J. Wheals and E. Bower, *OWDIN MultiLife and CMS Turbine Data Analysis Milestone 7 Report*, Internal Report, 2016.
[196] Guo Y. and J. Keller, *Investigation of high-speed shaft bearing loads in wind turbine gearbox through dynamometer testing*. Wind Energy, 2018. **21**(2): p 139-150.
[197] Ma, F., P. Ji, Z. Li, B. Wu, Q. An, *Influences of off-sized rollers on mechanical performance of spherical roller bearings*, Proceedings of the Institution of Mechanical Engineers, Part K: Journal of Multi-body Dynamics, 2015. **229**(4): p 344 – 356.
[198] Chen, G., F. Mao, and B. Wang, *Effects of off-sized cylindrical rollers on the static load distribution in a cylinder roller bearing*, Proceedings of the Institution of Mechanical Engineers, Part J: Journal of Engineering Tribology, 2012. **226**(8): p 687 – 696.
[199] Tong, V. and S. Hong, *Study on the stiffness and fatigue life of tapered roller bearings with roller diameter error*, Proceedings of the Institution of Mechanical Engineers, Part J: Journal of Engineering Tribology, 2017. **231**(2): p 176–188.
[200] Gupta, P., *On the Geometrical Imperfections in Cylindrical Roller Bearings*, ASME Journal of Tribology, 1988. **110**(1): p 13–18.
[201] Poplawski, J., S. Peters and E. Zaretsky, *Effect of roller profile on cylindrical roller bearing life prediction - Part II Comparison of roller profiles*, Tribology Transactions, 2001. **44**(3): p 417–427.

[202] Lugt, P., *Grease Lubrication in Rolling Bearings*, 1st Edition. 2013: John Wiley & Sons.
[203] Johnson, K., *Contact Mechanics*, 1st Edition. 1985: Cambridge University Press.

APPENDIX

Roller Load Measurement Algorithm for Barnesmore data

```
function [P_peaks,R_Ppeaks,P_minR,R_min1,RPM]=CMS2US_Batch4R(FileName)

animate=false;

d = TDMS_getStruct([pwd '\' FileName]);

v=isfield(d,'US_Streaming');

if v==1
    pLength = double(d.Signal_Configs.Props.US_Pulse_Range);
    pRate = double(d.Signal_Configs.Props.US_Pulse_Rate);
    us = double(d.US_Streaming.US_Ch1.data');
    F = 100; % MHz Sampling Frequency
    dT = 1/F; % microsecs

    pulseT = (dT:dT:pLength*dT)'; % time vector for a single pulse
    pulses = floor(length(us)/pLength); % number of pulses in the datastream
    us = us(1:pulses*pLength); % clip just incase there are any trailing zeros
    US = reshape(us,pLength,pulses); % convert to a matrix to make processing a bit easier
    % clip the first 12000 pulses as they are in the fluctuation zone
    clip=1;
    US=US(:,clip:length(US));

    p2p = range(US); % find the peak-to-peak amplitude of each pulse [same as p2p =
max(US)-min(US)]

    US = US(:,p2p ~= 0);
    p2p = p2p(p2p ~= 0);
    us = reshape(US,1,numel(US)); % reconstruct raw us matrix of one row reason maybe
                              % to filter out the zeros maybe?

    pulses = size(US,2); %returns no of columns of the US matrix
                     % equals to number of pulses in this raw ultrasonic data

    UST = (1/pRate:1/pRate:pulses/pRate)'; % time vector for ultrasonic data matrix
                                       % pRate is Pulse Repetition Rate!
    usT = UST(1)/pLength:UST(1)/pLength:length(us)*(UST(1)/pLength); % time vector for raw
ultrasonic datastream (vector)

% time between two usT points = UST(1)/pLength

ref = mode(US,2); % find the modal reference pulse

% most frequent value from all the 70 pulse points (each row)

% Spectral analysis
zPad = 1024; % zero pad width - for optimizing FFT
pulseF = linspace(0,F/2,(zPad/2)+1)'; % Frequency vector
refS = abs(fft(ref,zPad)/pLength); % frequency spectrum for reference pulse
                                   % not really sure why divide by pLength
refS = refS(1:(zPad/2)+1); % clip - remove half of the matrix
```

```
% find the peak spectral amplitude and -6dB bandwidth
[resAmp,resLoc] = max(refS); % determine resonant frequency amplitude and the column where
it occurred
resFreq = pulseF(resLoc); % extract resonant frequency from frequency vector
A1 = resAmp*10^(-6/20); % amplitude at -6dB of peak amp
                        % dB = 20 log (Gain)
                        % -6 dB of peak amp = (10^(-6/20)) x resAmp

% start and end points of the sensor bandwidth:
BWstart = find(refS >= A1,1,'first');
BWend = find(refS >= A1,1,'last');

% spectral analysis of full ultrasonic dataset
USS = abs(fft(US,zPad)/pLength);
USS = USS(1:(zPad/2)+1,:);

% calculate reflection coefficient only for the resonance location
R = (USS(resLoc,:)/refS(resLoc))';
```

One sided PSD - BPFO compute

```
normR=R-mean(R);
L=length(normR);
NFFT=max(256,2^nextpow2(length(normR)));
X=fft(normR,NFFT);
Px=X.*conj(X)/(NFFT*L); %Power of each freq components
fVals=pRate*(0:NFFT/2-1)/NFFT;

clip1=find(fVals==max(fVals(fVals<=250)));

Pxx=Px(1:clip1);

[~,BPFIdx] = findpeaks(Pxx,'MinPeakDistance',5,'MinPeakHeight',0.6*max(Pxx));
if min(R)<=0.9 && range(R)>=0.2
    if isempty(BPFIdx)==0
       BPFO=fVals(1,BPFIdx(1,:));
       RPM=BPFO*120/20/(1-(22.92/154.26)*cos(15.64*pi/180));
    else
        BPFO=0;
        RPM=NaN;
    end
else
    BPFO=0;
    RPM=0;

end
```

Get ToF and compute load

```
Href = abs(hilbert(ref)); % Hilbert transform reference signal to get its envelope
% interpolate envelope to increase resolution: this is to increase accuracy
pulseTi = (dT/100:dT/100:pLength*dT)'; % Increased resolution of time vector for a single
pulse
Href = interp1(pulseT,Href,pulseTi,'spline');
```

```
% envelope all ultrasonic pulses and interpolate these too:
Hmeas = abs(hilbert(US));
Hmeas = interp1(pulseT,Hmeas,pulseTi,'spline');

% normalise each measurement waveform (with max Hmeas value)
Hmeas = Hmeas./repmat(max(Hmeas),size(Hmeas,1),1);

% and the reference envelope (with max Href value)
Href = Href/max(Href);

% create a time vector for cross correlation
CT = [-1*(flipud(pulseTi(2:end)));pulseTi]; % create 1 column array of [-0.7:1e-4:0.7]
without 0 & -1e-4
I = find(CT >= -0.01,1,'first'); % find the row where CT >= -0.01
CT = CT(I:end); % create 1 column array of [-0.01:1e-4:0.7]
dToF = zeros(size(Hmeas,2),1); %create array of zeros of 14064 x 1 to record change in ToF

parfor iMeas = 1:size(Hmeas,2)
    % cross-correlate each ultrasonic pulse envelope with the reference
    % pulse envelope:
    C = xcorr(Href,Hmeas(:,iMeas));
    % get rid of any -ve peaks - (these can occur due to interference
    % fringes and will mess up the detection of the real time shift due to
    % deflection)...
    C = C(I:end);
    [~,maxLoc] = max(C);
    if animate
        if iMeas == 1
            figure(iFig)
            iFig = iFig + 1;
        end
        subplot(1,2,1)
        plot(pulseT,[ref US(:,iMeas)])
        grid on
        title 'Time Domain Pulses'
        ylabel 'Signal Amplitude'
        xlabel 'Time (\mus)'
        subplot(1,2,2)
        plot(pulseTi,[Href Hmeas(:,iMeas)])
        grid on
        title 'Normalised Signal Envelopes'
        xlabel 'Time (\mus)'
        pause(0.05)
    end
    dToF(iMeas) = CT(maxLoc)/1E6; % change in time of flight (seconds)
                                  % CT changes with each iMeas as the
                                  % maxLoc changes
end
clear C maxLoc iMeas

% convert time shifts to load using ROMULUS method:
dToF(dToF <= 0) = NaN;
Lzz = -2.26; % acousto-elastic constant
waveVelocity = 5960; % m/s
% deflection
defl=dToF*waveVelocity./(1-Lzz);
% Luc Point Contact Hertzian Eq
```

```
Kpc=1.79621E+11;
P=Kpc.*(defl).^1.5;
P=P/1000;

Href = abs(hilbert(ref));
Hmeas = abs(hilbert(US));
W=zeros(size(Hmeas,1),length(US));
for i=1:length(US)
    W(:,i)=Href-Hmeas(:,i);
    i=i+1;
end
PP=zeros(length(US),1);

if BPFO>=180
    WW=W(30,:);
    WW_w=WW>=20;
    for q=1:length(US)
        if WW_w(1,q)==1
            PP(q,1)=P(q,1);
        else PP(q,1)=NaN;
            q=q+1;
        end
    end
else
    WW=W(30,:);
    WW=WW/max(WW);
    WW_w=WW>=0.68;
    for q=1:length(US)
        if WW_w(1,q)==1
            PP(q,1)=P(q,1);
        else PP(q,1)=NaN;
            q=q+1;
        end
    end
end

PPP=PP;
po=isnan(PP);
x=1;
for x=1:length(PP)
    if po(x,1)==1
        PPP(x,1)=0;
    x=x+1;
    end
end
P=PPP;
dis=pRate*0.8/BPFO;
[Ppeaks,locs] = findpeaks(P,'MinPeakDistance',dis,...
    'MinPeakHeight',0.4*max(P));
```

```
[~,MinIdx] = findpeaks(-R,'MinPeakDistance',dis);

R_Ppeaks=R(locs);
R_Ppeaks(R_Ppeaks>0.95,:)=NaN;
R_Ppeaks=nanmean(R(locs));
% R_Ppeaks=R(locs);
R_min1=R(MinIdx);
```

```
R_min1(R_min1>0.95,:)=NaN;
R_min1=nanmean(R_min1);

P_peaks=mean(Ppeaks);
% P_minR=P(MinIdx);
P_minR=nanmean(P(MinIdx));
```

```
else
    P_minR=NaN;
    R_min1=NaN;
    RPM=NaN;
    R_Ppeaks=NaN;
    P_peaks=NaN;


end

clear v d
end
```